Thèse
de doctorat
de l'UTT

Haobing WANG

Comprehensive Performance Study and Optimization of S-DNTT-10-based Organic Thin-film Transistors

Champ disciplinaire :
Sciences pour l'Ingénieur

2024TROY0049 **Année 2024**

utt
UNIVERSITÉ DE TECHNOLOGIE
TROYES

THESE

pour l'obtention du grade de

DOCTEUR
de l'UNIVERSITE DE TECHNOLOGIE DE TROYES

en SCIENCES POUR L'INGENIEUR

Spécialité : MATERIAUX, MECANIQUE, OPTIQUE ET NANOTECHNOLOGIE

présentée et soutenue par

Haobing WANG

le 20 décembre 2024

Comprehensive Performance Study and Optimization of S-DNTT-10-based Organic Thin-film Transistors

JURY

M. Yvan BONNASSIEUX	PROFESSEUR DES UNIVERSITES	Président
M. Mamatimin ABBAS	CHARGE DE RECHERCHE CNRS – HDR	Rapporteur
M. Alfred J. MEIXNER	PROFESSOR DOCTOR	Rapporteur
Mme Anne-Laure BAUDRION-BÉAL	MAITRE DE CONFERENCES – HDR	Examinatrice
M. Martin BRINKMANN	DIRECTEUR DE RECHERCHE CNRS	Examinateur
M. Louis GIRAUDET	PROFESSEUR DES UNIVERSITES	Examinateur
M. Pierre-Michel ADAM	PROFESSEUR DES UNIVERSITES	Directeur de thèse
M. Olivier SIMONETTI	MAITRE DE CONFERENCES – HDR	Directeur de thèse

Acknowledgements

First and foremost, I would like to express my appreciation to my country, China, and China Scholarship Council (CSC) for providing this cherishing opportunity that I go aboard to do Ph.D. research in France.

I would like to express my deepest gratitude to my supervisor, Olivier Simonetti, at the University of Reims Champagne-Ardenne (URCA). During this 4 years-Ph.D. study, almost of the Ph.D. research and study was done at URCA. His invaluable guidance, insightful feedback, and continuous support throughout my overseas journey. His expertise and encouragement have been instrumental in shaping my research and academic development. And his personalities that kindness and friendly passion makes me not feel lonely in the life at foreign country. As well, I would like to sincerely thank my co-supervisor, Pierre-Michel Adam, at Université de Technologie de Troyes (UTT). I am grateful to him for providing me with the opportunity to obtain a PhD project that attracts me. Also, he provided me with guidance in Raman scattered technology. Additionally, they did not care about my low English level. Sometimes when I didn't express myself clearly, they listened to me actively and patiently. Anyway, I appreciate my sincere gratitude to them.

I would like to extend my heartfelt thanks to my colleagues and friends in the Light, nanomaterials, nanotechnologies (L2n) and NANO-PHOT School, at URCA and UTT. Their camaraderie, stimulating discussions, and collaborative spirit have made my time in the lab both productive and enjoyable. Special thanks go to Louis Giraudet, he provided me some precious suggestion on experiments. Nicolas Bercu, he patiently instructed me on the use of AFM and KPFM. He was very helpful in characterizing the device performance. Florence Etienne and Sylvain Potiron, they together assisted me so much on fabrication of OTFTs. Thanks them for helping me learning more knowledge about organic thin-film transistors, advanced nano-scale characterization tools and fabrication approach again. Additionally, I thank my colleges, Rakesh Mittapalli, Lucas Kaique Martins Roncaselli and Elias Makhoul. Thanks for helping me in the daily life.

I am also appreciative of the administrative staff at UTT and URCA for their assistance with all the logistical and bureaucratic aspects of my studies. Their efficiency and professionalism have allowed me to focus more on my research without worrying about the details.

On a personal note, I would like to express my deepest gratitude to my family, especially my parents for their unwavering love, patience, and encouragement. Their belief in me has been my anchor during the most challenging times of this journey. I am also grateful to my girlfriend, Xin Juan, for their understanding, support, and constant belief in my abilities. In addition, I would also like to thank my good brother, Jian Dou, who I have known for almost 20 years in China, for his encouragement and for making me stronger from failures.

To all those who have contributed to my academic and personal growth during this journey, I offer my sincere thanks.

Abstract

With technological advancements, semiconductor-based electronic devices have become indispensable in daily life and industrial production, closely linking them to each area in human civilization. Among these, thin-film transistors (TFTs) play a crucial role in electronic systems. Initially, TFTs were made from inorganic semiconductors, and with the development that physical and chemical sciences have shifted attention to organic thin-film transistors (OTFTs), which employed the organic semiconductor (OSC) material as the active layer. The performance has significantly improved, positioning them as a promising alternative to traditional inorganic TFTs and a potential driver for the next generation of electronics.

The electrical performance of OTFTs is influenced by various factors, with the characteristics of OSC molecules being particularly crucial. This thesis focuses on the new OSC material, S-DNTT-10, firstly reported in 2020, and investigates its molecular properties, the electrical characteristics of S-DNTT-10-based OTFTs, and strategies for optimizing device performance. The research explores molecular vibrations, charge transport mechanisms, and external factors impacting OTFT performance, as well as strategies to optimize the electrical properties of S-DNTT-10-based OTFTs.

In this study, we combined theoretical simulations with experimental techniques such as atomic force microscopy (AFM), Kelvin probe force microscopy (KPFM), and Raman spectroscopy, along with density functional theory (DFT) simulations. Raman spectroscopy, including surface-enhanced Raman scattering (SERS), was employed to investigate the molecular vibrations of S-DNTT-10, revealing and replenishing its detailed vibrational properties for the first time. Additionally, we conducted a comprehensive study on the effects of prolonged stressed electric field exposure and annealing treatment on the electrical performance of S-DNTT-10-based OTFTs. This study marks the first integration of AFM, KPFM, Raman spectroscopy, and *IV* characteristics to examine these effects, providing insights into how external factors influence device performance. Moreover, we proposed the addition of an extra OSC layer on the S-DNTT-10 surface to enhance device performance and stability. The results demonstrate that optimizing the fabrication process and device structure significantly reduces source contact resistance, improves charge injection, and enhances overall performance. These findings underscore the potential of S-DNTT-10 as a promising material for future flexible electronics.

Résumé

Avec les avancées technologiques, les dispositifs électroniques à semi-conducteurs sont devenus essentiels dans la vie quotidienne et l'industrie, impactant divers aspects de la civilisation. Les transistors à film mince (TFT) jouent un rôle clé dans les systèmes électroniques. Initialement fabriqués avec des semi-conducteurs inorganiques, les TFT ont évolué, attirant l'attention vers les transistors organiques à film mince (OTFT), utilisant des semi-conducteurs organiques (OSC) comme couche active. Leurs performances se sont améliorées, faisant des OTFT une alternative prometteuse aux TFT inorganiques et un moteur pour la prochaine génération d'électronique.

Les performances des OTFT sont influencées par plusieurs facteurs, notamment les caractéristiques des molécules de OSC. Cette thèse se concentre sur le nouveau matériau OSC, le S-DNTT-10, rapporté en 2020, et examine ses propriétés moléculaires, les performances électriques des OTFT basés sur le S-DNTT-10, ainsi que des stratégies d'optimisation. La recherche explore les vibrations moléculaires, les mécanismes de transport de charge, les facteurs externes influençant les performances et les approches pour améliorer les OTFT à base de S-DNTT-10.

Dans cette étude, nous avons combiné des simulations théoriques avec des techniques expérimentales comme la microscopie à force atomique (AFM), la microscopie à force Kelvin (KPFM) et la spectroscopie Raman, ainsi que des simulations basées sur la théorie de la fonctionnelle de la densité (DFT). La spectroscopie Raman, y compris la diffusion Raman amplifiée de surface (SERS), a révélé et complété pour la première fois les propriétés vibratoires détaillées du S-DNTT-10. Nous avons également étudié les effets d'une exposition prolongée à un champ électrique et d'un recuit sur les performances électriques des OTFT à base de S-DNTT-10. Cette étude intègre pour la première fois l'AFM, la KPFM, la spectroscopie Raman et les caractéristiques *IV* pour examiner ces effets, offrant des informations sur l'influence des facteurs externes. Nous avons proposé d'ajouter une couche supplémentaire d'OSC sur le S-DNTT-10 pour améliorer les performances et la stabilité des dispositifs. Les résultats montrent que l'optimisation du processus de fabrication réduit la résistance de contact, améliore l'injection de charge et renforce les performances. Ces résultats soulignent le potentiel du S-DNTT-10 pour l'électronique flexible.

Contents

Acknowledgements ..... **I**

Abstract ..... **III**

Résumé ..... **IV**

Contents ..... **V**

General Introduction **1**

1. Organic Thin-Film Transistors **9**

1.1 Introduction 9

1.2 Organic semiconductor 9

1.3 Charge transport in organic semiconductor 12

1.3.1 Band-like transport 12

1.3.2 Multiple Trap Release 14

1.3.3 Hopping transport 15

1.4 Organic thin-film transistor 18

1.4.1 Geometric configuration 18

1.4.2 Operation principle 20

1.4.3 Curent-voltage characteristics 22

1.4.4 OTFT operation parameters 25

1.4.5 The interfaces in organic thin-film transistors 28

1.4.6 Growth and morphology of organic semiconductor films 39

1.5 Conclusion 42

2 S-DNTT-10-based OTFTs fabrication and characterization techniques **44**

2.1 Introduction 44

2.2 S-DNTT-10 molecules 44

2.3 The fabrication in S-DNTT-10-based OTFT 45

2.4 Characterization tools utilized 49

2.4.1 *IV* characterization 49

2.4.2 Raman spectroscopy-*IV* characterization in-situ system 49

2.4.3 Atomic Force Microscopy 50

2.4.4 Kelvin Potential Force Microscopy 51

2.4.5 Contact angle measurement 58

2.5 Surface characteristics of S-DNTT-10 thin-film 59

2.5.1 S-DNTT-10 thin-film Topography by AFM measurement 59

2.5.2 Contact angle measurements for 25nm S-DNTT-10 thin-film 60
2.6 S-DNTT-10-based OTFTs electrical characterization 60
2.6.1 Non-linear *IV* characteristics in S-DNTT-10-based OTFT 61
2.6.2 Electrical surface potential profile 62
2.6.3 Early saturation effect 63
2.7 Summary 68
3 Raman scattered on S-DNTT-10 material 70
3.1 Introduction 70
3.2 Light-matter interaction 70
3.2.1 Raman scattered effect 70
3.2.2 Surface-Enhanced Raman scattered principle 71
3.3 Density Function Theory simulation of S-DNTT-10 74
3.3.1 Density Function Theory 75
3.3.2 Theoretical molecular vibration for S-DNTT-10 75
3.4 Light influence in electrical properties of S-DNTT-10-based OTFTs 80
3.4.1 Laser thermal effect on S-DNTT-10 thin-films 80
3.4.2 Influence of laser on electrical performance 82
3.5 Experimental S-DNTT-10-Raman spectrum 85
3.5.1 Laser wavelength effect on S-DNTT-10 Raman spectrum 85
3.5.2 Thin-film thickness effect on S-DNTT-10 Raman spectrum 86
3.5.3 Surface Enhanced Raman Scattered effect at S-DNTT-10 89
3.6 Conclusion 99
4 Investigated on the influence of bias-stress effect on S-DNTT-10-based OTFTs via Raman scattered technique 102
4.1 Introduction 102
4.2 Bias stress effecting electrical characteristics of S-DNTT-10-based OTFT 102
4.3 DFT simulating the BS effect influencing S-DNTT-10 MOs 103
4.4 Explored the bias-stress effect by Raman scattered technique 106
4.4.1 SERS at S & D Au electrodes 107
4.4.2 Conventional Raman measurements in the channel 110
4.5 Conclusion 113
5 Annealing treatment on S-DNTT-based OTFTs 116
5.1 Introduction 116
5.2 Post-annealing treatment on S-DNTT-10-based OTFT 116
5.2.1 Post-annealing temperature influence on electrical properties 119
5.2.2 Post-annealing temperature influence on material 123

5.3 Annealing treatment on deposited substrates for S-DNTT-10 thin-films 136
5.4 Conclusion 141
6 A way to improve the charge injection in S-DNTT-10-based OTFTs 144
6.1 Introduction 144
6.2 Top-contacted bi-layers-based OTFTs 145
6.2.1 Design idea of S-DNTT-10-based OTFTs with extra OSC layers 145
6.2.2 Changes in electrical performance 149
6.2.3 Characterization of contact resistances 158
6.2.4 Electrical stability of Bilayer-based OTFTs under long-term operation 173
6.2.5 Effect of post-annealing treatment on electrical performance 175
6.3 Conclusion 177
7 Summary 180
8 Bibliography 186
9 Appendix 196
9.1 Eerly saturation effect 196
9.2 The description S-DNTT-10 molecular vibration 208
9.3 KPFM for intrinsic mobility 212
9.4 Nano-characterization at Au drain electrode 214
9.5 Electrical performance of TCBG S-DNTT-10-based OTFT with 6.5 $cm^2 \cdot V^{-1} \cdot s^{-1}$ 216
9.6 Blurred effect caused shrinking channel length 218
9.7 Bottom-contacted bi-layers-based OTFTs 220
9.8 S-DNTT-10-based OTFTs with double injection-area 224
10 French Summary 228
List of contribution in Ph. D study 246

General Introduction

With the rise of computers, information technology has propelled us from the industrial era into the information age, enabling rapid and efficient data transmission and exchange. Optoelectronics and microelectronics have revolutionized modern information technology, with transistors and integrated circuits serving as crucial physical mediums driving these advancements. Among them, the transistor has had a profound impact on electronic information technology, marking the beginning of the microelectronics revolution. The field-effect transistor (FET), widely used in electronic products, is a fundamental component of modern integrated circuits and is essential to the development of modern information technology.

The evolution of semiconductor devices began in 1874, when German physicist Braun discovered the asymmetrical conductance of electric current at metal-semiconductor contacts. Although the mechanism was not understood, early devices made from metals and semiconductors were used in radio detectors. In 1906, Pickard patented the point-contact silicon semiconductor diode, and in 1907, Pierce studied the rectifying properties of diodes. The breakthrough came in 1931 when Schottky, Stormer, and Waibel explained that a potential barrier at the metal-semiconductor interface caused rectification. In 1938, Schottky and Mott independently proposed that this barrier resulted from the difference in work functions between the metal and semiconductor, explaining electron flow via drift and diffusion. With radar technology advancing, research on metal-semiconductor contacts progressed, leading to Bethe's hot electron emission theory, which argued that current between metal and semiconductor was determined by electron emission into the metal. In 1947, William Shockley, John Bardeen, and Walter Brattain at Bell Labs discovered the point-contact germanium transistor, sparking the microelectronics revolution. However, the point-contact transistor had drawbacks like a complex manufacturing process, high noise, and limited applications. To address these, Schottky proposed a rectifying junction design, leading to the development of the bipolar transistor in 1950. The invention of the metal-oxide-semiconductor field-effect transistor (MOSFET) in 1960 by Dawon Kahng marked another key milestone. Although its switching speed was slower than the bipolar transistor, MOSFETs offered advantages like small size, easy integration, and low power consumption. The MOSFET revolutionized semiconductor manufacturing by improving integration and stability while reducing costs. Today, unipolar FET, such as MOSFETs, dominate modern electronic products.

Applying organic materials to FETs which forming organic thin-film transistors (OTFTs), highlights their benefits in device performance, fabrication, and production cost. Compared to traditional inorganic devices like Si-TFT, OTFTs offer advantages such as diverse material sources, low processing temperatures, easy compatibility with flexible polymer substrates, suitability for large-scale production, and a simple film formation process. Large-area, low-cost films can be quickly produced through methods like thermal deposition [1–9]. OTFTs are widely used in displays, sensors, electronic labels, and large-scale integrated circuits. They are also expected to enable new applications, such as large-area sensor arrays, memory components, organic lasers, and superconducting materials. [2,10–15]

OTFTs can be categorized into small molecule-based and polymer-based types according to the used organic semiconductor materials (OSC) [16]. Small molecule materials and polymer OSC materials have different properties, leading to differences in their synthesis, purification, and preparation processes. Small molecule OSC typically form thin films through solution methods or thermal evaporation in high vacuum, while polymer semiconductors are processed into thin films primarily by solution methods [17–23]. Researchers can tailor the performance of organic semiconductor (OSC) materials by modifying their molecular structure, enabling the design of OSCs to meet various device needs. Both small molecule and polymer OTFTs offer excellent processing characteristics and relatively low cost, making them promising for large-scale industrial production. Their unique properties have attracted significant investment from academic and commercial research. Compared to inorganic TETs, OTFTs offer superior flexibility. Studies showed that OTFTs retained their electrical performance even after moderate bending and stretching, making them ideal for wearable electronics. Another key advantage of OTFTs over inorganic TETs is their ability to be fabricated at low temperatures. **Figure. a** shows the fabricating temperatures of OTFTs and other TFT, such as polycrystalline silicon TFTs, oxide TFTs, and amorphous silicon TFTs, along with the required mobility ranges for different devices. Generally, OTFTs are processed at temperatures below 200°C, while TFTs require temperatures above 200°C. For higher-mobility inorganic TFTs like polycrystalline silicon TFTs, the processing temperature needs to exceed 300°C. The performance of OTFTs fabricated below 200°C is sufficient for electronic paper, liquid crystal displays, and OLEDs. Additionally, OTFT materials are widely available, and OSC crystals can be tailored to be consistent with processing techniques by modifying molecular chains to adjust dissolution properties. These advantages simplify OTFT processing and reduce manufacturing costs.

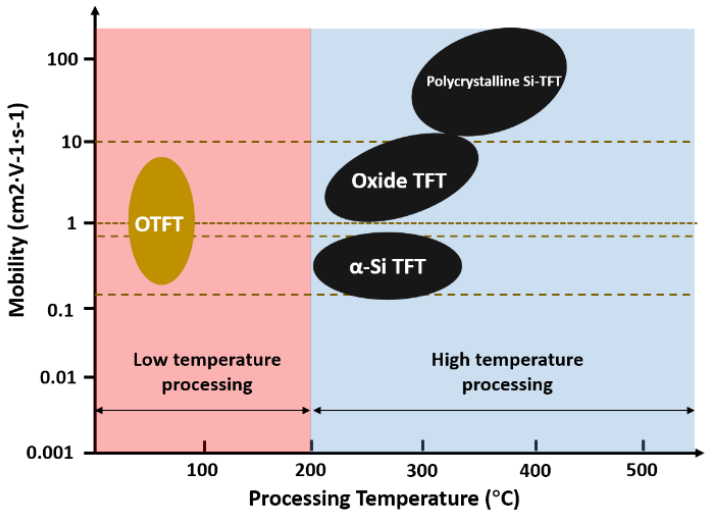


Figure. a The current correlation between the processing temperatures of diverse field-effect transistors and the device performances.

The development of OTFTs began later than that of inorganic TFTs. The first OTFT device was created in 1986, as shown in **Figure. b**, by Japanese scientists Tsumura et al. [24]. This device had a Bottom-Gate-Bottom-Contact structure, with silicon dioxide (SiO_2) as the insulating layer, Au/Cr as the source and drain electrodes, and polythiophene as the OSC material. The polythiophene was polymerized using an electrochemical method in an anhydrous, anaerobic environment as a p-type OSC, achieving a mobility of 10^{-5} $cm^2 \cdot V^{-1} \cdot s^{-1}$. From 1986 to around 1995, research focused on the prevalent OSC materials of the time, marking the early stage of OTFT research. The organic small-molecule materials studied during this period included oligothiophene, phthalocyanine dyes, pentacene, and fullerenes, while polymeric OSC materials included poly(3-ethylthiophene) (P3HT) and PPV derivatives. In 1989, Horowitz et al. were the first to use oligothiophene to fabricate OTFT devices, initiating the application of organic conjugated small molecules in OTFTs [25]. In 1991, Akimichi et al. reported that adding alkyl groups to the ends of oligothiophenes with three, four, and five thiophene units significantly enhanced the mobility of the devices. Pentacene was another extensively studied small-molecule semiconductor during this period [26]. In 1991, Horowitz et al. reported on the performance of pentacene-based OTFTs, but due to limited understanding at the time, the mobility was only 0.002 $cm^2 \cdot V^{-1} \cdot s^{-1}$ [27]. Additionally, there were reports on n-type OTFTs. In 1995, Bell Laboratories used C_{60} as the n-type active layer material. The thermally evaporated C_{60} layer formed a polycrystalline structure of 60-70 Å, and under high-vacuum conditions, the device achieved a field-effect mobility of 0.3 $cm^2 \cdot V^{-1} \cdot s^{-1}$. [28]

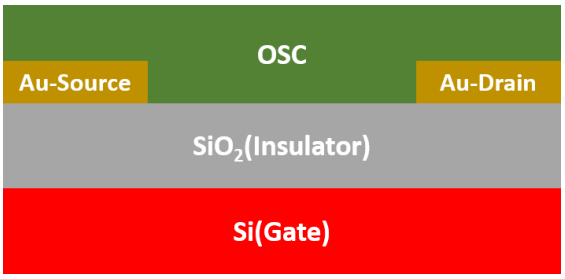


Figure. b The schematic diagram of first OTFT. [24]

From 1996 to 2000, it became increasingly recognized that processing technology significantly impacted OTFT-performance, and some OSC materials were applied in OTFT devices. In 1996, Bao et al. used poly(3-hexylthiophene) (P3HT) as the active layer and adopted solution processing for film formation. They found that different solvents and processing methods greatly affected device mobility [29]. Different processing techniques altered the stacking of active layer molecules, influencing device mobility. The molecular stacking was controlled by adjusting the evaporation temperature. In 1998, Jackson et al. fabricated OTFTs using pentacene, achieving a mobility exceeding 1 $cm^2 \cdot V^{-1} \cdot s^{-1}$. However, mobility varied significantly with temperature, indicating thermally activated hopping in pentacene thin films. Traps and contact characteristics also impacted performance at different temperatures [30]. During this period, researchers further studied the impact of molecular arrangement within OSC films. In 1999, Sirringhaus et al. found that when P3HT molecules were arranged perpendicularly to the substrate, this regular configuration promoted specific overlap of delocalized molecular orbitals between adjacent P3HT molecules, enhancing charge transport [31]. This discovery provided theoretical guidance for optimizing the film formation process. By controlling the film formation conditions, efforts were made to align organic molecules perpendicularly to the substrate to improve device mobility.

From 2001 to 2005, significant progress was executed in the development of single-crystal OTFT devices. Organic single crystals, which are out of grain boundary effect, enable better charge transport within the material. For insoluble OSC materials, vapor-phase deposition is commonly used to fabricate single-crystal semiconductor devices. In 2004, Palstra et al. reported on pentacene single-crystal OTFTs and investigated the impurities affecting performance of the device. Impurities in pentacene were identified by detecting C=O bonds through infrared spectroscopy. After multiple purification steps to remove these impurities, the room-temperature mobility increased to 35 $cm^2 \cdot V^{-1} \cdot s^{-1}$, further improving to 58 $cm^2 \cdot V^{-1} \cdot s^{-1}$ at 225 K [32]. In 2005, Kline et al. studied the effect of molecular weight on the film morphology and mobility of OTFTs [33]. At lower molecular weights, atomic force microscopy (AFM)

revealed a regular rod-like morphology, while higher molecular weights led to an amorphous nodular structure. Although the lower molecular weight produced a more regular morphology, the mobility was lower. However, techniques such as drop casting, annealing, or solvent modification improved mobility in low molecular weight films. Conversely, higher molecular weight films were less sensitive to processing conditions.

During the period ranging from 2006 to 2010, a crucial research advancement in the domain of OTFT was the discovery and application of BTBT and DPP structures. In 2007, Ebata et al reported on OTFT based on BTBT molecules, with a mobility approaching 3 $cm^2 \cdot V^{-1} \cdot s^{-1}$ [34]. In 2010, Li et al reported on OTFT fabricated based on polymeric semiconductor materials containing DPP structural units, attaining a mobility of 0.94 $cm^2 \cdot V^{-1} \cdot s^{-1}$. [35]

Since 2011, research on OTFT materials and devices has arrived at new heights, with significant advancements. In 2011, Hiromo et al. fabricated OTFTs using an organic small-molecule semiconductor with BTBT units via printing technology with the achieved mobility of 31.3 $cm^2 \cdot V^{-1} \cdot s^{-1}$ [36]. In the same year, Bao et al. used pentacene derivatives as OSCs and, by adjusting the blade coating rate, obtained a device with a peak mobility of 4.6 $cm^2 \cdot V^{-1} \cdot s^{-1}$, which was nearly six times higher than conventional methods [37]. The optimized blade coating process reduced the molecular stacking distance from 3.33 to 3.08 Å, increasing the overlap of pi (π)-electron clouds and enhancing mobility. This work demonstrated the close relationship between material microstructures and device performance through a simplified process.

Since the first OTFT device was created in 1986, the field has evolved over several decades. Due to space-limitation, herein, it is impractical to detail every advancement and research outcome. Despite significant progress and notable improvements in OTFT performance compared to earlier devices, challenges remain due to the material properties of OSCs, limiting further development and widespread application. These challenges include the strong dependence of device performance on the quality of the fabricated organic film, contact resistance, performance degradation over time, and sensitivity to other external factors. Therefore, understanding the underlying physical mechanisms is crucial for the future development of OTFTs.

This thesis focuses on OTFTs based on 3,10-Didecylnaphtho[2,1-b] naphtha [1',2':4,5]thieno[2,3-d]thiophene 21DNTT-10 (S-DNTT-10) [38]. This report showed that S-DNTT-10 can be used to fabricate OTFT films through thermal deposition. It exhibited the stability characteristics in air and excellent charge transport properties. The stability is due to its higher HOMO energy level, while the charge transport properties are linked to its molecular

structure and π-electron distribution. Although S-DNTT-10 material has potential applications in OTFTs, research on this material is restricted until now, particularly regarding molecular vibrations and certain electrical properties. To further understand S-DNTT-10 material characteristics and optimize S-DNTT-10-based-OTFT applications, OTFTs were fabricated using thermal deposition, with gold electrodes. Advanced characterization techniques, such as Atomic Force Microscopy (AFM), Kelvin Probe Force Microscopy (KPFM), and Raman spectroscopy, were employed to investigate the electrical performance of devices and the influence of factors like temperature and electric field. Strategies to enhance device performance, such as adding additional OSC layers and designing new architectures, are proposed. The following sections briefly outline the research conducted in this thesis.

Chapter 1 provides an overview of the theoretical foundations of OTFTs. First, the material properties of OSCs and charge transport theory will be introduced. Then, a summary of the basic theory of OTFTs is presented. Finally, the highlight shifts to the impact of interface characteristics on device performance.

Chapter 2 will detail the fabrication process of S-DNTT-10-based OTFTs in this thesis and the used characterization techniques and approaches, along with their underlying principles. The material properties of the S-DNTT-10 film surface are measured by using nano-technique characterization tools. Finally, the electrical properties of S-DNTT-10-based OTFTs we fabricated will be discussed.

Chapter 3 will focus on the molecular vibration characteristics of S-DNTT-10. Using Density Functional Theory (DFT) simulations, the molecular vibration modes and π-electron cloud distribution in S-DNTT-10 single molecule are investigated, addressing the lack of research on S-DNTT-10 molecular vibrations. Subsequently, we will study on the influence of wavelength-incident laser on electrical performance of Top-Contact-Bottom-Gate (TCBG) S-DNTT-10-based OTFTs, and S-DNTT-10 Raman scattered signal. Meanwhile, we will explore the influence of S-DNTT-10 thin-film thickness on S-DNTT-10 Raman spectrum. Additionally, we develop one approach to enhance S-DNTT-10 Raman signals. It will provide a solid experimental basis for further exploration of the impact of bias-stress on charge injection and collection efficiency in TCBG S-DNTT-10-based OTFTs.

Chapter 4, will mainly discuss about the influence of the bias-stress (BS) effect on the TCBG S-DNTT-10-based OTFT. It will analyze the effect of long-term operation or stressed electric field on the electrical performance. It is innovated by first using comprehensively characterization techniques to explore BS effect. Herein, the impact of the *BS* effect on the

charge injection and extraction efficiency of the device is explored by KFPM, in combination with in-situ measurement employing Raman scattered technology, including Surface-enhanced Raman spectroscopy (SERS) scattering at the electrode and conventional Raman spectra at the channel, to investigate this changed performance.

Chapter 5 will mainly explore the in-depth analysis of the impact of annealing treatments on the performance of TCBG S-DNTT-10-based OTFTs. The annealing treatments include post-annealing of the devices and adjusting the temperature of the deposited substrate during S-DNTT-10 thin-film deposition by PVD. For the former one, it will study on the influence of varied post-annealing temperature on electrical characteristics into TCBG S-DNTT-10-based OTFTs. The innovation point is that in-depth studying the influence of post-annealing treatment on electrical performance under different temperature by simultaneously using multiple characterization tools. During this studying process, it plans that AFM, Raman spectroscopy, and KPFM is respectively used to investigate the electrode and S-DNTT-10 film morphology, Raman spectra of the S-DNTT-10 molecules, and the contact resistance. For the latter one, we will study on the changes of T_{post} (which is the device's effective field-effect mobility reaches its peak) with the substrate deposition temperature, T_{sub}. By fitting the relationship between them, the effect of deposition temperature on device performance is initially revealed.

In the Chapter 6, in light of the relatively low charge injection efficiency phenomenon exhibited in TCBG S-DNTT-10-based OTFT devices based on Chapter 2, we will innovatively propose one improved method that introducing additional OSC material, pentacene thin-films. We plan to use the *I-V* measurements companying with KPFM characterization with the aim of evaluating the influence of pentacene on TCBG S-DNTT-10-based OTFTs. Moreover, we will innovatively introduce the optimized method of depositing the additional layer with purpose to further enhance the performance of TCBG S-DNTT-10/Pentacene-based devices. Then, we will introduce how the post-annealing temperature affects electrical performance of TCBG S-DNTT-10-based OTFTs stacked with pentacene thin-films. Ultimately we will explore the bias-stress effect impacting on the electrical performance of TCBG S-DNTT-10/Pentacene-based OTFTs, compared with pure TCBG S-DNTT-10-based OTFTs.

Chapter 7 will summarize the aforementioned work, elucidate the limitations existing in the experimental process, and present the prospects for the future.

1. Organic Thin-Film Transistors

1.1 Introduction

This chapter is mainly discussed about the related fundamental theory of organic thin-film transistors (OTFTs). Section 1.2 will briefly introduce the formation of hybrid orbitals in organic materials, taking organic materials based on carbon and hydrogen atoms and sp^2 hybrid orbitals as examples to describe it. And in Section 1.3, we introduce the mechanism of charge transport in organic materials. It will mainly focuse on band-like transport, multiple traps release (MRT) and hopping transport. Section 1.4 introduces the theory of OTFTs. It includes that the common structure of OTFT, fundamental mechanism of OTFT operation, *I-V* characteristics, the electrical characterization parameters and interface characteristics in OTFTs.

1.2 Organic semiconductor

Since Mendeleev created the periodic table of elements, persons gained one in-depth understanding of the properties of various atoms in nature. Carbon (C), with four electrons in its outer shell, has unique chemical properties that facilitate the formation of various hydrocarbons, forming the basis of organic chemistry. Among them, aromatic compounds are particularly notable for their electronic properties due to their characteristic conjugated systems, which feature alternating single and double bonds. According to Pauli-Exclusion Principle and Hund-Rule, the ground-state electron configuration of carbon atoms is $1s^2\ 2s^2\ 2p^2$, with the tetravalent electrons located in the doubly occupied $2s^2$ and singly occupied $2p_x$ and $2p_y$ orbitals. Carbon atoms can also form hybridized electronic systems, where the ground-state orbitals combine to form hybridized orbitals. For example, in the sp^2 hybridization of carbon atoms of conjugated systems, one 2s and two 2p orbitals combine to form three sp^2 hybridized orbitals, as shown in **Figure 1.1**. In this configuration, the tetravalent electrons are distributed among three singly occupied sp^2 hybrid orbitals and one un-hybridized $2p_z$ orbital. The three sp^2 hybrid orbitals lie in a plane, while the $2p_z$ orbital is perpendicular to it. In a typical conjugated system, each carbon atom forms two single bonds and one double bond with adjacent atoms. Single bonds are formed by the overlap of sp^2 orbitals, known as σ (sigma) bonds, while double bonds consist of a σ bond and a π (pi) bond formed by the overlap of $2p_z$ orbitals. [39,40]

The benzene molecule, considered the simplest aromatic compound, is also one crucial component of small molecules used in organic electronics. In the benzene molecule, twelve σ bonds are formed by the overlap of sp^2 orbitals among the six carbon atoms, and three π bonds are generated by the overlap of $2p_z$ orbitals. Since the $2p_z$ orbitals are perpendicular to the

atomic plane, the lateral overlap occurs between the two lobes, with zero electron density at the shared nodal plane passing through the bonding nuclei. As a result, π bond overlap is weaker than σ bond overlap, and the electrons in π bonds (π electrons) are highly delocalized across all six $2p_z$ orbitals [41]. Therefore, the π electrons in benzene form an electron cloud that is delocalized above and below the atomic plane. This delocalization is crucial for the charge transport properties of aromatic compounds. During σ bond formation, the strong overlap of sp^2 hybrid orbitals causes significant energy splitting into bonding σ and anti-bonding σ^* molecular orbitals. In contrast, due to the weaker overlap in $2p_z$ orbitals, the energy splitting during π bond-formation is much smaller, resulting in a narrower energy difference between π and π* molecular orbitals. In benzene, the overlap of $2p_z$ orbitals creates three bonding π orbitals occupied by electrons and three empty anti-bonding π* orbitals. The highest energy π orbital is known as the highest occupied molecular orbital (HOMO), while the lowest energy π* orbital is the lowest unoccupied molecular orbital (LUMO).

According to the energy band theory of inorganic semiconductors, the HOMO and LUMO, respectively, corresponds to the valence band and conduction band, and the energy difference between them being analogous to the band gap in inorganic solids. The HOMO-LUMO energy gap in benzene is about 6.8 eV [42], classifying it as an insulator. In polyphenylene compounds, as more benzene rings fuse, the aromatic chain lengthens, and consequently the number of overlapping $2p_z$ orbitals increases. It strengthens energy splitting between bonding and antibonding molecular orbitals, leading to more π and π* orbitals, reducing the HOMO-LUMO energy gap, and enhancing π electron delocalization [42]. Pentacene, one of the early and most notable OSCs, consists of five fused benzene rings, crystallizes easily, has a fishbone-like crystal structure, is insoluble in organic solvents but slightly soluble in hot benzene, and has a HOMO-LUMO energy gap of about 2.2 eV. [43–45]

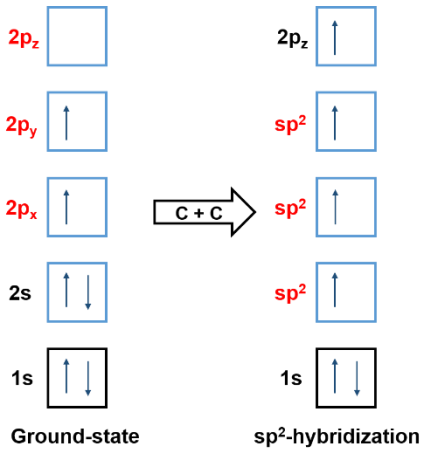


Figure 1.1 The diagram of hybridization of two carbon atoms.

Organic semiconductor (OSC) material, which is the one significant component for OTFTs, is correlated with carrier transport properties. Based on molecular weight, OSCs are classified into small-molecule and polymeric materials. Research have highlighted the distinct characteristics of these materials in decades. Polymeric OSCs exhibited advantages such as excellent film formation through solution processing, simple preparation, and low costs, making them suitable for large-area inkjet printing in organic optoelectronic thin-film devices. In contrast, small-molecule OSCs are easier to prepare and purify, and vapor deposition can produce thin films with high crystallinity and order, leading to excellent semiconductor performance.

OSC materials can be categorized by the type of charge-carriers transporting into OTFTs: n-type (electron transport), p-type (hole transport), and bipolar (both electron and hole transport). The intrinsic structure and properties of OSC materials determine carrier mobility, thermal and chemical stability, and thus regulate OTFT performance. Among OTFT materials, the HOMO/LUMO energy levels are critical factors. For p-type OSC materials, if the prevalently utilized electrode material Au (work function of -5.1 eV) is employed, the ideal HOMO energy level should approximately be -5 eV, forming a relatively low energy barrier, which is conducive to the injection of holes. Considering the material stability, the ideal LUMO energy level of n-type OSC materials is supposed to below -4 eV [46,47]. Currently, p-type OSC materials have witnessed a relatively rapid overall advancement, demonstrating high mobility and favorable air stability. The mobility of some OTFT materials using these materials has already reached or even exceeded the performance of amorphous TFT devices [36,48–50]. The two OSC materials employed in this work are: 3,10-Didecylnaphtho[2,1-b]naphtha [1',2':4,5]thieno[2,3-d]thiophene 21DNTT-10 (S-DNTT-10) and pentacene, as shown in **Figure 1.2**.

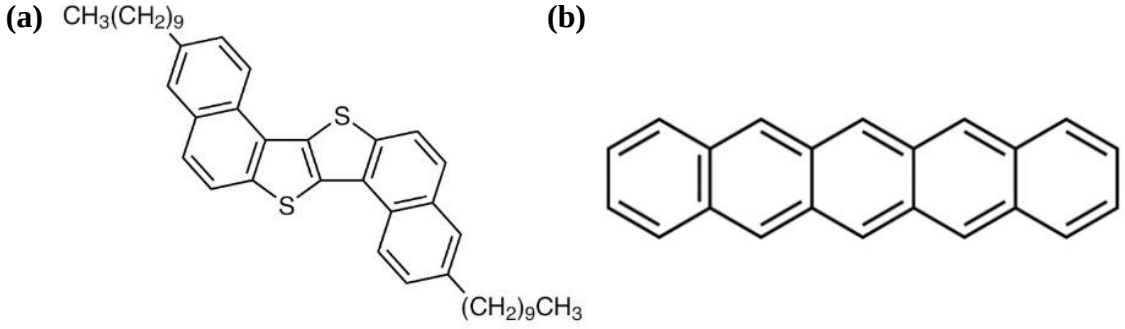


Figure 1.2 The schematic structure of (a) S-DNTT-10 molecule and (b) pentacene molecule.

1.3 Charge transport in organic semiconductor

In conjugated carbon systems, the delocalization of π orbitals enables charges to be transported along the molecule, constituting intramolecular charge transport. However, since the size of OTFTs generally is much larger than a single OSC molecule, establishing intermolecular charge transport is also essential. Charge transport properties in the conducting channel of OTFTs depends on the extent of π orbital overlap between adjacent molecules [51,52]. This section introduces the factors that influence charge transport, various models of charge transport behavior, and strategies to enhance charge transport. To clarify the different aspects of charge transport in organic semiconductors, it is important to define some key parameters. When an external electric field F is applied, charge carriers are accelerated to a drift velocity v_D, and the parameter used to characterize the transmission efficiency of electronic charges in solids is defined as the charge carrier mobility, μ,

$$\mu = \frac{v_D}{F} \tag{1.1}$$

as a consequence of the charge transport, the current density, j, is determined by the charge carrier density, n, and the drift velocity, v_D,

$$j = e \cdot n \cdot v_D = e \cdot n \cdot \mu \cdot F \tag{1.2}$$

Herein, e, is the element charge. The conductivity, σ, is defined as the ratio of current density and applied electrical field:

$$\sigma = \mu \cdot n \cdot e \tag{1.3}$$

1.3.1 Band-like transport

In OTFTs, the conductive channel consists of several OSC molecules arranged in the disorder pattern. Ideally, appropriate processing techniques enhance the overlap of π orbitals between adjacent molecules to achieve efficient charge transport [53–56]. During bonding with each molecule, the overlap of molecular orbitals causes the splitting of discrete energy levels. Depending on the number and proximity of adjacent molecules, this energy splitting results in the formation of one energy quasi-continuum or energy band. In inorganic semiconductors, such as monocrystalline silicon and gallium arsenide (GaAs), atoms are bonded by strong covalent bonds, which cause significant orbital overlap. Consequently, the electron wave function (Bloch wave) is delocalized over long distances in the lattice, forming a broad energy band. The charge transport mechanism in such materials is described as band transport, as shown in **Figure 1.3 (a)**. In band transport mechanism, phonon scattering causes charge carrier

mobility to decrease with increasing external temperature, and this kind of dependence follows a power-law behavior: [57,58]

$$\mu = \mu_{300} \times (T/300)^{-\alpha} \quad \textbf{(1.4)}$$

among them, μ_{300} represents the mobility measured under the temperature condition of 300 K, and α is a positive parameter dependent on the material, typically ranging within 1.5 to 3. Band transport has been observed in specific OSC crystals. This transport mechanism has gained significant attention because, theoretically, it offers the highest mobility (μ > 10 $cm^2 \cdot V^{-1} \cdot s^{-1}$). Consequently, numerous researches focus on developing crystalline OSCs to enhance π-electron delocalization.

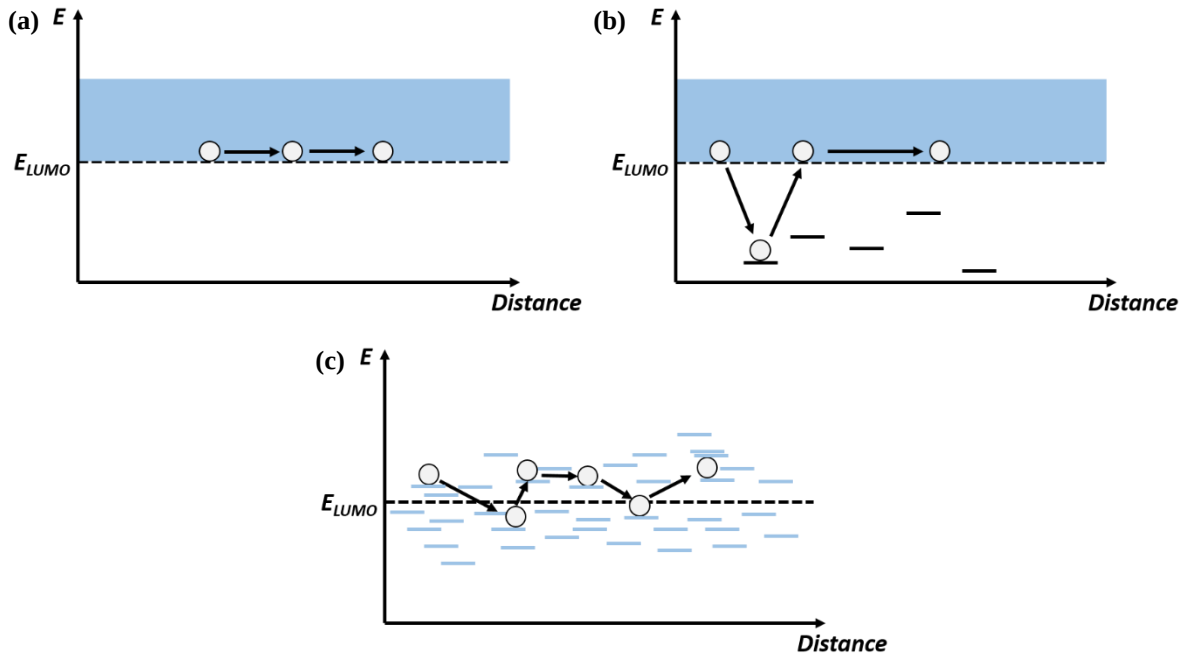


Figure 1.3 Schematic diagram of three conventional charge transport models: (a) band-like transport mode, (b) MRT transport mode, and (c) hopping transport mode.

In contrast, OSC material is inside formed by polycrystalline or amorphous layers, where molecules are connected together by weak Van der Waals forces, leading to relatively large intermolecular distances and weak orbital overlap. OSC films are also characterized by numerous defects and impurities. In particular, grain boundaries disrupt lattice periodicity, preventing the formation of long-range conduction bands. Impurities and defects introduce localized states within the HOMO-LUMO energy gap, which act as traps for charge carriers. Consequently, charge transport in OSC films is influenced by the distribution of these localized states. In most polycrystalline and amorphous semiconductor OTFTs, charge transport occurs via a hopping-manner, where charges move from one localized state to another state. Under

these conditions, charge carrier mobility increases with temperature, and the temperature dependence of mobility follows the Arrhenius equation: [59]

$$\mu \propto exp\left(\frac{-\Delta E_a}{kT}\right) \quad \textbf{(1.5)}$$

herein, ΔE_a is the activation energy, referring to the energy that local charges must obtain in order to escape from the local state and thus contribute to charge transfer [58]. k is the Boltzmann constant, and T represents temperature. Charge transfer in polycrystalline solids is the dominant mechanism in most OSC films. It involves both coherent transfer within the delocalized transfer band (observed in single crystals) and incoherent transfer through thermally activated hopping between localized states (seen in disordered or amorphous solids). Establishing a theoretical framework for charge transfer in OSC films is crucial for understanding and effectively controlling the electrical properties of OTFTs. However, due to the intricate structure-property relationship and the wide variety of available OSCs, this is an exceptionally challenging task [52,59,60]. Moreover, different manufacturing processes and minor deviations in process parameters result in OSC films with significant variations in properties, as well as impurities and defects at different levels. Consequently, a single, unified model akin to the band transport theory for inorganic semiconductors has not been developed to provide a comprehensive understanding and interpretation of charge transport in OSCs. Nevertheless, several models have been proposed that effectively explain certain aspects of charge transport under specific conditions, and the following sections will elaborate on this in detail.

1.3.2 Multiple Trap Release

The multiple trapping and release (MTR) model is well-suited for systems with a relatively high degree of order, such as most polycrystalline semiconductor thin films with minimal impurities, defects, and grain boundaries. This model incorporates both delocalized band transport and localized states, assuming that charge transport occurs within a narrow transport band primarily composed of delocalized states, while localized states within the HOMO-LUMO energy gap act as traps. These traps can exist either within the crystal or at grain boundaries in polycrystalline materials. Encountered with the presented traps, the mobility of OTFTs exhibits thermal activation behavior and often increases with higher gate voltages. The MTR model was proposed to explain these observations [61–66] and was originally developed for amorphous silicon thin-film transistors [67]. This model is based on band transport, but the charge trapping could reduces mobility, and they can be thermally released to escape from trap states, as shown in **Figure 1.3 (b)**. The total accumulated charge concentration is characterized

as $n_{total} = n_{free} + n_{trapped}$, where n_{free} stipulates the concentration of free charges within the transport band, and $n_{trapped}$ delineates the concentration of trapped charges [68].

For a given gate-channel voltage, these concentrations can be determined by resolving the Poisson equation for the gate/insulator/channel structure, within which free carriers and traps hold appropriate density of states (DOS) [69,70]. Only free carriers contribute to the drain current, while the trapped charges are considered immobile. In this model, the apparent mobility in a given position C in the channel is approximately proportional to the mobility μ_0 of the carriers in the transport band and is modulated by the ratio between free carriers and the total accumulated carriers:[67]

$$\mu = \mu_0 \times \frac{n_{free}(U_{GC})}{n_{free}(U_{GC}) + n_{trapped}(U_{GC})} \quad \textbf{(1.6)}$$

where U_{GC} is the gate voltage at position C in the channel. Within this model, the "capture and release" process is not regarded as a dynamic one but rather is construed as a quasi-static one, facilitating the filling and emptying of trap energy levels through the application of a gate voltage.

The MTR model has even been asserted to possess the capacity to simulate polymers exhibiting transport characteristics of exceptionally high mobility (up to 10 $cm^2 V^{-1} s^{-1}$) [65,71]. To account for the high mobility, Noriega et al. contend that ordered and disordered regions coexist within these polymers [52,65,72]. These authors explain the high mobility via the capability of certain molecules to interconnect ordered regions resembling wires and it is more applicable to polymers material. Simulations have shown that mobility increases with greater polymer interconnections [52,73–75]. If all ordered regions are interconnected, the transport mechanism would be band transport. However, according to the MTR model, sub-conjugated units within long polymer chains could create traps. The MTR model only represents band transport and does not account for other transport mechanisms. In this model, current is solely attributed to carriers in the delocalized state (band transport), while carriers in the localized state are trapped and do not contribute to conduction. This model has been used to explain the transport characteristics of various OSCs, including amorphous OSCs, where transport through localized states is expected.

1.3.3 Hopping transport

The accessible states within amorphous materials are localized. For the charges to be mobile, the charges in a state i with energy E_i must leap through tunneling processes to an adjacent vacant state j with energy E_j and spatially separated by a distance r_{ij}, as depicted in

Figure 1.3 (c). This process is characterized with a frequency ω_{ij} considering the presence of transition probability [69,70,76]. This transport mechanism is designated as hopping transport. 'Master Equation'(ME) is a nonlinear equation that takes into account complex interactions over nanoscale lengths [77,78]. In its simplified form, this equation relies on the hopping probability and the Fermi-Dirac distribution. For a given OSC film, at a specific density of states (DOS), a random spatial distribution of accessible states is established. The steady-state current density J resulting from an applied electric field F is computed by solving ME. Then the mobility is derived from $\mu = J/enF$.

The kinetic Monte Carlo (MC) method used by Bässler in earlier studies represents another approach for simulating charge transport in OSCs [69]. The MC model enables the simulation of systems governed by statistical processes. Hopping and recombination processes in organic semiconductors (OSCs) can be incorporated, with the probabilities of these processes being randomly selected in each simulation. Since each MC simulation is unique, multiple simulations are required to accurately capture the system behavior. The MC method accommodates arbitrary complexity, providing an advantage over the numerical solution of the ME, which often requires approximations [79]. Both the ME and MC methods are commonly used to validate or invalidate analytical and semi-analytical mobility models in the literature. In both methods, the frequency ω_{ij} of the jump transition from state E_i to E_j must be determined. It depends on the spatial distance r_{ij} and the energy difference $\Delta E_{ij} = E_j - E_i$ between states i and j. A widely used expression for ω_{ij} is the Miller–Abrahams (MA) relation: [59,80,81]

$$\omega_{ij} = \omega_0 exp\left(-\frac{2r_{ij}}{\gamma}\right) exp\left[-\frac{(E_j-E_i)+|E_j-E_i|}{2kT}\right] \qquad \textbf{(1.7)}$$

herein, γ corresponds to the extension of the carrier wave-function (the localization length of the carriers), while ω_0 represents the attempt frequency for escape. The MA relation describes well the local characteristics of the available states and consequently the impact of energy disorder in amorphous semiconductors. Nevertheless, it neglects the polaron effect. Hence, Marcus proposed another prevalent approximation for the frequency ω_{ij} of the hopping transition [59,81,82]:

$$\omega_{ij} = \frac{J_0^2}{\hbar}\sqrt{\frac{\pi}{4E_a}} exp\left(-\frac{2r_{ij}}{\gamma}\right) exp\left(-\frac{E_a}{kT}\right) \exp\left[-\frac{E_i-E_j}{2kT} - \frac{(E_i-E_j)^2}{16kTE_a}\right] \qquad \textbf{(1.8)}$$

In this model, E_a represents the polaron activation energy associated with the reorganization energy proximal to the carriers, and J_0 is correlated with the transfer integral

between sites E_i and E_j. By taking into account the frequency of the hopping transition relationship ω_{ij} (**Equation (1.7**) and

(1.8)) in conjunction with **Figure 1.4**, the dependence of mobility on disorder, temperature, charge concentration, or the applied electric field can be approximated. **Figure 1.4 (a)** schematically showed the movement of charges in disordered OSCs system through the hopping process when an external field is applied. The charge must overcome the energy barrier ΔE_{ij}, and the expanse of the DOS, assumed to follow a Gaussian profile, characterizes the energy disorder.

As the degree of disorder increases, the average energy barrier ΔE_{ij} rises, leading to a decrease in the average probability of hopping [52,81,83]. Consequently, mobility decreases as disorder intensifies. Referring to **Figure 1.4 (a)** or **Figure 1.4 (b)**, it is evident that an increase in charge concentration fills deep states, preventing carriers from falling into deep potential wells. **Figure 1.4 (b)** illustrates how the electric field lowers the effective potential barrier ΔE_{ij} between localized states, thereby promoting carrier hopping [81,84]. As charge concentration and electric field strength increase, mobility also increases. The influence of the electric field on charge concentration can be clearly defined: at low charge concentrations, only a strong electric field enables hopping, while at higher concentrations, the field helps charges overcome smaller energy barriers. Therefore, the electric field is closely linked to charge concentration and the configuration of the density of states (DOS).

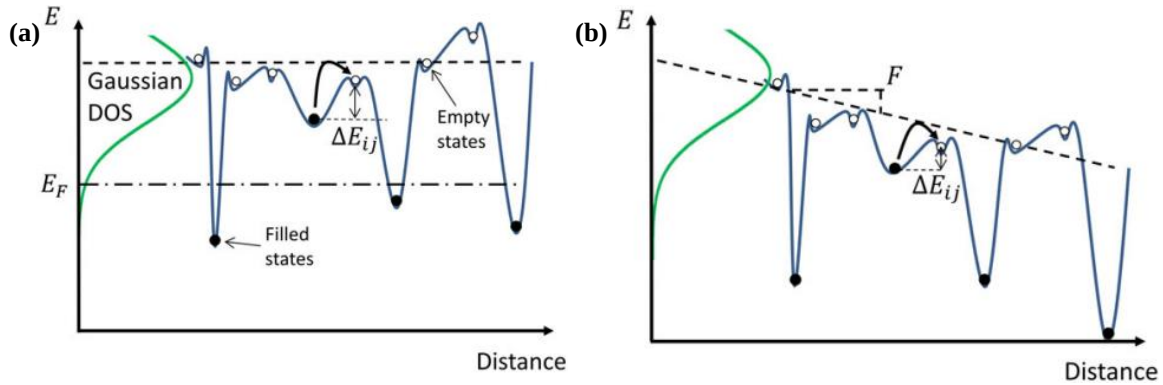


Figure 1.4 Schematic representation of the hopping transport process in amorphous OSCs (a) without electric field, (b) with applied electric field. The arrows represent a possible charge carrier hop [81].

Equation (1.7) and

(1.8) both predicate the inter-point distance r_{ij}. As charge hopping extends beyond the nearest points, the transport mechanism is called variable-range hopping. If only the nearest

points are considered, it is referred to as nearest-neighbor hopping (NNH). [85–87]. Some transport models presuppose the NNH process, but for other authors, this supposition is overly restrictive in disordered OSCs; thus, they assert that in this case, essentially the variable-distance hopping process is pertinent.

An accurate mobility model for amorphous OSCs should account for the DOS shape, temperature, and charge carrier concentration. The best models use the concepts of transport energy and variable-range hopping to develop a physical analytical framework. The most relevant mobility models for simulating OTFTs with amorphous OSCs are found in the following references. [59,81,88,89]

1.4 Organic thin-film transistor

1.4.1 Geometric configuration

Organic thin-film transistors (OTFTs) consist of a gate electrode (Gate, G), an insulator layer, a semiconductor layer, and two electrodes: a source (Source, S) and a drain (Drain, D). OTFTs can be fabricated in different structures. Based on the distinct relative positions of each functional layer, they are categorized into four fundamental structures, as shown in **Figure 1.5** [81]: (a) top-contact-bottom-gate, (b) bottom-contact-bottom-gate, (c) top-contact-top-gate, and (d) bottom-contact-top-gate.

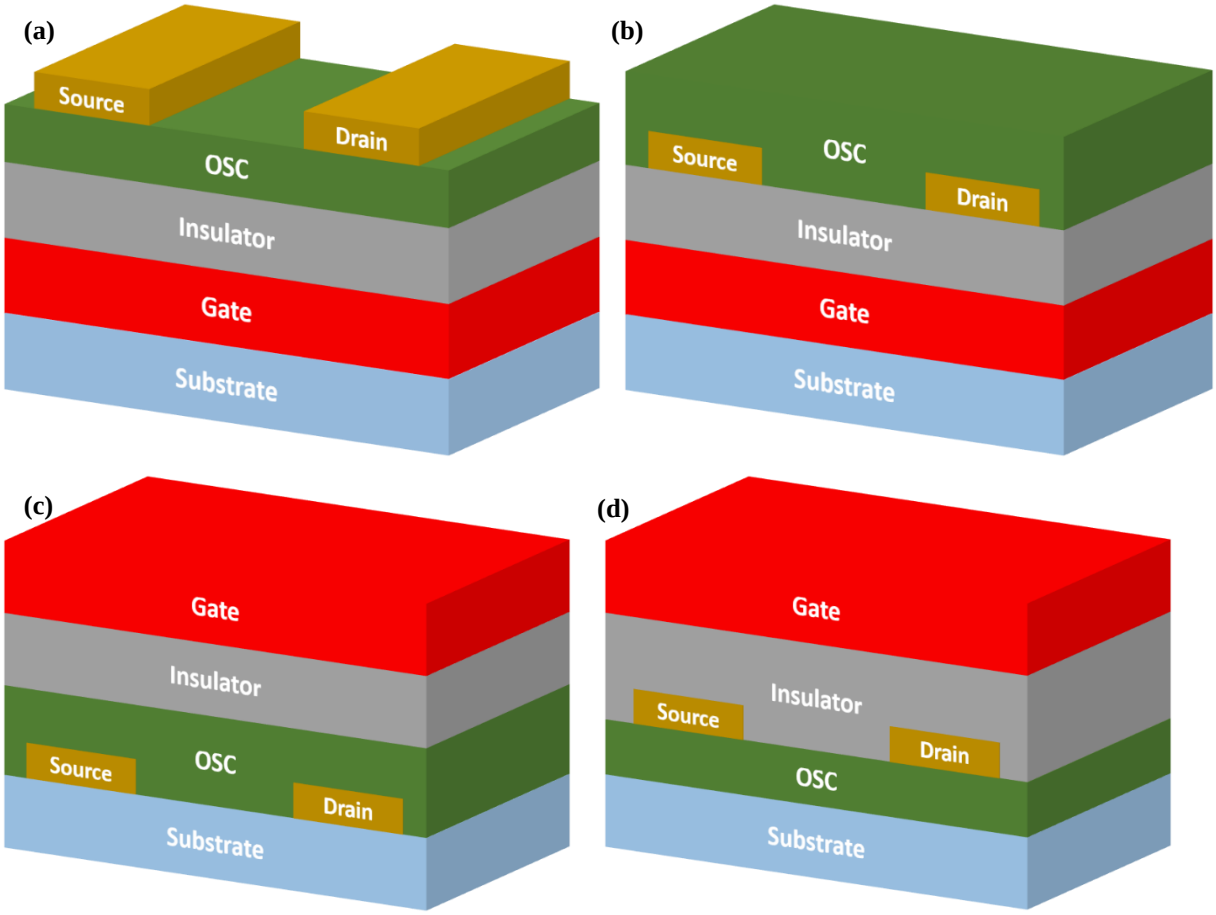


Figure 1.5 Four common types of OTFT geometric structures. (a) Top-contact-bottom-gate (TCBG), (b) bottom-contact-bottom-gate (BCBG), (c) top-contact-top-gate (TCTG), and (d) bottom-contact-top-gate (BCBG).

Briefly speaking, OTFT structures can be classified into top-contact and bottom-contact types based on the positions of the source (S) and drain (D) electrodes. In the top-contact-type structure, the source and drain electrodes are deposited on top of the active layer, creating a larger injection area and improved charge injection characteristics compared to the bottom-contact configuration. In contrast, in the bottom-contact-type, the electrodes are fabricated on the dielectric layer before the deposition of OSC thin films. It results in a smaller charge injection area, and consequently lower charge injection properties. Furthermore, in 2016, Kim et al. [90] reported an approach to enhance the device mobility from the perspective of device structure design as depicted in **Figure 1.6**. The significant concept is to adopt a vertical structure, transforming the channel layer from a horizontal to a vertical orientation and the film thickness serves as the channel length. This approach facilitates more precise control of the channel length and allows for the integration of emerging two-dimensional materials, such as graphene, to modify the channel.

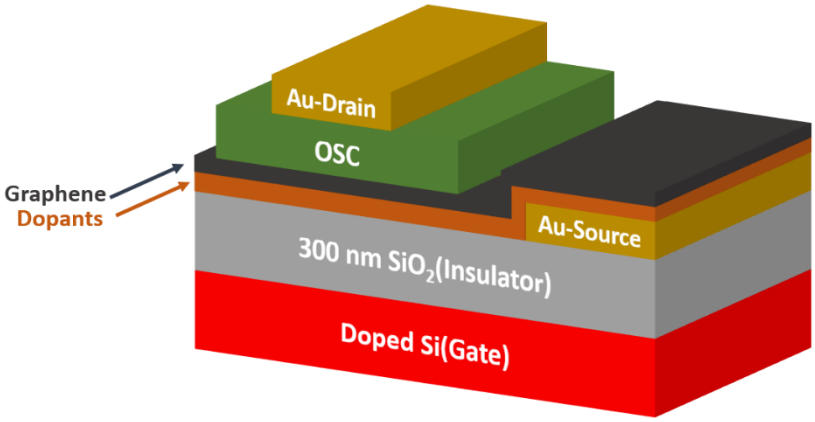


Figure 1.6 The vertical structure of OTFT with graphene layer and dopants.

1.4.2 Operation principle

An organic thin-film transistor (OTFT) is a device that regulates the current between the source and drain under modulating the gate voltage. OTFTs operate in accumulation mode, where the gate voltage (U_{GS}) induces an accumulation of charge carriers, forming a channel at the insulator/organic semiconductor (OSC) interface. If no gate voltage (U_{GS}) is applied and the OSC exhibits extremely low intrinsic conductivity, source-drain current (I_D) will disappear even when a source-drain voltage (U_{DS}) is applied, with its magnitude approaching zero. In this state, the device is in the off state, and the current flowing through it is referred to as the off-state current (I_{off}).

In accordance with the relationship between the Fermi energy level of the metiallic electrode material and the molecular orbitals (MOs) energy level of the OSC in the device, if an appropriate gate-source voltage U_{GS} is applied, under the influence of the U_{GS} electric field, the charges in the source electrode continuously inject into the active layer of the OSC and accumulate at the interface between the insulator layer and the OSC. At this point, if a voltage U_{DS} is applied the accumulated charge carriers in the channel region will start moving, thereby forming the source-drain current I_D. The device is in the on state and the current flowing through is the on-state current I_{on}.

Subsequently, at low U_{DS} with the continuous increase of U_{DS}, under ideal circumstances, I_D will increase linearly accordingly and the device operates in the linear region. When U_{DS} reaches to the threshold voltage in this devoce, a “pinch-off” region will form near the drain electrode. The resistance at the pinch-off region becomes extremely high. The increased source-drain voltage is nearly all applied to the pinch-off region, resulting in the voltages at both ends of the conductive channel remaining essentially unchanged and I_D no longer increasing with

the increase of U_{DS}. At this stage, I_D reaches a constant value and the device operates in the saturation region.

Generally, the MOs energy levels of OSCs, called HOMO and LUMO, have a low concentration of charges. For p-type OSC, when $U_{GS} < 0$ and $U_{DS} = 0$, an electric field is generated at the interface between the OSC and the insulator layer. Under the influence of this electric field in this direction, the HOMO/LUMO energy levels of the OSC shift relatively to the Fermi level of the electrode material. With the increased $|U_{GS}|$, the HOMO energy level approaches the Fermi level of the source electrode. At this point, electrons at the HOMO energy level overflow and move toward the source electrode, leaving positively charged holes in the HOMO level. It can be regared that holes are injected from the metallic source electrode into the HOMO level of the OSC, accumulating at the interface between the OSC and the insulator layer. If the U_{DS} (where $U_{DS} < 0$) is applied, a transverse electric field is formed, driving hole carriers toward the drain electrode, where they are collected, forming a hole conductive channel current. Similarly, for n-type OSCs, under the influence of positive U_{GS} (where $U_{GS} > 0$), electrons from the Fermi level of the metal source electrode flow to the LUMO energy level. If an appropriate transverse electric field is applied, these electrons move toward the drain electrode and are collected, forming an electron-type conductive channel current.

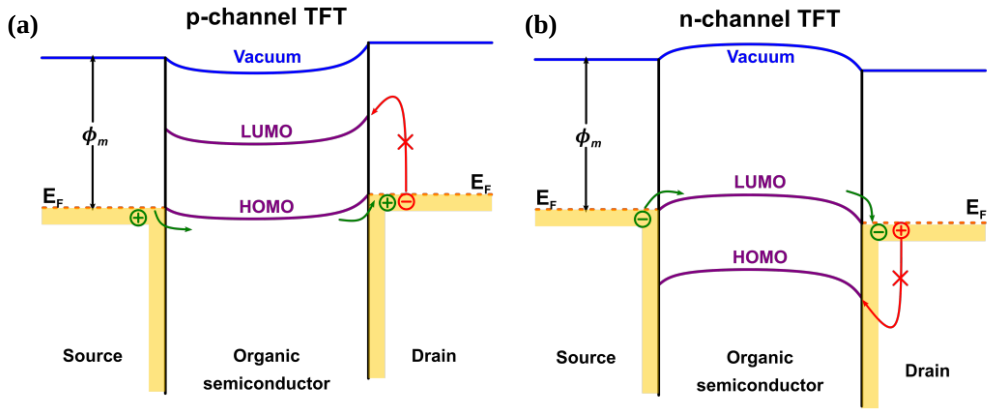


Figure 1.7 Relative alignment of energy levels between the Fermi energy level (E_F) of the contact material and HOMO-LUMO energy levels of the OSC in (a) p-channel and (b) n-channel OTFTs [40].

As shown in **Figure 1.7**, if the energy barrier between the Fermi level of the contact and the HOMO energy level of the organic semiconductor (OSC) is small, efficient injection and extraction of holes occur, making the transistor a p-channel transistor. Similarly, if the energy barrier between the Fermi level of the contact and the LUMO energy level of the OSC is small, electron injection and extraction become easier, making the transistor an n-channel transistor. For unipolar OTFTs, it is preferable to have a large energy barrier between the contact and the

opposite energy level of the semiconductor to prevent unwanted charge injection of the opposite carrier. Specifically, for a p-channel transistor, a large energy barrier should exist between the LUMO energy level and the contact, while for an n-channel transistor, a significant barrier should be present between the HOMO energy level and the contact. Many OSC materials possess a substantial energy gap between the HOMO and LUMO levels, enabling efficient injection and extraction of only one type of charge carrier. For example, when paired with gold contacts, the HOMO energy level of S-DNTT is around -5.3 eV [38], while the typical work function of gold is about -5.1 eV, though it may decrease due to air exposure or other layers within the device, particularly under the push-back effect [91–94]. Despite the potential for a larger energy barrier at the source, this still makes pentacene or DNTT suitable for use as p-channel OTFTs with Au electrodes.

1.4.3 Curent-voltage characteristics

Given that this study focuses exclusively on p-channel OTFTs, the following section wil show the operations of p-channel OTFTs. However, by reversing the polarity of the charge carriers, the same equations can be suitable to n-channel OTFTs as well. When a voltage U_{GS} is applied, charges are accumulated within the semiconductor due to the charge coupling on the dielectric in proximity to the semiconductor-dielectric interface. Since OSCs are typically intrinsic and the polarity of the channel is determined by the relative energy levels of the semiconductor and the contact materials, the accumulation of charge results in the formation of the conductive channel of the transistor. This conductive channel is located within only the first few monolayers of the OSC layer [95,96], adjacent to the semiconductor-dielectric interface; in other words, the thickness of the channel is extremely small compared to that of the overall semiconductor layer. The charge sheet model assumes as zero thickness for the channel, simplifying the analysis [97], which allows the metal-insulator-semiconductor structure to be modeled as a parallel plate capacitor, with the gate electrode and the semiconductor layer acting as the two plates separated by a dielectric insulator.

In the discussion of the *IV* characteristics of the OTFT, the output characteristic curve (I_D-U_{DS}) and the transfer characteristic curve (I_D-U_{GS}) are the two most significant characteristic curves. The parameters in these two curves are as follows: L represents the effective channel length, W represents the effective channel width, U_{GS} indicates the voltage drop between the gate and the source, μ stands for the effective carrier mobility, E_x represents the longitudinal electric field intensity, Q_{Th} represents the amount of charge of the carriers lost due to being

trapped by defects or impurities ('*Th*' representing for threshold), and C_i represents the capacitance of the insulating layer per unit area.

For p-type OTFT, the drain current I_D is below zero and U_{DS} and U_{GS} are defining as negative parameters. The amount of charge generated by the planar capacitance at the position *x* distant from the source electrode is, $Q(x) = -C_i [U(x)-U_{GS}]$, the current density at the position *x* away from the source electrode is, $j(x) = -en(x)\mu E_x(x)$. The charge density at the position *x* distant from the source electrode is, $-en(x) = Q(x)-Q_{Th}$, the current at the position *x* distant from the source electrode is, $I(x)=j(x)\cdot W\cdot d_{inj}$ (d_{inj} meaning the injecting thickness) and with $U_{Th} = -Q_{Th} / C_i$. Hence, [58,98]

$$\begin{aligned} I(x) &= -W \cdot \mu E_x [Q(x) - Q_{Th}] \\ &= -W \cdot \mu C_i [U(x) - U_{GS} + U_{Th}] \left[-\frac{\partial U(x)}{\partial x} \right] dx \end{aligned} \tag{1.9}$$

The total current is obtained by integrating over the entire channel length,

$$I_D L = -\int_0^L \mathrm{W} \cdot \mu C_i [U(x) - U_{GS} + U_{Th}] \left[-\frac{\partial U(x)}{\partial x} \right] dx \tag{1.10}$$

i.e.,

$$I_D = -\frac{W}{L} \cdot \mu C_i \left[U_{GS} - U_{Th} - \frac{U_{DS}}{2} \right] \cdot U_{DS} \tag{1.11}$$

The amount of charge induced by the planar capacitance at the position *x*, located between the source and drain electrodes, was analyzed. During the derivation ofthe aforementioned equation, the following assumptions were made: (1) Gradual channel approximation. Compared to the change in the electric field perpendicular to the channel, from the gate to the semiconductor (which determines the accumulation of charge carriers), the variation of the electric field along the channel (which drives the drain current) is significantly smaller [97,99]. (2) The charge carrier mobility μ is independent of the drain-source voltage U_{DS}. (3) The contact resistance is negligible compared with the channel resistance, and the applied U_{DS} is completely dropped across the channel. The above-mentioned derivation of the current-voltage characteristics of the OTFT represents a simpler version permitted by the assumption. [100]

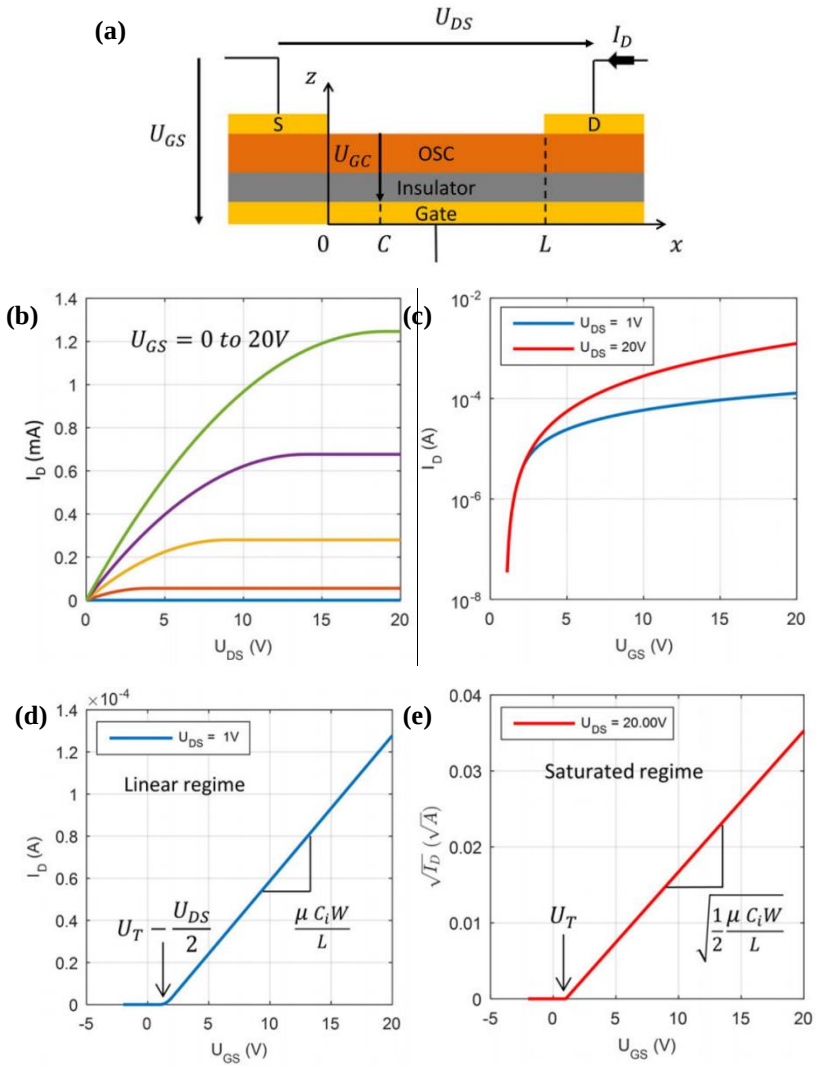


Figure 1.8. Schematic structure of an OTFT with applied voltages. Simulated *I*(*V*) characteristics of an ideal p channel transistor with $L = 5$ µm, $W = 1000$ µm, $C_i = 3.4 \times 10^{-8}$ F cm^{-2}, $\mu = 1$ cm^2 ·V^{-1} ·s^{-1} and $|U_{Th}| = 1$ V. (b) Output characteristics, (c) transfer characteristics in the linear and saturation-regimes, and (d), (e) extraction procedure of μ and U_{Th} in the linear regime (d) and in the saturation regime (e). [81]

The aforementioned formula delineates the drain current I_D for the condition $|U_{GS} - U_{Th}| > |U_{DS}|$, where the conducting channel is nearly uniform and can be modeled as a resistance as described above. Considering **Equation (1.11)** and the assumed conditions, the magnitude of U_{DS}^2 is negligible in comparison with the magnitude of $(U_{GS} - U_{Th})$, and this equation can be simplified to assume the linear dependence of I_D on U_{DS}, namely, $I_D = -\frac{W}{L} \cdot \mu C_i [U_{GS} - U_{Th}] \cdot U_{DS}$ and the operation under this condition is referred to as the linear operation state. For practical measurements, as the U_{DS} values increase in the linear state, I_D demonstrates a dependence on U_{DS} at a fixed U_{GS}, which is in line with the mathematical characteristics presented by the aforementioned formula. When U_{DS} keeps rising and the potential difference

U_{DS} exceeds the difference between the U_{GS} and the threshold voltage U_{Th}, that is, $|U_{DS}| \geq |U_{GS} - U_{Th}|$, the current between the source and drain electrode increases. However, this results in a reduction in the drain-gate potential difference $|U_{GD}|$ and, when $U_{DS} = U_{GS} - U_{Th}$ and $U_{GD} = U_{Th}$, charge depletion emerged at the drain, thereby causing I_D to gradually tend towards saturation due to channel pinch-off. The current-voltage relationship in the saturation region conforms to the following formula,

$$I_D = -\frac{W}{2L} \cdot \mu C_i (U_{GS} - U_{Th})^2 \quad \textbf{(1.12)}$$

Off-state Regime The drain current equations in the linear and saturation states are valid only when the charge sheet layer is formed, that is, only when $|U_{GS}| > |U_{Th}|$, as U_{Th} is the voltage required to overcome all obstacles for the accumulation of charge in the channel. When $|U_{GS}|$ is significantly smaller than $|U_{Th}|$, the device is in the off state, and the current under this operational condition is determined by the bandgap or doping circumstances. The current within this OTFT operation mechanism, namely the off-state current I_{off}, should be extremely small to reduce the power consumption of the transistor.

Subthreshold Region When the gate-source voltage $|U_{GS}|$ is marginally smaller than the threshold voltage $|U_{Th}|$ but greater than the turn-on voltage, the concentration of free carriers in the channel is extremely low. The turn-on voltage, U_{onset}, is the gate-source voltage at which the drain current begins to increase beyond the off state. The drain current in the subthreshold region is attributed to the injection of charges into the semiconductor layer through thermal excitation, having crossed the energy barrier at the source contact and having diffused to the drain contact.

1.4.4 OTFT operation parameters

In this section, we will briefly introduce several electrical parameters of OTFT. They are mainly field effect mobility μ (seeing in Section 1.4.4.1), threshold voltage U_{Th} (seeing in Section 1.4.4.2), on-off drain current ratio I_{on}/I_{off} (seeing in Section 1.4.4.3), and subthreshold slope (seeing in Section 1.4.4.4).

1.4.4.1 Field-effect mobility

The field-effect mobility, μ, is defined as the average drift speed of charge carriers under a unit electric field, reflecting the mobility of charge within the device influenced by the electric field; namely, the mobility is the velocity that charges obtain under a unit electric field [101]. From a microscopic perspective, charges are accelerated by the action of the electric field, but lose partial of their momentum during motion due to effects such as lattice scattering. This

process occurs extremely rapidly and is an average effect obtained by observing a large number of carriers. From a macroscopic level, the movement of charge carriers in solid materials is a flowing process.

In this study, the effective field-effect mobility of the device is generally obtained through the transfer characteristics (I_D-U_{GS}) curve, and it can be calculated respectively from the curves of the linear region and the saturation region, as **Figure 1.8 (d)** and **(e)** shown. In the linear region, it can be derived from the **Equation (1.11)**,

$$\mu_{lin} = \frac{L}{W \cdot C_i \cdot U_{GS}} \left(\frac{\partial I_D}{\partial U_{GS}} \right) \tag{1.13}$$

and in the saturation region, **Equation (1.12)** can be dedicated as,

$$\mu_{sat} = \frac{2L}{W \cdot C_i} \left(\frac{\partial \sqrt{I_D}}{\partial U_{GS}} \right)^2 \tag{1.14}$$

the unit of mobility is $cm^2 \cdot V^{-1}s^{-1}$.

The magnitude of mobility in devices is intrinsically associated with multiple factors. In OTFTs, factors such as the extent of π orbital overlap between adjacent molecules within the formed film, the film morphology, the orientation and degree of molecular order, the interface contact between the semiconductor and the electrode, and the interface between the semiconductor and the insulating layer, all exhibit a highly interdependent relationship. Since charges in the channel of OTFTs predominantly accumulate at the interface between the OSC layer and the insulator layer, scattering effects caused by internal defects and lattice interfaces hinder the transport of carriers. Generally, the mobility of OTFTs with nanoscale films is typically lower than that of bulk materials, and the mobility is extracted from **Equation (1.13)** and **(1.14)**.

1.4.4.2 Threshold voltage

The ideal gate dielectric exhibits a large band gap, and no electronic states exist either within the gate dielectric layer or at the interface with the semiconductor. However, actually, structural and chemical defects within the dielectric layer, the semiconductor layer, and at the dielectric-semiconductor interface give rise to the formation of trap states. Additionally, the energy levels between the semiconductor and the gate electrode metal often mismatch. Thus, a non-zero U_{GS}, defined as the threshold voltage U_{Th}, must be imposed to surmount these effects and thereby induce mobile charge carriers within the channel.

Several approaches can be employed to determine the U_{Th} of OTFTs [102–104]. Generally, there are two methods to obtain the U_{Th} of a device: The first one is based on the current formula

of the linear region of the OTFT. In the transfer characteristics curve, when the U_{DS} is relatively small, the portion of the transfer curve where $|U_{GS}| > |U_{DS} - U_{Th}|$ reflects the characteristics of the linear region of the device, like **Figure 1.8 (d)** showing. By extending the I_D-U_{GS} relationship curve region, the intercept on the U_{GS} axis is the voltage U_{Th} at zero current. The second one is to measure the specific value of U_{Th} by using the I_D-U_{GS} curve in the saturation region. When the device is in the saturation state, the square root of the source-drain current I_{DS} shows a favorable linear relationship with the U_{GS}. By fitting the relationship curve of $|I_D|^{1/2}$ and U_{GS}, the intersection point of the fitting line and U_{GS} constitutes the U_{Th} of the OTFT, as **Figure 1.8 (e)** illustrated. The U_{Th} derived from the linear and saturation regions of the transfer characteristics curve usually differ. It is also one effective parameter which is extracted from **Equation**.**(1.13)** and **(1.14)**.

In this study, this method is to be employed for characterizing the U_{Th} of the device. To be more precise, it is one effective parameter that is not only influenced by the charge trap density within the conducting channel but also contingent on factors such as the contact barrier at the interface between the source/drain electrodes and the OSC, as well as the presence or absence of a built-in conducting channel.

1.4.4.3 On-off drain current ratio

On-off drain current ratio, I_{on}/I_{off}, is defined as the ratio of the drain current I_D in the "on" and "off" states, constituting an indispensable performance parameter in OTFTs. It reflects the quality of the switching performance of device under a specific gate voltage, especially within fundamental display units used in display arrays and logic circuits, where the switching ratio is of paramount importance. A high switching ratio indicates superior stability and anti-interference capabilities. Conversely, if the switching ratio is low, the corresponding performance will deteriorate. Achieving a high switching ratio requires maximizing the on-current and minimizing the off-current. The current switching ratio reflects the device's ability to regulate current.

In the transfer characteristic curve, I_{on} initially increases as U_{GS} rises. Nevertheless, upon the gate voltage attaining a certain magnitude, the source-drain current ceases to undergo substantial alterations concomitant with the increase of U_{GS}, and at this juncture, I_D attains the maximum value, I_{on}. When the gate voltage amounts to zero, the value of I_D constitutes the I_{off} of the device. In actuality, I_{off} represents the leakage current of the device, which directly impacts the power consumption of the device and is determined by the fundamental attributes of the device. A higher *Ion* bespeaks a more potent driving capacity of the device, whilst a

lower I_{off} intimates a superior turn-off capacity of the device. For the application of OTFTs in active-driven displays, a ratio of the device typically reaching the order of 10^6 is requisite, while for applications in logic circuits, an even loftier current switching ratio is indispensable.

1.4.4.4 Subthreshold slope

As previously expounded, the subthreshold state is delineated by diffusion-dominated current within the channel, and the drain current is exponentially contingent upon the gate-source voltage. The reciprocal of the slope of the transfer curve in this region, namely $\partial U_{GS}/\partial log I_D$, is defined as the subthreshold slope in units of mV/dec, where 1 decade (dec) corresponds to a 10-fold increment in the source-drain current. Specifically expressed as,

$$S = \frac{\partial U_{GS}}{\partial log I_D} = ln10 \frac{kT}{e}\left(1 + \frac{eN_{it}}{C_i}\right) \quad \textbf{(1.15)}$$

typically, this quantity depends on the capacitance density C_i of the insulating layer. The smaller the value of S is, the faster the transition of the OTFT from the off state to the on state occurs. Furthermore, the subthreshold slope indicates the trap state density of the interface charges between the OSC and the insulating layer, that is, the quality of the interface contact.

1.4.5 The interfaces in organic thin-film transistors

From the perspective of a typical OTFT, the related electrical performance is primarily determined by the characteristics of employed materials and their corresponding interfaces. In general, one OTFT consists of three electrodes (source, drain, and gate), a dielectric layer, and an OSC layer. This structure contains two key interfaces into the OTFT: the electrode/OSC thin-film and the OSC thin-film/dielectric layer interfaces. The characteristics of the former interface correlate with the charge injection efficiency, while the latter one is associated with charge transport in the channel. Therefore, the electrode/OSC interface and the dielectric layer/OSC interface are the two principal factors influencing the device-performance.

1.4.5.1 Organic semiconductor-electrode interface

The physical properties of the source and drain electrode/OSC interfaces determine the charge carrier injection- and extraction- efficiency in the channel of the OTFTs.

1.4.5.1.1 Concept of barrier height

Typically, metallic materials are served as electrodes in OTFTs. The alignment between the Fermi energy level of the electrode at the contact surface and the HOMO or LUMO energy level of the OSC molecule is the primary factor influencing charge transport at this interface. When the two materials come into contact, charge rearrangement occurs at the interface,

bringing the system to thermal equilibrium and establishing a common Fermi level [105]. The equilibrium alignment of energy levels across this junction mainly determined charge transport at the interface during device operation. Specifically, at the source electrode, if the HOMO (or LUMO) energy level of the OSC is misaligned with the Fermi energy level of the source electrode, the resulting energy barrier Φ_B will hinder the injection efficiency of holes (or electrons).

To predict the height of Φ_B, several models have been put forward to indicate the particulars of the interface equilibrium process in terms of energy levels and charge transport within the semiconductor thin film, any intermediate regions, and at the metal surface. In the simplest model which initially developed for the contact of metals with inorganic semiconductors, known as the Schottky-Mott limit, the energy barrier (respectively $\Phi_{B,n}$ and $\Phi_{B,p}$) for electron or hole transfer at the contact metal-semiconductor interface is simply evaluated by the disparity between the metal Fermi energy of the contact (φ_m, defined as the energy difference between the vacuum level (E_{vac}) and the Fermi energy of the metal) and the semiconductor transport level of the insulating material (ionization energy (*IE*) for the hole injection barrier or electron affinity (*EA*) for the electron injection barrier). [91,106]

For OSCs, the expected energy barriers for charge injection can be evaluated analogously based on the positions of LUMO and HOMO relative to φ_m. For φ_m closer to LUMO (HOMO), more efficient electron (hole) injection is anticipated in the metal contacted with OSCs. However, this simplification has been proven to be highly inaccurate for the precise prediction of Φ_B or the description of the charge injection characteristics in actual devices. The origin of the contact differences with OSCs lies in the deviation of the vacuum level alignment resulting from the formation of interface dipoles (Δ) within the first few molecular layers of the OSC away from the contact with the metal surface [92]. It modifies the effective work function (φ_C) of the contact, such that it no longer coincides with φ_m, $\varphi_C = \varphi_m + \Delta$, and $\Phi_B = IE, EA - \varphi_C$.

It existed numerous prominent potential sources of interface dipoles, primarily related to the localized energy levels in OSCs. [107] They involve charge transport across the interface, resulting in the formation of surface charge sheets on the metals, with a corresponding image charge density in the OSC. Additionally, intense chemical reactions between OSC molecules and ultra-clean metal surfaces, changes in the orientation of molecules at the surface and within the semiconductor film, intrinsic dipole moments in the adsorbed molecules, and the interaction of the π-electron cloud of the physically adsorbed organic layer with the metal electron tail states also occur. They resulted in the reduction of the metal work function (known as the

"pillow" or "push-back" effect). The total work function of the metal depends on the bulk chemical potential and the electrostatic potential of the metal surface. The bulk chemical potential is not influenced by weakly physically adsorbed atoms or molecules on the surface, but the electrostatic potential of the metal surface is affected. When the positive charge density from the atomic nuclei drops abruptly to zero at the metal surface, the negative charge density from electrons could "leak" into the vacuum [93]. As shown in **Figure 1.9**, for a neutral metal film, the excess electron density outside the metal surface must be compensated by an insufficiency of electron density within the metal surface, thereby forming a dipole potential at the surface. Represented by the jellium model, the electron density of the metal decays exponentially from the surface plane of the metal nucleus and extends by several Å from the surface. [108] Generally, the greater the dipole potential energy at the metal surface, the more polarizable the electron density tail at the surface, and the greater the change in the physically adsorbed work function.

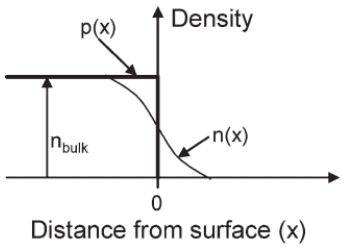


Figure 1.9 Simple illustration of positive p(x) and negative n(x) charge distribution at a metal surface. [93]

When a molecule approached to the metal surface, the electron tail states emerging from the metal surface interact with the π-electron cloud of molecule. This interaction causes compression of the electron density tail, leading to a reduction in the surface dipole potential energy of the gold surface in contact with the OSC. For instance, gold (Au) is usually regarded as one popular candidate for hole injection contacts since its work function is often stated as approximately (5.2 ± 0.1) eV. However, when gold contacting with the OSC, neither the top nor the bottom contact achieves this high work function; instead, a moderately effective work function of (4.5 ± 0.1) eV is observed [109,110]. Therefore, gold contacts deposited in this manner may have poorer hole injection than typically assumed. In the absence of chemisorption, the push-back effect is likely to occur for all organic-metal and metal-organic interfaces. Additionally, the specifics of the fabrication process can significantly influence interface properties. Work function values reported in the literature, typically measured under ultra-high vacuum (10^{-9} mbar or better), represent pristine surfaces. This pressure is 2–3 orders of

magnitude lower than that commonly used for depositing metals and organic molecules in device fabrication. Metal films fabricated at pressures like 10^{-6} mbar are expected to undergo slight oxidation, particularly at the surface. Substrates exposed to air typically have a thin hydrocarbon layer, as is often the case for gold and indium tin oxide (ITO). For hydrocarbon contamination on metal surfaces, there is little or no charge exchange between the adsorbed hydrocarbons and the metal. However, even without charge transfer or intrinsic dipoles, the push-back effect still alters the work function of metal substrate. [93]

For the optimization at the metal-OSC interface, interfacial modification substances are commonly employed to enhance the interface contact. Monomolecular self-assembly (SAM) constitutes the most prevalently used electrode interface modification material [111]. Introducing SAMs at the interfaces between source-drain electrodes such as Au, Ag, and Cu and the OSC represents a widespread and effective method for improving the interface contact. It is capable of introducing electric dipoles at the interface, thereby modulating the electrode work function and reducing the contact barrier. Initially, thiols were used as SAMs materials for modifying electrodes [112]. Over the decades years of development, a variety of SAMs materials have been developed, such as thioketones and thioesters [113,114]. Additionally, metal oxides and TCNQ and its derivatives can also be employed for electrode modification [115–118]. In practice, the Au S&D electrodes in our fabricated OTFT were not executed by any SAM treatment.

1.4.5.1.2 The Fermi level pinning

According to $\varphi_C = \varphi_m + \Delta$, and $\Phi_B = IE, EA - \varphi_C$, to decrease Φ_B, the disparity between φ_C and IE or EA, should be minimized. Furthermore, it is anticipated that the magnitude of Δ varies linearly with φ_m. Consequently, it is also supposed that Φ_B varies linearly with φ_C, such that the variation slopes (S) of the hole injection barrier ($\Phi_{B,p}$) and the electron injection barrier ($\Phi_{B,n}$) will follow,

$$S = \frac{d\Phi_{B,n}}{d\varphi_c} = -\frac{d\Phi_{B,p}}{d\varphi_c} = 1 \qquad \textbf{(1.16)}$$

This is denominated as the Schottky-Mott limit [91]. The conventional strategy is to deliberately introduce interlayers with intrinsic dipoles to shift φ_C for enhancing hole or electron injection [186]. Nevertheless, other elements influenced the scaling of the injection barrier, so that S is not 1 and the Fermi level at the interface is regarded as being fixed at a certain position and no longer varies with the work functions of the electrode and the semiconductor. This phenomenon is known as Fermi level pinning (FLP) [93,119]. This phenomenon results in the

potential difference at the interface not being explicable by simple energy level alignment and is typically ascribed to the presence of the density of states at the interface (N_{int}). A measurable indication of FLP, for instance, as measured by UPS, is the deviation of the dependence of the semiconductor work function on the substrate work function from the Schottky-Mott limit at high or low substrate work functions [93,120].

Generally, FLP is primarily attributed to the introduction of interface states at the metal electrode-OSC interface. Interface states are electronic states resulting from interface defects, impurities, and chemical reactions. These states can trap electrons or holes, forming electron traps or hole traps, thereby causing the fixation of the Fermi level. The defect states are due to the structural imperfection at the interface (such as lattice misalignment, broken bonds, etc.), electronic states are formed, and these states can capture electrons or holes, leading to the fixation of the Fermi level. Impurity states refer to the presence of impurities or dopants at the interface that introduce new electronic states, and these impurity states can also trap carriers. For chemical reaction states, it implies that when the metal electrode comes into contact with the OSC, chemical reactions may occur, forming new chemical bonds or products, thereby generating new electronic states. The practical significance of FLP for engineering organic devices resides in that it can significantly affect the efficacy of some common contact modification strategies, among which tuning φ_C is the main strategy for reducing Φ_B and achieving Ohmic contact.

1.4.5.1.3 Charge injection process

Charge injection constitutes the principal prerequisite for the establishment of a conductive channel and the internal flow of charges within OTFT. Commonly, metallic materials are utilized as the source and drain electrodes in OTFTs, leading to a common Fermi energy level within the contact surface with the OSC. Nevertheless, the energy barrier Φ_B, which is shaped by the energy disparity between the Fermi level of the source material and the accessible molecular orbital energy level of the OSC, influences the charge injection process. Briefly speaking, charges can transport since crossing or tunneling through the potential barrier; the prevalently employed one-dimensional charge injection model is depicted in **Figure 1.10**. The injected charge current density (J) is typically caused by the superposition of physical effects, encompassing field emission from metals and tunneling through the energy barrier. The primary injection pathways can be modulated by doping concentration, traps states, and external temperature.

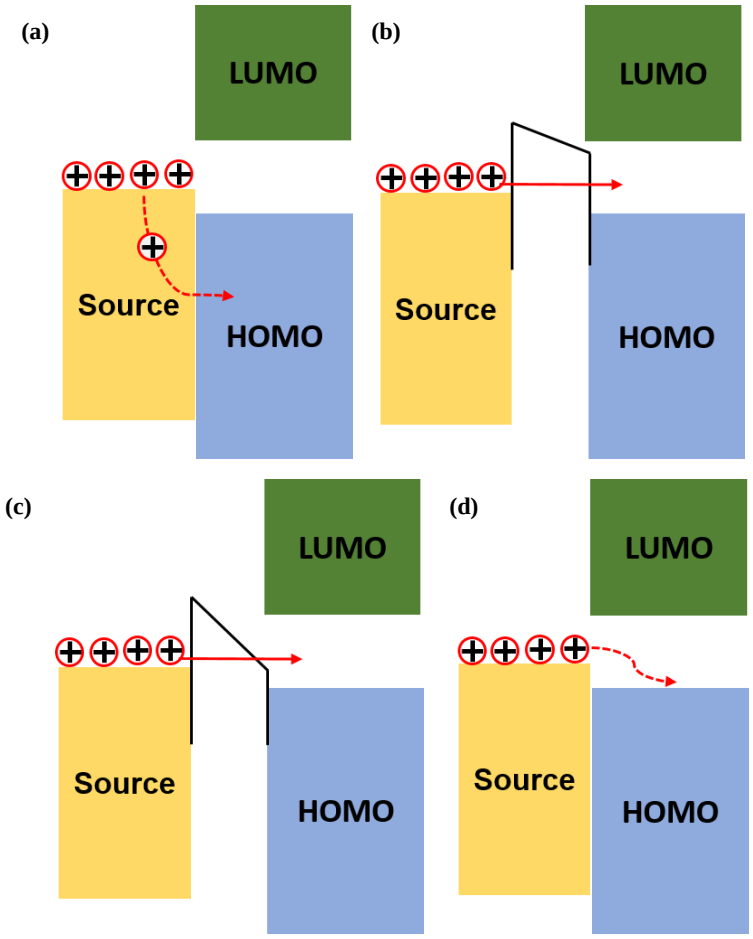


Figure 1.10 Injection of holes from a metal into an OSC: (a) thermionic field emission, (b) direct tunneling, (c) Fowler–Nordheim tunneling, and (d) diffusion. Dashed arrow shows recombination. [121]

1.4.5.1.3.1 Thermonic Field Emission

When the Schottky barrier height exceeds the thermal energy of charges, thermionic field emission (TFE) occurs as depicted in **Figure 1.10 (a)**. The charges within the metal that possess energy surpassing the barrier height, either thermally stimulated or arising from the applied field at the interface, are capable of overcoming the barrier and thus penetrating into the OSC material, thereby giving rise to the injection current. The injected charge current density (J) in the framework of the TFE is expressed as:

$$J = A^{*}T^{2}exp\left(-\frac{q\phi_B}{kT}\right)\exp\left(\frac{qV}{kT}\right) \quad (1.17)$$

$$A^{*} = \frac{4\pi q m^{*} k^{2}}{h^{3}}$$

where h is the Planck constant, m^* is the effective mass of the charge carrier in the metal and V is the applied voltage. This formula indicates the temperature dependence of the current. Without damaging the structure of the OTFT and the OSC material, under the same bias condition, the current increases with the rise in temperature. This model has been successfully

applied to organic semiconductors with various contact materials, including metals, carbon nanotubes, and metal oxides [122–124]. Li et al. demonstrated that the field dependence of the contact resistance follows the predicted behavior of TFE on the semiconductor 2,9-dialkyldibenzo [2,3b:2',3'-f] thieno [3,2-b] thiophene (C_{10}-DNTT) device with modified gold contacts [125]. They also found that minor changes in the work function of the contact material lead to significant alterations in the contact resistance, which implies the exponential dependence of the injection J on Φ_B. Sarker and Khondaker observed the temperature-dependent current behavior, indicating that a TFE injection process occur into pentacene in contact with carbon nanotubes, at a temperature above 200 K, and with an applied electric field less than 10^6 V cm^{-1} [122]. Xu et al. found that when the temperature is above 150 K, the temperature dependence of the OTFT structures of two copolymers diketopyrrolopyrrole-thieno [3,2-b] thiophene (DPPT-TT) and indacenodithiophene-benzothiazole (IDT-BT) conforms to the TFE model.[123]

1.4.5.1.3.2 Tunneling

If the OSC possesses sufficient empty states close to the contact and the depletion region is less than the average free path of charges within the OSC, charges can cross the energy barrier. In a system where thermionic field emission predominates at room temperature, the tunneling phenomenon can be discerned under low-temperature and high electric field strength circumstances. In organic light-emitting diodes (OLEDs) and OTFTs, with an applied electric field of approximately 10^6 V cm^{-1}, a transition from thermionic emission to tunneling is noted [122]. It existed two types of tunneling: direct tunneling and Fowler-Nordheim (FN) tunneling. Direct tunneling predominates in low fields, and the injection barrier is effectively "square" in **Figure 1.10 (b)**. This engenders the injection current [126],

$$J \sim V \cdot exp\left(-\frac{2d\sqrt{2m^*\phi_B}}{\hbar}\right) \quad \textbf{(1.18)}$$

where, $\hbar = h/2\pi$, d and V represented the tunneling thickness and applied voltage, respectively. Under the electric field with high intensity, one side of the injection barrier bends downward illustrating in **Figure 1.10 (c)**, and the injected charges subsequently experience a "trapezoidal" barrier, thereby generating the Fowler-Nordheim injection current. [126]

$$J \sim V^2 exp\left[-\frac{4d\sqrt{2m^*\phi_B^3}}{3\hbar qV}\right] \quad \textbf{(1.19)}$$

wherein, d and V respectively indicate the tunneling thickness and applied voltage. The above equation indicates that, without breakdown of the OTFT, the injection current density increases with the strengthen of electric field.

1.4.5.1.3.3 Diffusion

As the average free path of the charges is shorter than the depletion width, the charges injected into the depletion region at the contact can be backscattered and recombined at the metal interface, potentially resulting in recombination back to the injection contact as depicted in **Figure 1.10 (d)**. The charges entering the depletion region can also be construed as having an escape probability, such that the escaped charges constitute the current injected into the device [127]. Although this process is not conceptually analogous to the injection described in the aforementioned two models, it constitutes a significant modification of the charges injected into the semiconductor body at the contact, thereby giving rise to the device current. The diffusion injection current can be modelled as, [105]

$$J \approx q\mu N E_M exp\left(-\frac{q\phi_B}{kT}\right)\left[exp\left(\frac{qV}{kT}\right)-1\right] \quad \textbf{(1.20)}$$

herein, N is the effective density of states in the conduction band, E_M is the maximum electric field at the interface, and μ is the carrier mobility of the semiconductor.

1.4.5.1.4 Contact resistance

Resistance constitutes one unavoidable aspect for electronic devices. For OTFTs, the resistance system in the ideal situation merely encompasses negligible Ohmic resistance, and small channel resistance. However, in practice, the resistance system in OTFTs consists of channel resistance, and contact resistance (R_C) located at electrodes. The R_C in OTFT originates from the voltage necessary for charge injection through the source contact/OSC interface, ΔV_S, and the drain contact/OSC interface, ΔV_D. Thus, the total voltage applied between the source and the drain U_{DS} is distributed across the source-drain contacts and the channel,

$$U_{DS} = \Delta V_S + \Delta V_{ch} + \Delta V_D = I_D(R_s + R_{ch} + R_D) \quad \textbf{(1.21)}$$

herein, ΔV_{ch} represents the voltage drop across the channel, R_S and R_D are respectively the resistances of the source and drain terminals, and R_{ch} is the channel resistance. R_C is one of the main obstacles impeding the further development of OTFT circuits [91,121,128,129]. It influences OTFT in multiple manners. Firstly, it impacts the injection and extraction efficiency of charges within the device, and reduces the device performance of the OTFT. Secondly, if not properly considered, high R_C may cause inaccurate extraction of device parameters. For example, in the process of extracting the effective field-effect mobility based on the transfer

characteristics curve I_D-U_{GS} and **Equation**.**(1.13)** and **(1.14)**, it may result in overestimation or underestimation of mobility [101,130,131]. Any inaccuracies in parameter extraction may have a considerable influence on material development, ranging from generating incorrect structure-performance relationships to discarding OSCs whose effective intrinsic electrical properties are masked by inefficient contacts. Additionally, the higher R_C will reduce the response speed of the OTFT, limiting its applications in aspects such as analog, low power, and high frequency.[132]

The contact resistance R_C showing in **Figure 1.11**, can be expressed as the sum between the resistance $R_{C,int}$ related to the injection barrier and the bulk resistance $R_{C,bulk}$ associated with the charge transmission through the length L_0 between electrodes and channel. R_C being described in **Equation (1.22)** is given as follows,

$$R_C W = R_{C,int} W + R_{C,bulk} W \qquad \textbf{(1.22)}$$

wherein, the R_C is normalized to the width W of the transistor [124,133,134]. For bottom-contact type of OTFT, the second term approximates to zero given that charges are directly injected into the channel. The fundamental geometries of OTFT-structures can be classified as top contact and bottom contact, as **Figure 1.5** illustrated. In the bottom-contact structure, charges are predominantly injected at the edge of the source contact; accordingly, the metal/OSC injection interface is approximately ascertained by the lateral area of the electrode. In the top-contact structure, the charge injection area is larger in comparison with that of the bottom-contact, where it is roughly determined by the product of the channel width and the overlap between the source and the gate.

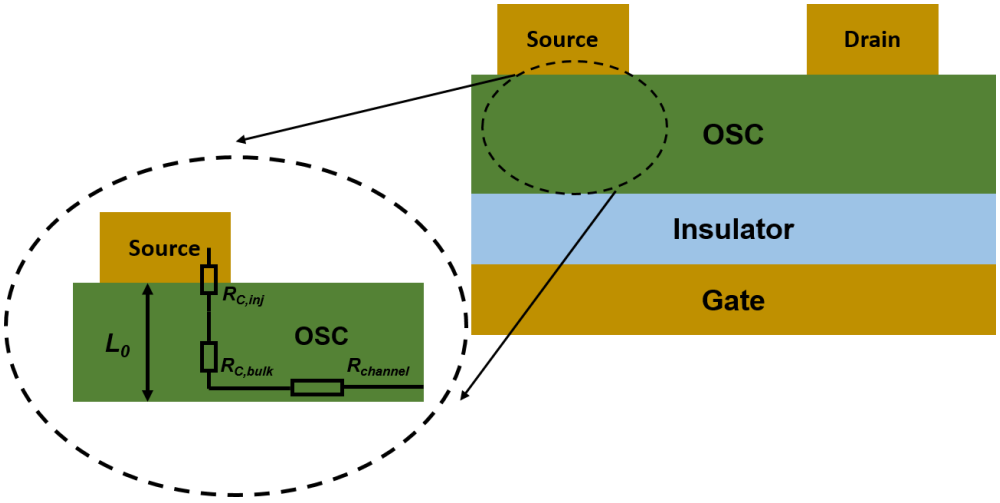


Figure 1.11 The schematic of contact resistance R_C into top-contact configuration of OTFT.

The physical origin of contact resistance R_C in OTFTs is a complex interplay of intrinsic and extrinsic factors that compete with each other. Typically, metals are utilized as electrode

materials for OTFTs, and the equilibrium (re)arrangement of energy levels and charge distributions at the interface between the metal contact and the OSC predominantly determines the charge transport process during device operation. As discussed in the previous Section 1.4.5.1.3, this process can be broadly categorized into carrier transport at the interface mediated by thermal activation and quantum tunneling [135]. Therefore, in these charge injection/extraction processes between the metal and the OSCs, the most critical factors to be considered are the energy barrier (Schottky barrier) Φ_B formed at the interface, the width of the van der Waals gap at the interface between the metal contact and the first layer of the OSC film, the existence of the interface dipole (Δ), and the width of the depletion region (W_d) determined by the energy landscape and charge density in the OSC [136]. For OTFTs with the lowest R_C, the charge injection can usually be well depicted by the thermionic emission theory of Schottky diodes, where the current density (J) is as follows, [137,138]

$$J = A^* T^{\alpha} exp\left(-\frac{\Phi_B}{k_B T}\right)\left[1 - exp\left(-\frac{\Delta\Phi_B + qU_{DS}}{k_B T}\right)\right] \quad \textbf{(1.23)}$$

herein, A^* is the effective Richardson constant, α is the dimensional constant (equal to 2 for bulk semiconductors and 3/2 for two-dimensional semiconductors), q is the elementary charge, and $\Delta\Phi_B$ is the reduction in the Schottky barrier height caused by the image force. When U_{DS} = 0 and α = 2, the following is the contact resistance R_C,

$$R_C = \left(\frac{k_B}{qA^*T}\right) exp\left(\frac{\Phi_B}{k_B T}\right) \quad \textbf{(1.24)}$$

The exponential dependence of the contact resistance R_C on Φ_B implies that it is, in principle, the most crucial parameter for enhancing the R_C. Whether the charge transport at the interface between the contact surface and the OSC further conforms to the thermionic emission theory depends on the charge density and the efficacy of charge transport in the OSC layer [139–141]. A key aspect determining the efficiency of charge transport in OSCs and the quality of the contact-OSC interface is the interaction between organic molecules, and crystallization occurs through weak Van der Waals forces rather than covalent bonds [142]. The effective transport of charges in OSCs largely depends on the extent of overlap of π orbitals between adjacent molecules, and this overlap degree is significantly affected by the differences in OSC morphology [143,144]. Therefore, compared to inorganic semiconductors, the average free path of mobile charge carriers in OSCs is typically very short (in the order of molecular separation distances) due to the disorder and is highly sensitive to factors such as thermal fluctuations and external factors (such as the surface roughness of the substrate and surface contaminants), resulting in smaller transfer integrals and diffusion-limited charge transport [139,140,143,145].

The actual physical interfaces within organic devices are not as atomically precise as those achievable in inorganic semiconductor devices and depend on many factors related to the device fabrication methodology. The architectures of OTFTs can be broadly classified into top-contact and bottom-contact configurations, as shown in **Figure 1.5**. In top-contact OTFTs, the thermally evaporated metal material process can lead to the diffusion of metal atoms onto the OSC surface and may also cause thermal damage. In contrast, in the bottom-contact structure, metal electrodes are fabricated on the substrate initially. Due to differences between the electrode surface and the gate dielectric surface, the electrode surface may exhibit substantial roughness or surface energy, causing the subsequently deposited OSC films to predominantly exist in amorphous or polycrystalline forms with high molecular disorder. This not only reduces the overlap of π electron clouds between molecules but also causes varying molecular orientations, which impact the molecular orbital energy levels, leading to an energy barrier between accessible states and decreasing the injection efficiency at the interface between the electrode and the OSC.

Furthermore, the reduction in the average free path leads to diffusion-limited charge injection, resulting in a large depletion region. Consequently, due to the space charge limited effect, the dependence of charge mobility near the contact interface on charge injection efficiency is further increased. [92,92,140,146]. This is important in numerous amorphous semiconductor polymers, where the carrier mobility is frequently low. On the whole, the contact resistance of OTFTs depends on the characteristics of the electrodes and semiconductor materials, the physical injection mechanisms at the interfaces, and device-related parameters; *i.e.*, $R_C \propto R_C(\Phi_B, F, T, L_0, \mu)$ [121]. L_0 is the distance from the electrode to the accumulation channel, the carrier mobility μ of the organic semiconductor is defined both in the direction perpendicular to the channel μ_{perp} and across the channel $\mu_{parallel} = \mu_{FET}$.

1.4.5.2 Organic semiconductor-gate dielectric interface

Generally, the charge transport properties of OSCs depend on the degree of overlap between the π-electrons of the OSC molecules. In OTFTs, charge transport primarily occurs within a few molecular layers of the OSC adjacent to the dielectric interface. Therefore, the contact interface between the OSC and the dielectric layer is of paramount significance [147–151]. Defects at the interface not only introduce trap states and increase the threshold voltage but also can scatter with the drifting carriers and reducing the mobility [48]. Meanwhile, the surface characteristics of the dielectric layer, such as roughness, disorder, and surface energy,

can further exert an influence on the film morphology of the OSC, thereby affecting the charge transport characteristics and consequently the device performance.

Similar to the contact interface between the metal electrode and OSC, self-assembled monolayers (SAMs) are widely used to improve the dielectric layer/OSC interface properties, particularly regarding trapped and transported charge [48,152–154]. The surface of the dielectric layer typically contains a significant number of defects. For example, many -OH groups exist on the surface of SiO_2, which are considered interface charge trap states and hinder charge transport [154]. SAM modification can significantly reduce these interface defects. Additionally, by adjusting the end groups, chain length, and phase state of SAMs, as well as surface characteristics like roughness, energy, and order, the morphology and molecular arrangement of the OSC can be optimized, improving the transport performance of holes or electrons [155–158]. Current research on SAMs focuses on different categories, such as using trichlorosilane, alkoxysilane, and silazane to modify SiO_2 substrates, and phosphoric acid to modify Al_2O_3 and HfO_2 substrates.

The types of modification materials on the dielectric layer surface can exert a significant influence on the morphology of the deposited OSC layer in contact with it. For instance, pentacene thin-films were respectively deposited on SiO_2 surfaces modified by octadecyltrichlorosilane (OTS) and hexamethyldisilazane (HMDS). Through AFM testing, it was discovered that in the devices modified by OTS, the pentacene thin-film manifested a dendritic morphology, while in the devices modified by HMDS, the pentacene thin-film exhibited a sheet-like morphology. This variation also had a considerable impact on the performance of the devices. Through testing, it was disclosed that the mobility of the former was 0.5 $cm^2 \cdot V^{-1} \cdot s^{-1}$, while that of the latter was 3.4 $cm^2 \cdot V^{-1} \cdot s^{-1}$.[159]

1.4.6 Growth and morphology of organic semiconductor films

Similar to inorganic semiconductors, aromatic hydrocarbon-based OSCs can also be synthesized as molecular crystals. However, the intermolecular Van der Waals bonds in organic single crystals are much weaker, which adversely affects their periodic arrangement and dimensions. Consequently, even the best organic single crystals cannot match inorganic semiconductors in terms of chemical purity and crystalline quality. As a result, OSCs are preferably fabricated as polycrystalline layers using solution or vacuum deposition methods. Specifically, for small-molecule OSCs like unsubstituted alkenes, which are hardly soluble in organic solvents, they can be relatively easily deposited as thin layers through thermal deposition. In this study, all the investigated OTFTs were fabricated using Physical Vapor

Deposition (PVD), so only the vacuum deposition techniques for organic semiconductor films are discussed.

Charge transport is facilitated by the overlap of molecular π orbitals between adjacent molecules. Therefore, the morphology of the organic molecules in the film must promote molecular orbital overlap. In this regard, the underlying surface on which the OSC is deposited, is crucial, as shown in **Figure 1.12**. Hence, nucleation and growth procedures of these films and their film morphology are of extreme significance for the charge transport characteristics of OTFTs. Some factors could actually influence growth and morphology of deposited OSC thin-films.

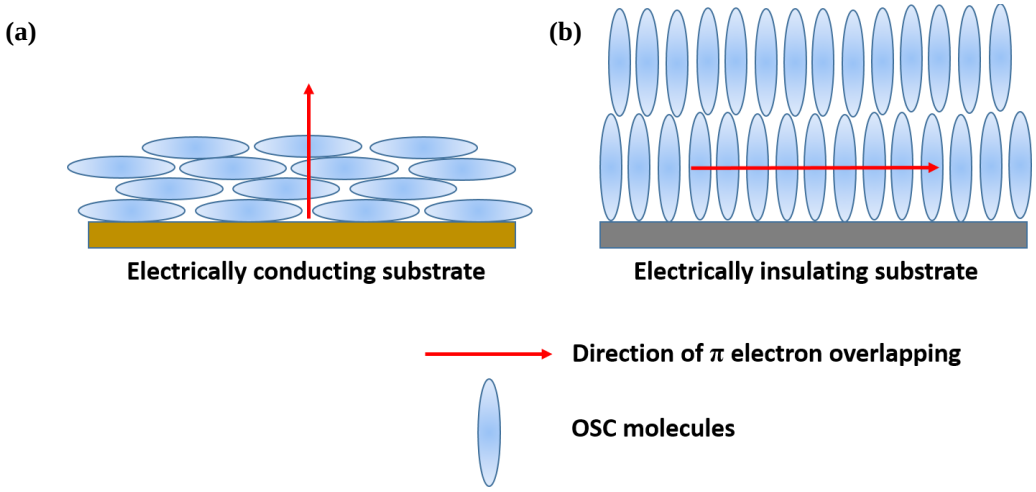


Figure 1.12 Schematic diagram of the organic semiconductor molecular orientation on (a) an electrically conducting substrate and (b) an electrically insulating substrate.[40]

Vapor Rate

The deposition rate is a critical parameter that requires strict control during the vacuum thermal sublimation process. Generally, an increase in the deposition rate enhances the nucleation rate in the film growth process, leading to smaller crystals and grains and thereby increasing the density of grain boundaries in the polycrystalline film. Nevertheless, at high deposition rates, and the fabricated films may be entirely amorphous. Consequently, in general, it is advisable to conduct the growth of organic semiconductor films using a relatively low deposition rate to reduce the nucleation density and increase the overall grain size. But, the specific optimization of deposited rate is determined by the organic material.

Substrate temperature

When the substrate temperature is relatively high, it promotes the formation of larger crystalline grains. However, as the temperature further increases, particularly beyond the

temperature-limition for material itself, it causes the re-evaporation of the deposited molecules. Hence, the ideal substrate temperature lies in achieving a balance between enhancing the crystallization of molecules on the substrate surface and reducing the temperature requisite for material evaporation. As for diverse OSC molecules, it is typically necessary to investigate the optimal substrate temperature on different substrates.

As for S-DNTT-10 thin-films in this thesis, the thermally depositing thin-films were initially executed under the rate of 0.4 Å/s and 20 °C-deposited-substrate. Subsequently, during the improved process of deposited rate from 0.3 to 1.0 Å/s and temperature of deposited substrate ranging from 20 to 140 °C, we discovered that the optimized deposited rate of 0.5 Å/s and 110 °C-deposited-substrate could make S-DNTT-10-based OTFT achieve the comparatively outstanding electrical performance.

Substrate surface characteristics

The influence of the surface properties of the gate dielectric in OTFTs is highly significant for fabricating high-quality OSC films, particularly the effects of the surface energy and surface roughness of the gate dielectric. The surface roughness of the dielectric can moderately enhance the coordination between the deposited molecules and the surface. Rough areas on the surface lower the nucleation barrier and raise the desorption barrier. However, on excessively rough surfaces, the grain quality of the film is adversely affected, leading to smaller grains, incorrect orientations, and degraded device performance.

The thickness of OSC material

The thickness of OSC films potentially exerts a considerable influence on their growth, morphology, and device performance. Depending on the device configuration and the relative positions of contact with the OSC, the thickness of the semiconductor layer affects the injection and extraction of charge carriers. Most of the charge carriers moving in the OTFTs, the channel takes place within the first one or two monolayers of the OSC layer, close to the dielectric-semiconductor interface. Commonly, the deposited thickness of the OSC thin-film is equivalent to multiple monolayers to stabilize the initial monolayer for charge transportation. With regard to S-DNTT-10-based OTFTs we fabricated, the type thickness of S-DNTT-10 thin-film is approximately 25 nm.

1.5 Conclusion

In this chapter, we briefly introduced the fundamental concepts related to charge injection and transport in OSC materials, the electrical performance and interface characteristics of OTFTs, and the deposition of OSCs by physical vapor deposition (PVD). These provide a solid foundation for the next section and the subsequent chapters.

2 S-DNTT-10-based OTFTs fabrication and characterization techniques

2.1 Introduction

One of the main questions examined in this study will concern the characterization of S-DNTT-10-based OTFT via advanced nano-characterization techniques. Section 2.2 will briefly introduce the molecular structure and synthesis process of S-DNTT-10 molecules. Currently, this is the sole academic paper found on S-DNTT-10. Subsequently, the fabrication process of S-DNTT-10-based OTFT will be described in Section 2.3. Section 2.4 will introduce the fundamental principles of the characterization techniques employed in this study, encompassing those for thin-film materials and those for the electrical properties of the devices. Specifically, a co-measurement system of *I-V* and Raman spectroscopy suitable for OTFT has been developed in our laboratory, which can be used for Raman spectroscopy measurements on operating OTFTs. Then, in Section 2.5, Atomic Force Microscopy (AFM) will be used to exhibit the surface conditions of the S-DNTT-10 films thermally deposited by PVD and the wettability of the S-DNTT-10 thin-film will be measured by the contact angle technique. In the last Section 2.6, the electrical characteristics of thermally deposited S-DNTT-10-based OTFTs will be presented and analyzed. We will analyze the conventional output (I_D-U_{DS}), transfer (I_D-U_{GS}) characteristic curves, the surface potential distribution of the S-DNTT-10-based OTFT by Kelvin Potential Force Microscopy (KPFM). Additionally, we will roughly discuss the "*early-saturation effect*" in our S-DNTT-10-based OTFT.

2.2 S-DNTT-10 molecules

In Chapter 1, we mentioned that the electrical properties of OTFT are associated with the extension of the molecular π conjugation and the degree of intermolecular interaction within the OSC active layer. In this respect, the pentacene has been profoundly investigated as prototype p-type OSC at the early beginning of organic electronics. [30] Currently, pentacene exhibit a high hole mobility of over 1 $cm^2\ V^{-1}\ s^{-1}$ in vacuum-deposited OTFTs. An effective strategy to enhance the (photo)oxidative stability of p-type OSCs is to introduce fused thiophene rings to form π-extended thiophenoacenes [160–162], which not only stabilizes the HOMO level but also enables a herringbone molecular packing similar to pentacene, a necessary condition to reach high carrier mobility. In 2007, Takimiya reported linear hexacyclic fused dinaphtho[2,3-b:2′,3′-f] thieno[3,2-b]thiophene 28 (DNTT), which is a promising p-type OSC that demonstrates high stability and effective field-effect mobility (2.9 $cm^2\ V^{-1}\ s^{-1}$) even

in air. It was discovered that the introduced long alkyl chains can facilitate the ordering of solid-state molecules through the van der Waals interaction between them, known as the molecular fastener effect [163], enabling the π conjugated cores to stack more closely and thereby enhancing the charge carrier mobility.

Here, we focus on an unconventional S-shaped π-core OSC molecule with long alkyl chains, namely 3,10-Didecylnaphtho[2,1-b]naphtho[1',2':4,5]thieno[2,3-d]thiophene 21DNTT-10 (S-DNTT-10), which is from TCI EUROPE N.V., Zwijndrecht, Belgium. In reality, it is a member of a new family of solution-processable organic semiconductors, S-DNTTs [38]. Its derivatives, namely dialkylated S-DNTT, possess high solvent solubility and thermal durability and can be employed to fabricate high-performance OTFT through vacuum deposition and solution processes. It was discovered that OTFTs based on S-DNTT-10 with two alkyl chains exhibit high hole mobility and sufficient operational and environmental stability. Since the core research question of this section is not organic molecule synthesis, a brief description of the synthetic method is merely provided as shown in **Figure 2.1**. Detailed synthetic procedures and characterization data of S-DNTT-n are described in the literature [38]. All these final products are purified by column chromatography and then undergo temperature-gradient vacuum sublimation to obtain high-purity materials for subsequent measurements and device evaluations.

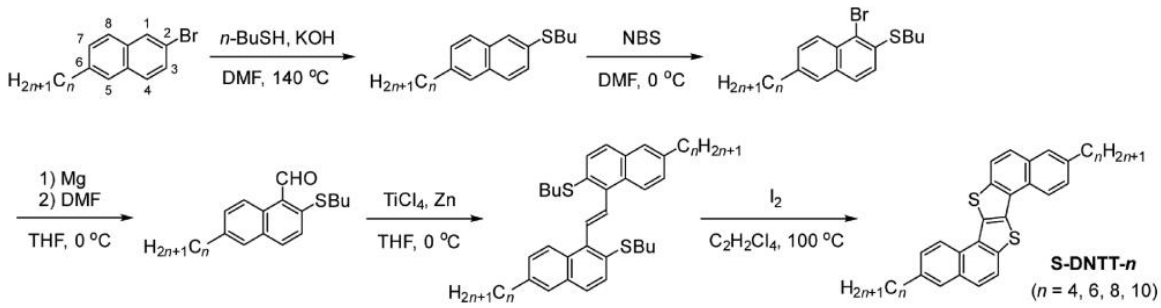
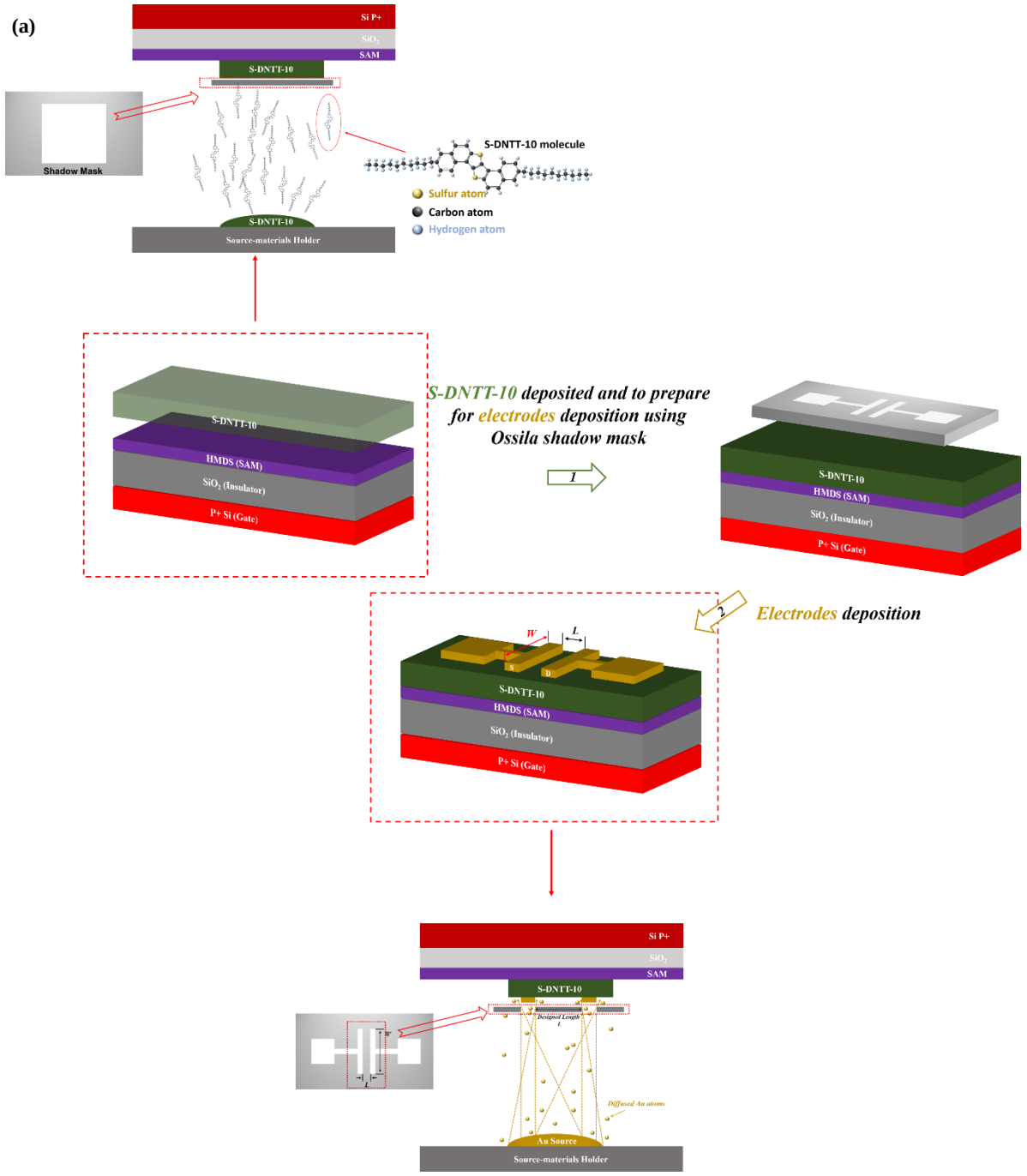


Figure 2.1 The schematic of brief fabrication process of S-DNTT-n [38].

2.3 The fabrication in S-DNTT-10-based OTFT

In this study, OTFTs were fabricated via Physical Vapor Deposition (PVD) as shown in **Figure 2.2 (b)**. The OTFTs featured a top-contact structure on heavily doped p-type Si <100> wafers (0.02 Ω·cm), topped with SiO_2 dielectric layers which the thickness from 90-300 nm. The Si/SiO_2 substrate was ultrasonicated in acetone, isopropanol, and Milli-Q® water to remove contaminants or impurities that might impair OTFT performance. After cleaning, we placed the substrate in a deposition chamber at room temperature for 16 hours to form a nanometer-thick

self-assembled monolayer (SAM) of HMDS (1,1,1,3,3,3-Hexamethyldisilazane). The purpose of the SAM layer was to optimize the configuration of the deposited S-DNTT-10 molecules and passivate the SiO_2 surface, as Section 1.4.5.2 shown. The schematic fabrication process of S-DNTT-10-based OTFTs is depicted in **Figure 2.2 (a)**. One 25 nm S-DNTT-10 thin-film is deposited on HMDS/SiO_2 through a shadow mask (**Figure 2.2 (c)**). (from TCI EUROPE N.V., Zwijndrecht, Belgium) The substrate is heated to 110°C and a deposition rate of 0.5 Å/s by PVD is used. Subsequently, we changed the thin-film shadow mask into electrodes-shadow mask to fabricate S & D gold electrodes (**Figure 2.2 (d)**). Gold films, approximately 25 nm thick, were then vacuum-deposited onto the S-DNTT-10 layers. Shadow masks are provided by the company Ossila. The channel width was set at 1000 μm, with lengths varying from 30 μm to 80 μm (**Figure 2.2 (e)** and **(f)**). All deposition steps were carried out in a vacuum environment (approximately 10^{-7} Pa). To avoid the leakage current, we scratched the OTFT by following the electrodes as **Figure 2.2 (e)** shown.


(a)
Si P+
SiO2
SAM
S-DNTT-10
Shadow Mask
S-DNTT-10 molecule
Sulfur atom
Carbon atom
Hydrogen atom
Source-materials Holder
S-DNTT-10 deposited and to prepare for electrodes deposition using Ossila shadow mask
1
HMDS (SAM)
SiO2 (Insulator)
P+ Si (Gate)
2
Electrodes deposition
W
L
S
D
Designed Length
Diffused Au atoms
Au Source

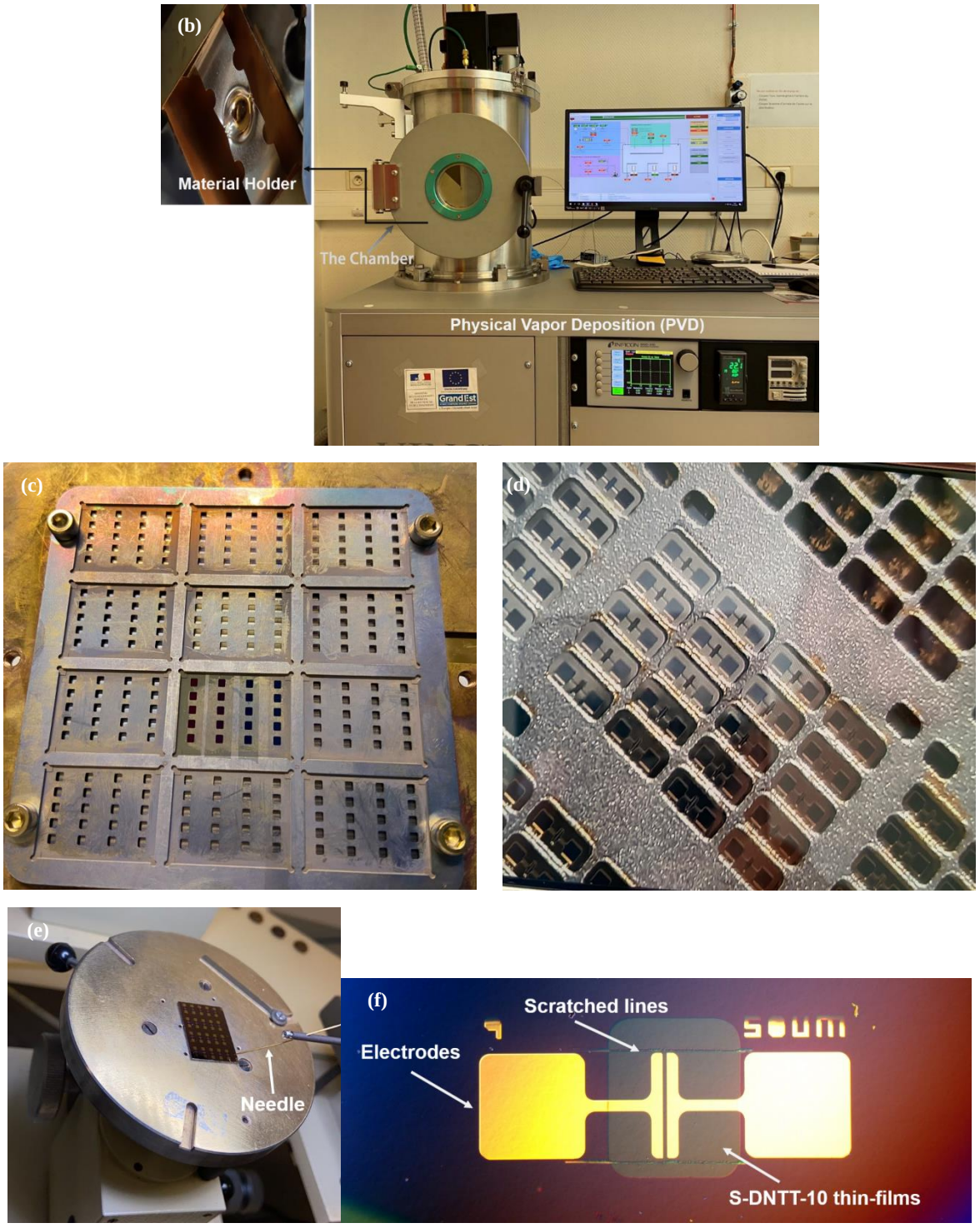


Figure 2.2 (a)The schematic fabrication process of Top-contact-Bottom-gate S-DNTT-10-based OTFT. (b) Physical Vapor Deposition (PVD) device in our lab. (c) Shadow mask for depositing S-DNTT-10 square thin-films. (d) Shadow mask for electrodes. (e) The fabricated samples, the needle for scratching channel-sides in OTFTs as Figure 2.2 (f) shown. (f) Top view of one device via optical microscopy.

2.4 Characterization tools utilized

Besides the electrical characterization of OTFTs, various surface and thin-film properties of semiconductors and dielectric layers have been characterized. This Section precisely delineates the fundamental working principles of the characterization techniques employed in this study: *IV* characterization in Section 2.4.1, Raman spectroscopy-*IV* characterization in-situ system in Section 2.4.2, AFM in Section 2.4.3, Kelvin Potential Force Microscopy in Section 2.4.4 and contact angle measurements in Section 2.4.5.

2.4.1 *IV* characterization

For characterization of electrical performance in OTFTs, we use a Keysight Technologies Precision *IV* Analyzer E5270B (**Figure 2.3**). The measurements could be executed with different probe stations available in the laboratory: in glove box, in vacuum or in air.

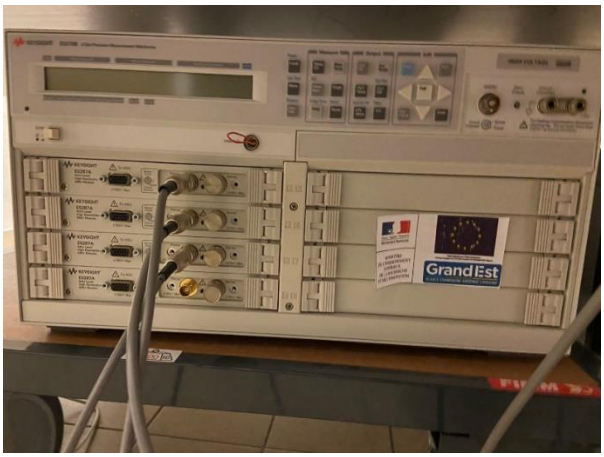


Figure 2.3 The *I-V* measurement platform of E52470B-KEYSIGHT, 8 Slot Precision Measurement Mainframe.

2.4.2 Raman spectroscopy-*IV* characterization in-situ system

Figure 2.4 shows the schemed image of the homemade coupled Raman spectrometer / current-voltage (*IV*). The Raman spectrometer used in this study was the LabRAM HR Evolution Nano, from Horiba, and it linked with the *I-V* measurement platform of E52470B-KEYSIGHT. In the *IV*-Raman in situ experiment process, the measured OTFT is place on a chuck (the gate electrode) and the Source and Drain electrodes are connected via micro-probers IMINA bot (**Figure 2.4**). The Raman spectrometer has three different wavelength laser, that 532 nm, 633 nm and 785 nm. This *IV*-Raman system is enabled to measure the Raman spectrum on operating OTFT.

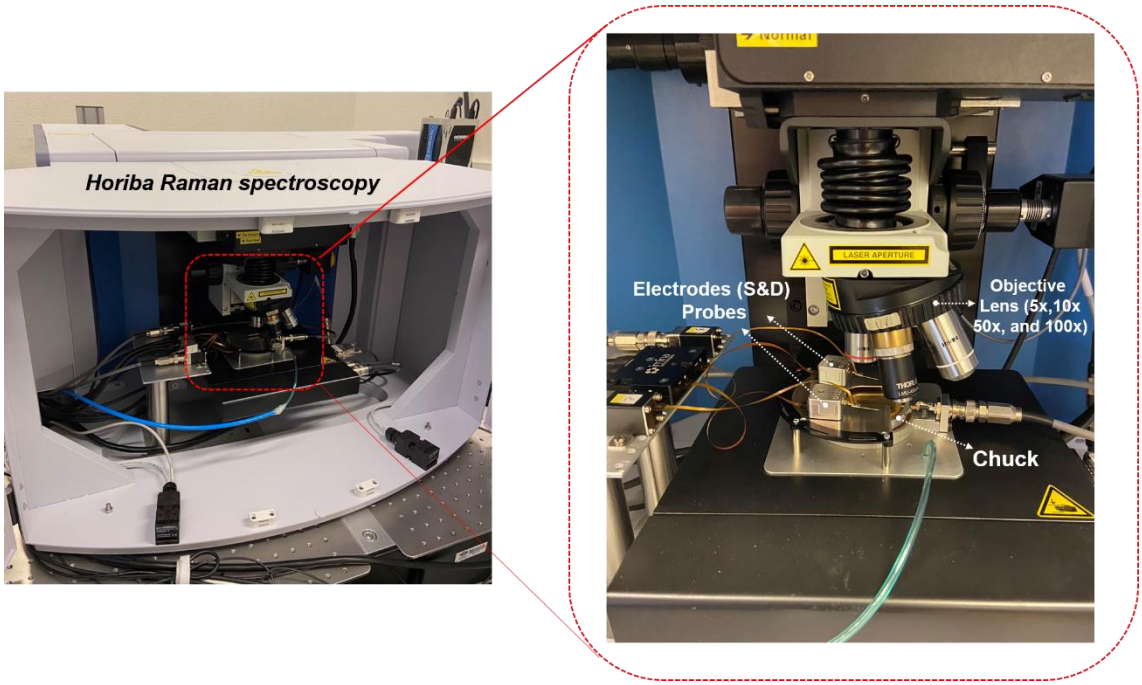


Figure 2.4 Measurement System of Raman spectrum and integrated prober.

2.4.3 Atomic Force Microscopy

Atomic Force Microscopy (AFM), a scanning probe microscopy technique, is employed for topographic imaging with a resolution reaching fractions of a nanometer. A schematic diagram of the essential operational configuration is shown in **Figure 2.5**. A cantilever with a sharp tip oscillates at its resonance frequency, and a laser beam is reflected from the top of the cantilever onto a split photodetector. As the sharp tip probes the sample surface, the force between them adjusts the oscillation amplitude, where the deflection of the cantilever corresponds to the surface topography.

In this study, AFM was utilized to acquire topographic information of the OSC films and observe variations in topography induced by external factors through repetitive scanning of the same area. Additionally, AFM was used to collect surface characteristic information, such as the surface roughness of the materials. The AFM used in this study was a Dimension Icon from Bruker

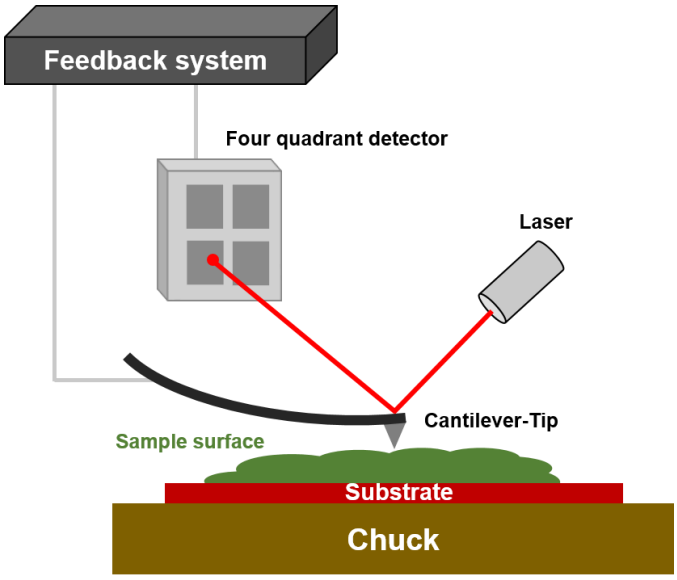


Figure 2.5 Basic principles of AFM operation.

In this investigation, AFM was employed to measure the surface topography of the sample. Based on the relative heights of each point on the measured surface, the roughness of the sample surface was characterized by calculating the Root-Mean-Square Roughness (R_{RMS}) parameter. The root mean square surface roughness is determined as follows: all topographical features obtained by AFM are transformed relative to the average plane (Z) into a profile by considering the absolute values of all amplitudes or profile heights. These profile heights are then squared, highlighting all protruding features on the sample surface. The squared values are integrated and averaged across the entire surface. Finally, the square root of this average is taken to account for the initial squaring of the profile height values, thereby determining the RRMS surface roughness.

2.4.4 Kelvin Potential Force Microscopy

2.4.4.1 Surface potential profile

Surface potential measurements of electronic devices, conducted under normal operating conditions with applied voltages and employing Atomic Force Microscopy (AFM), are commonly known as Kelvin Probe Force Microscopy (KPFM). The AFM-based potential measurement method utilizes a conductive probe tip to detect electrostatic forces. When a voltage is applied between a conductive probe tip and a surface under the tip, electrostatic equilibrium is attained. Consider a sample surface with a constant potential (V_{surf}) that characterizes its entire interaction with the probe tip. The electrostatic force between the tip and the surface is invariably attractive, and the modulus of its vertical component (F_{el}) varies with the potential difference between the probe tip and the surface as follows: [164]

$$F_{el} \approx \frac{1}{2}\frac{\partial C}{\partial z}\left(V_{tip} - V_{surf}\right)^2 \quad \textbf{(2.1)}$$

where *z* is the vertical axis distance, *C* is the tip-to-surface capacitance, and V_{tip} is the potential applied on the tip. Electrostatic force is cancelled when V_{tip}, is equal to V_{surf}. Knowing the applied V_{tip} which minimize the electrostatic force allow to obtain V_{surf}. The literature suggests multiple implementations to obtain V_{surf}. An effective detection technique entails inducing forced oscillations in a cantilever and gauging the resultant changes due to electrostatic force showing in **Figure 2.6 (a)**. The deflection and the oscillations of the tip are detected via a reflected laser spot on a photodetector as shown in **Figure 2.6 (a)**.

Accurate local surface potential measurements demand taking into account the contribution of the tip apex relative to that of the cantilever. This demands the employment of a method that is more responsive to the force gradient rather than the mere force. Sensitivity can be achieved by equipping the cantilever with a piezoelectric element to induce oscillations. The phase or frequency shift of the oscillation, induced by electrostatic interaction, is measured in contrast to the cantilever's free oscillation. Small phase shifts, denoted as $\Delta\phi$, are approximated by the following expression,

$$\Delta\phi \approx -\frac{Q}{2k}\frac{dF_{el}}{dz} \approx -\frac{Q}{2k}\left(\frac{d^2C}{dz^2}\right)\left(V_{tip} - V_{surf}\right)^2 \quad \textbf{(2.2)}$$

where *Q* represents the quality factor, and *k* denotes the spring constant of cantilever. Knowing the applied V_{tip} which minimize the phase shifts $\Delta\phi$ allow to obtain V_{surf}. For a profound understanding of the measurement mechanisms, procedures, and calculations, kindly refer to the referenced article. [164]

The KPFM employed in this study is Dimension Icon, Bruker. The adopted type of probe is SCM-PIT-V2 from Bruker, with the associated tip radius being 25 nm, the length being 225 μm, the thickness being 2.8 μm, and the width being 35 μm (**Figure 2.6 (d) and (e)**). The frequency amounts to 75 kHz, and the spring constant is 3.0 N/m. The material of the cantilever is 0.01-0.025 Ohm cm Antimony-doped Si and coated with Platinum-Iridium. In this study, KPFM was utilized to characterize the surface potential along the channel of operating OTFTs in ambient and extract the voltage drop at electrodes to obtain contact resistance R_C, intrinsic mobility in the channel, and other parameters, for instance, threshold voltage and the distribution of electrical field along the channel. The lateral resolution of our setup is in the range of 40-150 nm depending on the lift height (distance between the and the surface during potential measurement). [165]

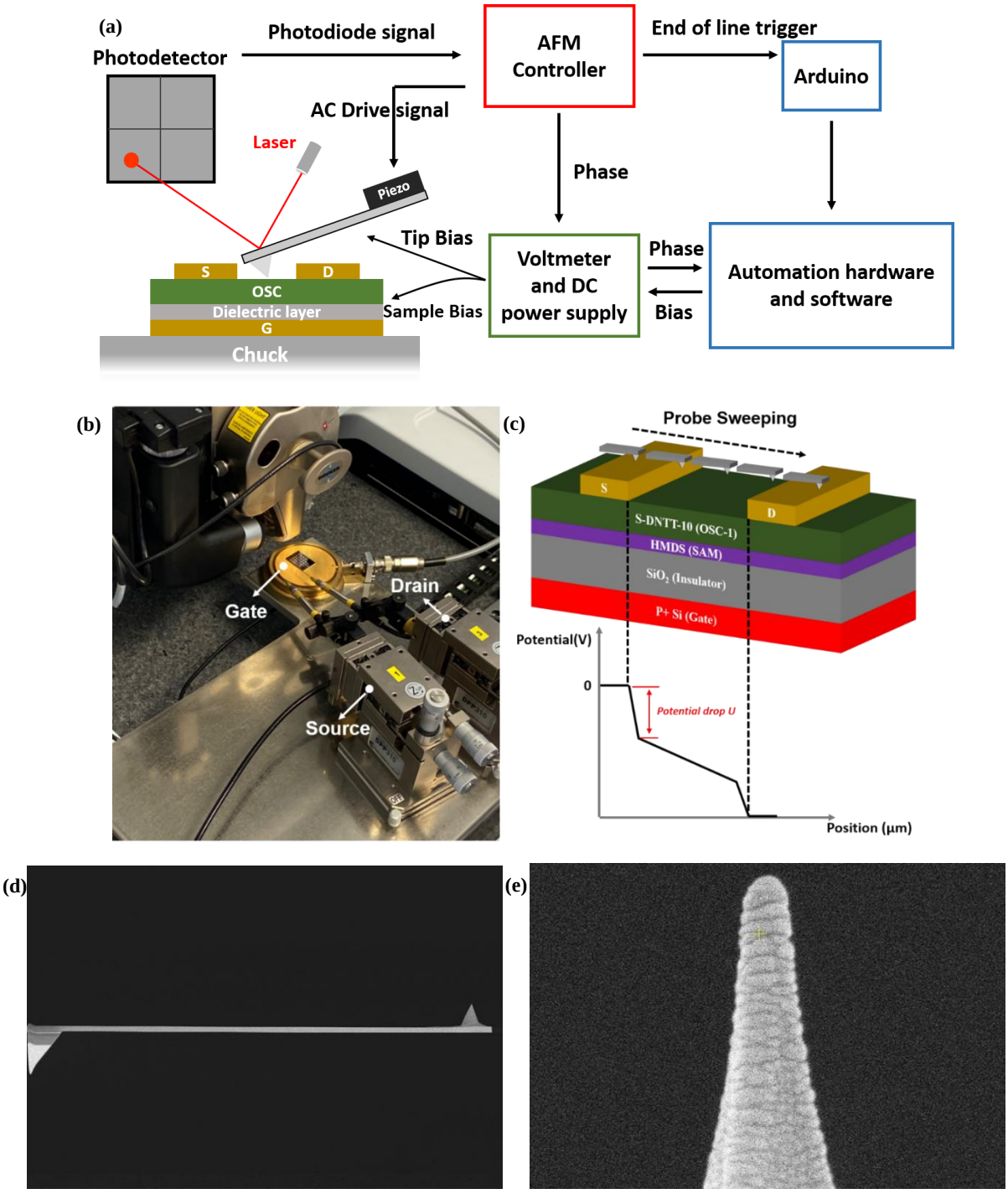


Figure 2.6 (a) The schematic representation of KPFM facility [164], (b) the consumed Bruker AFM/KPFM we used in the lab,(c) the diagram of profile-surface potential in S-DNTT-10-based OTFTs, (d) the substrate of Si-cantilever, and (e) the tip of probe.

In this study, we mainly utilized the KPFM approach to characterize the intrinsic contact resistance and the intrinsic mobility in the channel. In the following two sections, we briefly introduce the related knowledge about them.

2.4.4.2 Characterization of contact resistance

In Section 2.4.4.1, it exhibited the simple process of extracting profile of surface potential. In general, we can evaluate the contact resistance based on the surface potential through KPFM characterization, as **Figure 2.7** illustrated. It exhibited the surface potential (seeing in the upper image) with the corresponding position at the channel in the stressed OTFT (seeing in the bottom image). The voltage at the source was referenced as zero. The "***C***" was indicated one measured position at the channel, and the related voltage drop was marked as U_{CS} with respect to gate voltage. And it was obtained the intensity of the electric field ($\boldsymbol{E} = -\frac{\partial U_{CS}}{\partial x}$) based on the slope value at the point in the sweeping curve.

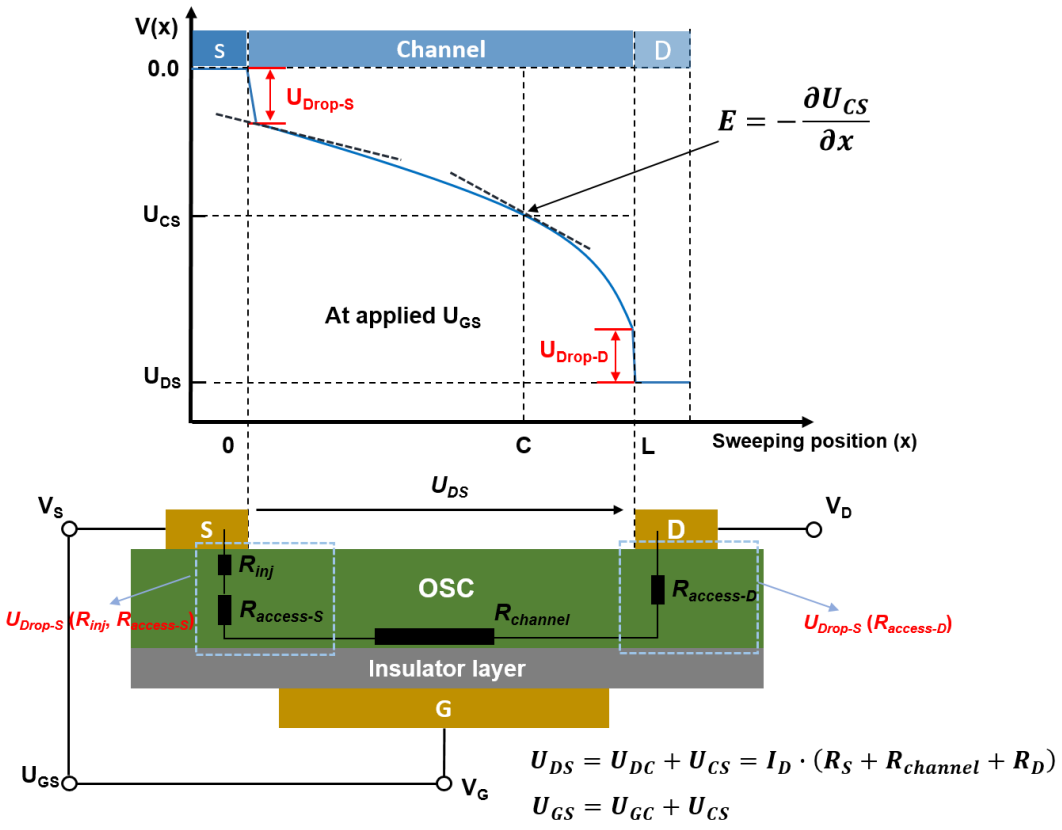


Figure 2.7 The schematic representation of the surface potential profile corresponding to the measured OTFT.

Particularly, the upper image displayed the voltage drop (U_{Drop}) at the channel and electrodes. It correlated with the contact resistance (R_c) into the OTFT. For the Top-Contact-Bottom (TCBG) configuration, the voltage drop at the source ($U_{Drop\text{-}S}$) represented the source contact resistance (R_s), which is consisting of injection resistance (R_{inj}) and access resistance ($R_{access\text{-}S}$), and with regard to Bottom-Contact-Bottom-Gate configuration, the R_{inj} can be estimated as approximately zero and consequently R_s is nearly closed to $R_{access\text{-}S}$. On the other

hand, the voltage drop at the drain indicated the emergence of drain contact resistance (R_D), which is mainly determined by the $R_{access\text{-}D}$. Subsequently, the R_C can be extracted by the value of slope into I_D-U_{Drop} curve, *i.e.*, $\frac{1}{R_C} = \frac{\partial I_D}{\partial U_{Drop}}$. It was noted that for R_s, the recorded current should be flowed through the source area by source-terminal probe (I_S), siminlarily, for R_D, the current should be collected at the drain area by drain-terminal probe (I_D).

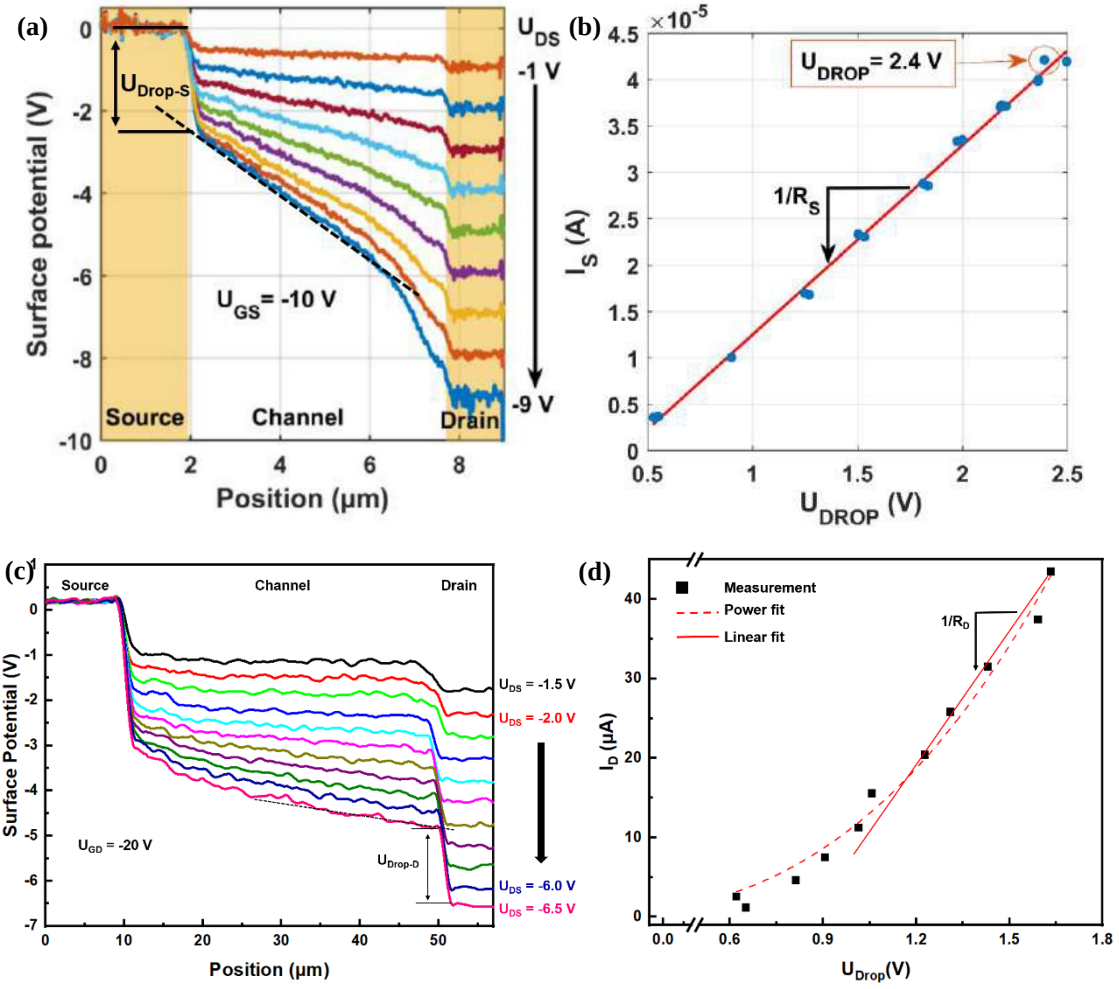


Figure 2.8 The representation of (a) surface potential profile in the TCBG DNTT-based OTFT by KPFM approach under the different U_{DS}, (b) the corresponding relationship of voltage drop at the source and the simotineous recorded drain current I_D, and the estimation of R_s [166]. (c) The surface potential profile under the varied U_{GD}, (d) and the related I_D-$U_{Drop\text{-}D}$.

As for extracting R_s by KPFM method, the stressed condition was the changed U_{DS} under the fixed U_{GS} with the aim of the source area remaining at the contant voltage drop. Subsequently, it was extracted the $U_{Drop\text{-}S}$ under the each own U_{DS} and obtained the I_S-$U_{Drop\text{-}S}$ characteristics. For instance, **Figure 2.8 (a)** displayed the measured profile of surface potential into TCBG DNTT-10-based OTFT under the U_{GS} of -10 V and the U_{DS} ranging from -1 to -9 V. It suggested that the voltage drop was increased with the applied U_{DS}. And **Figure 2.8 (b)** showed the correlation of extracted U_{Drop} with the collected current at source I_S. Thus fitted the

line in the term of linear state with ingoring the non-linear area, and consequently the R_s was estimated by the slope of this linear line.

However, with regard to characterize R_D by KPFM approach, the applied condition should be fixed U_{GD} (U_{GD} = U_{GS} - U_{DS}) with purpose of drain area maintaining constant voltage drop. Hence, the U_{GS} and U_{DS} should be simultaneously with the indetical increment. For instance, **Figure 2.8 (c)** illustrated the profiles of surface potential during extracting R_D under U_{GD} of -20 V and U_{DS} ranging from -1.5 to -6.5 V. Hence, the U_{GS} and U_{DS} should be respectively set from -21.5 to -26.5 V and from -1.5 to -6.5 V, with the same step of -0.5 V. Consequently, the voltage drop $U_{Drop\text{-}D}$ is extracted at the drain at each different combination of U_{GS} and U_{DS} and fitting the line by selecting linear region, and obtained drain contact resistance. Not that R_D cannot extract in saturation regime because the potential drop $U_{Drop\text{-}D}$ is hidden by the huge potential drop due to the pinch-off near the drain electrode.

To have more details and the method of contact resistance extraction from KPFM refer to the references [166,167].

2.4.4.3 Characterization of intrinsic channel mobility

In Section 1.4.4.1, according to **Equation.(1.13)** and **(1.14**), we can obtain the linear mode and saturation mode effective field-effect mobility (μ_{lin} and μ_{sat}) from transfer characteristics I_D-U_{GS}. Nevertheless, these extracted parameters can not absolutely or accurately characterize the intrinsic charge transport properties in the channel. Since the contact characteristics at the interface between electrodes and OSC thin-films, could influence the characteristics of extraction mobility. The developed KPFM method could evaluate the intrinsic mobility in the channel by measuring the surface potential profile under varied U_{GS} and one fixed U_{DS}.

Ignoring the minimal contribution of diffusion current compared to drift current [164,168], the I_D of a P-Type field-effect transistor can be expressed as $\boldsymbol{I_D = -WQ_{acc}\mu E}$, herein, Q_{acc} is the accumulated surface charge density and E is the longitudinal electric field. Above the threshold voltage U_{Th}, the density of holes accumulated in the channel can be well approximated by $\boldsymbol{Q_{acc} = -C_i \cdot (U_{GC} - U_{Th})}$, where U_{GC} is the gate-to-channel voltage at a given position C along the channel [169]. This equation is valid along the entire channel except near the drain (where the channel may pinch off) and near the source (where an injection barrier may affect charge density). Using the source as the reference potential, $\boldsymbol{U_{GC} = U_{GS} - U_{CS}}$, where U_{CS} is the channel potential referenced to the source contact. Where applicable, the drain current can be written as $\boldsymbol{I_D = WC_i(U_{GC} - U_{Th}) \cdot \mu \cdot \left(dU_{CS}/dx\right)}$.

It is important to be aware that this equation is only valid for channel positions where the accumulated charge can be approximated by the relation $Q_{acc} = -C_i (U_{GC} - U_{Th})$, and where the diffusion current is negligible. Keep in mind that this relationship does not hold, particularly in the saturation region near the drain.

At any point in the channel, the sheet resistance $\boldsymbol{R_{sheet} = 1/\sigma d}$, where σ is the local channel conductivity and d the semiconductor film thickness. Given the current density $\boldsymbol{I_D/(Wd) = \sigma E}$, one can write $\boldsymbol{I_D/(WE) = 1/R_{sheet}}$. The intrinsic channel mobility can then be expressed as, [164]

$$\boldsymbol{\mu_{intrinsic} = \frac{1}{C_i} \cdot \frac{\partial(I_D/WE)}{\partial U_{GC}}} \qquad \textbf{(2.3)}$$

The principle of potential profile processing is illustrated in **Figure 2.9**. For each point on the profile, the voltage U_{GC} and the longitudinal electric field E are obtained, as shown in the left image of **Figure 2.9 (a)**. The inverse of the sheet resistance is then plotted as a function of U_{GC}, as depicted in the right image of **Figure 2.9 (a)**. In the following, the ratio $I_D / EW = 1/R_{sheet}$ will be referred to as conductance without further explanation. In the case shown, a significant number of points on the curve correspond to U_{GC} voltages that are too close to the threshold (highlighted in yellow in **Figure 2.9 (a)**), making it impossible to extract mobility from a single profile. To obtain a wider range of U_{GC} voltages, a series of profiles at different U_{GS} is generated. For instance, **Figure 2.9 (b)** shows the simulated potential profiles along the channel of an OTFT with a channel length of 20 μm, for a given U_{DS}. The simulations were performed using a simulator with realistic material parameters, assuming constant mobility and no defects at the contacts. The plot of conductance versus U_{GC} in **Figure 2.9 (c)** uses all the simulation points to derive mobility. From the slope of this straight line, we can extract the mobility, while the threshold voltage is determined by the x-axis intersection. The extracted mobility is 0.096 $cm^2 \cdot V^{-1} \cdot s^{-1}$, and the threshold voltage is -2.2 V. For more details on the specific process of extracting mobility, please refer to the cited references [164,166,167].

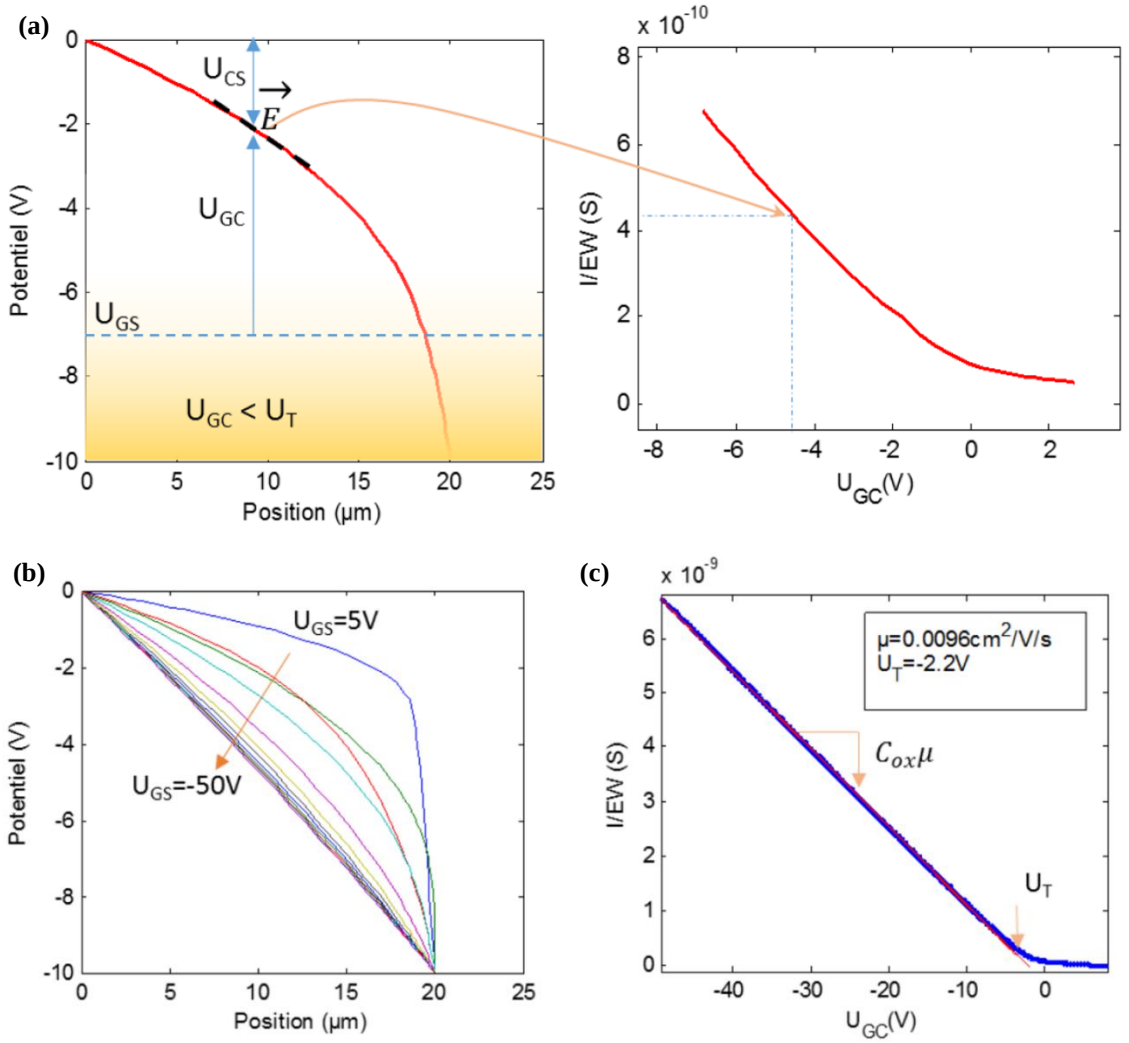


Figure 2.9 (a) Principle of processing potential profiles to obtain mobility. The U_{GC} raster/channel voltages and local electric field E (left image) were extracted from the potential profile. Some points in the potential profile cannot be used to extract mobility because they are too close to the threshold (yellow) (right image). (b) Simulated potential curves of an OTFT channel with constant mobility at different gate voltages and -10 V drain-source voltage. (c) Description of the methodology for extracting the mobility from the simulated potential profile in (b). A straight-line approximation of the extracted mobility and threshold voltage is shown in red. [166,167]

2.4.5 Contact angle measurement

The hydrophobicity of the samples is gauged through the static contact angle measurement approach. In this approach, a droplet is placed on the surface of interest (typically deionized water) and left stationary for 1-3 minutes to enable sufficient mutual infiltration between the liquid and the sample surface. Subsequently, the static contact angle θ is measured using an optical microscope, as depicted in the following **Figure 2.10**. When $\theta > 90°$, it indicates that the surface is hydrophobic; conversely, it indicates that the material is hydrophilic. During the testing process, it should be noted that the liquid landing point should be as close as possible to the edge of the substrate to ensure that the liquid edge and the substrate edge can be

simultaneously distinct and minimize the error of the test results. Moreover, based on the contact angle, the surface energy can be approximately calculated.

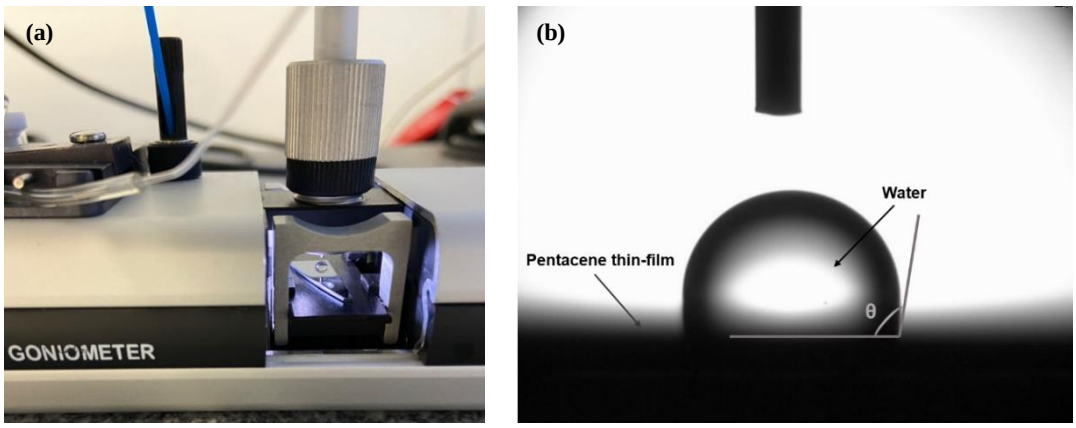


Figure 2.10 (a) The used contact-angle analysis and (b)the zoom of water-contact-angle.

2.5 Surface characteristics of S-DNTT-10 thin-film

2.5.1 S-DNTT-10 thin-film Topography by AFM measurement

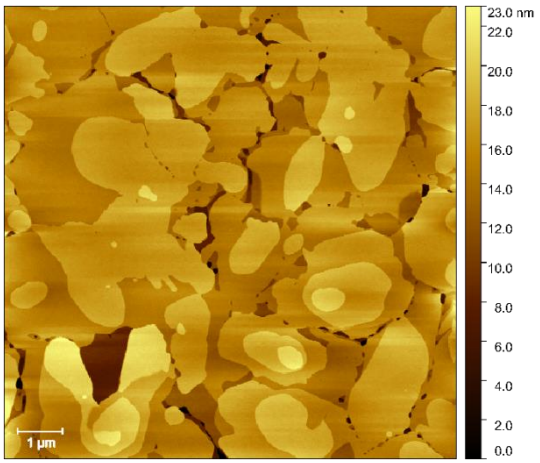


Figure 2.11 The AFM-topography of 25 nm S-DNTT-10 thin-film depositing under vacuum on SiO_2 modified with HMDS.

Different OSC materials have their own organic molecular structures, which result in various surface morphologies. For example, pentacene molecules mostly have a herringbone-shaped grain morphology, while DNTT has larger grain sizes and a rough, snowflake-like edge. Herein, we characterized the surface morphology of a 25 nm S-DNTT-10 thin film by AFM, as shown in **Figure 2.11**. Unlike the dendritic grains exhibited in the pentacene film, it shows a laminated structure, and the layers' overlap each other, indicating that the π-π electrons within S-DNTT-10 molecules have a strong interaction and may have strong charge transport properties.

2.5.2 Contact angle measurements for 25nm S-DNTT-10 thin-film

In the OTFT samples, the majority of the S-DNTT-10 thin-films are thermally deposited on the HMDS-modified SiO_2 surface. The water is employed as the measuring liquid and the contact angle of the S-DNTT-10 thin-film is measured by Contact angle to determine the hydrophobicity of the material. It should be noted that since S-DNTT-10 possesses good air stability and the air contains oxygen and water molecules, it can be considered that S-DNTT-10 molecules will not be degraded by water molecules in the short term. Hence, water can be used as the testing liquid resolution.

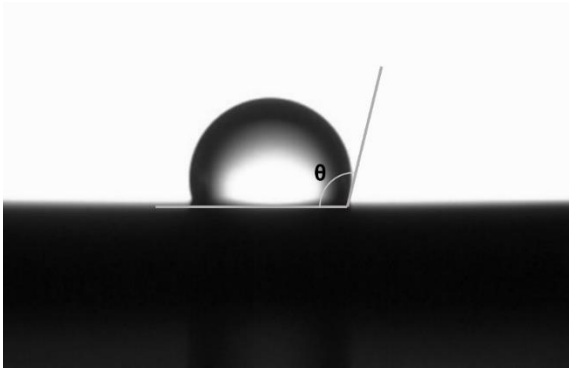


Figure 2.12 The contact angle measurement for S-DNTT-10 thin-film by employing water as probe solution.

After 3 mins-stationary as **Figure 2.12** illustrated, the measured results showed that the contact angle for 25 nm S-DNTT-10 thin-film depositing on SiO_2 layer modified with HMDS, is approximately 101.8°. It demonstrated that the S-DNTT-10 thin-film possesses the hydrophobicity in some degree.

2.6 S-DNTT-10-based OTFTs electrical characterization

S-DNTT-10 molecules are the primary focus of this thesis, particularly S-DNTT-10-based OTFTs. These OTFTs were fabricated using thermal deposition via the PVD method, mainly in a top-contact structure. Initially, the S-DNTT-10-based OTFTs fabricated in our lab exhibited poor electrical performance, including lower effective field-effect mobility, hysteresis, and higher threshold voltage. After optimizing the fabrication process—such as adjusting the substrate temperature, deposition rate of S-DNTT-10, and thickness of the dielectric layer (SiO_2)—the device performance improved, with some devices achieving effective field-effect mobility as high as 6.5 $cm^2 \cdot V^{-1} \cdot s^{-1}$. Hundreds of S-DNTT-10-based OTFTs were fabricated, and their electrical characteristics were measured. This section will present the electrical characteristics of S-DNTT-10-based OTFTs with typical features, including *IV* characteristic

curves (seeing in Section 2.6.1) and surface potential distributions (seeing in 2.6.2). Additionally, a briefly analysis of the *early saturation effect* (seeing in 2.6.3) that emerged in the initial samples will be carried out.

2.6.1 Non-linear *IV* characteristics in S-DNTT-10-based OTFT

During the discussion on the performance of OTFTs, output characteristic curves (I_D-U_{DS}) and transfer characteristic curves (I_D-U_{GS}) are typically utilized for characterization. **Figure 2.13** depicts the typical IV measurement curves of the Top-Contact-Bottom-Gate S-DNTT-10-based OTFT.

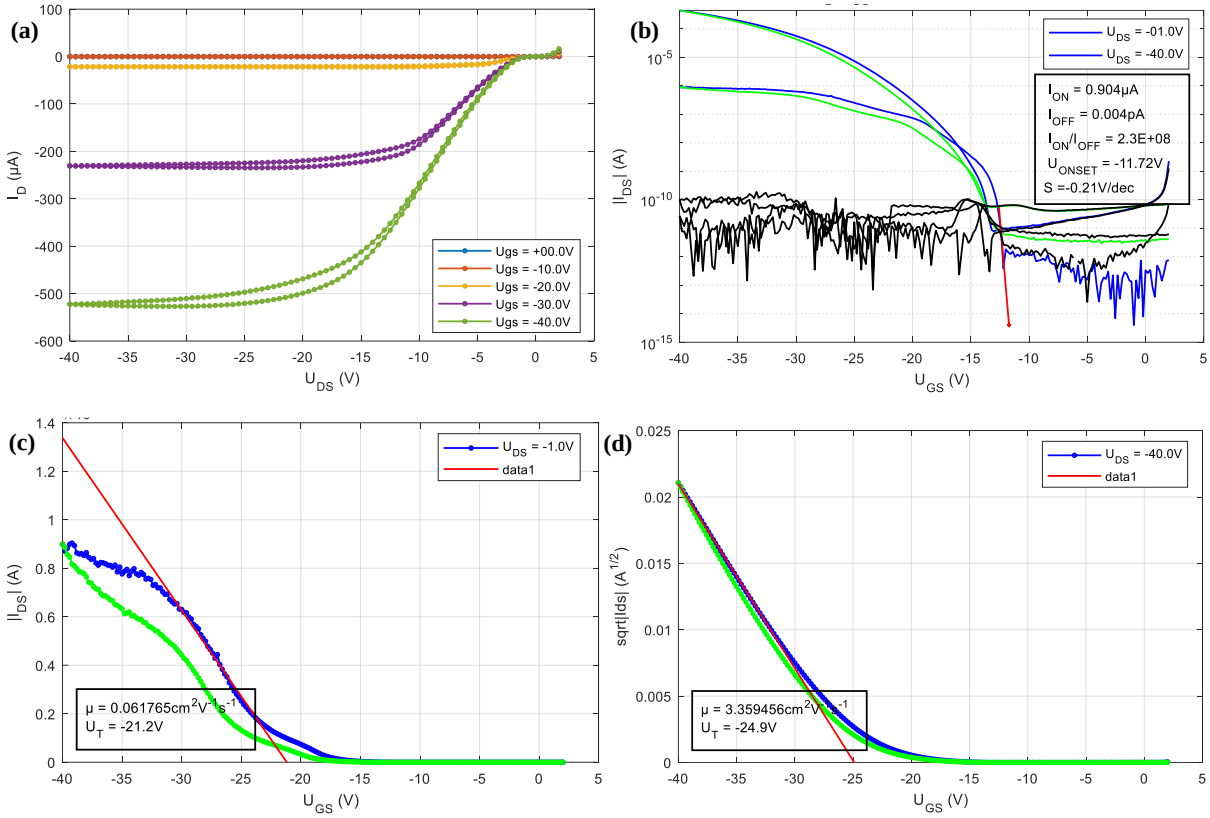


Figure 2.13 The electrical characteristics of Top-contact-Bottom-gate S-DNTT-10-based OTFT (channel of 30 μm, width of 1000 μm, C_i = 0.00038781 F/m): (a) Output characteristics I_D-U_{DS}, U_{GS} is ranging from 0 to -40 V, with a step of -10 V; U_{DS} is 2 to -40 V, with a step of -0.5 V. (b) Transfer characteristics I_D-U_{GS}, U_{GS} ranging from 2 ~ -40V with step of -0.2 V, stressed U_{DS} of -1 V and -40 V.(c) The linear state drain current changing with U_{GS} and the related extraction of mobility and threshold voltage. (d) The saturation-state drain current changing with U_{GS} and the related extraction of mobility and threshold voltage.

Through the *I-V* measurements, the I_D-U_{DS} curve reveals that the S-DNTT-10-based OTFT can not only stably output the drain current, exhibit the linear increase region and saturation current region of the drain current, but also possess a relatively high saturation current.

Simultaneously, by testing the transfer characteristic curve as shown in **Figure 2.13 (b)**, the results initially indicate a low leakage current, suggesting the good quality of the dielectric layer of the device. The extracted I_{on}/I_{off} is 2.3×10^8, the turn-on voltage is approximately -11.72 V, the sub-threshold slope is -0.21 V/dec, and the extracted linear effective field-effect mobility is nearly 0.062 $cm^2 \cdot V^{-1} \cdot s^{-1}$, and the corresponding $U_{Th\text{-}lin}$ is approximately -21.2 V as shown in **Figure 2.13 (c)**. The saturation-mode effective field-effect mobility is ~3.36 $cm^2 \cdot V^{-1} \cdot s^{-1}$, and the corresponding $U_{Th\text{-}sat}$ is approximately -24.9 V as shown in **Figure 2.13 (d)**, presenting good charge transport characteristics.

According to the formula $\boldsymbol{I_D = \frac{W}{L} C_i \mu \left[(U_{GS} - V_{Th}) U_{DS} - \frac{1}{2} U_{DS}^2\right]}$, in an ideal OTFT when U_{DS} is small, the drain current I_D increases linearly with the increase of U_{DS}. Nevertheless, we discovered that in the transfer characteristic curve of the S-DNTT-10-based OTFT, when U_{DS} is relatively small, within the range of 0 to -3 V, the output drain current I_D is small. With the increase of $|U_{DS}|$ (> 3 V), the device begins to effectively output the drain current. This non-linear effect in electrical characteristics has also appeared in Reference [38]. Therefore, this situation is not caused by our fabrication process but is a common phenomenon. This non-linear effect phenomenon not only makes the device unable to effectively output the drain current under a small U_{DS} but also resulted in the overestimation of the linear field-effect mobility, μ_{lin}.

As shown in **Figure 2.13 (c)**, in the linear-state I_D-U_{GS} curve, the value of $\boldsymbol{\partial|I_{DS}| \big/ \partial|U_{GS}|}$ is not fixed. Approximately when $|U_{GS}|$ > 30 V, the slope begins to deviate and decrease. In practice, the μ_{lin} of the device becomes smaller, making it impossible to accurately evaluate the electrical performance of the S-DNTT-10 OTFT. The measured nonlinear effect is attributed to the nature of the contact between S & D electrodes and the OSC enclosed in a non-negligible contact resistance *Rc*. The specific reasons and relatively innovative solutions will be elaborated in detail in the Chapter 6.

2.6.2 Electrical surface potential profile

Kelvin Probe Force Microscopy (KPFM), by scanning the channel in the operating OTFT, enables the acquisition of the electrical surface potential distribution along the channel between source and drain electrodes. Here, KPFM is performed on Top-contact S-DNTT-10-based OTFT to evaluate the charge carrier injection efficiency at the electrodes and the intrinsic charge transport into the channel of the device as explain in the previous sections 2.4.4.2 and 2.4.4.3. The channel length of the S-DNTT-10-based OTFT to be measured is approximately

30 μm, the channel width is approximately 1000 μm. The bias U_{GS} is fixed at -20 V, and U_{DS} varies from 0 to -5 V with a step of -0.5 V. The results are presented in **Figure 2.14**.

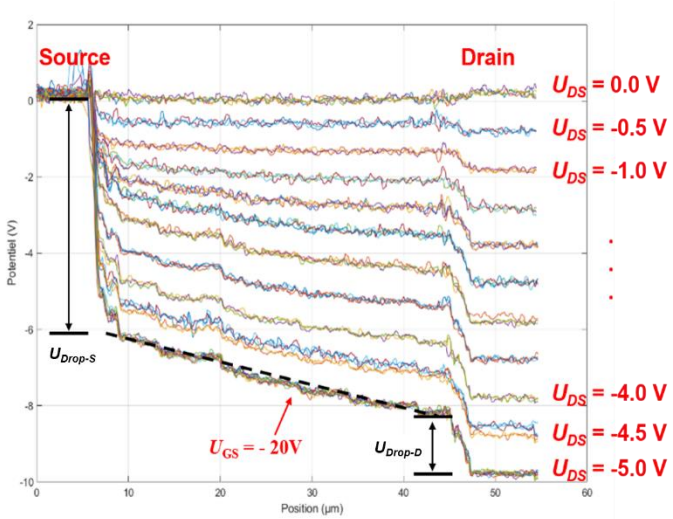


Figure 2.14 The profiles of surface potential via KPFM in S-DNTT-10-based OTFT, stressed U_{GS} = -20V, U_{DS} from 0 to -5 V with the step of -0.5 V.

In this picture, the left and right sides represent the source and drain areas respectively, and it shows the appearance of voltage drops at the electrodes, namely U_{Drop-S} and U_{Drop-D} These KPFM measurements present two features: firstly, the absolute value of voltage drops (U_{Drop-S} or U_{Drop-D}) seemingly increases with the applied U_{DS}; on the other hand, the voltage drop located at the source is commonly greater than that at the drain. Regarding the latter one, it indicates that the existence of contact resistance at the source plays the dominant role in the S-DNTT-10-based OTFT under the assumption that the total resistance system in OTFT consists of source contact resistance, channel resistance, and drain contact resistance. It is also the response to the non-linear effect in the electrical characteristics. More details and further research are displayed in Chapter 6.

2.6.3 Early saturation effect

Early saturation effect is common phenomenon in the OTFT, in which the saturation drain current is launched to appear earlier ($|U_{DS}|<|U_{GS}-U_{Th}|$) than the Gradual Channel Approximation (*GCA*) theory of $|U_{DS}|>|U_{GS}-U_{Th}|$ [170], where the U_{Th} is threshold voltage. For S-DNTT-10-based OTFTs which we fabricated in the early phase, we encountered with premature saturation effect. In this part, we displayed the *early saturation effect* in TCBG S-DNTT-10-based OTFT and simulated this effect from the *GCA*.

2.6.3.1 Description of results

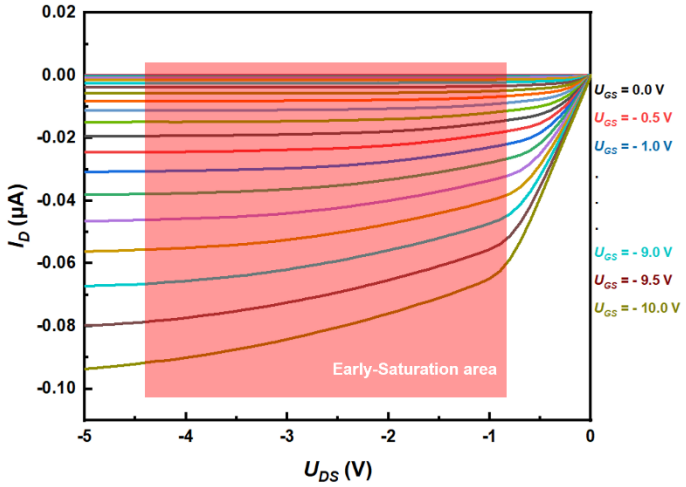


Figure 2.15 S-DNTT-10-based OTFT, Width (*W*) = 1000 μm, Channel Length (*L*) = 30 μm, $T_{S\text{-}DNTT10}$ = 25 nm, T_{ox} = 300 nm, C_i = 0.00011505 F/m^2, Output characteristics, U_{DS} = 2 ~ -5 V, Step- U_{DS} = 0.1 V, U_{GS} = 2 ~ -5 V, Step-U_{GS} = 0.5 V. (The apparent red area is noted as the area of emerging early saturation effect, and the collected drain current suddently appeared into saturation-regime tendence)

As **Figure 2.15** above showed, the slope of the output characteristic curve I_D-U_{DS} varied with a slightly increased U_{DS} at a given U_{GS}. That is, it had two different linear slopes of I_D-U_{DS} at a small U_{DS} interval and tended to enter the saturation-mode prematurely, as the apparenet red area marked.

2.6.3.2 Mathematic simulation model

Herein, we plan to list the rough calculated process of this model. The details in simulation are exhibited in Section 9.1, **Appendix**.

To explore the effect, it was calculated on the differential of drain current I_D corresponding to U_{DS}, *i.e.*, conductivity (G_{diff}), at a given gate-source voltage drop U_{GS},

$$G_{diff} = \frac{\partial I_D}{\partial U_{DS}} \tag{2.4}$$

based on **Figure 2.15** showed the experimental data in the I_D-U_{DS}, then calculated as **Figure 2.16** showed that the value of differential initially occurred larger reduction at small drain voltage, and then the G_{diff} almost performed linear property from U_{DS} of -1 to -5 V. The distinctive result was that the rapid reduction of G_{diff} within a small drain interval or the sudden increase in total resistance based on Ohm's Law ($dR=dV/dI=1/G_{diff}$).

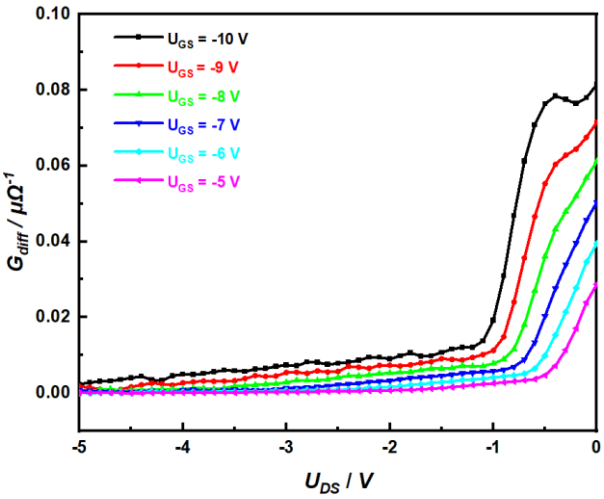


Figure 2.16 The differential of drain current I_D corresponding to drain voltage U_{DS} under variable gate voltage U_{GS} and source penitential referenced to V_S = 0 V.

According to Equation. **(1.11)**, the G_{diff} can be express as the following equation [140],

$$G_{diff} = \frac{\partial I_D}{\partial U_{DS}} = \frac{W}{L}\mu_{eff}C_i[U_{GS} - U_{Th} - U_{DS}] \qquad (2.5)$$

still applied the I_D-U_{DS} under the U_{GS} of -10 V as the explored objective and it supposed the threshold voltage U_{Th} as -2.8 V roughly extracting from **Figure 2.15**. To compare with the characteristics of the I_D-U_{DS} experiments on gate voltage U_{GS} of -10 V, it was also calculated on I_D-U_{DS} based on *CGA* theory, the corresponding parameter in the following **Table 2.1** and **Figure 2.17** were respectively relationships of I_D - U_{DS} and G_{diff} -U_{DS}.

Table 2.1 Setting parameters in the Equation. (1.11) and (2.5).

Parameter	W/μm	L/μm	T_{SiO2}/nm	C_i /F·m^{-2}	μ_{eff}/cm^2·V^{-1}·s^{-1}	U_{GS}/V	U_{Th}/V
Value	1000	30	300	1.1505·10^{-4}	0.0285	-10	-2.8

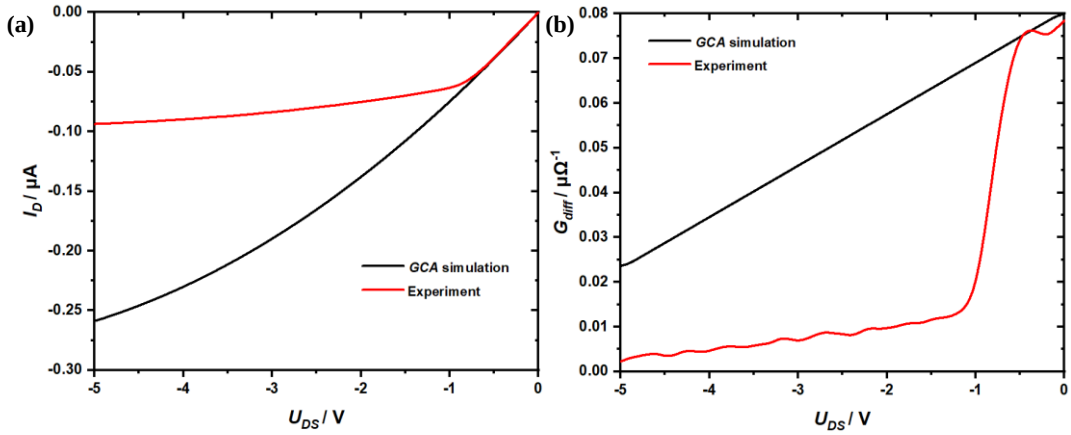


Figure 2.17 (a) Experimental I_D-U_{DS} of the S-DNTT-10-OTFT at U_{GS} = -10 V showed in Figure 2.15, (b) the corresponding to the differential calculation through the differential function. (The calculation is respective from the Equation. (1.11) and (2.5))

As shown in **Figure 2.17**, compared to the general *GCA* theory calculation (black solid line), the experimental curve (red solid line) displayed the following characteristics: (1) In the I_D-U_{DS} curve, within the drain voltage range of 0 V to -1 V, both curves had nearly the same drain current. However, as the drain voltage U_{DS} increased, the drain current of the red line rose more slowly, and the difference between the two curves became more pronounced. Eventually, the drain current I_D seemed to stabilize, indicating the OTFT sample might have entered saturation mode. (2) In the G_{diff} curve, unlike the linear variation of the black line, the G_{diff} value of the red line rapidly decreased when U_{DS} ranged from -0.5 V to -1 V. Given that the GCA theory assumes constant effective mobility (μ_{eff}), **Equation.(2.5)** could not accurately simulate this *early saturation effect*. Therefore, based on the above simulation, it can be inferred that the effective mobility μ_{eff} may vary with the drain voltage U_{DS} at a given gate voltage U_{GS}, particularly, encountered with the drastic changes in the value of G_{diff} at almost U_{DS} of -0.5 V. Considered that the physical model of charge transport [58,171,172], $\mu = \beta[-(U_{GC} - U_{Th})]^{\alpha}$, was quoted, in which α and β were the fitting parameters, U_{GC} the gate voltage at a point C in the channel. The formula described the relationship between the mobility and the local concentration of accumulated charge with variable potential along the channel. This model is generally employed into simulating the effective mobility behavior in OTFTand it refers to the fact that in OSC with disorderd arrangments the mobility increases with charge carrier concentration or applied U_{GS}. However, this mode could not simulate *the early satation effect*. Following the above analysis, combined with **Figure 2.17 (b)** it presented the rapidly decreased the value of G_{diff}, it was considered an exponential form, a calculated mobility-model μ (U_{GS}, U_{CS}) was finially established,

$$\mu(U_{GS}, U_{CS}) = (\beta \cdot |U_{GS}|^{\gamma}) exp(k \cdot U_{CS}) \quad \textbf{(2.6)}$$

the fitting parameters of β, γ, and k. Since the experimental sample was p-type OTFT, the γ and k were both positive constants. After the complicated optimization (details in the Section 9.1, **Appendix**), the obtained **Figure 2.8** displayed the comparison of the simulation correlating with **Equation (2.6)** and measured results, including I_D-U_{DS} curve and G_{diff}-U_{DS} curve.

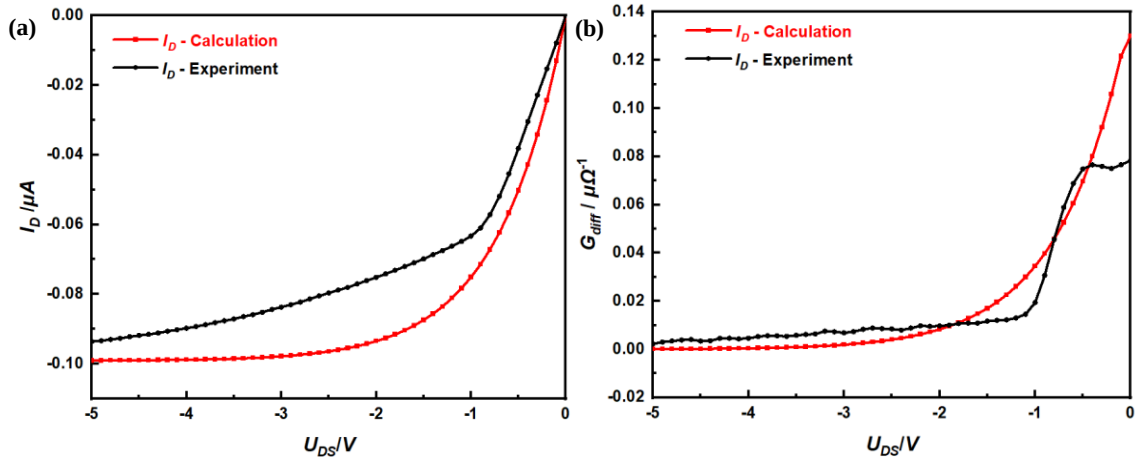


Figure 2.18 The calculation compared with measured data on (a) I_D-U_{DS}, and (b) G_{diff}-U_{DS}. (The calculation mode is correlating with Equation (2.6))

As **Figure 2.17 (a)** showed, the calculated results, noted as the red solid line, were somewhat similar. However, the corresponding G_{diff} differed significantly from the experimental data. Then it was concluded that the channel resistance (R_{ch}) was not dominant in the total resistance system. Thus, other types of resistance should be considered. The utilized fundamental equation was Ohm's Law, I_D=U_{DS}/R_{tot}. It assumed that the injection contact resistance R_{inj} was not dominated in total resistance system R_{tot}, and the R_{tot} in linear operation of OTFT can be regarded to consisting of bulk resistance (R_{bulk}), channel resistance R_{ch}, and one parasite resistance (R_0) which it could be regarded as one effective parameter correlating with charge injection barrier and the fabricated lower quality or disorder arrangement of OSC [172], *i.e.*, $R_{tot} = R_0 + R_{bulk} + R_{ch}$.

And if it were taken into account that the total serious resistance within the sample comprised R_{bulk}, R_{ch}, and one R_0. After several steps to establish the model and find the good fitting parameters (details seeing in Section 9.1, **Appendix**), it was obtained the **Figure 2.19** which was a comparison between simulated calculation and measured results.

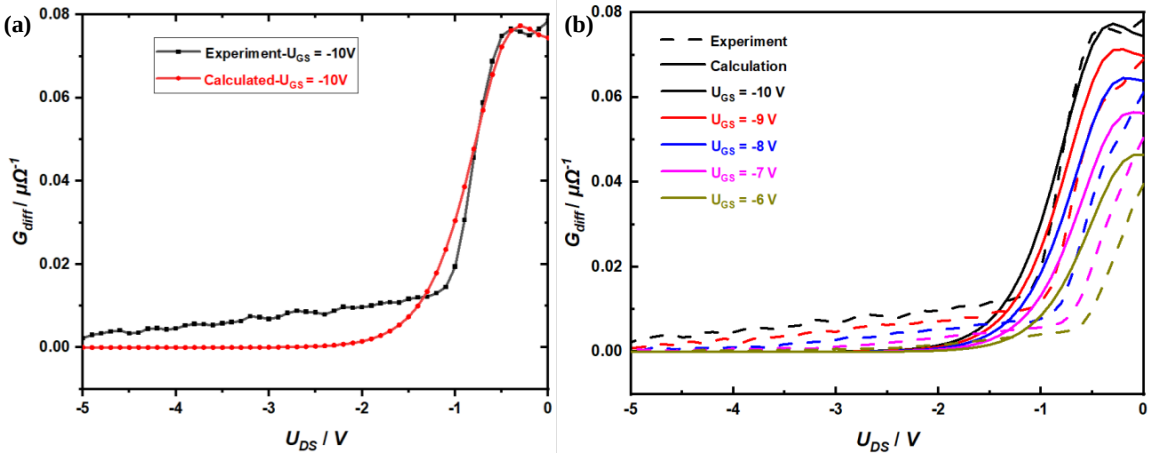


Figure 2.19 (a) The graphic of calculated G_{diff}- U_{DS} compared with measured data. And (b) the diagram of calculation of G_{diff} under different U_{GS}. (The calculation mode is correlating with Equation (2.6))

Figure 2.19 (a) showed that the calculated results had a better match with the experiments, especially the curve considering other factors of R_{bulk} and R_0 in the G_{diff}-U_{DS} relation, which was more obvious. Then it is indicated that the mobility model as expressed in **Equation (2.6)** can better describe the *early saturation effect*.

Ultimately we simulated this modele in other stressed U_{GS} and the corresponding results are shown in **Figure 2.19 (b)**. In the figure, the solid line represents calculated data, while the dashed line represents experimental data, with different colors indicating varying U_{GS}. Overall, the figure demonstrates an excellent match between the calculations and experimental results, confirming that the mobility model described by **Equation. (2.6)**, along with the considerations of greater R_{bulk} and R_0, is relatively accurate, the details seeing in Section 9.1, **Appendix**. It was concluded that certain factors caused the R_0 to be higher, dominating the total resistance system at low U_{DS}. As the drain voltage increased, the R_{ch} and R_{bulk} became significant compared to R_0. Additionally, another factor was the variation of effective mobility with U_{DS}.

Herein, this section not only showed the *early saturation effect* in the initial TCBG S-DNTT-10-based OTFT we fabricated, more significant, it was mathematically simulated based on **Equation (2.6).** Despite we could not clearly explain the mechanism behind this effect even such this effect has already been simulated [88], it was first time to explore the *early saturation effect* on S-DNTT-10-based OTFT and we think the above analysis and simulation still provide some inspiration on exploring this effect in future.

2.7 Summary

In this section, it was introduced the information of S-DNTT-10-based OTFT we explored in this study. Initially, it exhibited that the molecular structure and basic chemical process of S-

DNTT-10 molecules were initially presented in a brief manner. Laterly we presented the fundamental fabrication process of the S-DNTT-10-based OTFTs used in this study. The manufacturing equipment was introduced, along with the electrical test platform and material characterization equipment used in this study, including the homemade *IV*-in-situ Raman spectrometer combined test platform, the AFM, the KPFM and the contact angle techniques.

Through AFM and contact angle tests, the morphology of the S-DNTT-10 thin film and its contact angle of 101.8° were observed. The AFM results revealed that the S-DNTT-10-layer overlap with each other, while the contact angle measurement indicated that the S-DNTT-10 thin film possesses hydrophobic properties. Subsequently, the electrical characteristics of S-DNTT-10-based OTFT were presented like I_D-U_{DS} output characteristics, I_D-U_{GS} transfer characteristics, effective field-effect mobility and threshold voltage, encompassing non-linear electrical characteristics. In this case, the linear-mode effective field-effect mobility μ_{lin} of nearly 0.062 $cm^2 \cdot V^{-1} \cdot s^{-1}$ and the related threshold voltage $U_{Th\text{-}lin}$ of -21.2 V. The saturation-mode effective field-effect mobility μ_{sat} of almost 3.395 $cm^2 \cdot V^{-1} \cdot s^{-1}$ and the related threshold voltage $U_{Th\text{-}sat}$ of -24.9 V. The potential distribution of the S-DNTT-10-based OTFT was obtained through a KPFM characterization, revealing that the majority of the potential drop occurs at the source, suggesting the presence of considerable source contact resistance, which indicates that charge injection is impeded. Lastly, we discussed the results of the *Early Saturation effect* in the S-DNTT-10-based OTFT. Although we did not arrive at a conclusive physical explanation, it was successfully simulated using a mathematical model. The results suggest that this effect may be related to changes in U_{DS}, and we plan to investigate this further in future studies.

3 Raman scattered on S-DNTT-10 material

3.1 Introduction

In this chapter, the molecular characteristics of S-DNTT-10 plan to be primarily investigated using Raman scattering techniques, including conventional Raman scattering spectroscopy and Surface-Enhanced Raman Spectroscopy (SERS). First, the fundamental principles of Raman scattering and SERS will be briefly introduced in Section 3.2. Next, the Raman scattering spectrum of S-DNTT-10 will be simulated and computed using Density Functional Theory (DFT), and the molecular vibration modes are obtained in Section 3.3. Since in situ Raman scattering tests of OTFTs are required in subsequent experiments, it is essential to determine whether the excitation light wavelength affects the OTFT's electrical characteristics. Therefore, electrical measurements will be performed under illumintion in Section 3.4. Finally, Raman scattering measurements are conducted on the S-DNTT-10 thin film in Section 3.5.

3.2 Light-matter interaction

3.2.1 Raman scattered effect

The interaction between photons and matter has gained significant importance, driving research and applications in various industrial fields. In optical technology, Raman spectroscopy plays a crucial role in identifying chemical bonds (such as C-H, C=C, N-H, etc.) by analyzing the vibrational characteristics of substances. Vibrational spectroscopy can be served as the fingerprint of each substance. Any physical or chemical change in a structure will alter its vibrational spectrum.

Raman Scattering is a light scattering phenomenon named after the Indian physicist Chandrasekhara Venkata Raman, who discovered it in 1928 [173] and was awarded the Nobel Prize in Physics in 1930. Raman Scattering occurs when photons interact with molecules, causing some photons to be scattered at frequencies different from the incident photons. This frequency-shift results from energy exchange between photons and the vibrational or rotational energy levels of molecules. The method is highly practical due to its sensitivity and non-destructiveness, as long as the excitation light does not thermally damage the sample. Raman spectroscopy provides valuable information on chemical properties, charge states, interface processes, and the structural order of organic materials. It is based on the inelastic interaction between light and matter. When light is scattered by matter, the energy of most photons remains

unchanged, corresponding to elastic or Rayleigh scattering. A minuscule number of photons, approximately one in a million, are implicated in the inelastic scattering process (Stokes process) or annihilation process (anti-Stokes process) excited in the medium. Hence, the energy of the scattered photons will be lower (Stokes) or higher (anti-Stokes) than that of the incident light [174–177]. The majority of conventional Raman experiments employ the red-shifted Stokes peak as they are more intense at room temperature.

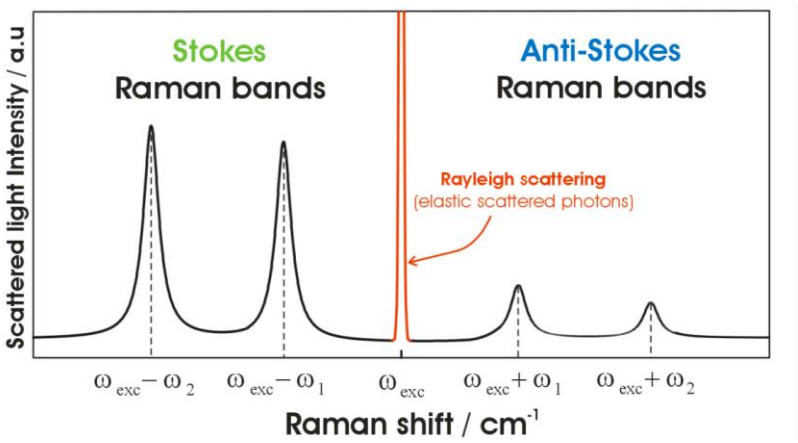


Figure 3.1 Spectrum of scattered light showing the Raman Stokes, Rayleigh, and Raman anti-Stokes bands [39].

Figure 3.1 depicts the Stokes, Rayleigh, and anti-Stokes processes, wherein a photon with energy $\hbar\omega_{exc}$ and momentum $\boldsymbol{k}_{exc}$ is scattered through the generation or annihilation of a fundamental excitation with energy $\hbar\omega_i$ and momentum $\boldsymbol{q_i}$. The scattered photon possesses energy $\hbar\omega'$ and momentum $\boldsymbol{k'_{exc}}$. This indicates that each scattered photon in the Stokes component is correlated with an energy loss of the sample. Likewise, for each scattered photon in the anti-Stokes component, the sample acquires energy $\hbar\omega_i$. Energy conservation is expressed as $\hbar\omega' = \hbar\omega_{exc} \pm \hbar\omega_i$, where the negative (positive) sign represents the Stokes (anti-Stokes) process. Momentum conservation demands $\boldsymbol{k'_{exc}} = \boldsymbol{k}_{exc} \pm \boldsymbol{q_i}$. Here, the positive (negative) sign indicates the Stokes (anti-Stokes) process. A schematic diagram of the Raman spectrum with energy $\hbar\omega_i$ is presented in **Figure 3.1**. Among them, there exists a strong component of elastically scattered photons, namely, photons with energy $\hbar\omega_{exc}$ (Rayleigh process).

3.2.2 Surface-Enhanced Raman scattered principle

In 1974, Fleischmann et al. reported a significant enhancement of the Raman signal when pyridine was adsorbed on an electrochemically roughened silver electrode [178]. In 1977, research teams led by Van Duyne (static field enhancement) and Creighton (resonance Raman

scattering due to the broadening of molecular electronic energy levels) independently confirmed this finding [179,180]. This phenomenon, known as Surface-Enhanced Raman Spectroscopy (SERS), demonstrates ultrahigh sensitivity at the molecule level. [181,182]

A definitive conclusion regarding the SERS mechanism remains elusive due to the extreme complexity of common SERS systems. Numerous factors influence SERS spectra, including surface morphology and electronic structure, the interaction between light and the rough surface, the interaction between light and molecules, the adsorption configuration, orientation, bonding status of molecules on the surface, and properties of the incident light. This complexity leads to diverse interpretations of SERS. While some models can partially explain certain experimental phenomena, they often conflict with other results. Consequently, a comprehensive SERS mechanism that accounts for all experimental observations has yet to be clarified. Currently, the generally accepted SERS mechanisms are divided into two types: the physical enhancement mechanism, known as the Electromagnetic Mechanism (EM), and the chemical enhancement mechanism (Charge Transfer, CT). [174,183–186]

3.2.2.1 Electromagnetic Mechanism

Subsequent to the validation of SERS, the electromagnetic (EM) and chemical mechanisms were proposed by the researchers. Despite the prolonged controversy over the operation of these mechanisms, it is incontrovertibly established that surface plasmon resonance (SPR) is a crucial factor for SERS in metal nanostructures.

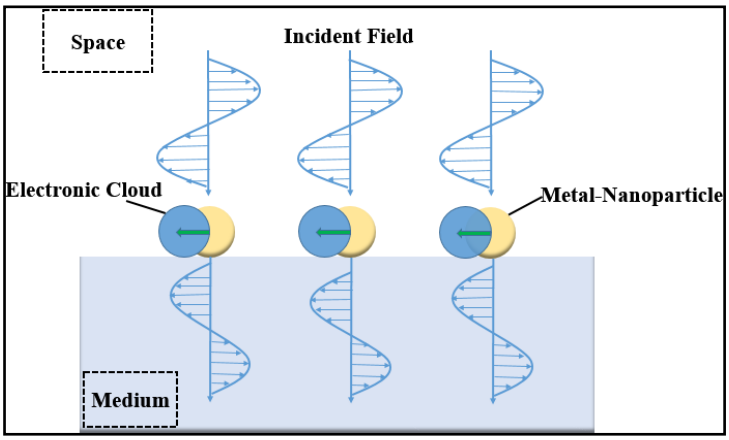


Figure 3.2 The schematic diagram of inducing localized surface plasma resonance (LSPR) effect [187].

When light (oscillating electromagnetic waves) is incident on metal nanoparticles (NPs) or NP arrays that are significantly smaller than the incident wavelength, the free electrons within the NPs are influenced by the external electric field and deviate from their initial positions, thereby resulting in collective oscillations. In such circumstances, when the

frequency of the incident light aligns with the oscillation frequency of the electrons in the NPs, a local surface plasmon resonance (LSPR) effect is induced, thus forming an enhanced local electromagnetic field near the surface of the NPs [174,188], as illustrated in **Figure 3.2**. This local field (E_{local}) encompasses two steps, namely the enhancement of the absorption of the incident excitation light (ω_0) and the generation of the Raman scattered light (ω_R). When the incident frequency coincides with the frequency capable of exciting LSPR, the maximum excitation enhancement effect can be attained.

At this point, the Raman signal will deviate from resonance with the red-shift wavelength against incident light. To maximize signal enhancement, the geometric parameters of the nanoparticles (NPs), such as structural size and period, can be adjusted to align the excitation LSPR frequency with the excitation wavelength. To fully understand this phenomenon, the optical properties of metals should be reexamined, and the resonance conditions leading to strong SERS enhancement should be identified. Given that the size of the sphere is significantly smaller than the incident wavelength, the polarization of the metal sphere can be described as follows, [188]

$$\alpha = 4\pi\varepsilon_0 r^3 \frac{\varepsilon_m(\omega)-\varepsilon_r}{\varepsilon_m(\omega)+2\varepsilon_r} \quad \textbf{(3.1)}$$

herein, r is the radius of the spherical surface, and ε_m and ε_r correspond to the dielectric constants of the metal and the environment, respectively. Generally, the relative dielectric constant of a metal consists of the real part and the imaginary part, that is, $\varepsilon_m = \varepsilon_a + i\varepsilon_b$, which respectively characterize the propagation and dissipation characteristics of the incident light within the metal material. Different metals possess different relative dielectric constants. However, when the real part Re(ε_m) = -2ε_r (ε_a = -2ε_r) and the imaginary part (Im) is extremely small, a larger even one maximum polarizability can be attained at the frequency (ω) [176,187]. It should be noted that the real and imaginary part of the metal respectively determine the position and intensity of the LSPR, which is highly related to its electron density. In this regard, all SERS-active metals have a similar valence electron distribution (semi-filled subshell), enabling collective oscillations of high-density free electrons. Nevertheless, the configuration of extra-nuclear electrons leads to distinct optical properties within different wavelength ranges. Therefore, in the visible light region, Ag readily meets the resonance conditions; in the red-light region, Cu and Au do; Al readily meets the resonance conditions in the ultraviolet region.

3.2.2.2 Chemical Mechanism

During SERS measurements, electromagnetic and chemical enhancements interact. Even slight changes in the chemical environment can lead to variations in SERS spectral characteristics. The overall enhancement effect depends on whether the excitation light is tuned to the resonance states of LSPR and charge transfer (CT). It is important to note that when the excitation light frequency deviates from the LSPR excitation range, the contribution of chemical enhancement may become more significant. This was confirmed by Lombardi et al. in 1978 [183]. Generally, chemical enhancement can be subdivided into resonant Raman, CT resonance between the substrate and molecules or between the molecule and substrate, and adsorption-induced polarity changes (mainly for non-resonant molecules).

The most fundamental CT pathway of the metal surface is the Herzberg-Teller coupling (*i.e.*, energy level overlap or orbital hybridization) between the adsorbed molecule and the metal [189]. Owing to this coupling, the gap between HOMO and LUMO will narrow, and the resonance of this "CT moment" (μ_{CT}, borrowed from the allowed molecular transition ($\mu_{H\text{-}L}$)) can be triggered by energy lower than that required by free molecules. Photo-generated electrons can be excited from HOMO to the Fermi energy level of the metal through the transition moment from the molecule to the metal ($\mu_{H\text{-}L}$). Eventually, the electrons transition back to HOMO, releasing a Raman photon that encodes the fingerprint information of the adsorbed molecule. [174]

To date, a large number of experimental accomplishments have demonstrated that neither physical enhancement nor chemical enhancement can independently account for all SERS phenomena, and both typically coexist within the investigated systems.

3.3 Density Function Theory simulation of S-DNTT-10

Currently, there is a rare report on the Raman spectrum of S-DNTT-10. To ensure the accuracy of the Raman spectrum measured in this study, it is crucial to first perform a simulation calculation of S-DNTT-10 as a reference. This approach allows for a deeper understanding of the Raman spectrum and the molecular vibrational information represented by each Raman peak. Density Functional Theory (DFT) simulation can achieve these requirements by not only providing the theoretical Raman spectrum, but also detailing molecular vibration modes in the Raman-shift bands through animations.

3.3.1 Density Function Theory

In the 1960s Kohn and Sham proposed one calculated theory as named "***Density Functional Theory***" (DFT) that was performed in quantum chemistry [190,191]. It was known as one effective method which can carry out the relatively accurate theoretical molecular properties, such as Raman spectrums and the details of vibrational modes in this study.

The Gaussian software package is a leading tool for performing DFT calculations. To execute these calculations, the structure of the target molecule is input, and calculation tasks and methods are defined. The choice of basis set is also a critical factor in DFT calculations, as different sets can significantly influence the final results. Generally, higher-grade basis sets yield more accurate results but also increase computation time. In the following simulation, the input file was prepared using **Gauss View 6.0**. The DFT simulation was conducted with **Gaussian16 A.03**, using the **B3LYP** functional method and the **6-311G (d, p)** basis set.

3.3.2 Theoretical molecular vibration for S-DNTT-10

3.3.2.1 Simulated Raman spectrum

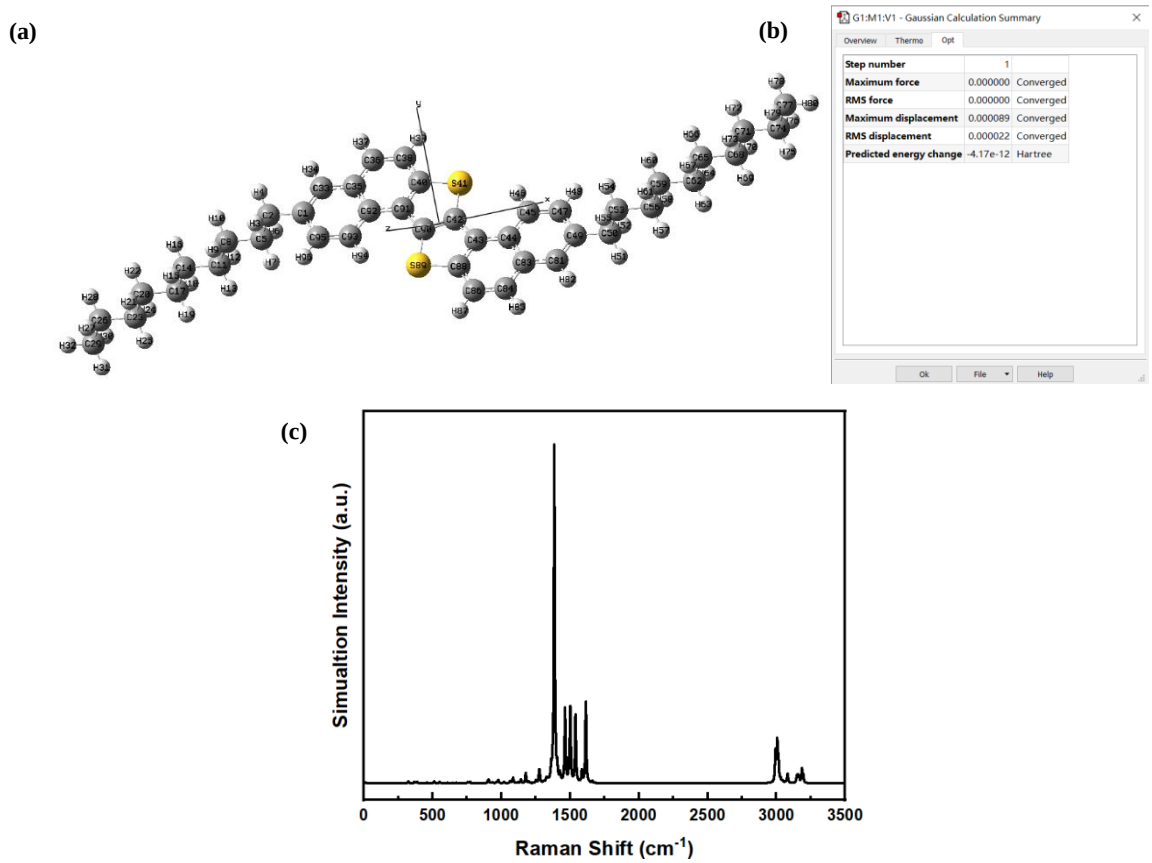


Figure 3.3 The process of DFT simulation in one S-DNTT-10 molecule: (a) the visualized S-DNTT-10 molecule with Cartesian coordinate system in Gauss view 6.0 software, (b) the calculation summary of non- resonant Raman spectrum of S-DNTT-10, and (c) the simulated non- resonant Raman spectrum.

The structure was modeled on the website platform named ***Molview***. It was open-source website with easily operational interface. It saved kinds of conventional molecular information in the database. It supported the structure files which can be input into relevant calculated engineering software such as ***Gaussian 16W***. And we modelled the molecular structure of S-DNTT-10. **Figure 3.3 (a)** displayed the S-DNTT-10 molecule in the **Gaussian View 6.0**.

In DFT simulations by ***Gaussian 16W***, such as for Raman spectra, there is a key principle for evaluating the reliability of the results: four criteria—***Maximum Force***, ***RMS Force***, ***Maximum Displacement***, and ***RMS Displacement***—must all be marked as converged. **Figure 3.3 (b)** shows the summary of the simulation for the S-DNTT-10 molecule, indicating that all four criteria are converged, confirming the accuracy of the simulation. **Figure 3.3 (c)** presents the simulated theoretical non-resonant Raman spectrum for a single S-DNTT-10 molecule, ranging from 0 to 3500 cm^{-1}. The vibrational modes are primarily located in the regions of 750-1750 cm^{-1} and 3000-3250 cm^{-1}.

3.3.2.2 Vibrational mode

In the investigation of the molecular dynamics of S-DNTT-10, a comprehensive simulation using Density Functional Theory (DFT) was initiated. **Figure 3.4 (a)** clarifies the theoretical non-resonant Raman spectrum within the range of 1100-1550 cm^{-1},which is from **Figure 3.3 (d)**, depicting a series of Raman-shift peaks, numerically identified as 1 to 12. These peaks exhibit distinct vibrational modes within the molecule, each signifying unique patterns of atomic displacements. For instance, modes 1 and 7, as shown in **Figure 3.4 (b)** and **Figure 3.4 (c)** respectively, exemplify the diversity of molecular vibrations encountered. In these figures, the directional movement of atoms is illustrated by red arrows, with their length proportional to the magnitude of displacement. Specifically, mode 1 is characterized by the bending vibrations of C-H bonds within alkyl chains. In contrast, mode 7 reveals significant deformations in both aromatic and thiophene rings, coupled with the bending of C-H bonds, indicating a complex interaction of vibrational phenomena within the molecule's framework. A comprehensive enumeration and description of the remaining vibrational modes ranging from 1100 to 1550 cm^{-1} are systematically presented in **Table 3.1**.

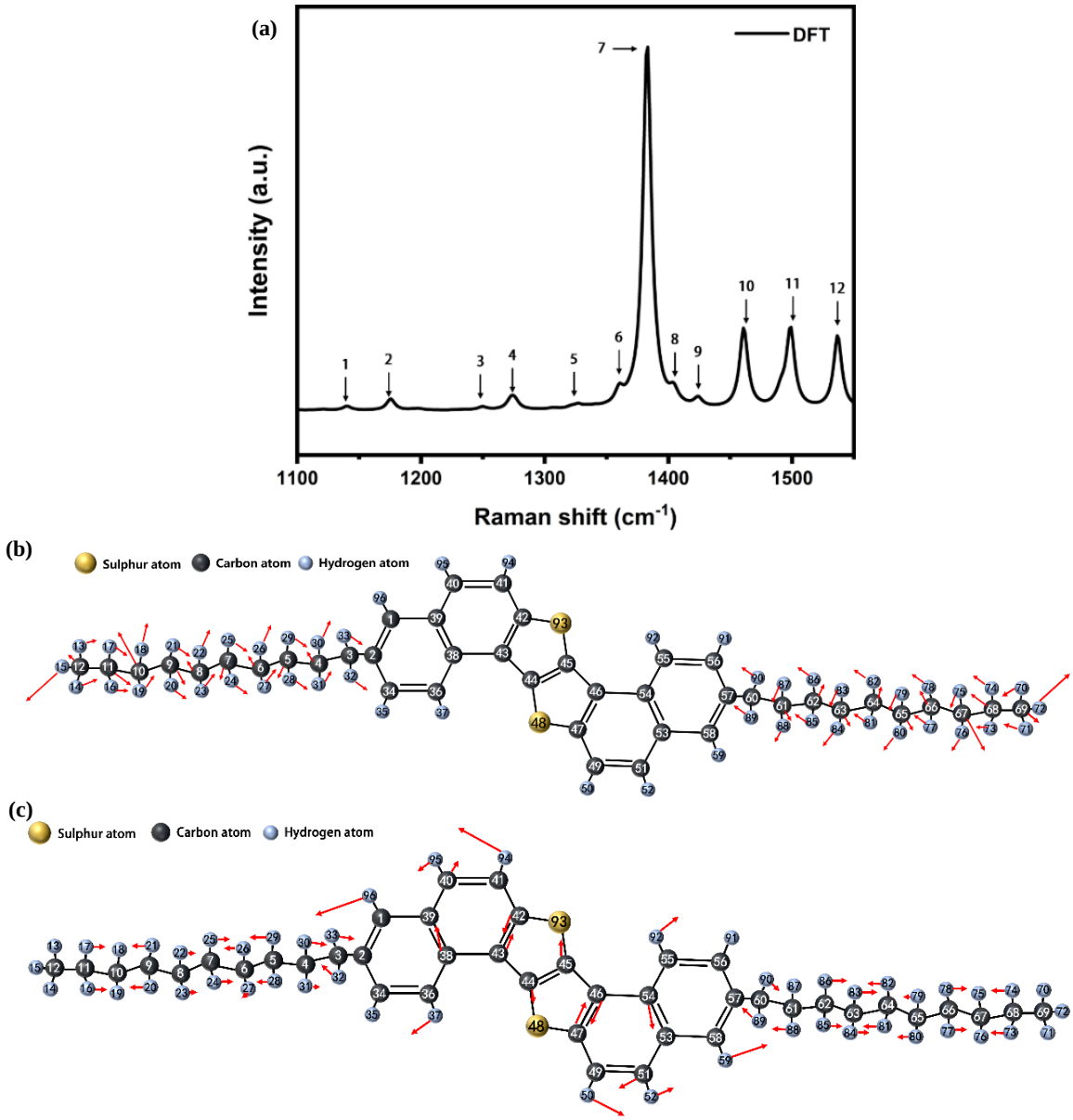


Figure 3.4 (a) The DFT simulation of non-resonant Raman spectrum of S-DNTT-10, (b) the vibrational mode 1, and (c) the vibrational mode7.

Table 3.1 Theoretical S-DNTT-10 molecular vibration in the range of 1100-1550 cm^{-1}. (The details are listed in Section 9.2, Appendix)

Mode	Raman shift/cm^{-1}	Vibrational descriptions
1	1141.79	C-H bond bending at alkyl chains
2	1177.11	C-H bond bending located at the aromatic rings and coupled with few slight deformations of thiophene rings
3	1251.53	C-H bond bending at alkyl chains; C-H bond bending coupled with slight breathing stretching aromatic rings and thiophene rings deformed

4	1274.84	C-H bond bending at alkyl chains; some serious C-H bond bending located at C(38), C(33), C(93), C(86), C(81) and C(45), and coupled with few slight deformation of aromatic and thiophene rings
5	1328.95	C-H bond anti-symmetry bending at alkyl chains coupled with C-C bond movement at aromatic and thiophene rings
6	1362.20	C-H bond bending at alkyl chains; deformation of thiophene rings and linked aromatic rings; seriously C-H bond bending located at C(36), C(95), C(84) and C(47); C-C bond stretched at aromatic and thiophene rings
7	1384.79	C-H bond slightly bending at alkyl chains; strongly C-H bond bending located at C(38), C(33), C(86) and C(81) coupled with deformation of aromatic and thiophene
8	1406.24	C-H bond slightly bending at alkyl chains; strongly C-H bond bending located at C(36), C(93), C(84) and C(85) and C(42)=C(90) double-bond stretching coupled with deformation of aromatic and thiophene
9	1426.09	Slight C-H bond bending at the end of alkyl chains; strong C-H bond bending at C(36), C(33), C(95), C(86), C(81) and C(47) coupled with deformation of aromatic and thiophene rings.
10	1462.96	C(42)-C(43) and C(90)-C(91) strongly stretching coupled with deformation of aromatic and thiophene rings
11	1500.85	C-H slightly bending at the end of alkyl chains; deformation of aromatic and thiophene rings
12	1539.00	strongly C(42) = C(90) double-bond stretching coupled with deformation of aromatic and thiophene rings

3.3.2.3 Simulated Molecular orbitals energy level

In the Gaussian simulated calculation software, the molecular structure of S-DNTT-10 was initially optimized to obtain the steady-state structure. Based on this, the molecular orbital energy levels could be obtained by calculating the **single-point energy** and choosing **Job type** is ***Energy***. **Figure 3.5 (a)** presents the simulated molecular orbital energy levels of the S-DNTT-10 single molecule. The molecular orbitals marked as **168 (a)** and **169 (a)** respectively represent the Highest Occupied Molecular Orbital (HOMO) and the Lowest Unoccupied Molecular Orbital (LUMO) of the S-DNTT-10 molecule. The calculation results reveal that the HOMO and LUMO molecular orbital energy levels of the S-DNTT-10 single molecule are -0.06512 Hartree Energy and -0.20083 Hartree Energy respectively. According to the conversion relationship, that is, 1 Hartree energy = 27.211 Electron-volt (eV), ultimately, HOMO (S-

DNTT-10) ≈ -5.46 eV, LUMO (S-DNTT-10) ≈ -1.77 eV, and the bandgap is 3.69 eV. Additionally, some small squares in **Figure 3.5 (a)** have two small arrows in opposite directions with respectively indicating electron spin up and down, while some squares are empty. This indicates that the orbitals are filled and unfilled with electrons, respectively.

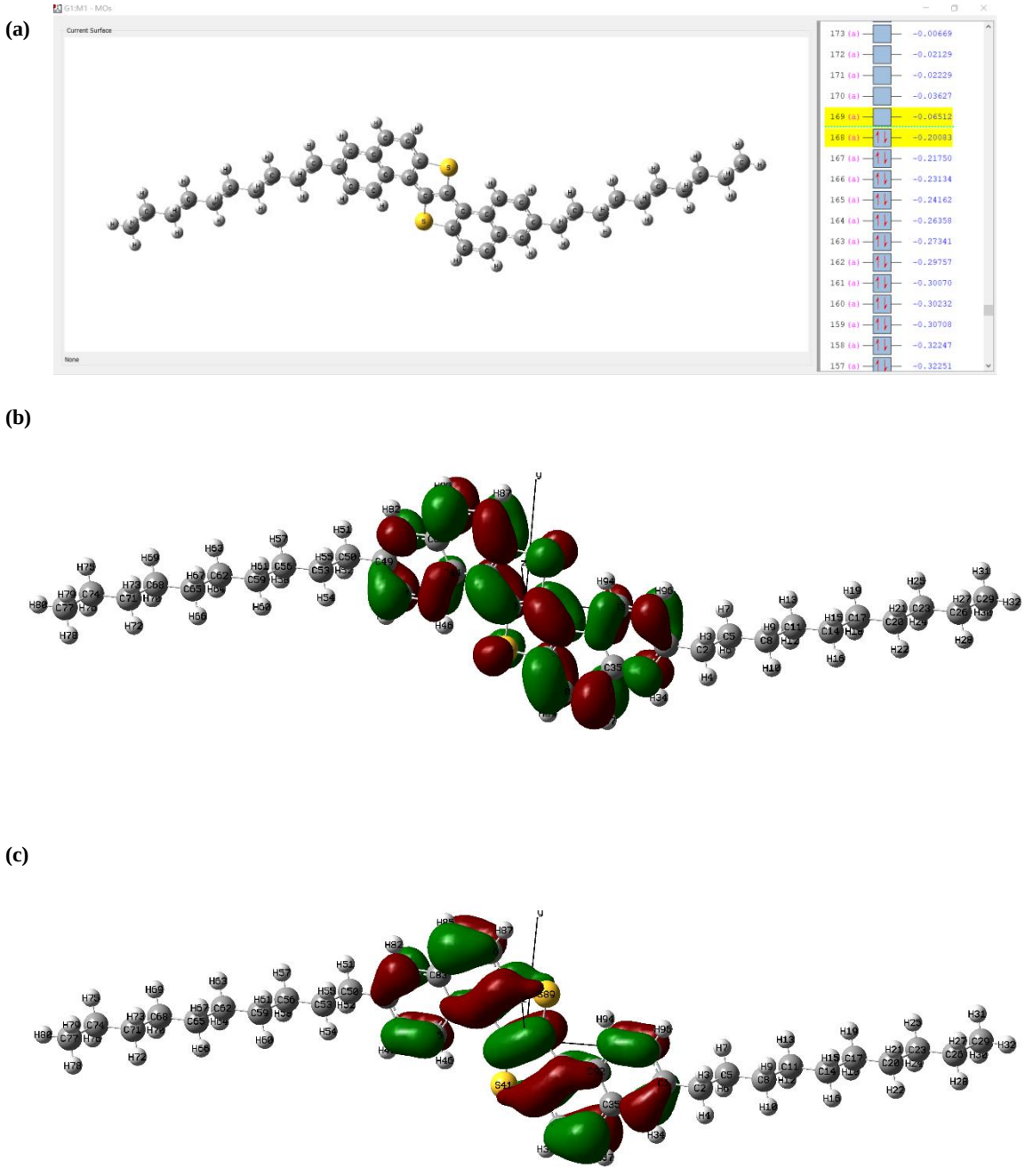


Figure 3.5 The molecular orbitals (MOs) of S-DNTT-10: (a) the interface of simulated MOs of S-DNTT-10, the distribution of the π-electron wave function of (b) HOMO and (c) LUMO molecular orbitals.

Figure 3.5 (b) and **(c)** respectively display the distribution of the π-electron wave function of the HOMO and LUMO molecular orbital energy levels of the S-DNTT-10 single molecule.

This information is useful for explaining the impact of long-term electric fields on the electrical performance of S-DNTT-10-based OTFTs, as detailed in Chapter 4. The first point that needs clarification is that the displayed molecular orbitals are not "π-electron clouds" responsible for charge transport. The π-electron cloud represents the probability of an electron's presence, while the molecular orbital refers to the wave function of the electron's motion. Squaring the wave function gives the probability of an electron being at a specific location. The two colors, red and green, in the molecular orbitals represent different phases of the wave function, corresponding to positive and negative signs. Although the electron density is related to the square of the wave function, a change in the phase does not affect the electron density distribution. However, the phase determines whether bonding or antibonding orbitals are formed between atoms.

3.4 Light influence in electrical properties of S-DNTT-10-based OTFTs

OSCs materials feature HOMO and LUMO molecular orbital energy levels comparable to those of inorganic semiconductors. This gives rise to the phenomenon that OSCs also present optical responses to specific wavelengths of incident light. And, since OSC is sensitive to external environment, it possibly results in thermal damage on the OSC material under the illumination with high energy. Hence, it is necessary to investigate on the power and wavelength of illumination affecting on S-DNTT-10 thin-films and the related OTFTs.

3.4.1 Laser thermal effect on S-DNTT-10 thin-films

Unlike ordinary light sources, lasers are a distinct type of optical source, known for their high directionality, monochromaticity, and brightness. These characteristics make lasers ideal for stimulating Raman scattering. High directionality allows the excitation light to be concentrated at a single point, minimizing energy loss and enhancing the collection and amplification of Raman signals. However, this concentration of energy increases the risk of thermal damage to samples, especially organic semiconductors (OSCs), which are more sensitive than inorganic semiconductors. In Raman scattering tests on OTFTs, it is important to set illumination parameters that generate sufficient Raman signals while avoiding thermal damage to the OSC, which can lead to degradation. This study aims to characterize both the Raman spectra and vibrational modes of the S-DNTT-10 molecule and perform in situ Raman scattering measurements on S-DNTT-10-based OTFTs. To protect the sample and obtain accurate Raman spectra, it is essential to evaluate whether excessive laser energy could cause

thermal damage to the S-DNTT-10 molecule, a novel and relatively unknown OSC, from a molecular vibration perspective.

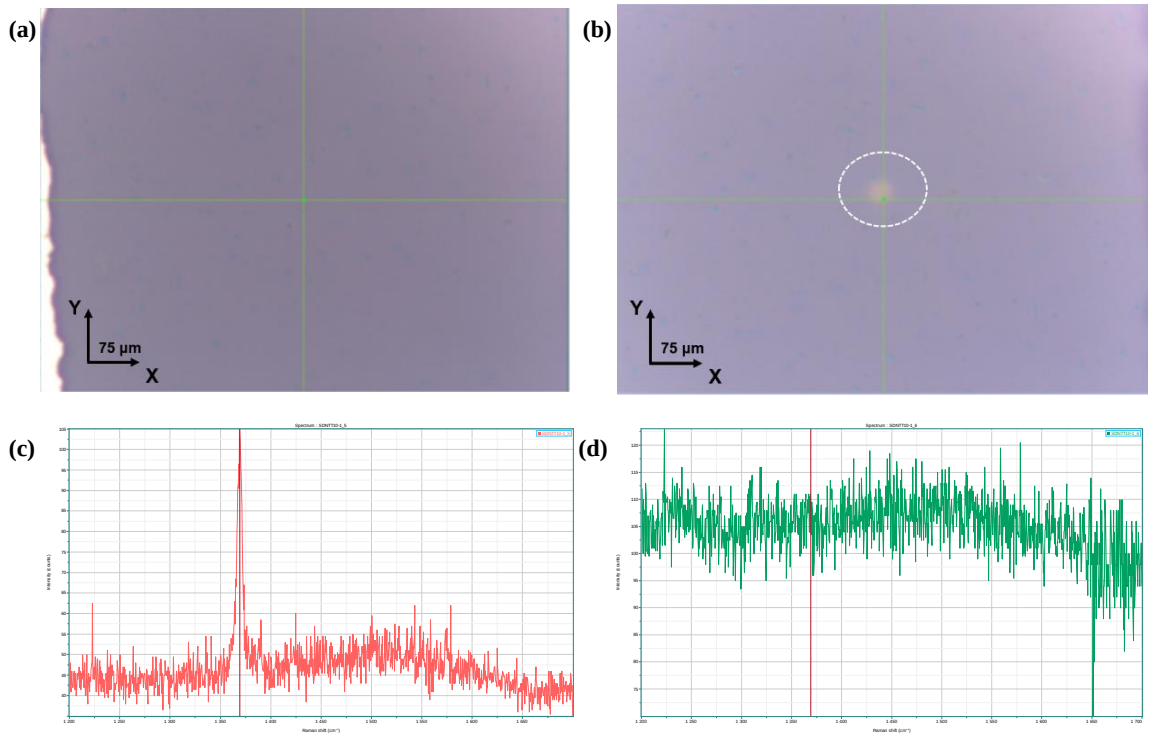


Figure 3.6 The top view of S-DNTT-10 surface illuminating by 532 nm-laser under (a)low power and (b) high power, the thermal damage remarked with white dash circle. The Raman spectrums in (c) and (d) is respectively corresponding to (a) and (b).

Subsequently, it was ascertained that 532 nm should be utilized as the incident wavelength of the excitation source for S-DNTT-10. Since, in accordance with the simulation calculation of the orbital energy levels of the S-DNTT-10 single molecule in Section 3.3.2.3, the bandgap energy between its HOMO and LUMO is approximately 3.69 eV. According to the intrinsic absorption wavelength limit formula: [192]

$$\lambda_0 \approx \frac{1240}{E_g}(nm) \qquad \textbf{(3.2)}$$

the "absorption wavelength limit" of S-DNTT-10 is approximately 336.04 nm. However, deviations could potentially emerge in practice as the thin-film is constituted by numerous molecules. The relative molecular orientations and the interactions among the molecules can have an impact on the molecular orbital energy levels, thereby resulting in deviations in the absorption wavelength limit. Considering that the Raman spectrometer utilized in this study offers three distinct wavelengths of excitation light, namely 532 nm, 633 nm, and 785 nm. Herein, it was decided that the laser light source with a wavelength of 532 nm should be employed as the excitation light.

Under the same illumination time and spectral accumulation times, Raman scattering measurements with low-power and high-power incident light were separately performed on the 25 nm S-DNTT-10 thin-film deposited on the SiO_2 layer, as depicted in **Figure 3.6 (a)** and **(b)**. The results revealed that when commencing with a low-power illumination condition, not only were there no discernible burning marks on the surface of the S-DNTT-10 thin-film, but also valid Raman spectra were collected by the equipment. A detailed analysis of the Raman spectra of the S-DNTT-10 thin film will be conducted in the subsequent section and will not be elaborated herein, as illustrated in **Figure 3.6 (c)** and **(d)**. Nevertheless, when the high-power excitation light was employed, it was discovered that not only were there obvious burning marks on the surface of the S-DNTT-10 thin film, but also, in comparison with the Raman spectra obtained under the low-power illumination condition, the equipment failed to collect valid Raman spectra.

The aforementioned results show that during the process of Raman spectroscopy, the thermal damage phenomenon of the material resulting from the illumination conditions of the excitation light source also demands attention.

3.4.2 Influence of laser on electrical performance

In the previous section, it was confirmed that higher incident light energy, rather than photon energy, could induce thermal damage to the S-DNTT-10 film. This underscores the need to establish safe and appropriate illumination parameters for the excitation light source during Raman spectroscopy measurements. The objective of this section is to assess the impact of laser light in Raman spectroscopy on the electrical performance of S-DNTT-10-based OTFTs. DFT calculations indicate that the energy gap between the HOMO and LUMO levels of the S-DNTT-10 molecule is approximately $E_g \approx 3.69$ eV ($\lambda \approx 336.04$ nm). However, it is possible that the disordered arrangement in the thin film could cause the overall response of the S-DNTT-10 film to incident light to differ from the DFT results. Therefore, excitation light with a wavelength longer than 336.04 nm might also affect the performance of S-DNTT-10-based OTFTs. To verify whether Raman spectroscopy using 532 nm and 633 nm laser light sources can be employed for in-situ measurements of S-DNTT-10-based OTFTs, these sources were used to irradiate the channel, and changes in effective field-effect mobility were compared. This allowed us to determine whether the Raman spectrometer's light source would significantly impact the performance of S-DNTT-10-based OTFTs.

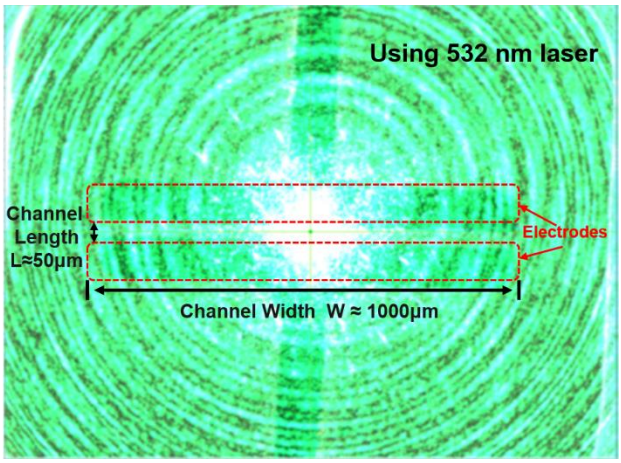


Figure 3.7 The excited source illuminated on the almost channel.

Since the performance of the device is governed by the charge transport characteristic within the device, an endeavor was made to direct the light source onto the channel during this experiment. In order to illuminate the whole channel we adjusted the working distance between the objective lens and the device surface as illustrated in **Figure 3.7**. During the measurement process, the device parameters employed were as follows: the thickness of the dielectric layer SiO_2 was 89 nm, the thickness of the S-DNTT-10 layer was 25 nm, the thickness of the gold electrode was 25 nm, the channel length was 50 μm, and the channel width was 1000 μm. By comparing the effective field-effect mobility (the linear-mode mobility μ_{lin} and the saturation-mode mobility μ_{sat}), before illumination and after different illumination wavelengths and durations.

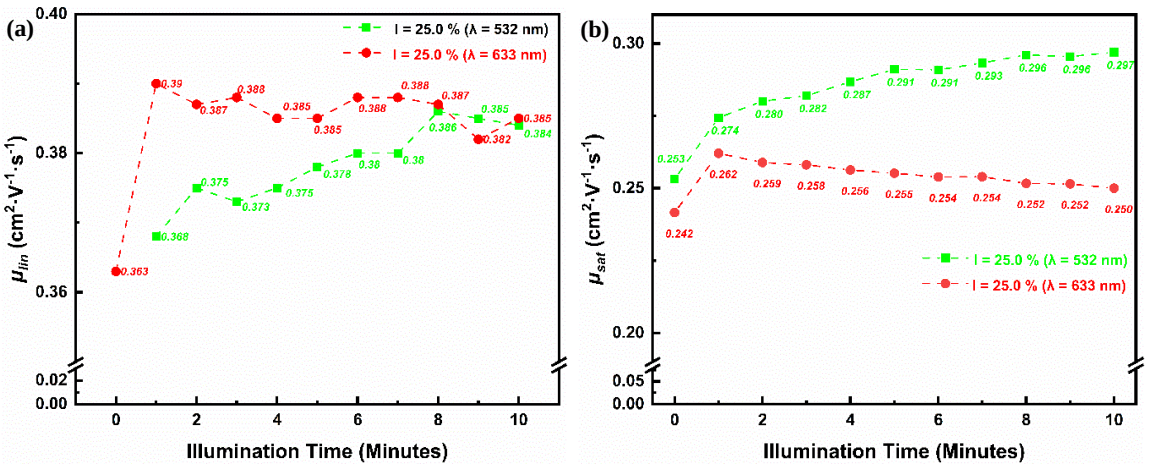


Figure 3.8 The effective field-effect mobility changed with illumination time under 532 nm and 633 nm: (a) linear-mode effective field-effect mobility μ_{lin} and (b) saturation-mode effective field-effect mobility μ_{sat}.

Figure 3.8 (a) and **(b)** respectively exhibit the linear-mode effective carrier mobility μ_{lin} at stressed U_{DS} = -1 V and saturation-mode effective carrier mobility μ_{sat} at stressed U_{DS} = -30 V

under incident lights of wavelengths 532 nm and 633 nm and different illumination times, which are derived through the transfer characteristic I_D-U_{GS} curves. The illumination time t of 0 represents the effective mobility of the device prior to illumination.

When illuminated with a 532 nm light source, before illumination, μ_{lin} (@ t=0) = 0.330 $cm^2 \cdot V^{-1} \cdot s^{-1}$ and μ_{sat} (@ t=0) = 0.253 $cm^2 \cdot V^{-1} \cdot s^{-1}$. In comparison with that before the illumination, μ_{lin} manifested a slight variation, increasing from 0.330 to 0.368 $cm^2 \cdot V^{-1} \cdot s^{-1}$. However, with the increase of the illumination time, μ_{lin} did not significantly augment but slightly ascended, changing from μ_{lin} (@ t=1 min) = 0.368 $cm^2 \cdot V^{-1} \cdot s^{-1}$ to μ_{lin} (@ t=10 min) = 0.384 $cm^2 \cdot V^{-1} \cdot s^{-1}$. Correspondingly, for μ_{sat}, after the illumination, it transformed from μ_{sat} (@ t=0) = 0.253 $cm^2 \cdot V^{-1} \cdot s^{-1}$ to μ_{sat} (@ t=1 min) = 0.274 $cm^2 \cdot V^{-1} \cdot s^{-1}$. Similarly, with the increase of the illumination time, μ_{sat} did not exhibit a significant enhancement but a slight increment.

When illuminated with a 633 nm light source, in comparison with that before illumination, μ_{lin} (@ t=0) transformed from 0.363 $cm^2 \cdot V^{-1} \cdot s^{-1}$ to μ_{lin} (@ t=1 min) = 0.39 $cm^2 \cdot V^{-1} \cdot s^{-1}$. Subsequently, with the increasing illumination time, although the results indicated that μ_{lin} slightly declined to μ_{lin} (@ t=10 min) = 0.385 $cm^2 \cdot V^{-1} \cdot s^{-1}$, it can essentially be regarded as remaining invariant. Furthermore, during the process of applying different illumination times, it was found that the variation in μ_{lin} was also extremely small, and the mobility can be considered constant. Correspondingly, for μ_{sat}, after illumination, μ_{sat} shifted from 0.242 $cm^2 \cdot V^{-1} \cdot s^{-1}$ to μ_{sat} (@ t=1 min) = 0.262 $cm^2 \cdot V^{-1} \cdot s^{-1}$. However, in the subsequent measurement process with different illumination times, it was discovered that μ_{sat} began to slowly and slightly decrease to μ_{sat} (@ t=10 min) = 0.250 $cm^2 \cdot V^{-1} \cdot s^{-1}$

During the process of 532 nm illumination, varying the illumination time revealed a slight enhancement in the performance of the S-DNTT-10-based OTFT, as indicated by changes in μ_{lin} and μ_{sat}. In contrast, under 633 nm illumination, the device exhibited stable performance, with μ_{lin} and μ_{sat} remaining essentially unchanged. This suggests that, due to the disorder in the arrangement of S-DNTT-10 molecules during thin-film deposition, the HOMO and LUMO energy levels were broadened, narrowing E_g. As a result, some regions of the material responded to the 532 nm incident light, which is closer to 336.04 nm, generating a certain concentration of photo-generated carriers and slightly enhancing device performance.

Based on the extracted effective field-effect mobility, the results suggest that under the illuminations of 532 nm and 633 nm, they exert certain influences on the performance of the S-DNTT-10-based OTFT; however, the changes are extremely small and do not give rise to obvious variations in the device's performance. Hence, it is hypothesized that employing 532

nm and 633 nm for in-situ Raman spectroscopy measurements on the S-DNTT-10-based OTFT would not significantly impact the device's performance or induce additional error effects on the experimental results.

3.5 Experimental S-DNTT-10-Raman spectrum

This section presents and discusses the experimental non-resonant Raman spectra of the S-DNTT-10 thin film, covering various film thicknesses and different excitation wavelengths. It was observed that the low molecular concentration of S-DNTT-10 due to low film thickness resulted in a low signal-to-noise ratio in the Raman spectra. To address this issue, the Raman signal was effectively enhanced by depositing gold nanostructures on the surface of S-DNTT-10, thereby creating a SERS effect.

3.5.1 Laser wavelength effect on S-DNTT-10 Raman spectrum

Figure 3.9 (a) depict the 700 nm S-DNTT-10 thin-film thermally deposited on the SiO_2 layer under magnifications of 100× within the optical imaging system of the Raman spectrometer. It showed that a heterogeneous mixture of bright and dark areas was manifested on the surface of S-DNTT-10, signifying that its surface exhibits a certain degree of roughness and disparate reflection capabilities for incident light.

In order to exhibit the non-resonant Raman signal of S-DNTT-10 and observe the wavelength of excitation light sources affecting Raman scattering signal of S-DNTT-10. Considering that the photon energy E_{ph} is related to its own frequency ν as $E_{ph} = \hbar\nu$, this implies that 532 nm, 633 nm, and 785 nm possess different photon energies, namely E_{ph} (532 nm) ≈ 2.33 eV, E_{ph} (633 nm) ≈ 1.96 eV, and E_{ph} (785 nm) ≈ 1.58 eV. This necessitates the incidence of the same number of photons of different wavelengths onto the identical S-DNTT-10 thin-film area. Consequently, different illumination times were set for these three different wavelengths of excitation light sources, which are 20 s, 17 s, and 14 s, respectively. In addition, the grating number is 300/mm.

Figure 3.9 (b) shows the Raman scattering spectra within the range of 1000 - 1700 cm^{-1} for a 700 nm S-DNTT-10 thin film under various excitation wavelengths, all with comparable incident photon numbers. It is evident that the 532 nm incident light produces a more intense Raman scattering signal compared to 633 nm and 785 nm. As the incident wavelength increases, the intensity of the collected Raman signal gradually decreases. This is because the intensity of Raman scattering is related to the wavelength of the incident light. For non-resonant Raman scattering, the intensity is typically inversely proportional to the fourth power of the incident

wavelength λ_0, $I_R \propto \frac{1}{\lambda_0^4}$,[193]. Thus, the shorter the wavelength (higher energy) of the incident light, the stronger the Raman scattering signal. Under 532 nm excitation, a high-intensity Raman signal is collected, and distinct Raman-shift peaks are clearly visible. According to the previous DFT calculations shown in **Figure 3.4**, these peaks represent different molecular vibration modes.

The aforementioned results imply that the excitation light source with a wavelength of 532 nm is more appropriate for inducing the Raman signal of the S-DNTT-10 material in this study.

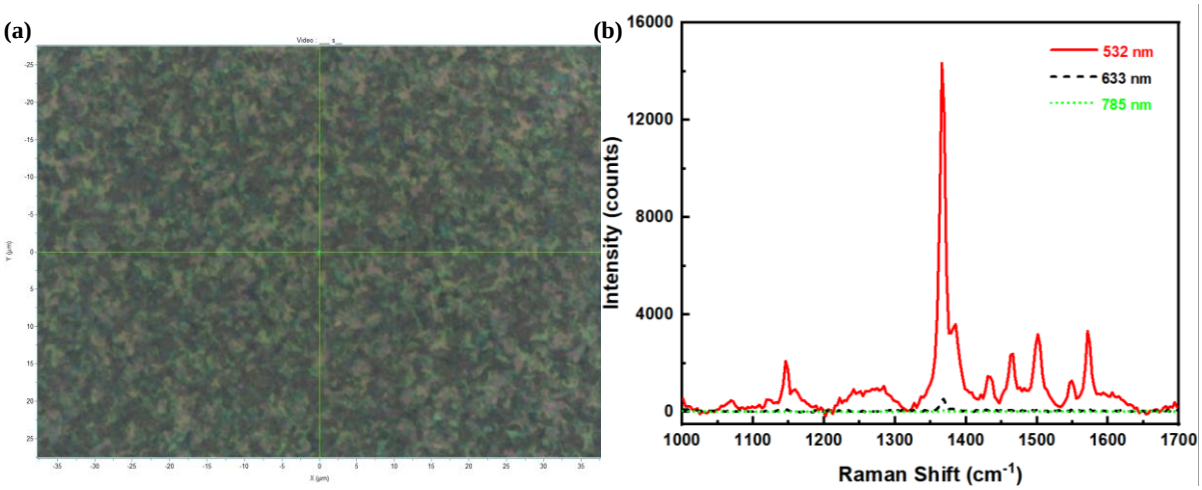


Figure 3.9 (a) The 700 nm S-DNTT-10 thin-film depositing on 89 nm SiO_2 modified with HMDS. (b) The non-resonant Raman spectrum of S-DNTT-10 under 532nm, 633 nm and 785 nm.

3.5.2 Thin-film thickness effect on S-DNTT-10 Raman spectrum

In the previous results, not only were the Raman scattering spectra of S-DNTT-10 presented, but it was also found that the 532 nm excitation source has a higher Raman scattering efficiency for S-DNTT-10. The intensity of Raman scattering is influenced not only by the wavelength of the excitation source but also by the concentration and physical state of the sample (e.g., solid, liquid, or gas), assuming no self-absorption by the sample. Generally, the higher the molecular concentration of the sample, the stronger the Raman scattering signal.

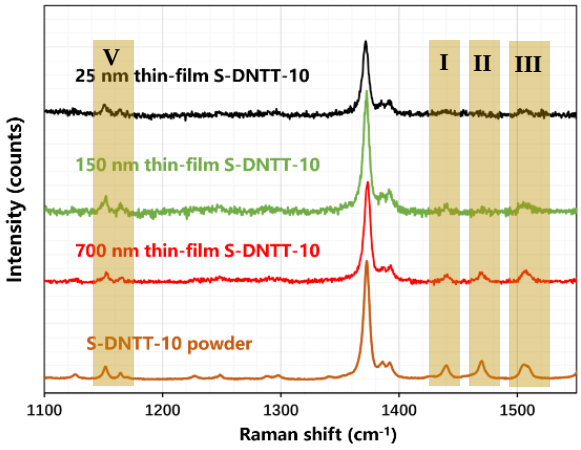


Figure 3.10 The S-DNTT-10 non-resonant Raman spectrum under different states.

Figure 3.10 shows the Raman spectra of S-DNTT-10 with various thicknesses under 532 nm excitation: 25 nm, 150 nm, 700 nm, and S-DNTT-10 powder. These represent the measured molecular concentration of S-DNTT-10 interacting with incident photons from low to high. It was observed that as the thickness of the S-DNTT-10 thin film increases, the signal-to-noise ratio of the Raman spectra improves. This is evident from the fact that Raman scattering peaks, initially obscured by noise in the low-concentration spectra, become more pronounced as the thickness increases, making the Raman signals more distinct, as seen in regions **I, II**, and **III** in **Figure 3.10**. In the low-concentration spectra, such as that of the 25 nm S-DNTT-10 film, no obvious Raman peaks were detected in these three regions. However, as the concentration of S-DNTT-10 molecules increases, the Raman peaks in these regions become increasingly prominent. Nevertheless, the signal-to-noise ratio of some Raman peaks is not significantly affected by the concentration of S-DNTT-10 molecules, as in the case of the Raman peak in region **V**. Although the curve for the 25 nm film is not as smooth as those for the 700 nm film or powder, it still shows a distinct Raman signal.

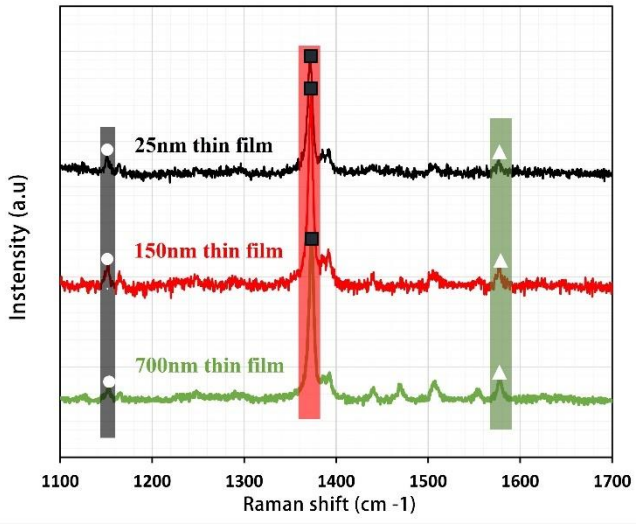


Figure 3.11 The non-resonant Raman spectrum with three peaks marked with different geometric symbol (●, ■, and ▲).

Additionally, since the thicker thin films of S-DNTT-10 were thermally deposited on the OTFT devices under the vacuum environment, approximately 10^{-7} Pa. The deposition rate of 150 nm-thick at 0.5 Å/s was equivalent to that of 25 nm-thick, while the rate of 700 nm-thick was 0.1 Å/s. Consequently, it was proposed that a variance of Raman shift occurred in the Raman spectrum of S-DNTT-10 thin film with different thicknesses. To distinctly observe the distinctions, three peaks were designated by different labels (●, ■, and ▲) as shown in **Figure 3.11**, and the shift information was presented in **Table 3.2**. In the table, the acquired peak-frequency in 25 nm thin film displayed a relatively minor blue or red shift compared with the thicker S-DNTT-10 thin films. Regarding this effect, it was conjectured that there was an influence of the deposition rate of S-DNTT-10 thin film and the thickness on the Raman scattered signal. Since **Ref [**194**]** suggested modifying the molecular orientation in the DNTT thin film to enhance the OTFT performance through the lower deposition rate, and it was indicated that the Raman signal could be affected by the thickness of the S-DNTT-10 thin-film due to alterations in the interaction of S-DNTT-10 molecules.

Table 3.2 The position of marked peaks under different thickness of S-DNTT-10 thin-film.

	25 nm thin-film	**150 nm thin-film**	**700 nm thin-film**
Peak-● (cm^{-1})	1151.21	1151.66	1152.12
Peak-■ (cm^{-1})	1373.03	1372.15	1373.46
Peak-▲ (cm^{-1})	1578.19	1577.33	1577.76

The aforementioned results demonstrated that with regard to S-DNTT-10 material, the signal-noise-ration in the corresponding Raman spectrum is affected by concentration of measured molecules. Moreover, we observed that the position of Raman-shift peaks S-DNTT-10 material is changed by external factors, such as deposited rate and the utilized thickness of S-DNTT-10 thin-films. This indicates that these factors might influence the molecular vibrations and intermolecular interactions of S-DNTT-10, and such alterations may potentially exert an influence on the charge transport properties within the S-DNTT-10 thin films.

Herein, we would like to talk about one proposal. According to result in **Table 3.2**, we think that it can evaluate whether or not the S-DNTT-10 thin-film can perform well intrinsic charge transport characteristics based on the position of Raman-shift band. It supposes that initially we fabricate S-DNTT-10 thin-film in which molecular orientation is vertical to the substrate since its direction is beneficial to charge transport, and it possesses the excellent order molecular arrangement. Subsequently, to measure the Raman spectrum as a reference standard. And based on results that the degree of derivation of Position-Raman-shift bands in other deposited S-DNTT-10 thin-film with the same thickness versus the reference, it can characterize the order or disorder molecular arrangement, which can be used to indirectly estimate the charge transport characteristics.

3.5.3 Surface Enhanced Raman Scattered effect at S-DNTT-10

In the previous section, the Raman spectra of S-DNTT-10 thin films of varying thicknesses were presented. It was found that when the film is thin, with a low molecular concentration, the signal-to-noise ratio decreases, and the intensity of some Raman peaks weakens, with some signals even obscured by noise. While increasing the thickness of the S-DNTT-10 film improves the Raman signal, it negatively impacts the performance of S-DNTT-10-based OTFTs. Specifically, in TCBG devices, a thicker organic layer increases contact resistance, hindering charge transport. Therefore, the Surface-Enhanced Raman Scattering (SERS) effect is proposed to enhance the Raman signals of S-DNTT-10 molecules [195]. In this section, gold nanostructures are used to induce the SERS effect in S-DNTT-10 molecules. The gold both enhances the Raman signal and serves as electrodes of the OTFT, facilitating the study of the relationship between charge transport and molecular vibrations. This approach lays the foundation for future research on the impact of bias stress on electrical performance.

3.5.3.1 Gold nanostructures deposition

To increase the Raman signal of thin-film S-DNTT-10 we plan to induce SERS. For acheveing it, we must have a nanostructured metal on S-DNTT-10 surface. But initially it is required to estimate if the thermal deposited nano-scale Au thin-film could form nano-structures.

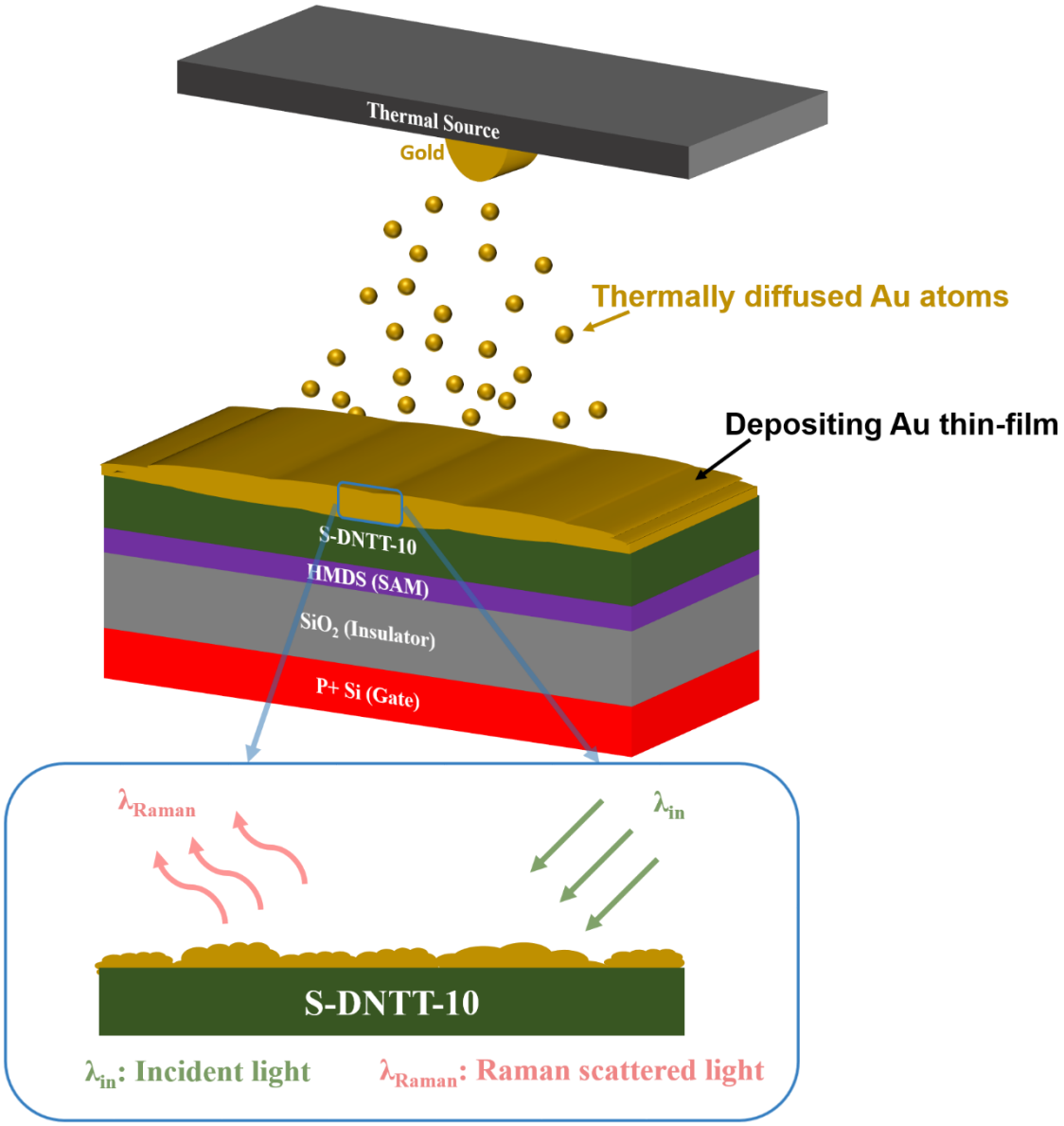


Figure 3.12 The schematic representation of Au nanostructure depositing on S-DNTT-10 thin-film.

Figure 3.12 illustrates the process of forming a gold film on the surface of the S-DNTT-10 layer through thermal deposition. The proposed method involves using Physical Vapor Deposition (PVD) to deposit gold atoms onto the S-DNTT-10 thin film, creating a nanostructured gold film. While silver (Ag) is also an excellent material for inducing the SERS effect, its chemical stability is lower than that of gold, making it prone to oxidation in air compared to Au material. Post-annealing at high temperatures is a common method for forming

metal nanostructures in thermally deposited films. However, since the substrate is composed of S-DNTT-10 molecules, high-temperature annealing could damage the molecules and lead to material degradation. Therefore, the gold nanostructures are formed solely by depositing nano-scale Au thin films through thermal deposition.

Firstly, an undertaking was initiated to deposit gold films of nanoscale thickness on the surface of SiO_2 at a deposition rate of 1.0 Å/s, as depicted in **Figure 3.13 (a)**, with the objective of observing whether such a rate could engender nanostructures. Au thin-films of different thicknesses were thermally deposited by PVD through a 4×5-shadow-mask. We use aluminum (Al) to cover the square-holes on the mask, as shown in **Figure 3.13 (b). Figure 3.13 (c)** exhibits the different gold films thermally deposited on the surface of SiO_2. From left to right, the gold films in each column are 1 nm, 3 nm, 5 nm, and 6 nm, respectively. It was approximately ascertained that they manifested distinct colors, and the greater the thickness, the brighter the color.

To confirm that the gold films fabricated at a deposition rate of 1.0 Å/s possess nanostructures, SEM nano-characterization was employed to examine the morphology of the gold films. The results, shown in **Figure 3.13 (d)-(g)**, present SEM images of four different thicknesses of Au films—1 nm, 3 nm, 5 nm, and 6 nm—at 12000× magnification. The insertion is that the corresponding optical images under 10× objective lens. And it was hypothesized that it might be attributed to the fact that the gold films of different thicknesses thermally deposited on the SiO_2 surface formed nanostructures of different geometric magnitudes, resulting in different optical responses to incident light.

It was observed that, despite the absence of post-annealing treatment after thermal deposition, the films did not form continuous layers but rather appeared as irregularly shaped nanoparticles. Additionally, it was noted that the average size of the nanostructures tends to increase with the thickness of the deposited Au film. The aforementioned results indicate that depositing nanoscale gold films on the surface of SiO_2 at a deposition rate of 1.0 Å/s through the PVD method, without undergoing post-annealing treatment. It indicated that this approach can create Au nano-structures on S-DNTT-10 thin-film.

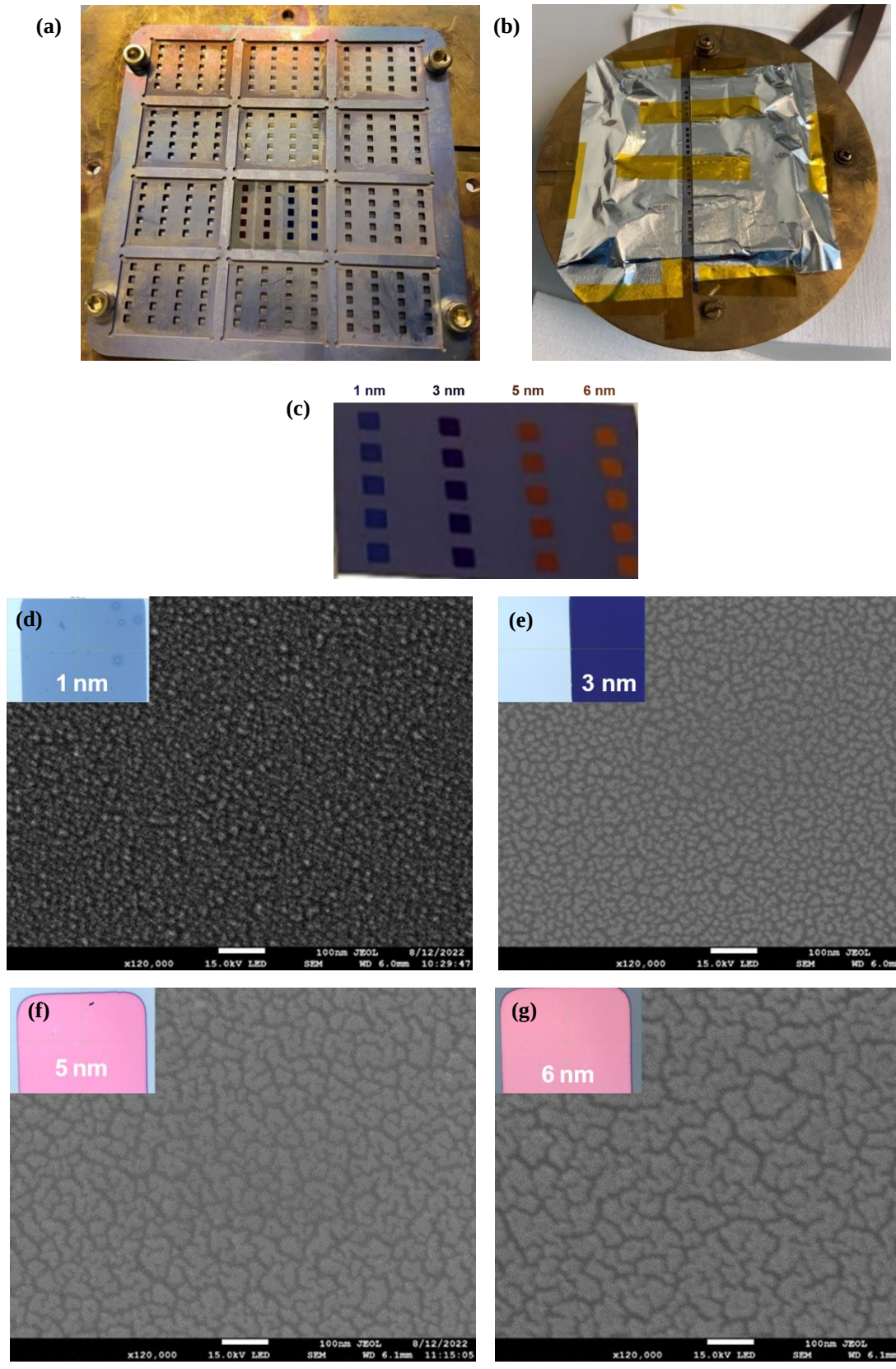


Figure 3.13 (a) The shadow mask for depositing Au nano-structures, (b) depositing different Au nano-structures on the same substrate by using aluminum to covering other squares, (c) the fabricated samples. The SEM with 120000 times for the corresponding structures with insertion of optical images; (d) 1 nm, (e) 3 nm, (f) 5 nm and (g) 6 nm Au thin-films.

3.5.3.2 Experimental Surface Enhanced Raman Scattered spectrum of S-DNTT-10

We have deposited nanoscale gold films on the surface of SiO_2 at a deposition rate of 1.0 Å/s and successfully achieved gold nanostructures without high-temperature post-annealing treatment. The objective is to deposit gold nanostructures on the surface of the S-DNTT-10 thin-film to have a SERS effect. Thus, regarding the thickness of the gold thin-film, we need to simultaneously consider two aspects: (1) Forming nanostructures that can stimulate the SERS phenomenon and enhance the Raman scattering signal of S-DNTT-10 molecules; (2) As electrodes, enabling the S-DNTT-10-based OTFT to operate normally. To accomplish this, we attempted to deposit Au thin-film with thicknesses of 3 nm, 5 nm, 10 nm, and 20 nm on the surface of the S-DNTT-10 thin-film at a deposition rate of 1.0 Å/s under the vacuum environment through the PVD method with aim of simultaneously reaching the above requirements.

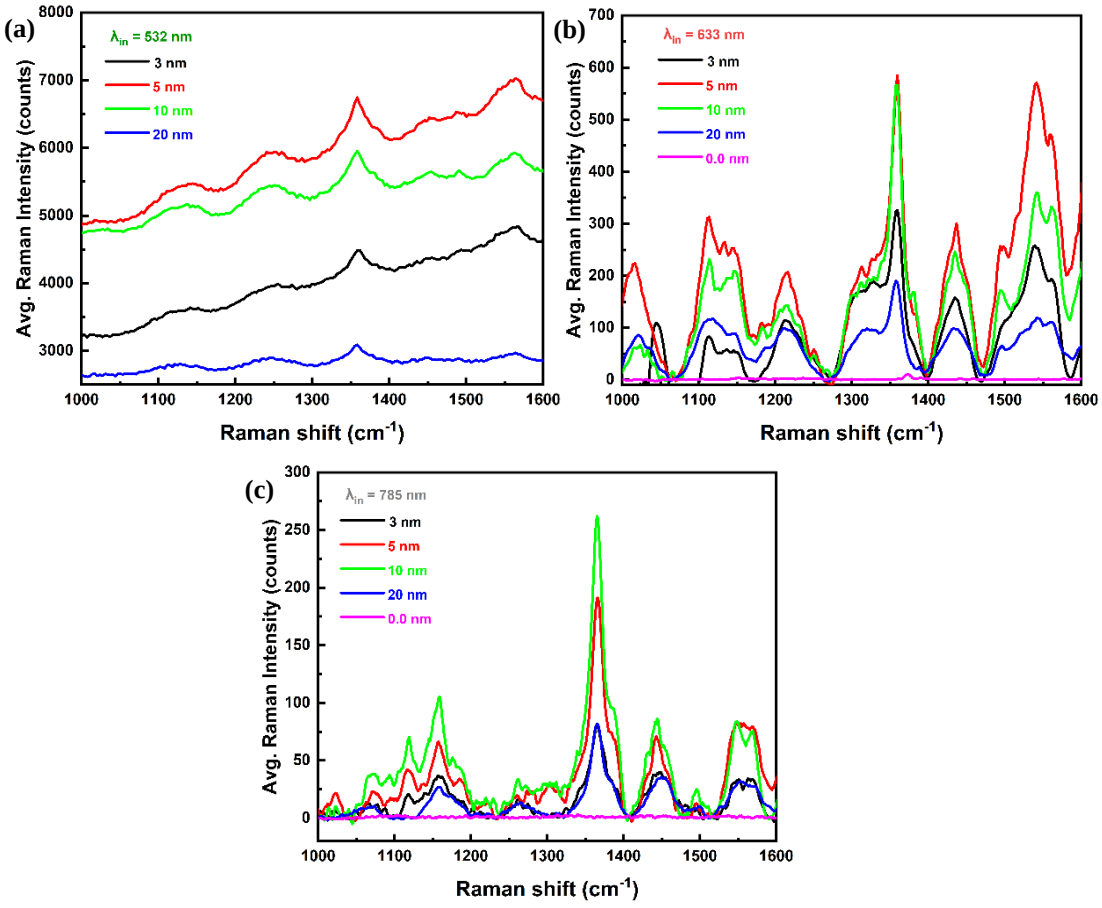
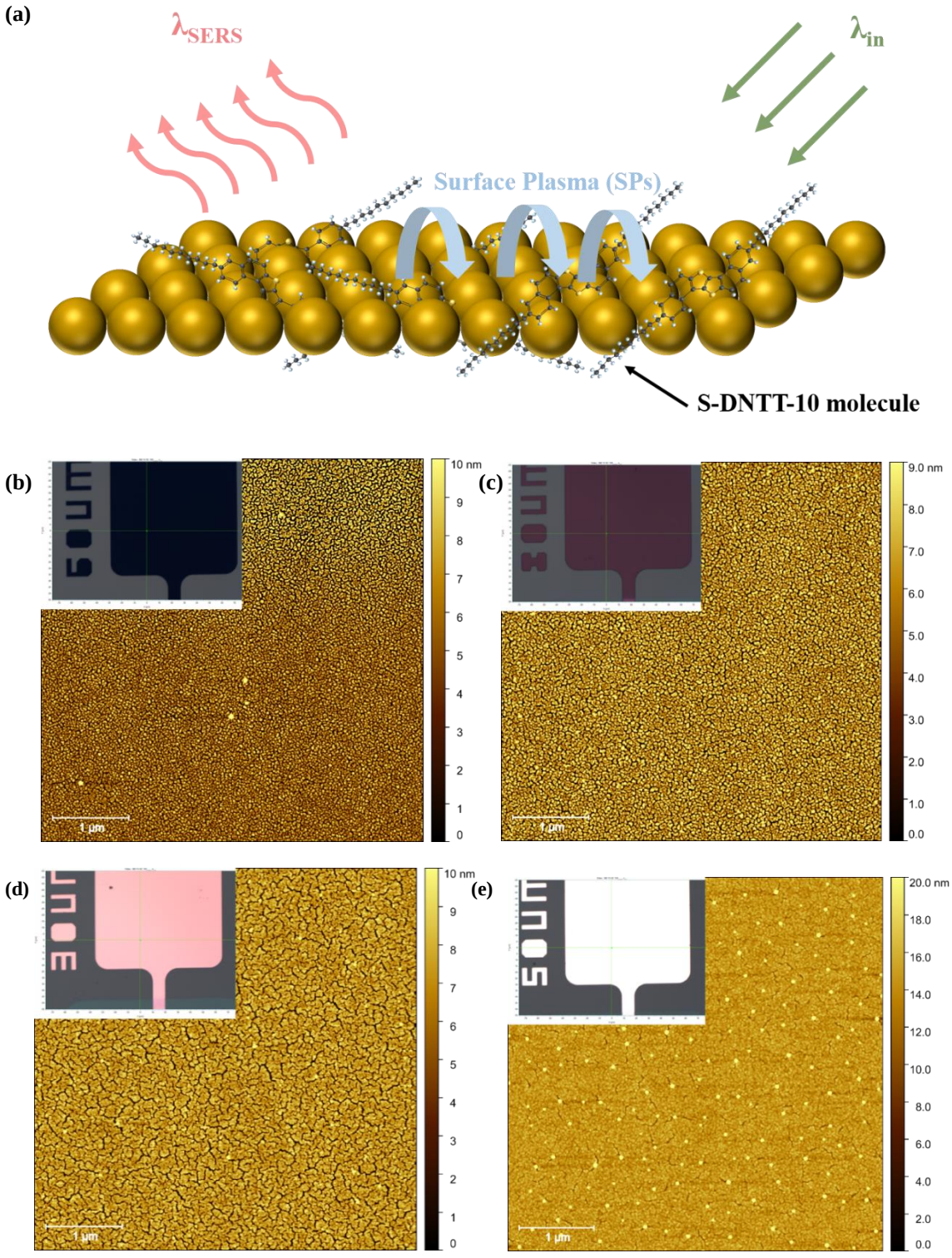


Figure 3.14 The SERS spectrums for S-DNTT-10 molecules depositing by different thickness of Au thin-films under lasers of (a) 532 nm, (b) 633 nm with baseline-treatment and (c) 785 nm with baseline-treatment.

Figure 3.14 (a) shows the spectrum induced under 532 nm, which exhibited great background noise. This suggests that 532 nm may not be suitable for inducing the SERS effect

in Au nanostructures. Additionally, reference [195] confirms that 532 nm is not appropriate for SERS applications. Therefore, the following research focuses on 633 nm and 785 nm wavelengths. To ensure consistency in the number of incident photons, based on the relationship that single photon energy reduced with increased light wavelength, acquisition times were set at approximately 17 seconds and 14 seconds for the 633 nm and 785 nm lasers, respectively, each at the same power. As depicted in **Figure 3.14 (b)** and **(c)**, effective Raman signal induction, with smoothing and baseline correction, was observed under 633 nm and 785 nm lasers. This wavelength-dependent Raman signal induction aligns with existing literature, indicating varying Raman signal intensities for different incident wavelengths on Au-film/S-DNTT-10 structures. Notably, '0 nm' in these figures represents the Raman signal from the pure 25 nm S-DNTT-10 thin film without Au deposition. To ensure reliability, multiple devices with the same Au thin-film thickness were fabricated, and Raman signals were collected from the source of each device. The Raman intensities for each thickness were averaged across 10 randomly measured positions to calculate the *Average Raman Intensity* (**Avg. Raman Intensity**). The employment of 633 nm and 785 nm wavelengths led to enhanced Raman signals compared to the pure S-DNTT-10 thin film. This enhancement was obvious from the higher intensity and signal-to-noise ratios in the Raman-Shift peaks showing in **Figure 3.14 (b)** and **(c)**, indicating the successful implementation of strengthening Raman signal by SERS.

Figure 3.14 (b) and **(c)** show how Raman shift intensity varies with the thickness of Au thin films under 633 nm and 785 nm excitation, respectively. In **Figure 3.14 (b)**, it was observed that the intensity in several bands, such as 1100-1200 cm^{-1}, 1300-1400 cm^{-1}, and 1500-1600 cm^{-1}, depended on the Au film thickness. The trend revealed that intensity first increased and then decreased as the Au film thickness increased from 3 nm to 20 nm, with peak intensity observed at 5 nm, indicated by the red solid line. In **Figure 3.14 (c)**, the highest intensity across most of the spectrum was found at a thickness of 10 nm. However, within the 1510-1580 cm^{-1} range, the intensities at 5 nm and 10 nm were nearly identical, showing no significant difference. Despite this, the 10 nm thickness appeared to be optimal for enhancing the Raman signal under 785 nm excitation. These observations suggest that a 5 nm Au film thickness is generally optimal for enhancing Raman signals under 633 nm laser excitation. This finding is crucial for SERS studies of S-DNTT-10 materials, as it identifies the appropriate Au film thickness for optimal signal enhancement.


(a)
λSERS
λin
Surface Plasma (SPs)
S-DNTT-10 molecule
(b)
10 nm
9
8
7
6
5
4
3
2
1
0
1 µm
(c)
9.0 nm
8.0
7.0
6.0
5.0
4.0
3.0
2.0
1.0
0.0
1 µm
(d)
10 nm
9
8
7
6
5
4
3
2
1
0
1 µm
(e)
20.0 nm
18.0
16.0
14.0
12.0
10.0
8.0
6.0
4.0
2.0
0.0
1 µm

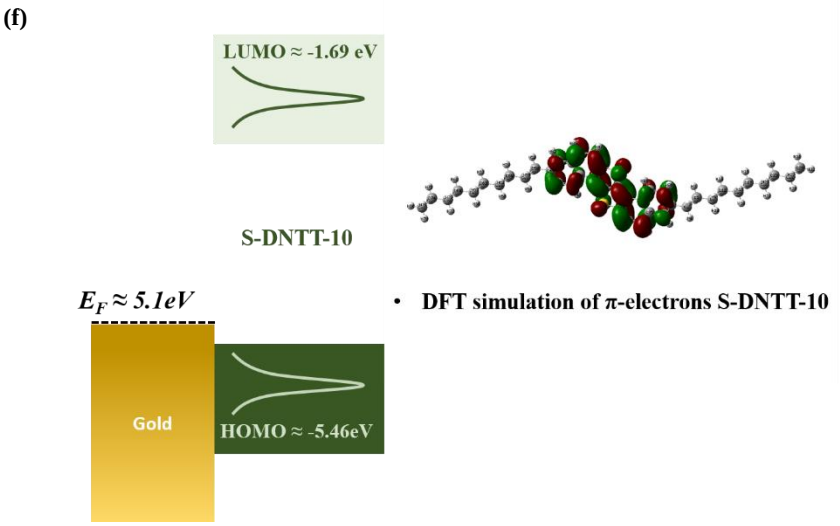


Figure 3.15 (a) The schematic representation of fundamental surface plasmas (SPs) mechanism of SERS. The AFM topography with top-view optical-image in different thickness of Au thin-films: (b) 3 nm, (c) 5 nm, (d) 10 nm and (e) 20 nm. (f) The diagram of Fermi level of gold and molecular orbitals of S-DNTT-10 molecule.

In this case, we briefly explored the fundamental mechanisms underlying Surface-Enhanced Raman Scattering (SERS). It recognized two primary theories to explain SERS effect: The Enhanced Electromagnetic (EM) mechanism in Section 3.2.2.1, involving the induction of surface plasmons (SPs) showing in **Figure 3.15 (a)**, and the chemical mechanism. Both theories gained significant acceptance in the scientific community[184,196]. Atomic Force Microscopy (AFM) measurements were carried out to obtain the topography on variable Au thicknesses (**Figure 3.15 (b)-(e)**). The average size of Au nanostructures is obtained by using the software **Gwyddion**. Within a consistent measurement area of 5×5 μm, the average grain sizes for 3 nm, 5 nm, 10 nm, and 20 nm thicknesses were found to be approximately 31.82 nm, 41.39 nm, 61.53 nm, and 122.4 nm, respectively. Correspondingly, the density of Au nano-structures is determined to be 388.6/ μm², 238.1/μm², 51.84/μm², and 1.72/μm². A notable observation was the variation in Raman intensity with different nanostructure thicknesses. This variation suggested a correlation between the degree of induced SPs and the nanostructure size. The insertions of optical images showing in **Figure 3.15 (b)-(e)** further confirmed these findings, revealing distinct colorations on the surfaces for each specific thickness. This suggests that the size of the deposited Au nanostructures was crucial in modulating the optical response to external light. It was inferred that Au nanostructures of varying sizes can excite SPs under incident light at certain wavelength bands. This excitation led to reduced light reflectivity on the surface for these bands, while wavelengths that do not effectively excite SPs exhibit higher reflectivity, under white light. Additionally, combining results from **Figure 3.14 (b)** and **(c)**

showed that Raman intensity varies with both the wavelength of incident light and the thickness or average size of Au nanoparticles. The analysis indicated that the extent of SERS effect was influenced by the geometric parameters of the Au nanostructures, especially their ability to affect SPs. This phenomenon was consistent with findings from related research, as cited in references [184,185,196–198]. Consequently, the study suggests that the observed SERS effect was primarily due to the EM mechanism. Furthermore, the possibility of a chemical mechanism, such as charge transfer, cannot be discounted. This assertion was based on the alignment of Fermi energy level of gold (at ~ -5.1 eV from the vacuum level) with the molecular orbital (MO) levels of S-DNTT-10, specifically the LUMO at ~ -1.69 eV and the HOMO at ~ -5.46 eV, as **Figure 3.15 (f)** illustrated. This alignment facilitated electron excitation in gold to the LUMO, leading to the emission of scattered light when these electrons return to the Fermi energy level.

The Raman scattered signal is generally assumed to be independent of the excitation wavelength. However, this study identified deviations from this norm. Specifically, a comparison of the Raman spectrum of a 700 nm S-DNTT-10 thin film excited by a 532 nm laser revealed significant discrepancies in the SERS spectrum, as shown in **Figure 3.16 (a)**. The SERS spectrum displayed a broader high-intensity range (1300-1420 cm^{-1}) compared to the narrower band (1350-1375 cm^{-1}) in the conventional Raman spectrum. Additionally, several distinct bands in the Raman spectrum appeared to merge into a single, wider band in the SERS spectrum. For instance, two peaks in the 1200-1300 cm^{-1} range of the Raman spectrum coalesced into a broader peak in the SERS spectrum. The broadening and merging of bands are attributed to molecular structure changes caused by the deposition of the Au thin film on S-DNTT-10 molecules. This finding aligns with studies on the SERS effect of pentacene molecules using Au thin films, where spectral changes were linked to molecular alterations due to Au atom deposition [195,198].

In this study, DFT simulations also confirmed that adding a hydrogen atom to the pentacene molecule altered its molecular vibrations. Based on these findings, we propose that the thermal deposition of Au nanoparticles could penetrate and distort the S-DNTT-10 thin film, leading to disordered arrangements of S-DNTT-10 molecules [195,199]. To support this hypothesis, we conducted similar DFT simulations by introducing an additional hydrogen atom into the thiophene ring of the S-DNTT-10 molecule, as shown in **Figure 3.16 (c)**. **Figure 3.16 (b)** compares the theoretical Raman spectra of the normal S-DNTT-10 molecule (Normal DFT, black line) versus the modified molecule with an additional hydrogen atom (Disorder DFT, red line). The disorder DFT simulation highlighted key differences, including a reduced peak height

in the 1350-1400 cm^{-1} range and a peak shift around 1450-1530 cm^{-1}. Notably, there was a tendency for two peaks in the 1350-1400 cm^{-1} range to merge into a broader band. The study also observed peak shifts when comparing the SERS spectrum with the spectrum of the 700 nm S-DNTT-10 thin film. Specifically, a peak at roughly 1373.03 cm^{-1} in the 700 nm thin film shifted to about 1370.96 cm^{-1} in the SERS spectrum. This shift, notably towards the left in the SERS spectrum, aligns with similar variations reported in the research studies concerning the SERS effect [189,193]. Their results shown that changes in Raman spectrum of pentacene deposited with Au nano-structures under excited SERS source. Since the Raman scattered correlated with changes in molecular polarizability, directly linking molecular structure to the Raman signal. Hence, the vibrational modes suggested that Au nanostructures mainly cause deformations in thiophene rings or alkyl chains. Consequently, thermally deposited Au nanoparticles likely induced distortions in S-DNTT-10 molecules, especially near the interfacial layers of the OSC thin films and electrodes like **Figure 3.17** depicting [200]. And it resulted in Raman spectrum changed, offering a plausible explanation for the observed shifts and highlighting the complex interaction between metallic nanostructure deposition and OSC molecular dynamics.

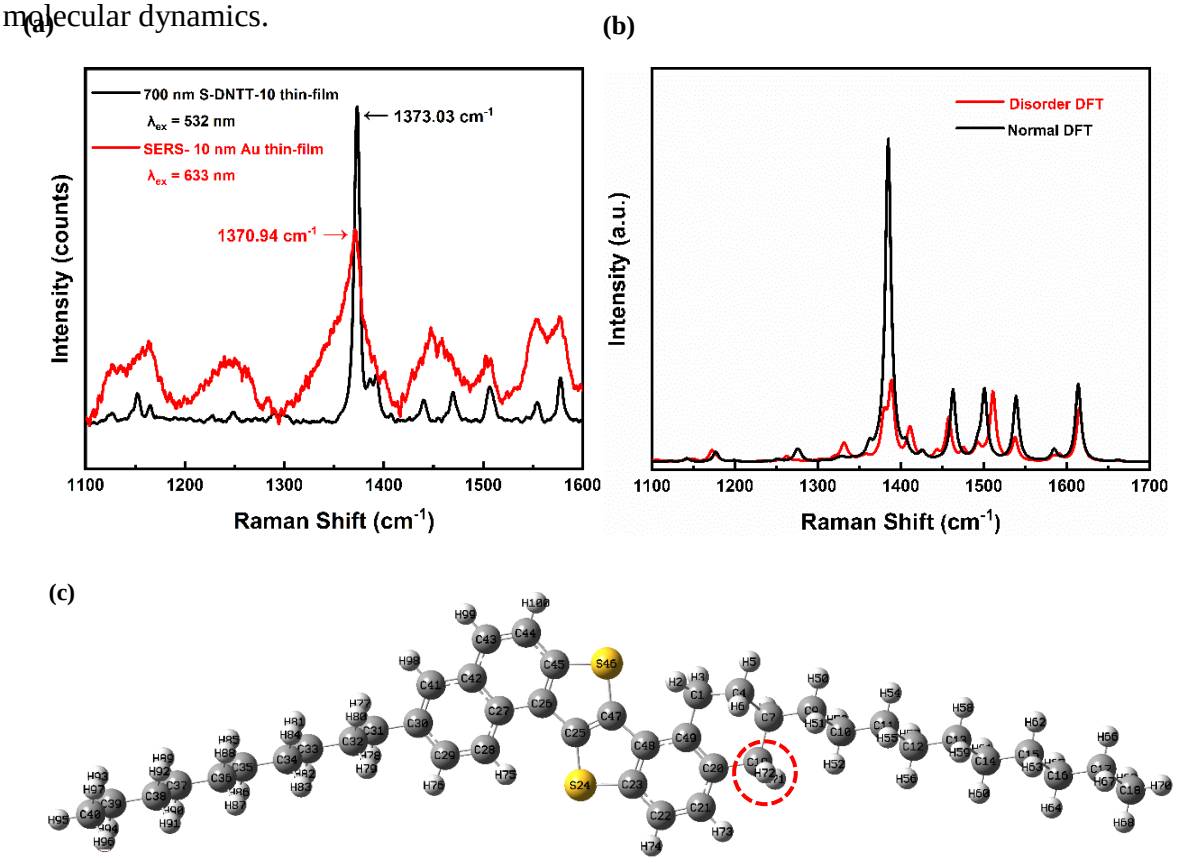


Figure 3.16 (a) The comparison of S-DNTT-10-SERS spectrum under 633 nm and S-DNTT-10-conventional Raman spectrum under 532 nm. (b) The comparison of simulated Raman spectrum of one

single S-DNTT-10 molecule and hybridized S-DNTT-10 molecule. (c)The hypothetical S-DNTT-10 hybridized with marked hydrogen molecule.

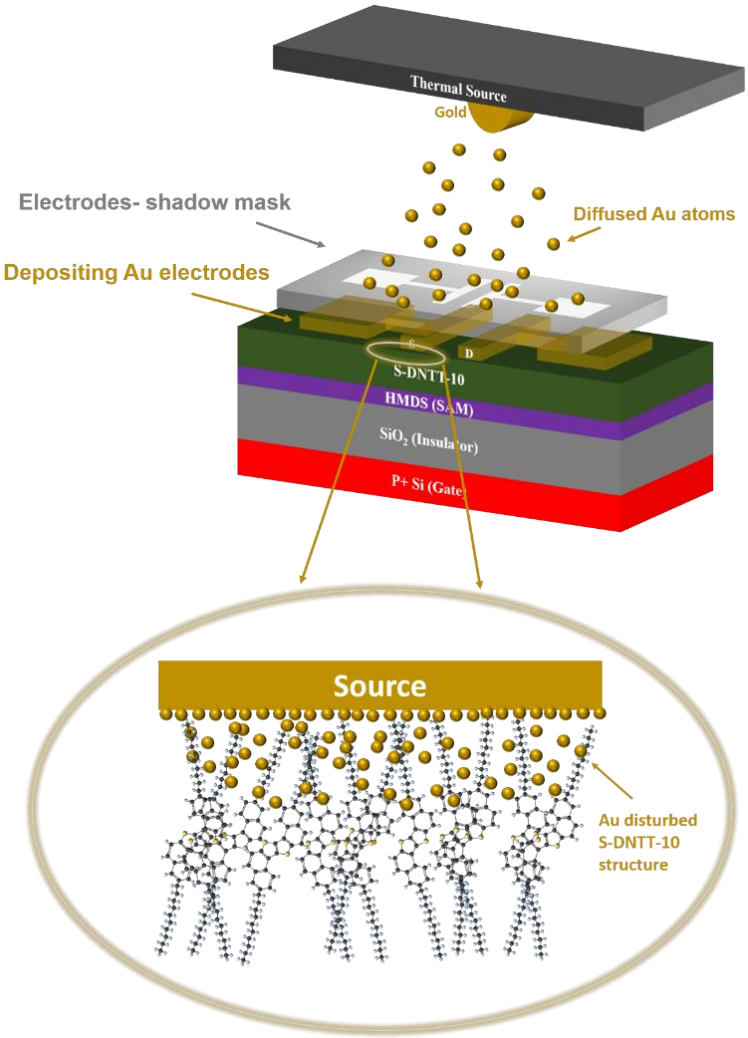


Figure 3.17 The schematic representation of Au atom potentially diffusing into S-DNTT-10 molecules.

The findings suggested that the differences observed in the SERS spectrum, compared to the Raman spectrum of the 700 nm S-DNTT-10 thin film, primarily result from the effects of Au thin film deposition. It was hypothesized that Au thin film deposition modified the molecular structure and vibrational dynamics of S-DNTT-10 molecules. These modifications were thought to cause the observed variations in the Raman scattering spectrum.

3.6 Conclusion

This chapter primarily investigates the molecular vibrations of S-DNTT-10, addressing gaps in the understanding of its material properties. Using DFT, we simulated the Raman spectra of S-DNTT-10, providing both the Raman scattering spectra and detailed insights into the molecular vibrations associated with different Raman modes. The findings show that the

molecular vibrations of S-DNTT-10 are mainly centered on the vibrations of the central thiophene ring and the combined vibrations of the thiophene ring and alkyl chains. Additionally, the DFT simulations provided the energy levels of the HOMO and LUMO and revealed the distribution of the π-electron wave function, which is crucial for understanding the charge transport characteristics of S-DNTT-10. Experimental Raman spectra of S-DNTT-10 were measured at different excitation wavelengths, revealing that the Raman scattering signal is influenced by the thickness of the S-DNTT-10 thin film. To enhance the Raman signal via SERS, an Au nanostructured thin film was deposited on the surface of the S-DNTT-10 film. This study provides valuable reference information for future detection of Raman scattering signals from S-DNTT-10 thin films.

4 Investigated on the influence of bias-stress effect on S-DNTT-10-based OTFTs via Raman scattered technique

4.1 Introduction

After decades of development, OTFTs gradually became the strong candidates commercial electronic applications [170,201,202]. However, the electrical stability of OTFTs for prolonged operation is crucial. In practice, as one OTFT operates continuously in the air environment, it inevitably encounters the influence of several parasitic factors. For instance, the applied electric field, joule heating, and the degradation of the OSC material.

In this chapter, we will explore the influence of bias stress (*BS*) effect on the electrical characteristics of Top-Contact-Bottom-Gate (TCBG) S-DNTT-10-based OTFTs in the air environment. During this process, we mainly exhibit one innovated proposal that we will execute multiple characterized methods to invesitage on the influence of BS effect on TCBG S-DNTT-10-based OTFT, including IV characteristics (seeing in Section 4.2), Kelvin probe force microscopy (KPFM) method (seeing in Section 4.2), DFT simulation (seeing in Section 4.3) and Raman scattered techniques that conventional Raman and SERS (seeing in Section 4.4). We think that not only it enables to characterize the changes in electrical performance which is correlating with affected molecular characteristics after BS effect, but also, it will exhibit the long-term electric field impacting on the charge injection and extraction efficiency by using KPFM method. It can further reveal the potential factor that mainly causes the degradation of the electrical performance of TCBG S-DNTT-10-based OTFT.

4.2 Bias stress effecting electrical characteristics of S-DNTT-10-based OTFT

Ensuring electrical stability under operational stress remains a challenge in OTFT technology [203–206]. This study investigated the *BS* effect, a key factor in the reduced electrical performance of S-DNTT-10-based OTFTs. The *BS* effect refers to the changes in device performance due to prolonged exposure to biased electric fields, a common scenario during real-life device operation.

In the experimental protocol, the OTFT device, with a channel length of 40 μm and a width of 1000 μm, was subjected to continuous operation for 8 hours. This operation was conducted in an ambient air environment, with both the U_{GS} and the U_{DS} set to -40 V, the results showing in **Figure 4.1** and **Table 4.1**. The experiment was structured to provide real-time insights into

the effect of electric fields on molecular characteristics and, by extension, on device performance.

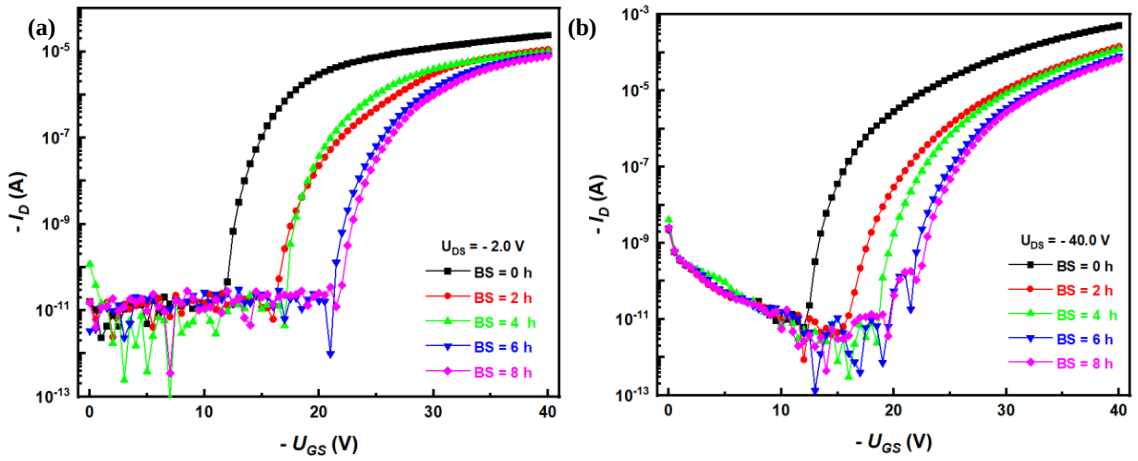


Figure 4.1 The transfer characteristics of the measured S-DNTT-10 OTFT under the before- and after-8 hours-*BS* effect. (a) Linear-mode (stressed U_{DS} = -2 V) and (b) saturation-mode (stressed U_{DS} = -40 V).

Table 4.1 The comparison of OTFT before and after 8 hours bias stressed (*BS*) effect.

Parameters	Before 8hours *BS*	After 8hours *BS*
μ_{lin} (U_{DS} = -2 V)	0.62 $cm^2 \cdot V^{-1} \cdot s^{-1}$	0.385 $cm^2 \cdot V^{-1} \cdot s^{-1}$
$U_{Th\text{-}lin}$ (U_{DS} = -2 V)	-20.3 V	-29.2 V
μ_{sat} (U_{DS} = -40 V)	3.842 $cm^2 \cdot V^{-1} \cdot s^{-1}$	1.03 $cm^2 \cdot V^{-1} \cdot s^{-1}$
$U_{Th\text{-}sat}$ (U_{DS} = -2 V)	-23.5 V	-28.8 V

Examination through I_D-U_{GS} characteristics, as shown in **Figure 4.1 (a)** and **(b)**, under constant biases of U_{DS} = -2 V and -40 V, respectively, with bias U_{GS} ranging from 0 to -40 V with the step of -0.5 V, elucidated a progressive decline in drain current over the *BS* duration of 0 to 8 hours. This phenomenon suggested a degradation in effective field-effect mobility over time. Quantitative analysis reveals a decrease in μ_{lin} from approximately 0.620 to 0.385 $cm^2 \cdot V^{-1} \cdot s^{-1}$ and a negative shift in threshold voltage ($U_{Th\text{-}lin}$) from -20.3 to -29.4 V; μ_{sat} diminished from about 3.842 to 1.03 $cm^2 \cdot V^{-1} \cdot s^{-1}$, accompanied by a negative threshold voltage shift ($U_{Th\text{-}sat}$) from -23.5 to -28.8 V. These findings are consistent with existing literature on the *BS* effect [203,204,206], highlighting the combined influence of reduced mobility and altered threshold voltage in contributing to the observed reduction in drain current.

4.3 DFT simulating the BS effect influencing S-DNTT-10 MOs

Given the unique molecular structure of S-DNTT-10, which features *S*-shaped central thiophene rings, it was initially hypothesized that this material would demonstrate enhanced

stability under electrical stress compared to other organic semiconductor (OSC) materials, as related research suggested that the curved molecular shape contributes to thermal stability. However, the experimental results contradicted this assumption, revealing a degradation in the *I-V* performance, as shown in **Figure 4.*1*** and **Table 4.1**. To thoroughly assess the effects of prolonged electric field exposure on the performance of S-DNTT-10-based OTFTs, we conducted in-depth investigations using Raman scattering and Kelvin probe force microscopy (KPFM). A comprehensive understanding of these mechanisms is crucial for developing effective strategies to mitigate the bias stress (BS) effect, thereby enhancing the long-term reliability and expanding the application potential of S-DNTT-10-based OTFTs.

Regarding the degraded performance, we hypothesize that this effect resulted from alterations in charge transport characteristics caused by prolonged exposure to the electric field. IT was supposed that charge transport properties in OSCs can be characterized by the hopping frequency, a critical parameter that depends on the spatial overlap of each valid energetic position of the transported state, as expressed in **Equation (1.7)**. This equation describes the hopping frequency (ω) and indicates that the predominant transport mechanism involves charge hopping at each localized state at room temperature [80,81]. It suggests that the transfer frequency of charges is correlated with the molecular orbitals (MOs) at each position within the OSC material. Since these MOs are significantly influenced by the energetic splitting resulting from the overlap of the p_z orbital in sp^2 hybridization, and it possibly enables to offer a view of the electronic structure of OSC molecules, therefore, we think it can estimate one relationship between the potentially changed energy level of MOs and charge transport under *BS* effect. It is reasonable to assume that a prolonged electric field could perhaps influence the MOs and subsequently the transfer rate by altering molecular characteristics in the thin films. In this investigation, density functional theory (DFT) simulations were used to explore the impact of electric fields on the MOs of S-DNTT-10, specifically the energy level of HOMO and LUMO.

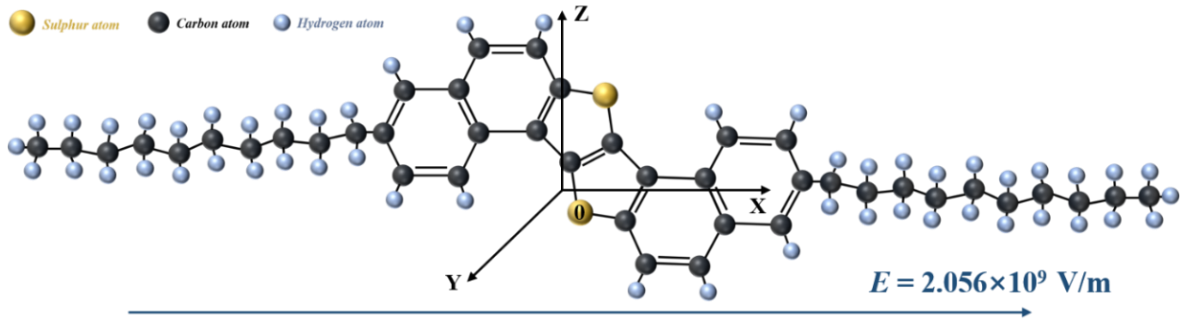


Figure 4.2 The schematic model of S-DNTT-10 molecule stressed electric field. The diagram of simulated molecular orbitals of S-DNTT-10. (Gaussian16. A. 03, DFT simulation with B3LYP functional method companied with the basis set of 6-311G (d, p)).

The key word in this DFT simulation of electrial field influencing S-DNTT-10-MOs that defining of an electric field was "**field = x + 40**", which denotes the orientation of the electric field along the X-axis with a strength of 0.04 atomic units (a.u.), equivalent to approximately 2.056×10^7 V·cm^{-1} (1 a.u.= 5.142206×10^9 V·cm^{-1}) showing in **Figure 4.2**. In this case, it is noted that the defined value of a.u. is referenced by the U_{GS} of -40 V stressing on 90 nm SiO_2. Considering the relative dielectric constant into SiO_2 (ε_r = 3.9), and the relationship of intensity of electrical field inside (E_{in}) and outside dielectric layer (E_{ex}) , $\varepsilon_r = E_{ex} / (E_{ex}-E_{in})$, the intensity should be approximately of 3.305×10^6 V·cm^{-1}. Additionally, the condition that $U_{GS} = U_{DS}$ of -40 V made OTFT operate into saturation state, and it induced parasite strong electric field around drain area due to the emergence of pinch-off regime [164]. To better simulate the influence of electric field on energy level of S-DNTT-10 MOs, we preferred to used higher value of atomic units. The simulation conditions employed the **B3LYP** functional method with the **6-311G (d**, **p)** basis set. The results showed slight modifications in the LUMO and HOMO levels compared with MOs affecting without electrical field, from -1.760 eV to -1.759 eV and from -5.428 eV to -5.429 eV, respectively. This suggests that the electric field might influence sp^2 hybridization, thereby affecting the HOMO and LUMO energy levels.

However, the observed changes were minimal, raising questions about the definitive impact of the electric field on the molecular structure of S-DNTT-10 and its charge transport characteristics. Several limitations of the DFT simulation in this context are noteworthy: (i) The *BS* effect, characterized by prolonged electric field application, has been experimentally shown to degrade the electrical performance of OTFTs. While the simulation elucidates the immediate impact of an electric field on molecular orbitals (MOs), it does not record the temporal dynamics and accumulated effects of extended field exposure on the molecular properties of S-DNTT-10. (ii) The simulation examines only a single molecule, failing to account for the complex interactions among molecules within an S-DNTT-10 thin film. These interactions can significantly influence the MOs, potentially leading to behaviors that differ from single-molecule predictions. Therefore, although the DFT simulation offers some theoretical insights into the impact of electric fields on the MOs of S-DNTT-10, it may not fully represent the long-term effects of electric fields on the molecular properties and electrical performance of S-DNTT-10-based OTFTs.

Previous studies have established Raman spectroscopy as a crucial tool for elucidating charge transport mechanisms and OTFT performance by probing the molecular characteristics of OSCs [184,191,195,198]. To further investigate this, particularly in assessing the *BS* effect

on S-DNTT-10-based OTFTs, a dual Raman spectroscopic approach was employed. This involved measuring the surface-enhanced Raman scattering (SERS) spectrum at the electrodes using 633 nm light to characterize changes in charge injection and extraction, and acquiring a conventional Raman spectrum from the channel using 532 nm light to examine molecular characteristics. The selection of 532 nm for channel analysis was based on its effectiveness in generating a stronger Raman signal from S-DNTT-10 molecules, as indicated by preliminary observations shown in **Figure 3.9 (b)**. This study aims to clarify the complex relationship between molecular structure, charge transport, and device performance under *BS* conditions.

The choice of electrode thickness is crucial, as it directly affects the electrical characteristics of OTFTs and, consequently, the accuracy and validity of Raman spectroscopy analysis. While 5 nm thick Au electrodes provided the highest Raman signal intensity, they resulted in instability in OTFT output. To maintain consistent and stable OTFT operation along with a strong Raman signal, 10 nm Au electrodes were used.

4.4 Explored the bias-stress effect by Raman scattered technique

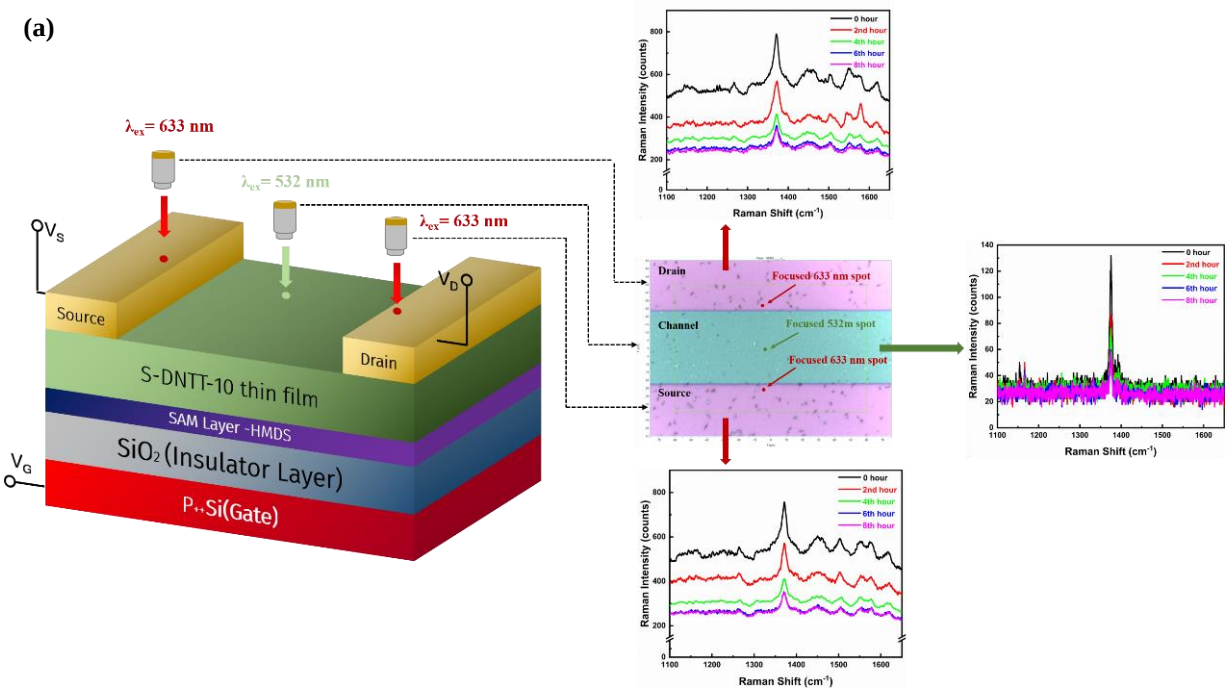
To further elucidate the molecular basis of this degraded performance, additional Raman spectroscopic measurements were conducted. The schematic overview presented in **Figure 4.3 (a)** outlines the approach for correlating the observed electrical changes with molecular dynamics, providing a comprehensive understanding of the *BS* effect from both electrical and molecular perspectives.

DFT simulations of non-resonant Raman spectrum of a single S-DNTT-10 molecule showing in Section 3.3, revealed that the vibrational modes are primarily associated with the deformation of the thiophene rings. Additionally, the simulated distribution of π-electrons suggests that the thiophene ring is closely linked to the charge transport properties in S-DNTT-10 material. We believe that the observed reduction in effective field-effect mobility under continuous electric field stress indicates significant changes in charge transport characteristics, directly related to the behavior of π-electrons within the S-DNTT-10 molecules. This implies that the impact of the electric field on the electrical performance of S-DNTT-10-based OTFTs is due to intra-molecular dynamics, which significantly influence the distribution and activity of π-electrons. As indicated by the simulations, these intra-molecular effects are manifested through changes in the central thiophene rings. [199,207]

4.4.1 SERS at S & D Au electrodes

Surface-enhanced Raman scattering (SERS) spectra were initially acquired at predetermined positions after each 2 hours of continuous device operation, while conventional Raman mapping was performed on the channel with the device remaining active. This approach was based on the hypothesis that removing the biased electric field could lead to reversible changes in the molecular structure of S-DNTT-10 molecules, potentially obscuring the true impact of electric field stress. Therefore, maintaining the device in an active state during Raman measurements was essential for preserving the accuracy of data regarding electric field-induced molecular modifications. After each Raman mapping session, the device characteristics were evaluated through transfer characteristics I_D-U_{GS}, with U_{GS} varying from 0 to -40 V.

Given these insights, future analyses will be directed towards the Raman spectral ranges of 1100-1650 cm^{-1} corresponding to the vibrational modes associated with thiophene ring deformation, respectively. These spectral ranges are critical in assessing the specific molecular changes induced by *BS*, offering a more targeted understanding of how prolonged electric field exposure influences the charge transport properties in S-DNTT-10-based OTFTs.



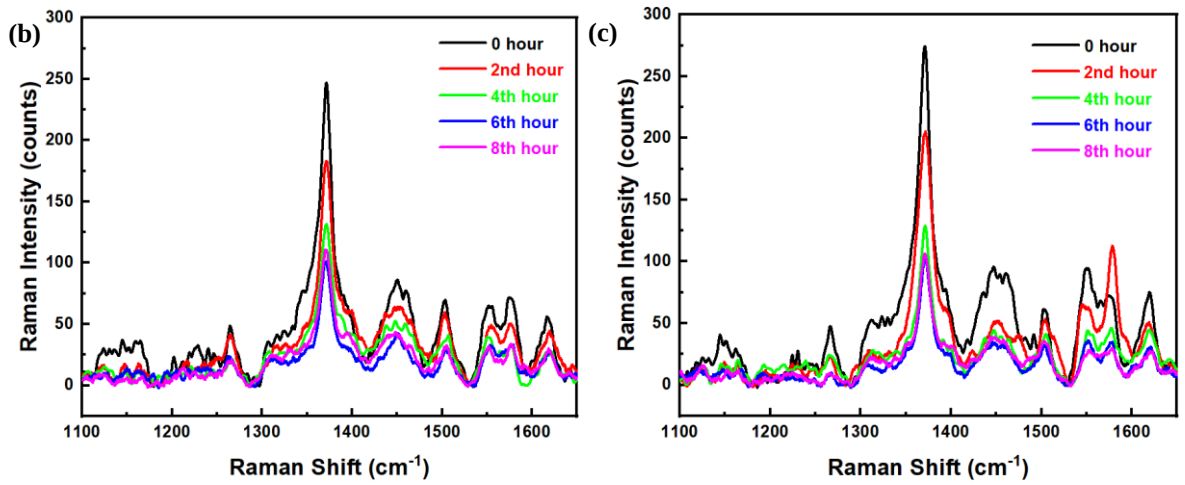


Figure 4.3 (a) The schematic representation of non-resonant Raman spectroscopy in channel and electrodes correlating with *I-V* measurement system in 8 hours-Bias Stressed. The related SERS spectrum using 633 nm at (b) source and (c) drain.

Figure 4.3 (b) and **(c)** respectively illustrate that the SERS spectrum with baseline treatments at the source and drain electrodes varied with *BS* time. At the source, the intensity of certain Raman-shift bands decreased as the device operated, such as those in the ranges of 1250-1290 cm^{-1}, 1340-1400 cm^{-1}, and 1418-1480 cm^{-1}. However, these intensities tended to stabilize with prolonged operation, particularly at the 6th and 8th hours. In addition to changes in band intensity, variations in peak-splitting were also observed. For example, in the 1150-1180 cm^{-1} band, the initial left split-peak height was higher than that of the right split-peak, but by the start of the 2nd hour, the heights of both peaks became similar. In the 1530-1594 cm^{-1} band, the left split-peak was initially greater than the right split-peak; however, as *BS* duration progressed, the left peak became shorter than the right, and eventually, the heights of both peaks were nearly identical. Similarly, the Raman intensity at the drain decreased as the device continued to operate. Notably, the 1100-1200 cm^{-1} Raman-shift band initially appeared as a single mixed peak, but it gradually split into multiple distinct peaks during the operation.

The change in intensity suggests a link with molecular orientation and chemical bond polarizability, according to Raman scattering theory [208,209]. Based on the appearance of split peak which is usually associated with the inter-molecular forces between the adjacent molecules with different orientation in a unit cell, the changes in the height of split peaks suggest that the electric field possibly disturbed the molecular orientation, *i.e.*, the scattering cross section with respect to incident light, which resulted in the reduced intensity of Raman signal [177,193]. The continuous electric field, as a primary external factor, altered the Raman intensity. In particular, for the 1340-1380 cm^{-1} Raman-shift band, it presented the strongly deformation of central

thiophene rings referencing to the mode 7 in **Table 3.1**. Therefore, in the on-state of OTFTs, S-DNTT-10 molecules at electrodes responded to the additional electric field stress. Consequently, the altered molecular orientation within the cell influenced the overall electronic energy levels. Thus, the impact of the electric field on molecular structure may affect charge transport in these molecules.

Another hypothesis suggests that the long-term operation of S-DNTT-10-based OTFTs could induce Joule heating as a potential mechanism. Joule heating, where current passing through a conductor generates heat-energy, is an unavoidable consequence of electrical resistance in devices. Since a normally operating OTFT can be regarded as a circuit with resistance, it inevitably produces Joule heating energy during prolonged operation [170,210,211]. This phenomenon could influence the local spatial organization of S-DNTT-10 molecules and charge transport properties, this assumption could be referenced in the following Section 5.2.2.3, where it illustrated the influence of post-annealing temperature on contact resistance. The Raman signal, under fixed polarization of incident light, could be correlated with these changes, potentially explaining the decrease in Raman intensity. Heat-induced reorientation may disrupt π-electron overlap and molecular polarizability, directly affecting the Raman signal. However, measuring localized temperature changes in the active layer of an OTFT is challenging, making it difficult to definitively link Joule heating with molecular orientation changes and variations in Raman intensity. Without a method to detect localized temperature variations, the impact of Joule heating on molecular orientation and the Raman spectral characteristics of S-DNTT-10 remains speculative. Ultimately, the unchanged Raman spectrum observed at the 6th and 8th hours of operation suggests that the molecular characteristics of S-DNTT-10 tend to stabilize over time.

Overall, the results indicate that the long-term electric field influences Raman scattered signals, reflecting changes in the molecular characteristics of S-DNTT-10. When the electric field affects the molecules, changes in atomic spatial distances and positions alter potential energy, which in turn affects the electron wave function and molecular orbitals (MOs). The observed decrease in μ_{lin} and μ_{sat}, along with changes in the Raman spectrum, suggests that the long-term electric field impacts charge transport by affecting π-electrons. MOs, which describe π-electrons, are linear combinations of atomic orbitals related to the electron wave function. These changes could disturb the π-electrons in S-DNTT-10 molecules, influencing charge transport and leading to decreased mobility. As effective mobility also decreases with increasing contact resistances, we speculate that this may be reflected in increased source

contact resistance (R_s) and drain contact resistance (R_d). To demonstrate this, Kelvin Probe Force Microscopy (KPFM) was used to measure R_s and R_d as showing in Section 2.4.4.2, before and after 8 hours of *BS* operation (U_{GS} and a U_{DS} of -40 V) on the S-DNTT-10-based OTFT.

Nevertheless, the results showed the reduction in $R_s \cdot W$ from 36808 to 29634 Ω·cm, under a U_{GS} of -30 V and a U_{DS} varying from 0 to -5 V in -0.5 V increments. This shows that the charge injection efficiency of the device does not degrade under the influence of a prolonged electric field. Meanwhile, it implemented the KPFM measurements on R_d under a U_{GD} of -30 V and a U_{DS} varying from 0 to -5 V in -0.5 V increments. The results as well shows that the $R_d \cdot W$ slightly decreased from 8918 to 8668 Ω·cm, and it indicated that the charge extraction efficiency is not affected by the *BS*. These KPFM results suggest that the long-term electric field does not degrade the charge injection and extraction efficiency in this device. Therefore, it seems reasonable that the reduction in effective mobility, as discussed in Section 1.4.4.1 and described by **Equation (1.13**) and **(1.14**), as well as the shift in threshold voltage, are both associated with the impact of the electric field on the channel.

4.4.2 Conventional Raman measurements in the channel

To demonstrate the influence of continuous electric field on S-DNTT-10 molecules located at the channel, it is determined to measure the conventional Raman spectrum by using 532 nm excited laser. The results, as shown in **Figure 4.4 (a)**, initially display the reduction of Raman scattered light intensity. It is worth mentioned that the Raman-shift bands varied with the biased electric field, for instance, the bands labelled as Band **I-V** illustrating in **Figure 4.4 (b)**.

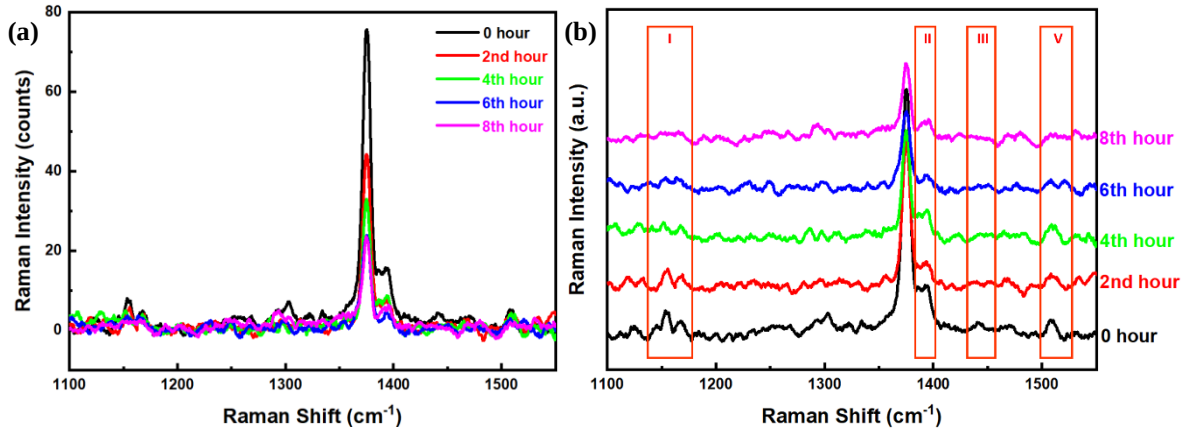


Figure 4.4 S-DNTT-10 Raman spectrum in the channel using 532 nm laser varied with bias stress time. (a) After smooth and baseline treatment and (b) after stack treatment.

With regard to Band-**I** (1137-1177 cm^{-1}) and Band-**II** (1383-1403 cm^{-1}), it shows that the bands in the form of split two peak at before the bias stress measurement. Subsequently, the

initial split peaks are gradually disappeared and mixed as one broad peak. It suggested that the S-DNTT-10 molecular orientation is changed and the S-DNTT-10 inter-molecular reaction with adjacent molecules within unit cell is affected by the continuously long-term electric field. As for the Band-**III** (1428-1455 cm^{-1}), it displays that the peak is evolved as the two split peaks at the 2nd hour and indicated the changes in molecular orientation of crystal unit by the electric field affecting. Then, with the continuous electric field stress, it disappeared the characteristic of split peaks and is exhibited as one broader band. It indicated the lower lifetime of phonon and the appearance of disorder S-DNTT-10 molecules [212]. With regard to Band-**V** (1500-1530 cm^{-1}), it initially shows that one narrow peak, however, the sustaining electric field caused the peak broadened at 2nd hour. And at the 4th hour, the peak is seemed to have the split trend. It indicated that the S-DNTT-10 molecular orientation is changed by the electric field. Subsequently, split peaks are transformed to one broad band. It suggested the disorder S-DNTT-10 molecular arrangements affecting by the electric field. Therefore, based on the obtained changes in Raman spectrum of S-DNTT-10, it indicated that the interactions between the electric field and S-DNTT-10 molecules in the channel, causing the disturbation in the π-electrons. These changes directly impact the charge transport properties of device, leading to a reduction in μ_{lin} and μ_{sat}. The response of molecular characteristics to electric fields, particularly the behavior of π-electrons crucial for charge transport, is evident in the observed changes in Raman spectra. This phenomenon indicates a complex interaction between the electric field and molecular dynamics in OTFTs, where the field affects both the immediate electronic states within S-DNTT-10 molecules and induces long-term structural changes impacting the device electrical performance.

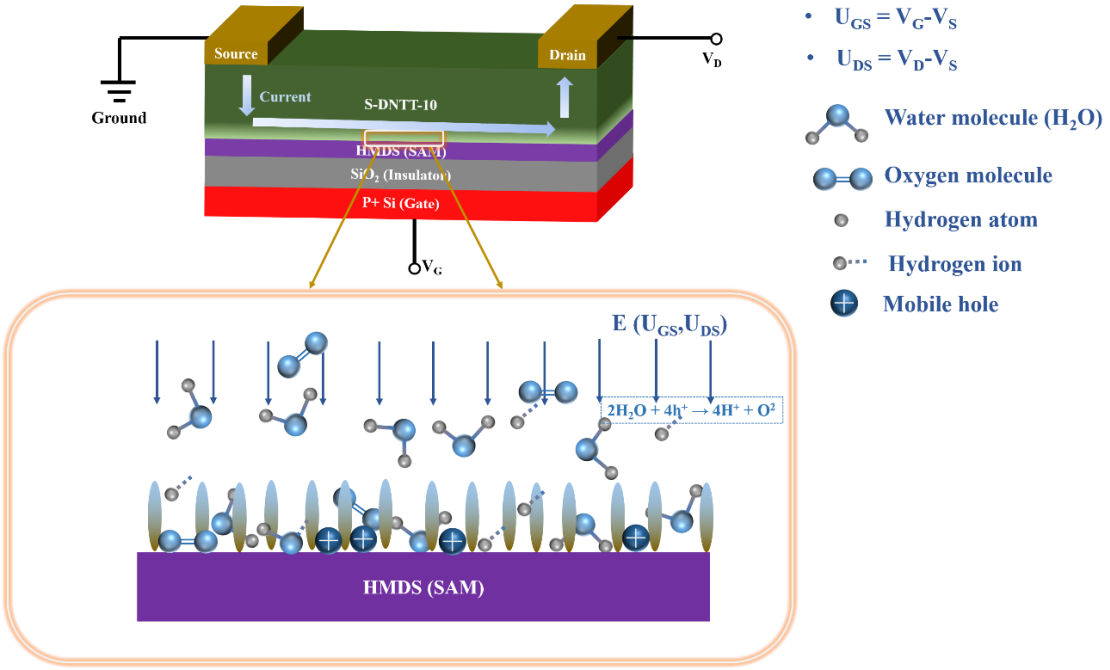


Figure 4.5 The schematic diagram of electrically water molecule structure breaking.

As the above mentioned changes in electrical performance by *BS* effect, not only the lower effective field-effect mobility, but also the negative shift of threshold voltage (U_{Th}). The U_{Th} can be regarded as one effective parameter, and it depends on the contact resistances. Here as mentioned before, the *BS* does not affect contact resistances. Therefore, U_{Th} is mainly influenced by the trap states at the interface between the OSC thin-film and the insulator. Therefore, we speculate that the negative shift of U_{Th} is mainly linked with the changes in S-DNTT-10 molecules located at the channel by prolonged stress. In practice, it suggested that OTFTs inevitably encounter disturbances from water molecules (H_2O) in the air environment. Base on Proton Migration model [206,213,214], OSCs with to their relatively loose structure compared with inorganic material showing in **Figure 4.5**, allows H_2O molecules to diffuse at the interface between the OSC and the gate dielectric, where mobile holes (h^+) accumulate due to gate bias. However, these holes can be transformed through the electrolytic reaction $2H_2O + 4h^+ \rightarrow 4H^+ + O_2$, herein, the H^+ represented the proton. The additional protons generated at the interface can migrate reversibly in the gate dielectric, leading to screen charge accumulation by the gate electric field. This effect reduces the quantity of induced accumulated hole charges in the channel. Hence, a larger bias condition, characterized by a shift in U_{Th}, is seemingly reasonable to fill the trap states and accumulate mobile charge in the channel. Furthermore, the long-term electric field likely causes the density of states (DOS) of the trap states within the insulator to overlap more with the charge transport state within OSC, increasing the number of trap states [206] and thus affecting the *I-V* performance of S-DNTT-10-OTFTs.

4.5 Conclusion

In this chapter, we mainly focused on exploring the influence of *BS* effect on electrical characteristics of TCBG S-DNTT-10-based OTFT at the 8 hours U_{GS} and U_{DS} of -40 V under the air environment. In particular, during this process, we skillfully utilized several characterized methods together. After the 8 hours-stressed execution, it was observed that the effective field-effect mobility μ_{lin} and μ_{sat} was, respectively, decreased from 0.62 to 0.385 $cm^2 \cdot V^{-1} \cdot s^{-1}$, and from 3.842 to 1.03 $cm^2 \cdot V^{-1} \cdot s^{-1}$. The corresponding threshold voltage $U_{Th\text{-}lin}$ and $U_{Th\text{-}sat}$ was, respectively, shifted from -20.3 to -23.5 V, and from -29.2 to -28.8 V. Meanwhile, the Raman scattered measurements exhibited the changes in Raman spectrum of S-DNTT-10 molecules at electrodes and channel area due to the long-term electric field interference. However, the results from KPFM for extracting contact resistance at electrodes before and after *BS* effect, showed that the reduction in source contact resistance $R_s \cdot W$ from 36808 to 29634 Ω·cm, and drain contact resistance $R_d \cdot W$ decreased from 8918 to 8668 Ω·cm. It indicated that the long-term electric field didn't degenerate the charge injection and extraction efficiency in this device, at least not created destroyed.

Therefore, we suggested that the observed degradation in effective mobility and the shift in threshold voltage were mainly correlated with the effect of the long-term electric field on the S-DNTT-10 molecules in the channel region. This implied that the reduction in TCBG S-DNTT-10-based OTFT performance under the electric field originated from changes in the molecular characteristics at the channel. Additionally, it should be noted that the above analysis and conclusions are likely specific to the measured TCBG S-DNTT-10-based OTFTs and may not be directly applicable to other OSC material-based electronic devices, as the charge transport characteristics, governed by π-electron overlap or delocalization, depend on the molecular structure of each material.

While this study offers valuable insights, it acknowledges the limitations of Raman scattering in fully characterizing charge transport mechanisms in OTFTs. Although Raman spectroscopy effectively demonstrates the impact of electric fields on S-DNTT-10 molecules and π-electrons, contributing to electrical performance degradation, it does not fully capture the extent of π-electron overlap. This is crucial, as charge transport in organic semiconductors (OSCs) fundamentally depends on π-electron delocalization and overlap within and between molecules. The difficulty in directly assessing π-electron overlap via Raman spectroscopy highlights the need for further methodological advancements and the integration of complementary techniques. Such improvements would enhance our understanding of the

complex interactions between molecular structure, electron delocalization, and charge transport in organic electronics.

5 Annealing treatment on S-DNTT-based OTFTs

5.1 Introduction

Research showed that the morphology of fabricated OSC thin films is correlated with charge transport characteristics, thereby affecting the electrical performance of OTFTs. Post-annealing treatment has been observed to effectively influence the arrangement or crystallinity of organic molecules in thin films, which impacts OTFT properties [215,216]. For example, Cho reported that post-annealing P3HT thin films at 150 °C for 10 minutes improved crystallinity and brought the thin film closer to the electrodes [217]. This method is effective not only for polymer materials but also for small molecular OSCs. Iino et al. demonstrated that Ph-BTBT-10, a small molecule with great application potential, formed polycrystalline films with good homogeneity and thermal stability when spin-coated films were annealed at 200 °C [218]. The study showed that the effective mobility of TCBG-OTFTs, using Si/300 nm-SiO_2 layer as the substrate and Ph-BTBT-10 as the organic layer, was only 2.1 $cm^2 \cdot V^{-1} \cdot s^{-1}$ at room temperature. However, after thermal annealing at 120 °C, the mobility increased by about an order of magnitude, reaching 14.7 $cm^2 \cdot V^{-1} \cdot s^{-1}$. This improvement is attributed to changes in the crystal structure of Ph-BTBT-10 during the annealing process, resulting in enhanced device performance.

In this chapter, we will focus on the influence of annealing treatment on the electrical performance of top-contact bottom-gate (TCBG) S-DNTT-10-based OTFTs. We aim to explore this influence using comprehensive system consisting of several advanced nanoscale characterization tools, including AFM, KPFM, and Raman scattering techniques. These approaches will be employed to examine changes in the molecular characteristics of S-DNTT-10, the S-DNTT-10 thin film and gold electrodes, as well as the interfaces between the S-DNTT-10 thin film/electrodes and the S-DNTT-10 thin film/HMDS layers (as discussed in Section 5.2). Additionally, we will investigate the specific post-annealing temperature (T_{post}) that achieves optimal device performance, as it varies with the S-DNTT-10 deposition substrate temperature (as discussed in Section 5.3).

5.2 Post-annealing treatment on S-DNTT-10-based OTFT

Appropriate post-annealing helps to improve the uniformity and stability of the OSC thin film and therefore improve the OTFT performance. However, the temperature of the post-annealing treatment needs to be strictly controlled. Excessive or inappropriate annealing

temperatures can cause cracks in the thin-film and damage its crystallinity, thereby reducing the performance of the OTFT.

The impact of post-annealing treatment on S-DNTT-10-based OTFTs and the optimal annealing temperature were investigated. For example, we conducted post-annealing on the TCBG S-DNTT-10-based OTFT (with a channel length of 50 μm, channel width of 1000 μm, SiO_2 insulator thickness of 89 nm, capacitance per area C_i of 0.00038781 F/m², and Au electrode thickness of 25 nm) at temperatures ranging from 40 to 110 °C, in 10 °C increments, with each treatment lasting 30 minutes. The saturation effective field-effect mobility μ_{sat} values extracted from the transfer characteristic curves versus post-annealing temperature are shown in **Figure 5.1**. We found that as the post-annealing temperature increased, the μ_{sat} increased from 1.26 to 3.09 $cm^2 \cdot V^{-1} \cdot s^{-1}$ at 80 °C. However, as the temperature continued to rise, μ_{sat} gradually decreased to 1.92 $cm^2 \cdot V^{-1} \cdot s^{-1}$ at 110 °C. The extracted μ_{sat} is an effective parameter influenced not only by the characteristics of the OSC thin film but also by factors such as the contacts between the OSC and the electrodes (**Figure 5.2**). On the other hand, one additional potential effect of post-annealed SAMs on the morphology of the OSC thin film should also be considered (**Figure 5.2**).

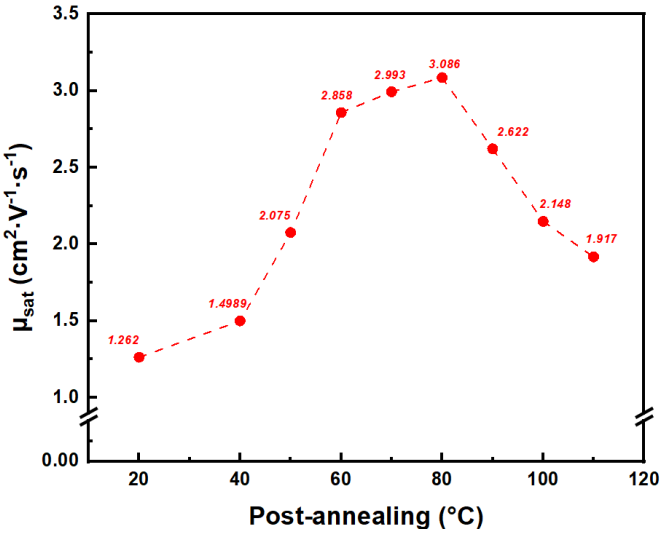


Figure 5.1 Effective field-effect mobility in saturation-regime μ_{sat} variation with 30 mins post-annealing treatment and varied post-annealing temperature. (The designed channel-length of 50 μm, channel-width of 1000 μm, the capacitance per area C_i of 0.00038781 F/m², the Au-electrodes-thickness of 25 nm).

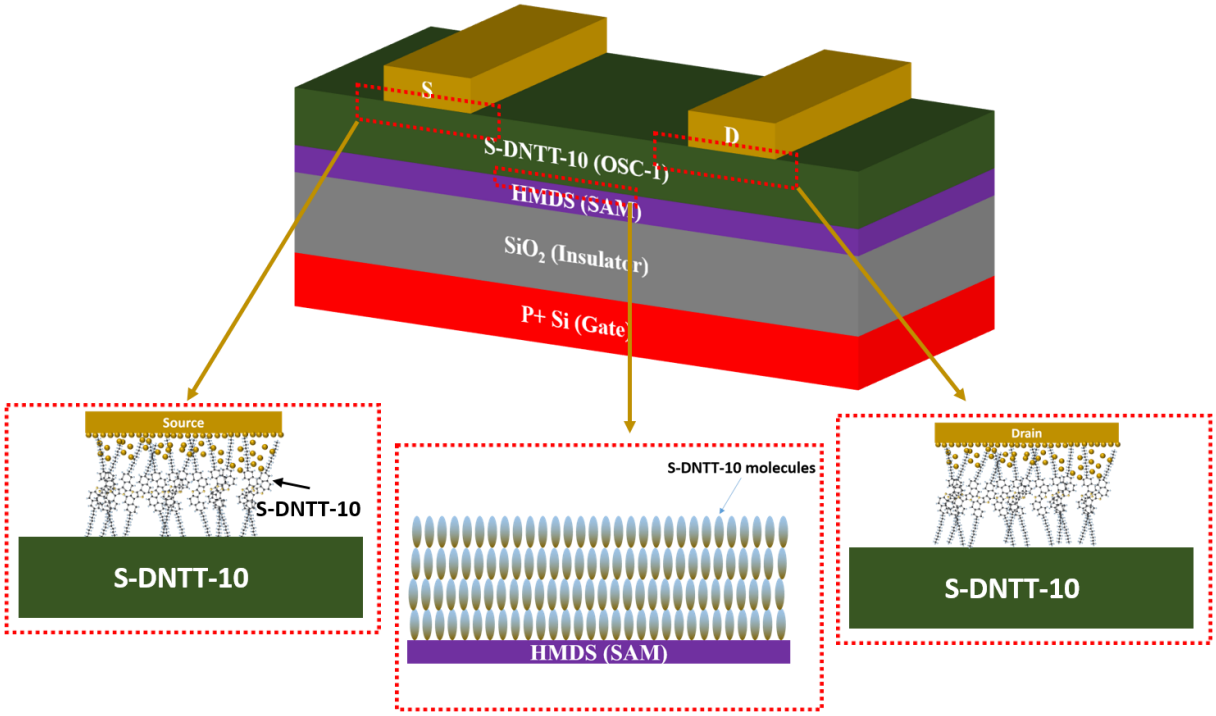


Figure 5.2 The interface characteristics in Top-contact-Bottom-gate S-DNTT-10-based OTFT.

To explore the influence of variations in the post-annealing treatment on the S-DNTT-10-based OTFT, we plan to observe the effects of different post-annealing temperatures on the S-DNTT-10 thin-film itself, the contact characteristics near the electrodes, and the molecular characteristics of S-DNTT-10 beneath the electrodes, as **Figure 5.2** shown.

- Firstly, we study the influence of different post-annealing temperatures on the overall electrical performance of S-DNTT-10-based OTFT with 10 nm-Au electrodes (seeing in Section 5.2.1).
- Subsequently, we focus on the 25 nm S-DNTT-10 thin-film in Section 5.2.2.1. We use AFM to measure the changes in the topography of the S-DNTT-10 thin-film with different post-annealing temperatures (Section 5.2.2.1.1). KPFM method is used to extract intrinsic mobility in the channel (Section 5.2.2.1.2) and Raman spectroscopy to observe the changes in the molecular characteristics of S-DNTT-10 (Section 5.2.2.1.3).
- In our device, the S-DNTT-10 thin-film is deposited on the SiO_2 modified by the HMDS layer. HMDS can be affected by different post-annealing temperatures. However, due to its thickness of only a few nanometers and the extremely low concentration, Raman spectroscopy and AFM cannot measure effectively some changes in the HMDS-SAM. Therefore, we plan to use contact-angle analysis to observe and characterize the changes in the HMDS layer with different post-annealing temperatures (Section 5.2.2.2).

- Additionally, we measure the surface potential distribution along the channel by using KPFM and calculate the intrinsic mobility which characterizes the properties of charge transport in the channel without the influence of contact characteristics from the affected source and drain electrodes by post-annealing temperature.
- Subsequently, we explore the morphology of Au-electrodes changing with different temperatures via AFM and also extract source and drain contact resistances by KPFM to evaluate the effect of different post-annealing temperatures on charge injection and collection efficiency.
- Meanwhile, it implements measurements of Raman scattered light to explore the changes in molecular characteristics of S-DNTT-10 which is under electrodes. It is noted that to measure the Raman spectrum, the thickness of the electrode is 10 nm, which could induce the SERS effect. Otherwise, the use of thicker Au-electrodes cannot effectively induce and collect the Raman signal of S-DNTT-10 molecules.

Hence, only for the related KPFM measurements including surface potential profile, extracted contact resistance at electrodes and intrinsic mobility in the channel, they are executed on the S-DNTT-10-based OTFTs with 25 nm-Au electrodes. The explanations and details are shown in Section 5.2.1.

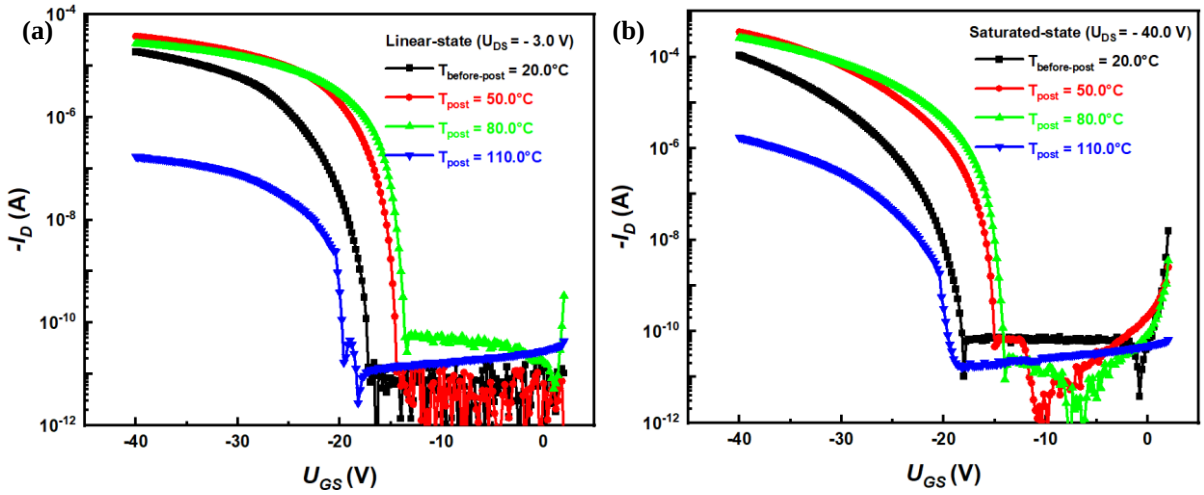
5.2.1 Post-annealing temperature influence on electrical properties

In this section we study the influence of different post-annealing temperatures on the overall OTFTs electrical performance.

The structural parameters of the measured S-DNTT-10-based OTFT are as follows: The width of the channel is 1000 μm, the length of the channel is 50 μm, the thickness of the S-DNTT-10 thin-film is 25 nm at a deposition rate of 0.5 Å/s on the 110 °C substrate surface, and the thickness of the SiO_2 layer is 89 nm, and the thickness of the Au-electrode is 10 nm at a deposition rate of 1.0 Å/s. It is required to explain that the utilized thickness of electrodes is referenced from Section 3.5.3 and Chapter 4, since it implements the SERS spectrum technique into investigating on the influence of post-annealing treatment on electrical performance of S-DNTT-10-based OTFTs.

It was conducted a 30-minutes post-annealing treatment on S-DNTT-10-based OTFT at 50 °C, 80 °C, and 110 °C respectively, and extracted the effective field-effect mobility before post-annealing (marked as “20 °C” at X-axis in **Figure 5.3**) and the relevant electrical characteristics measured after the post-annealing treatment based on the measured transfer

characteristics curves. as shown in **Figure 5.3**. **Figure 5.3 (a)** and **(b)** exhibit the transfer characteristic curves in the linear mode at U_{DS} = -3 V and the saturation mode at U_{DS} = -40 V after different temperatures of post-annealing. It is noted that we observed the slight hysteresis effect in the recored electrical characteristics curve under the different post-annealing temperature. Hence, we exhibited the measurements without hysteresis effect. Results indicated that, compared with before post-annealing treatment (black-square-solid-line at 20 °C), the drain current in the transfer characteristic curves was enhanced after the 50 °C post-annealing treatment (red-circle-solid-line). After the 80 °C post-annealing treatment (green-upper-triangle-solid-line), the collected drain current was slightly enhanced, approximately when U_{GS} ranged from -15 to -23 V. However, as U_{GS} increased, the drain current began to be smaller than that measured after the 50 °C post-annealing. Finally, after the 110 °C post-annealing treatment (blue-lower-triangle-solid-line), the drain current was overall reduced. Based on the corresponding transfer characteristic curves, the results of the extracted effective field-effect mobility, μ_{lin} and μ_{sat}, varying with different post-annealing treatments are shown in **Figure 5.3 (c)**. In this figure, the black-square-dash-line and red-circle-dash-line respectively represented μ_{lin} and μ_{sat}. It illustrated that the enhancement of μ_{lin} and μ_{sat}, respectively, as 0.83 $cm^2 \cdot V^{-1} \cdot s^{-1}$ and 3.01 $cm^2 \cdot V^{-1} \cdot s^{-1}$, in comparison of μ_{lin} = 0.56 $cm^2 \cdot V^{-1} \cdot s^{-1}$, μ_{sat} = 1.67 $cm^2 \cdot V^{-1} \cdot s^{-1}$ at before post-annealing. Subsequently, with the post-annealing temperature increasing, it emerged the reduction of the effective field-effect mobility. In particularly, the obvious degeneration of electrical performance appeared at after 110 °C post-annealing treatment. The μ_{lin} and μ_{sat} is respectively descended as 0.001 $cm^2 \cdot V^{-1} \cdot s^{-1}$ and 0.070 $cm^2 \cdot V^{-1} \cdot s^{-1}$.



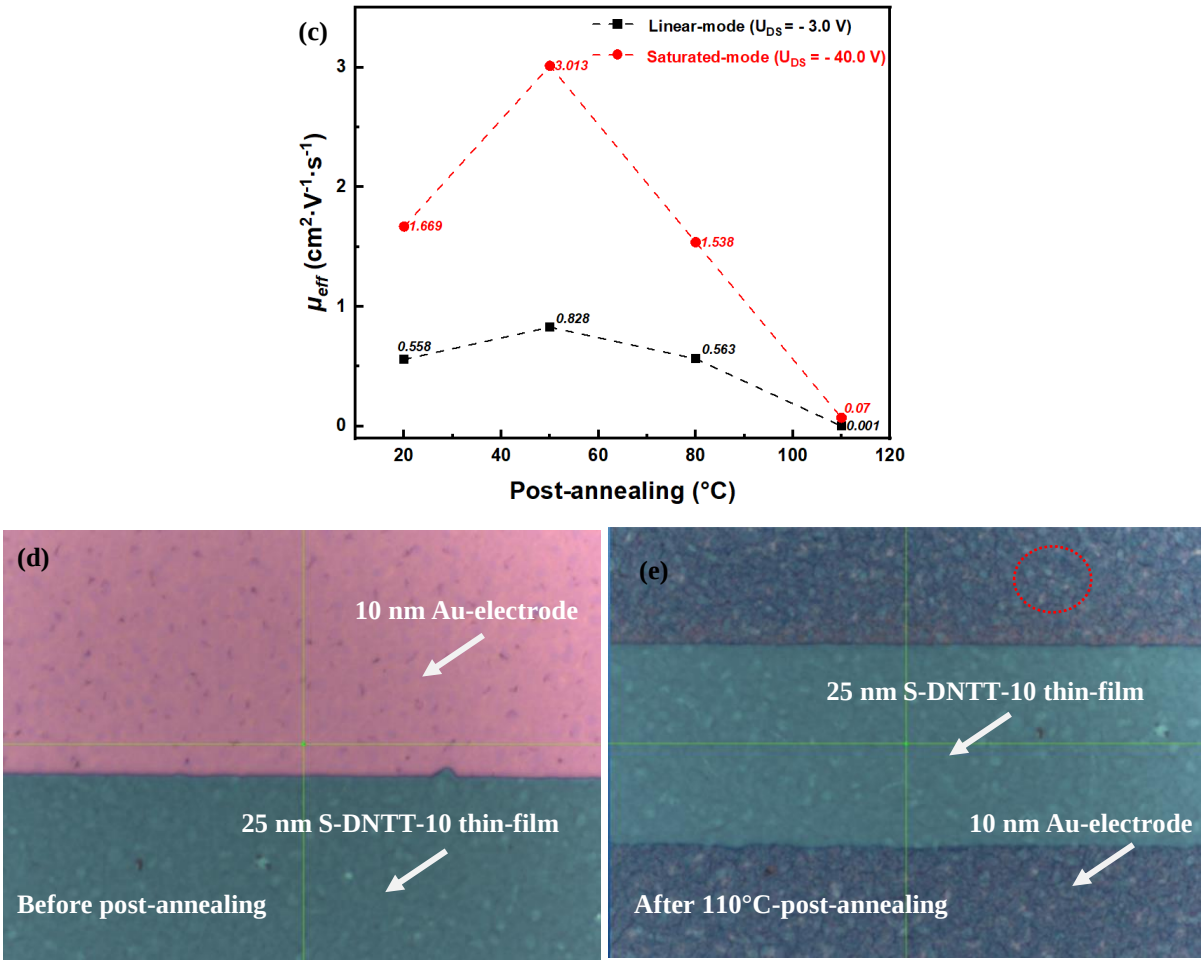


Figure 5.3 The transfer characteristics in S-DNTT-10-based OTFT varying with different post-annealing temperature: (a) Linear state and (b) saturation-state. (c) The related extraction of effective field-effect mobility. (The designed channel-length of 50 µm, channel-width of 1000 µm, the capacitance per area C_i of 0.00038781 F/m^2, the Au-electrodes-thickness of 10 nm, and results for $T_{before\text{-}post}$ = 20 °C correspond to the extracted mobility before heating). The topography of electrodes at (d) before and (e) after 30-mins 110°C post-annealing treatment.

Similar results were observed in the study of OTFTs based on PDBPyBT, where the highest mobility of 6.3 $cm^2 \cdot V^{-1} \cdot s^{-1}$was achieved after post-annealing at 100 °C, but degradation occurred at higher temperatures [219]. These findings illustrate that the electrical performance of S-DNTT-10-based OTFTs follows a pattern of enhancement followed by degradation under different post-annealing temperatures. Specifically, for μ_{sat}, there was a significant improvement after the 50 °C post-annealing treatment, more so than the change in μ_{lin}. Based on the measurement results in **Figure 5.1**, for S-DNTT-10-based OTFTs with the S-DNTT-10 thin film deposited at a rate of 1.0 Å/s on a substrate at 110 °C, the optimal post-annealing temperature range for improving electrical performance is 50-80 °C. Furthermore, after post-annealing at 110 °C, there was severe degradation in the collected drain current I_D in transfer

characteristics I_D-U_{GS} and the corresponding extracted effective mobility, compared to the performance after 80 °C post-annealing, as shown in **Figure 5.3 (a)-(c)**.

This issue is likely related not only to the influence of post-annealing treatment on the morphology of the S-DNTT-10 thin film but also to thermal changes in the electrodes. Due to their thinness, the electrodes may undergo topographical changes at higher temperatures, damaging the interface between the metal electrodes and the OSC, which could contribute to the device's poor performance. Using the optical imaging system of the Raman spectrometer, it was observed that before post-annealing, the 10 nm Au electrodes appeared as a smooth and continuous thin film, as shown in **Figure 5.3 (d)**. However, after 110 °C post-annealing, the electrodes exhibited increased surface roughness and degradation, as seen in **Figure 5.3 (e)**. In some areas, such as the red-marked circle, the color of the electrodes was similar to that of the S-DNTT-10 thin film, indicating that the S-DNTT-10 was exposed without electrode coverage. This suggests that the 10 nm electrodes suffered significant damage, severely impacting charge injection and collection efficiency. In the next section, we will examine the morphology in detail using AFM.

To demonstrate that the extremely poor performance by 110 °C post-annealing mainly resulting from the destroyed electrode, we attempted to execute the similar post-annealing process on the S-DNTT-10-based-OTFT with 25 nm Au-electrodes. We think that the thicker electrodes can withstand 110 °C post-annealing. The effective field-effect mobility μ_{lin} and μ_{sat} extracted from the transfer characteristics characterize the influence of different post-annealing temperatures on the device. The results are shown in **Figure 5.4**, with the black-square-dash line and the red-circle-dash-line representing μ_{lin} and μ_{sat}, respectively. Herein, the change of the field-effect mobility with the post-annealing temperature is similar to that in the above device with 10 nm-electrodes, where the highest enhanced mobility appeared at 50°C and the mobility decreased with the increase of the post-annealing temperature. It was observed that the mobility at 110 °C post-annealing was also reduced; however, it did not show the extremely poor performance as in the 10 nm-electrode device illustrating in **Figure 5.3**. Therefore, we suggest that the low mobility in the 10 nm-electrodes-OTFT was mainly caused by the degradation of the electrodes.

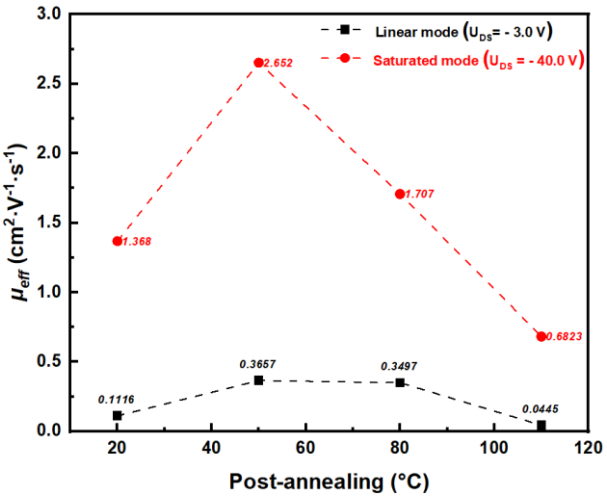


Figure 5.4 The effective field-effect mobility changing with varied post-annealing temperature. (The designed channel-length of 50 μm, channel-width of 1000 μm, the capacitance per area C_i of 0.00038781 F/m^2, the Au-electrodes-thickness of 25 nm)

5.2.2 Post-annealing temperature influence on material

In the previous section, it displayed the response of S-DNTT-10-based OTFT to different post-annealing treatment temperatures. We supposed that it is caused by the changes in S-DNTT-10 thin-film morphology, and the contact characteristics of OSC-electrodes interfaces and the molecular characteristics of S-DNTT-10 molecules under electrodes. To investigate on whether or not post-annealing temperature affecting the above factors, we plan to implement the nano-characterization technique. It is noted that the following characterizations were simultaneously performed when measured electrical performance under each different post-annealing temperature.

5.2.2.1 Post-annealing treatment on S-DNTT-10 thin-films

In this section we focus on the characterization of the S-DNTT-10 thin-film using different techniques: AFM, KPFM and Raman spectroscopy.

5.2.2.1.1 AFM measurements

After completing the post-annealing treatment at each different temperature, we measured the topography of the 10×10 μm annealed S-DNTT-10 thin-film via the AFM approach. Since the annealing platform and the AFM are not in the same location, it is necessary to transfer the samples between these two devices. Therefore, in order to measure the morphology at the same position as much as possible after post-annealing at different temperatures, we utilized the inherent imaging system of **Bruker**-AFM to record the position to be measured, as shown in **Figure 5.5 (a)**, which showed one red-cross used to record the pre-measurement region. **Figure**

5.5 (b)-(e) respectively show the topography after and before post-annealing treatment, 50 °C post-annealing, 80 °C post-annealing, and 110 °C post-annealing. Here, we used ***RMS-Roughness*** to characterize the response of the topography of the measured S-DNTT-10 thin-film to different post-annealing temperatures. Herein, ***RMS-Roughness*** was calculated through the open-source software ***Gwyddion***. The results show that the ***RMS-Roughness*** in these four different cases is 2.399 nm, 2.305 nm, 2.267 nm, and 3.274 nm, respectively.

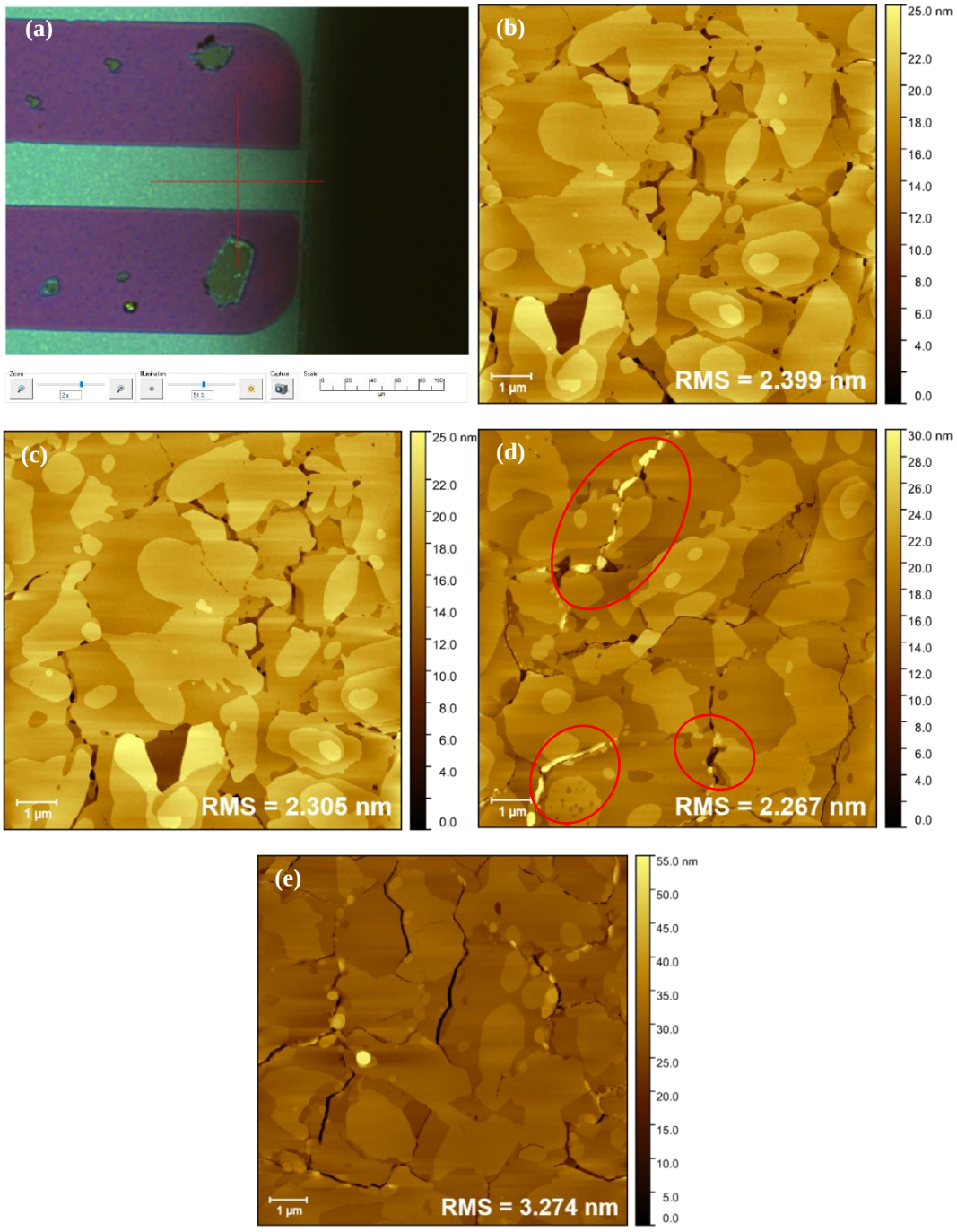


Figure 5.5 (a) The position of AFM-topography on the channel. The morphology changed with varied post-annealing temperature: (b) before post-annealing, (c) 50 °C post-annealing treatment, (d) 80 °C post-annealing treatment, and (e) 110 °C post-annealing treatment.

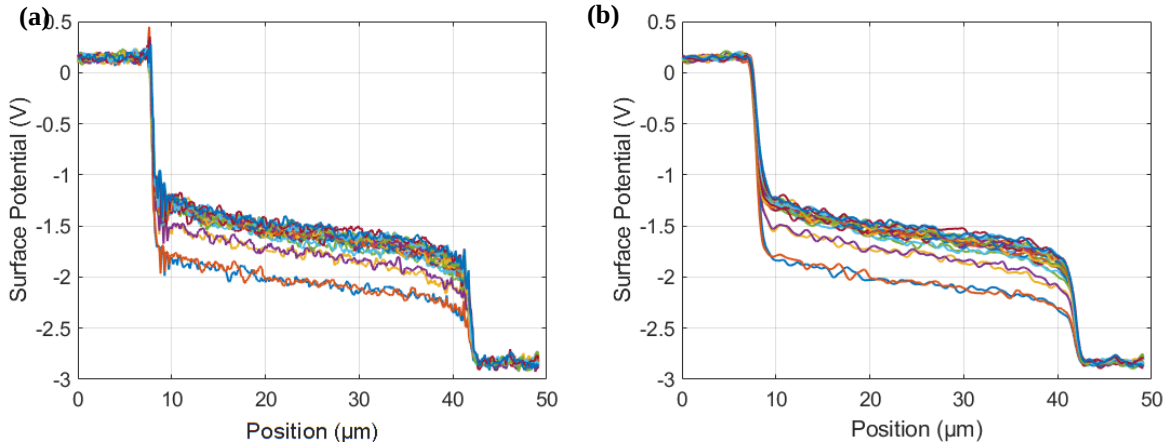
Compared with the before post-annealing treatment, the topography after 50 °C post-annealing presented a slight change, as reflected in the calculated ***RMS-Roughness*** values, *i.e.*, 2.399 nm and 2.305 nm. This implies that the uniformity of the S-DNTT-10 thin-film was also slightly enhanced. Subsequently, after the 80 °C post-annealing treatment was completed, as shown in **Figure 5.5 (d)**, although the calculated ***RMS-Roughness*** was 2.267 nm, through the measured morphology, it was observed that cracks on the surface of the S-DNTT-10 thin-film. Moreover, more importantly, we discovered bright areas at the crack edges, as marked by the red circles in the figure. Based on the surface height corresponding to the color on the color-bar, this indicates that the height of this area is relatively large. It considered that the 80 °C post-annealing temperature might have promoted the thermal motion of molecules, resulting in the aggregation of S-DNTT-10 molecules and causing a change in the uniformity of the local area of the S-DNTT-10 thin-film. Finally, after the 110 °C post-annealing treatment, the morphology of this area is shown in **Figure 5.5 (e)**. Compared with the morphology of the 80 °C post-annealing shown in **Figure 5.5 (d)**, it showed that the cracks on the surface of the S-DNTT-10 thin-film have increase. This suggests that a relatively high temperature like 110 °C led to the surface of the S-DNTT-10 thin-film becoming rougher, which was characterized by the increased ***RMS-Roughness*** of 3.274 nm and damaged the uniformity and crystallinity of the S-DNTT-10 thin-film, which is consistent with the reduction of extracted mobility as illustrated in **Figure 5.3**.

5.2.2.1.2 KPFM for intrinsic mobility

The above outcomes suggest that the morphology of the S-DNTT-10 thin-film is influenced by the elevated post-annealing temperature. As result shown in **Ref.** [218], the changed mobility resulted from the crystallization affecting by 120 °C post-annealing temperature. This promotes the thermal motion of molecules and modifies the uniformity and crystallinity of the thin film. It supposed that this will bring about alterations in the charge transport properties within the channel region. To investigate the impact of various post-annealing temperatures on the charge transport capacity in the channel, we use KPFM measurements to extract the intrinsic mobility (based on Section 2.4.4.3) in the channel. Indeed, we can extract the intrinsic mobility from the KPFM surface potential distributions measure under the linear mode at different post-annealing temperatures, and subsequently calculate the average intrinsic carrier mobility. It should be noted that a more rigorous methodology is typically to carry out the KPFM test on the same S-DNTT-10-based OTFT with 10 nm-Au electrodes measured by AFM. However, as shown in **Figure 5.4 (a)** and **(b)**, after post-

annealing at 110 °C, the 10 nm-Au electrodes were severely damaged, leading to the inability to obtain accurate potential distribution with the KPFM and accurate intrinsic mobility extraction. Considering that the alterations in the thin film morphology and intrinsic charge transport characteristics of the S-DNTT-10 thin-film are not affected by the electrode thickness, it is intended to conduct the KPFM measurements on another S-DNTT-10-based OTFT with 25 nm Au-electrode under different post-annealing treatments and extract the intrinsic mobility.

Figure 5.6 represents the surface potential distributions measured by KPFM and the extraction of intrinsic mobility under varied post-annealing temperature. Based on section 2.4.4.3, we could extract the intrinsic mobility in the channel. **Figure 5.6 (a)** and **(b)** respectively exhibited the measured surface potential distribution for before post-annealing at before and after data treatments including removing noise and smoothing curves. As for results at before post-annealing, 80 °C and 110 °C, they are displayed at Section **0** in the **Appendix**. The measured conditions were U_{DS} = -3 V, U_{GS} = -10 to -40 V with a step of - 2 V. The relationship between the extracted average intrinsic carrier mobility and the post-annealing temperature is shown in **Figure 5.6 (c)**. The average intrinsic mobility has been extracted in the channel. It was found that this trend is similar to that of μ_{eff} extracted via transfer characteristics. It showed that after the 50 °C post-annealing treatment, the average carrier mobility increased from 1.26 to 1.44 $cm^2 \cdot V^{-1} \cdot s^{-1}$. Subsequently, with the increase in temperature, the mobility gradually decreased to 0.84 $cm^2 \cdot V^{-1} \cdot s^{-1}$ and 0.15 $cm^2 \cdot V^{-1} \cdot s^{-1}$. This indicates that due to the influence of the post-annealing at higher temperatures on the morphology of the S-DNTT-10 thin-film, the charge transport characteristics of the S-DNTT-10 thin-film decreased and deteriorated the electrical performance of the S-DNTT-10-based OTFT. The changes in the topography of the S-DNTT-10 thin film and the related intrinsic mobility values were consistent with the effective mobility correlating with the post-annealing temperature.



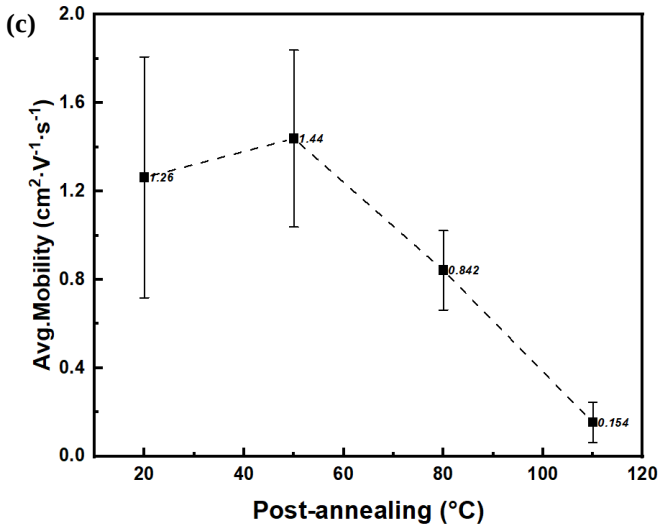


Figure 5.6 The schematic of the profile of surface potential: (a) 50 °C curves-treatment, *i.e.*, raw data, (b) after smooth curves-treatment, (c) The extraction of average intrinsic mobility changing with different post-annealing temperature. (The average value is derived from dividing the channel region equally into five parts and extracting the intrinsic mobility in the corresponding regions, after which the mean-value of these five values is calculated, resulting in the average intrinsic mobility in Fig.5.6 (c))

5.2.2.1.3 Raman spectroscopy

Based on the results in Section 5.2.2.1.1 and 5.2.2.1.2, we assumed that changes in intrinsic mobility under varied post-annealing temperature not only resulted from the change of morphology of the S-DNTT-10 thin-film, but also the change in the molecular characteristics of the S-DNTT-10. The properties of charge transport in OSC is essentially originated from π-electrons and it is sensitive to molecular structure. The affected morphology perhaps indicated that change in the interaction between the S-DNTT-10 molecules. Herein, to further explore the influence of post-annealing on charge transport properties in the channel, we also measured the Raman spectroscopy of S-DNTT-10 thin-films by 532 nm excited source under varied post-annealing temperature. It is noted that the measured device is the above mentioned OTFT with 10 nm Au-electrodes.

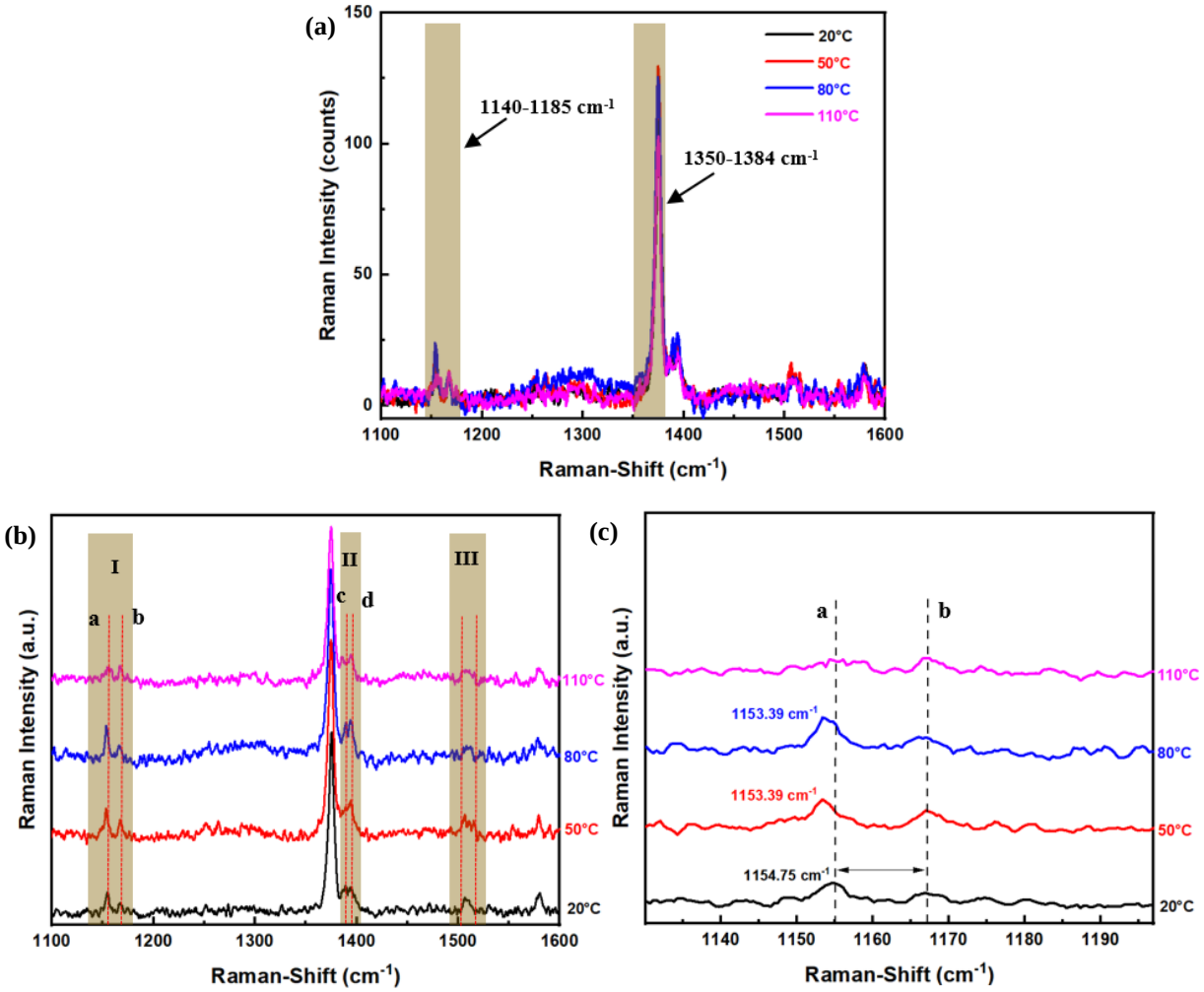


Figure 5.7 The spectrum with smooth and baseline treatments ranging from 1100-1600 cm^{-1} under different post-annealing temperature. (b) The stack treatment in (a). (c) The range of nearly 1128-1197 cm^{-1} in corresponding (b).

These measurements were carried out as much as possible in the same area. **Figure 5.7 (a)** show the Raman spectrum of S-DNTT-10 thin-film under different post-annealing temperature. To improve the resolution, we use the higher number of grating as 1800/mm. The low intensity of Raman spectrum is due to the thin layer of S-DNTT-10 (25 nm). Changes in spectrum has been detected. For instance, the height of 1350-1384 cm^{-1} Raman-shift band seemingly is increased at 50 °C and then descended with higher post-annealing temperature. Changes in split peaks located at nearly 1140-1185 cm^{-1} band can also be observed. To clearly exhibit the changed Raman spectrum, we plot the stack for these four spectra (**Figure 5.7 (b)**). Herein, we can notice three areas (**I**, **II**, **III**). A zoom on Area-**I** with split peaks is shown in **Figure 5.7 (c).** It shows that the height of left-peak-**a** increased after 50 °C and 80 °C post-annealing treatment, but decreased after 110 °C. For right-peak-b, its height increased after post-annealing and remained basically unchanged. Moreover, the distance between the two split peaks increases.

Similarly, in Area-**II**, the distance of the two split peaks increases with temperature. This information implies that due to heating and the gradual increase in heating temperature, the interaction between S-DNTT-10 molecules in the lattice changed due to the intense thermal motion. This effect affects the degree of π-electron overlap and thereby reduce the charge transport efficiency. Additionally, it was observed that the width of the Raman-shift band located in Area-**III** began to broaden when the post-annealing temperature was 80 °C and 110 °C. This indicates that the disorder of molecular arrangement within S-DNTT-10 thin-films started to increase. Similarly, it might also weaken the degree of π-electron overlap and ultimately reduce the intrinsic charge transport efficiency in the channel.

The analysis indicates that the degree of π-electron overlap is affected, confirming that the intrinsic charge transport efficiency in the S-DNTT-10-based OTFT channel changes with post-annealing temperature. However, the Raman spectrum measurement has limitations. For example, the low molecular concentration in the 25 nm S-DNTT-10 thin film reduces the Raman scattering signal intensity and signal-to-noise ratio, potentially affecting the accuracy of the relationship between the Raman spectrum and post-annealing at different temperatures. The issue of low Raman intensity in such thin films is a recurring problem that impacts the characterization of S-DNTT-10 molecules. In the future, we plan to explore methods for fabricating metallic nanostructures on the channel to induce SERS or TERS effects, thereby enhancing the Raman signal of S-DNTT-10 without compromising device operation.

5.2.2.2 Post-annealing treatment on HMDS

The topography of the S-DNTT-10 thin film is influenced by the post-annealing temperature, likely due to the intensified thermal motion of molecules at higher temperatures. In this sample, the S-DNTT-10 thin film is thermally deposited on a SiO_2 layer modified by HMDS as illustrated in **Figure 5.8 (a)**, which is used to remove surface defects and optimize the arrangement of S-DNTT-10 molecules. However, HMDS properties are perhaps also affected by high temperatures, suggesting that the changes in S-DNTT-10 morphology during post-annealing may be related not only to the S-DNTT-10 molecules but also to alterations in the HMDS.

Initially, it was difficult to obtain valid material characterization information using both Raman and AFM on HMDS. It was believed that this was due to the fact that HMDS was only a few nanometers thick, and the low molecular concentration could not map out the characterization signal. Therefore, it was decided to use contact-angle analysis to obtain the contact angle and calculate the corresponding surface energy (SE). *SE* is an important concept

in physics and materials science [154], describing the energy possessed by the material surface. This energy is higher compared to the bulk of the material because the environment of surface atoms or molecules is different from that of internal atoms or molecules. Surface energy is affected by the arrangement of surface molecules. The *SE* of each organic interlayer was determined by measuring the contact angle θ of two probe liquids (namely, water and diiodomethane (Dim)). The values were calculated by fitting the Owens-Wendt equation as shown below [154,220,221],

$$(1 + cos\theta)SE_{lv} = 2\sqrt{SE_s^d SE_{lv}^d} + 2\sqrt{SE_s^p SE_{lv}^p} \quad \textbf{(5.1)}$$

herein, SE_s and SE_{lv} are the SE of the organic interlayer and the probe liquid respectively, and the superscripts ***d*** and ***p*** refer to the dispersion and polar (non-dispersion) terms respectively. HMDS-modified SiO_2 was subjected to post-annealing treatment at different temperatures for 30 mins.

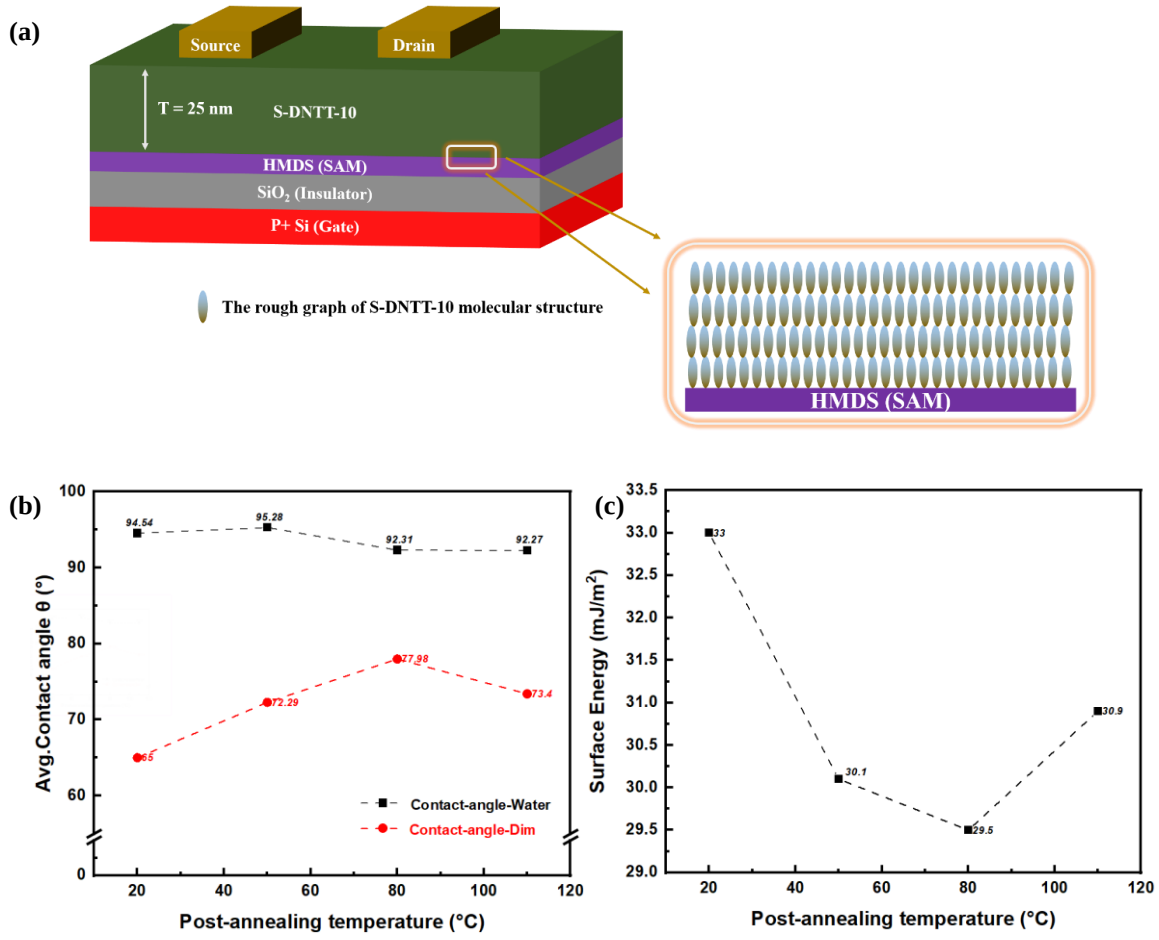


Figure 5.8 (a) The schematic representation S-DNTT-10 molecules depositing on SiO_2 layer modified with HMDS layer. (b) The contact angle by using probe solutions of water and Dim is changed with post-annealing temperature, and (c) the calculated surface energy (SE).

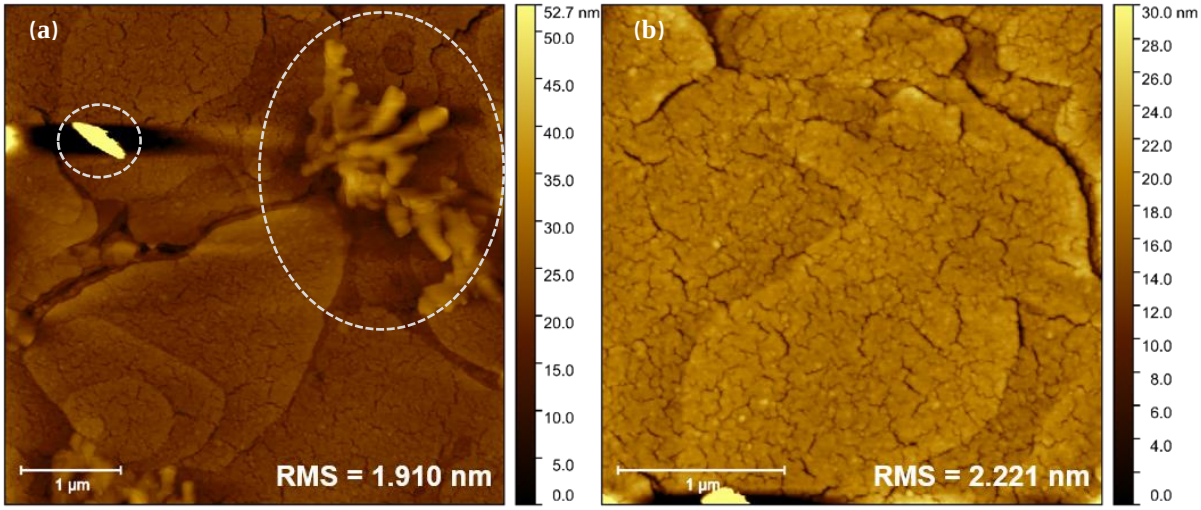
Figure 5.8 (b) shows the changes in contact angles measured using water and diiodomethane after different post-annealing temperatures. The black-square-dash line and the red-circle-dash line represent the changes in the contact angles of the probe-liquid of water and Dim with the post-annealing temperature, respectively. It showed that the contact angle of water exhibited a minor change, gradually decreasing from 94.54° to 92.27° as the temperature increased. This indicates a slight reduction in the hydrophobicity of the material. The contact angle of Dim gradually increased from 65.0° to 73.4°. **Figure 5.8 (c)** shows the corresponding surface energy decreased from 33.0 mJ/m^2 to 30.9 mJ/m^2. Although the change was not particularly obvious, it indicated that the molecular characteristics of the SAM layer were affected by the post-annealing treatment, perhaps indirectly changing the topography of the S-DNTT-10 thin-film under various post-annealing temperatures.

5.2.2.3 Post-annealing treatment on Au-electrodes

AFM topography shows that the S-DNTT-10 thin-film changed with the post-annealing treatment temperature, and it was considered as one of the reasons for the overall performance change of the device. We believed that a higher post-annealing temperature would have an impact on the morphology of Au-electrodes too, leading to changes in the characteristics of the interfacial layers of Au-electrodes and OSC. In the previous images as shown in **Figure 5.5**, it was observed that after the 110 °C post-annealing treatment, the morphology of the 10 nm Au-electrodes has significant changes compared to the morphology before the post-annealing treatment leading to a severe degeneration of the device performance. To explore the changes in the electrodes-OSC interface properties with the post-annealing temperature, we measure the change in the morphology of 10 nm Au-electrodes by AFM, and the change in the characteristics of S-DNTT-10 molecules around the electrodes by Raman spectroscopy. During the process of charge injection from the source to the channel and charge extraction from the channel to the drain, a good charge transport is required in these regions. The characteristics of S-DNTT-10 molecules near the electrodes would affect the charge transport efficiency at the corresponding positions. To study the post-annealing temperature influence on both the interface contact and the charge transport efficiency of S-DNTT-10 molecules under the electrodes, we extract the contact resistance R_c from KPFM measurements. It should be noted that due to the device's own structure, top-contact-bottom-gate, like **Equation (1.22)** and **Figure 1.5** describing, the potential drop at the electrodes obtained by KPFM technique was jointly determined by the S-DNTT-10/Au-electrodes contact characteristics (R_{int}) and the charge transport characteristics into S-DNTT-10 thin-film under the electrode (R_{bulk}). Therefore,

R_{int} and R_{bulk}, could not be characterized separately via the KPFM method, as mentioned in Section 2.4.4.2. Additionally, in the part of the intrinsic mobility measurement mentioned earlier in Section 5.2.2.1.2, the reason for the need to use the S-DNTT-10-based OTFT with 25 nm electrodes was mentioned and will not be repeated here. The OTFT for measuring the contact resistance was the same device as that for measuring the intrinsic mobility, and the measurement of the intrinsic mobility was carried out immediately after the completion of the contact resistance measurement.

Initially, we plan to perform AFM, SERS, and KPFM measurements at the source electrode, followed by identical measurements at the drain electrode. AFM will be used to investigate the topographical changes of the Au electrode under different post-annealing temperatures. SERS will study the molecular characteristics of S-DNTT-10 at the electrodes. KPFM will analyze the variation in charge injection/extraction with post-annealing temperatures at the source and drain by extracting contact resistance. It is necessary to note again that AFM and SERS will be conducted on S-DNTT-10-based OTFTs with 10 nm electrodes, while KPFM measurements will be carried out on devices with 25 nm electrodes.



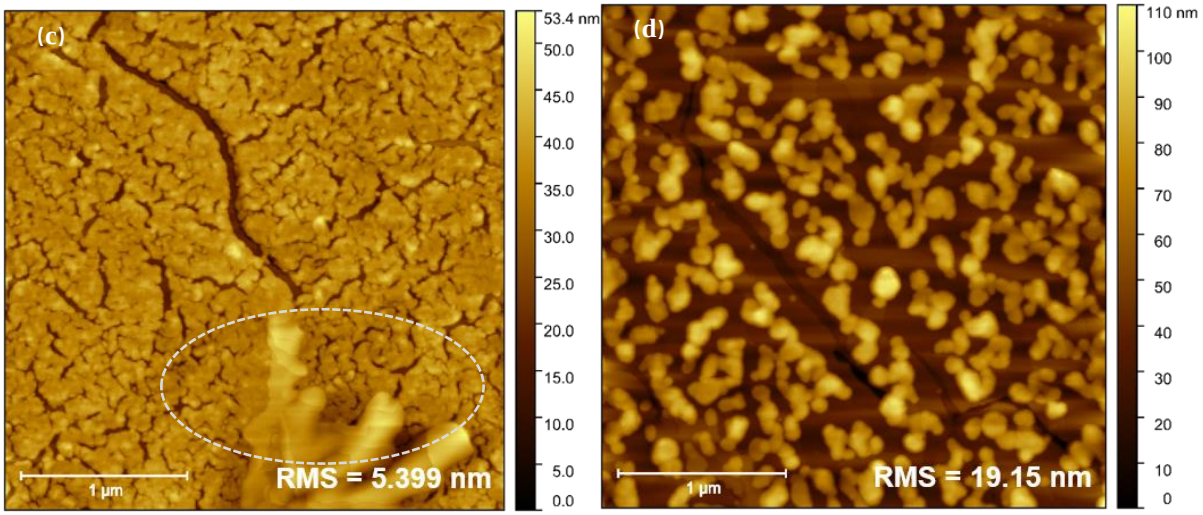


Figure 5.9 The AFM-topography with calculated RMS-roughness located at 10 nm-source under different post-annealing temperature: (a) before post-annealing, (b) after 50 °C post-annealing,(c) after 80 °C post-annealing and (d) after 110 °C post-annealing.

Firstly, it was observed that the influence of different post-annealing temperatures on the topography of the source. After the 30-mins post-annealing treatment of the S-DNTT-10-based OTFT, the AFM test was conducted on the morphology of the 10 nm-Au electrodes. The results are presented in **Figure 5.9 (a)-(d)**, which respectively represent the morphologies before post-annealing, after 50 °C-, 80 °C- and 110 °C-post-annealing treatment. It should be noted that during the AFM measurement prior to the post-annealing, it was discovered that irregular electrode morphologies frequently occurred in the local areas of the electrode surface, such as the areas marked by the white dashed lines in **Figure 5.9 (a)** and **(c)**. It was hypothesized that during the process of thermal deposition of Au electrodes, local gold atom aggregation occurred. However, the specific reasons will be investigated in the future. After several unsuccessful attempts, in order to avoid the irregular morphology area and protect the AFM probe, it was planned to reduce the measurement area from 5×5 μm to 3×3 μm. It was roughly observed that after post-annealing at a higher temperature, likely 80 °C, more cracks emerged on the topography of the Au-electrode compared with that after the 50 °C post-annealing treatment. In particular, **Figure 5.9 (d)** illustrated that the gold electrode seemed to have deformed after the 110 °C post-annealing treatment, changing from a film-like state to a granular state. The ***RMS-roughness*** under different post-annealing temperatures was calculated through the software ***Gwyddion***. It indicated that when the post-annealing temperature was low, such as 50 °C, the roughness underwent a minor change, slightly increasing from 1.91 nm to 2.22 nm. But subsequently, with the increase in the post-annealing temperature, the roughness significantly rose to 5.40 nm. Finally, after the 110 °C post-annealing, the roughness sharply increased to

19.15 nm. According to the above results, it suggested that the 10 nm electrode topography became rougher under the action of a higher post-annealing temperature for 30 mins, especially after the 110 °C post-annealing treatment. This indicated that the interface contact characteristics of the Au-electrodes/S-DNTT-10 thin-film would change, and the changed topography of the Au-electrode also suggested that the thermal motion of Au-atoms intensified under the action of a higher post-annealing temperature, which might penetrate into the S-DNTT-10 thin-film under the electrode and affect the corresponding S-DNTT-10 molecular characteristics.

To explore whether the characteristics of S-DNTT-10 molecules under the gold electrodes were affected, Raman spectroscopy was simultaneously used. To attain the SERS effect, the Raman spectrum have been acquired under 633 nm laser. After "smooth and baseline" processing, the Raman spectra of different post-annealing temperatures at the same measurement position are shown in **Figure 5.10 (a)**. It shows that the Raman intensity is enhanced with the post-annealing temperature. It is required to note that **Figure 5.10 (a)** doesn't display the Raman spectrum under 110 °C post-annealing since it was observed that the serious background noise was emerged, as shown in **Figure 5.10 (b),** and indicated the invalidation.

Hence, we discuss about the SERS spectrums only under 20 °C, 50 °C and 80 °C. Initially, after 50 °C post-annealing, it was observed that the intensity of Raman-shift bands increased excluding 1200-1300 cm^{-1} and 1400-1500 cm^{-1}. After 80 °C post-annealing treatment, the overall intensity of the Raman signal is strengthened. It is thought that it results from two factors: (i) The influence of the post-annealing temperature on the morphology of Au nanostructures. In the above-mentioned results, it shows changes in the nanostructure. Hence, under the identical illumination conditions, the affected Au nanostructures are attributed to the Raman intensity. (ii) The changed molecular characteristics. The Raman intensity is mainly correlated with the molecular orientation and the polarizability of chemical bands. As for the enhancement after 50 °C post-annealing, it seems that the chemical bands in S-DNTT-10 molecules are affected. Here, it is considered that the possibility of the post-annealing Au-nanostructure affecting the S-DNTT-10 molecular characteristics is relatively small because the post-annealing temperature is low and the influence on the electrodes is not significant, as can be seen from the AFM measurement results. Subsequently, after 80 °C post-annealing, it perhaps not only impacted the chemical bands but also the molecular orientation. For instance, the marked two bands, they obviously showed that the degree of splitting peaks gradually emerged with a high post-annealing temperature. It suggested that the interaction of S-DNTT-10

molecules in the cell is affected by the higher annealing temperature. Upon further analysis, it is believed that the S-DNTT-10 molecules themselves were thermally displaced to 80 °C after annealing. On the other hand, the affected Au thin-films were possibly attributed to impacting the S-DNTT-10 molecular characteristics.

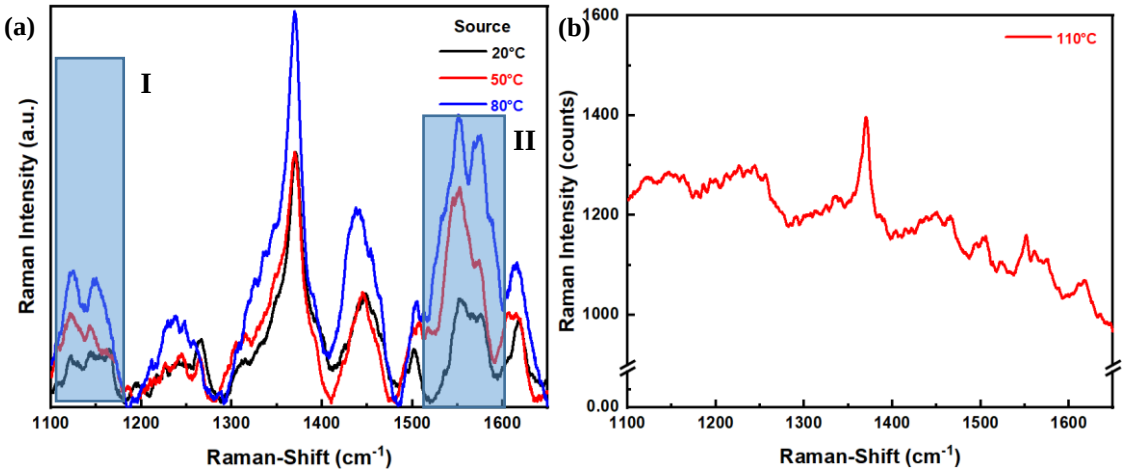


Figure 5.10 (a) The related SERS spectrum (Illumination time of 20 s, accumulation time of 2, grating number of 1800/mm, laser of 633 nm) at source under different post-annealing treatment temperature. (b) The invalid spectrum under 110 °C post-annealing treatment.

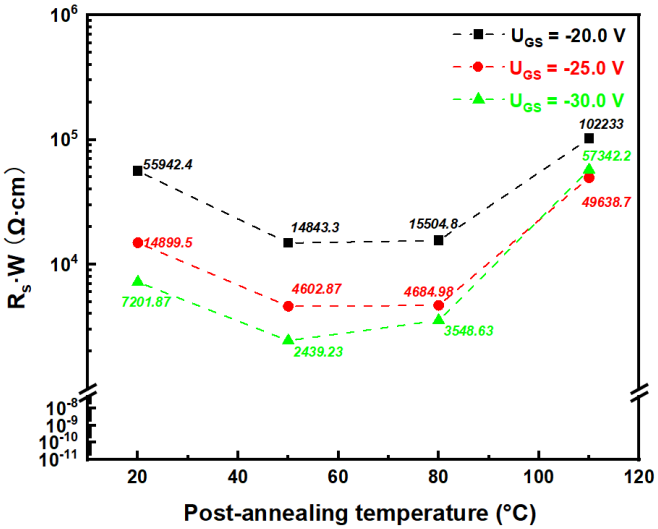


Figure 5.11 The width-contact resistance at source, $R_S \cdot W$, changed with temperature by using device with 25 nm Au-electrodes.

The above results and analysis suggested that the characteristics of S-DNTT-10 molecules located under electrodes were influenced by the post-annealing treatment, especially at higher temperatures. Hence, it was speculated that the charge injection efficiency, characterized as the contact resistance at the source, likely changed with various post-annealing temperatures. To demonstrate this, the extraction of the contact resistance at source electrode from KPFM

measurement was implemented simultaneously, as shown in **Figure 5.11**. It shows that the width-contact resistance at the source, $R_S \cdot W$, changed with the post-annealing temperature under different stressed U_{GS}. At the stressed U_{GS} of -20 V, the $R_S \cdot W$ of 55942.4 Ω·cm decreased to 14843.3 Ω·cm after 30 mins of 50 °C post-annealing treatment. Subsequently, the $R_S \cdot W$ slightly increased to 15504.8 Ω cm with a higher post-annealing temperature. Ultimately, it significantly increased to 102233 Ω·cm after 110°C post-annealing. The changes similar to those at U_{GS} of -20 V were observed at U_{GS} of -25 V and -30 V. As mentioned earlier, in the measurement process of KPFM-post-annealing, the electrodes of the device used were 25 nm. It was thought that changes in the topography of the Au electrode could not have caused the drastic increase in $R_S \cdot W$. Consequently, it mainly resulted from the S-DNTT-10 molecular characteristics affected by the higher post-annealing temperature. Hence, it was suggested that the affected molecular characteristics of S-DNTT-10 could impact the charge transport properties under the source.

As for results at drain electrode, we observed that they are similar to that at source. Hence, we decided to set them at Section 0 in **Appendix**.

In summary, we investigated on the influence of post-annealing temperature on electrical performance of S-DNTT-10-based OTFT from the perspective of materials themselves, which contain the S-DNTT-10 thin-films, Au electrode thin-films and interface of S-DNTT-10/Au thin-film and S-DNTT-10 thin-film/SiO_2 layer modified with HMDS. During this process, the study was associated with several advanced nano-characteristics methods, AFM, Raman spectrum and with SERS effect, KPFM and contact-angle analysis. We suggested that changes in electrical performance of S-DNTT-10-based OTFT are not only correlated with the charge transport characteristics affected in the channel by higher post-annealing temperature, which resulting from S-DNTT-10 molecules changed by themselves and HMDS layer, but also are caused by the affected S-DNTT-10 molecules under electrodes and the contact characteristics of S-DNTT-10 thin-films with electrodes.

5.3 Annealing treatment on deposited substrates for S-DNTT-10 thin-films

References [222,223] pointed out that when the molecular geometric structure of OSCs is curved, for instance DNBDT, C_{10}–DNBDT–NW, and TBBT–V, not only displaying effective intermolecular orbital overlap, but also they exhibit relatively high temperature resistance compared to OSC molecules with linear geometric structures. In **Figure 1.2 (a)**, it exhibited the molecular structure of S-DNTT-10, which has a similar S-shaped curved structure. In the article

[38], during the process of fabricating S-DNTT-10-based OTFT, the substrate deposition temperature of S-DNTT-10 thin-film was at room temperature. Then, the device was subjected to a 20-mins post-annealing treatment with different temperatures in an N_2 environment. It shows that before heating, the average effective field-effect mobility, μ_{avg}, of the device is 1 $cm^2 \cdot V^{-1} \cdot s^{-1}$. Subsequently, as the temperature increases, μ_{avg} gradually improves until μ_{avg} of 3.1 $cm^2 \cdot V^{-1} \cdot s^{-1}$ at a post-annealing temperature of 140 °C. Finally, after completing the 180 °C post-annealing treatment, μ_{avg} was drastically degenerated to 0.18 $cm^2 \cdot V^{-1} \cdot s^{-1}$ due to the emergence of degradation in S-DNTT-10 thin-films by higher temperature. **Figure 5.12** displays that the connection of the deposited thin-film was enhanced after the 140 °C post-annealing treatment in comparison with the topography before post-annealing. It suggested that the improved morphology is beneficial to charge transport. Nevertheless, after the 180 °C post-annealing treatment as **Figure 5.12 (c)** illustrated, it exhibited the appearance of degradation, destroying the connection of the S-DNTT-10 thin-film and possibly blocking the charge transport inside the material.

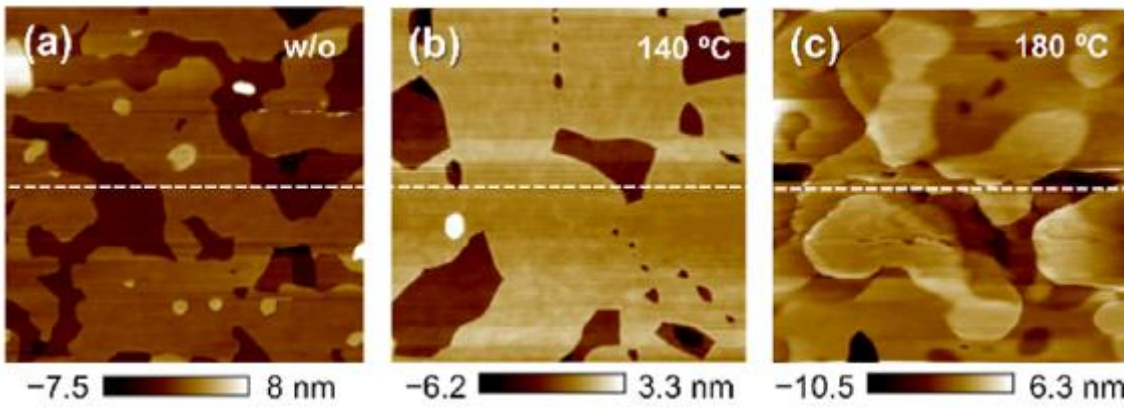
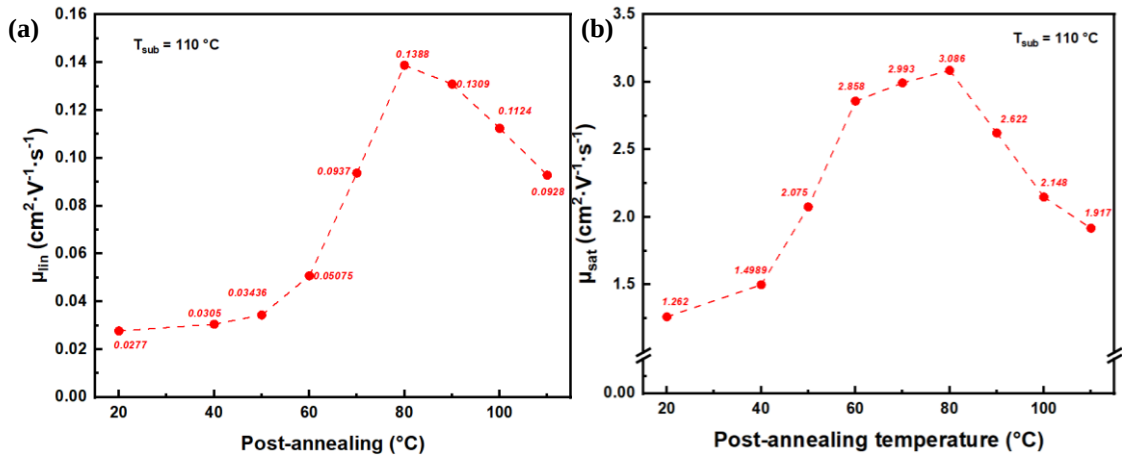


Figure 5.12 The AFM-Topography of S-DNTT-10 thin-film. (a) w/o (meaning without, *i.e.*, before post-annealing), (b) after 140 °C, and (c) after 180 °C post-annealing treatment. [38]

According to the above results, it seems that for S-DNTT-10-based OTFTs with ambient temperature of deposition, the most appropriate post-annealing temperature T_{post}, which improving device to carry out the comparatively excellent performance, is 140 °C. However, our results are different of those shown in the article [38]. One possible reason is that the temperature of deposited substrate, T_{sub}, for S-DNTT-10 molecules is 110 °C. **Figure 5.13 (a)** and **(b)** respectively exhibited the correlated S-DNTT-10-based OTFT performing the linear-mode effective field-effect mobility μ_{lin} (stressed U_{DS} = -1 V) and saturation-mode effective field-effect mobility μ_{sat} (stressed U_{DS} = -40 V) under 30 mins post-annealing with temperature ranging from 20 to 110 °C. For changes in μ_{lin}, it illustrated that the μ_{lin} of 0.028 $cm^2 \cdot V^{-1} \cdot s^{-1}$

before the treatment increased with post-annealing temperature until μ_{lin} as 0.139 $cm^2 \cdot V^{-1} \cdot s^{-1}$ at 80 °C. Subsequently, with further higher temperature, the emergence of a decrease in μ_{lin}. Likewise, the μ_{sat} displayed the identical variation as the above μ_{sat}, in which the related highest value appeared at 80 °C and then the μ_{sat} reduced with post-annealing temperature. It suggested that the T_{post} is changed as 80 °C for S-DNTT-10-based OTFT which the temperature of deposited substrate of S-DNTT-10 is T_{sub} = 110 °C. It implied that the T_{post} for S-DNTT-10-based OTFT is seemingly affected by the temperature of S-DNTT-10 deposited substrate. Not only for the T_{sub} = 110 °C deposited substrate, but also for the device with the T_{sub} = 140 °C deposited substrate of S-DNTT-10 molecules shown in **Figure 5.13 (c)** and **(d)**, it as well performed the different T_{post} with that in the above 110 °C-S-DNTT-10-based OTFT. The temperature of post-annealing for T_{post} = 140 °C-S-DNTT-10-based OTFT is mainly ranging from 80 to 140 °C with step of 10 °C. The changes in μ_{lin}, as **Figure 5.13 (c)** shown, displayed that the comparatively highest value of μ_{lin} appeared at 80 °C and then decreased with temperature. However, with regard to μ_{sat} showing in **Figure 5.13 (d)**, it exhibited the overall reduction with post-annealing temperature. It is noted that the measured temperature of post-annealing ranging from 80 to 140 °C in this process, despite the μ_{sat} is decreased, due to the lacking measurements between 20 °C and 80 °C and combined with results that changes in μ_{lin}. It implied that the T_{post} is possibly located at the range from 20 °C and 80 °C and then it actually appeared within S-DNTT-10-based OTFT with 140 °C deposited substrate.



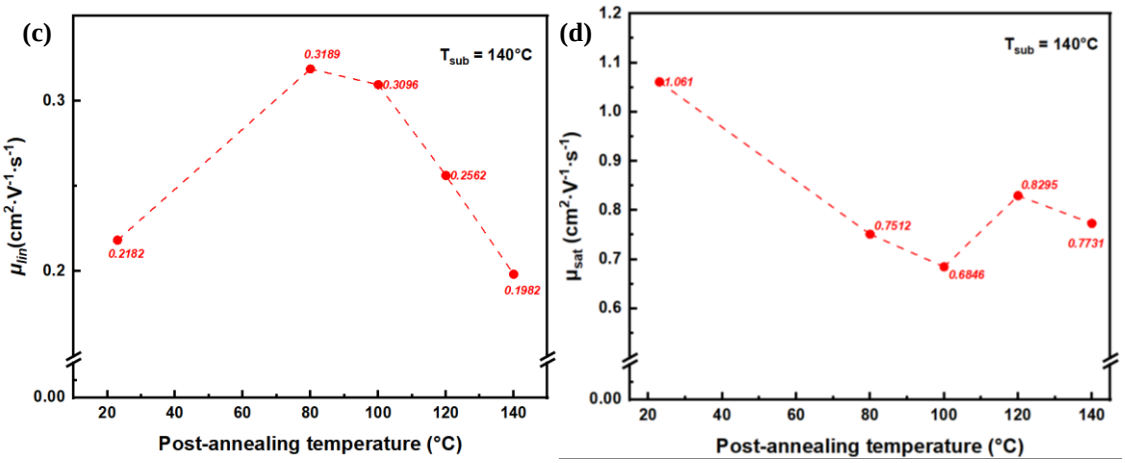


Figure 5.13 The effective field-effect mobility in S-DNTT-10-based OTFT changing with post-annealing temperature in which the thin-film was deposited on 110 °C substrate: (a) Linear-state mobility μ_{lin} and (b) saturation-state mobility μ_{sat}. The effective field-effect mobility in S-DNTT-10-based OTFT changing with post-annealing temperature in which the thin-film was deposited on 140 °C substrate: (c) Linear-state mobility μ_{lin} and (d) saturation-state mobility μ_{sat}.

According to the above results, it was found that although it was the same material, due to the change in the temperature of the deposited substrate of S-DNTT-10 molecules, their T_{post} parameters were different. The organized results are shown in the following **Figure 5.14**. Although for the device with 140 °C S-DNTT-10 deposited substrate, it did not show a relatively accurate T_{post}, based on the relationship between μ_{lin} and post-annealing temperature, it was speculated that the device located at the post-annealing temperature ranging from 20 to 80 °C also had T_{post}. It is speculated that the T_{post} could be decreased with a higher deposited substrate temperature.

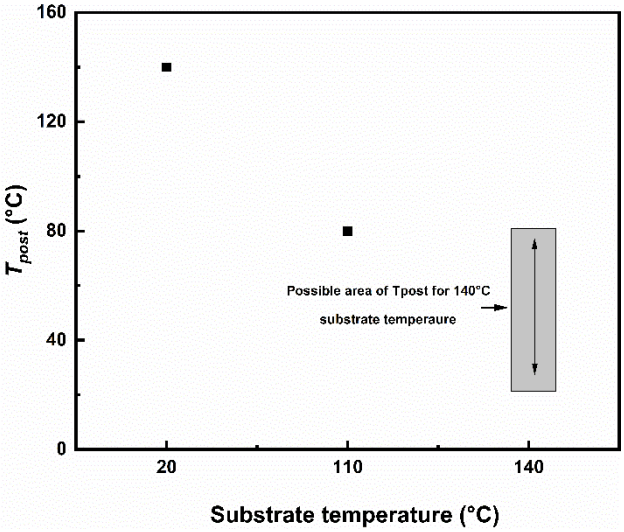


Figure 5.14 The rough relationship between T_{post} and T_{sub}.

Encountered that the T_{post} changed with T_{sub}, it was supposed that it resulted from the environment condition. Since we considered that the environment of thermal evaporation of depositing S-DNTT-10 thin-films via PVD was high vacuum, hence, the changes in organization of several monolayers of S-DNTT-10 closing to the dielectric layer were mainly caused by deposited substrate with higher temperature. However, it was distinct to conditions on post-annealing treatment. The obvious difference we analyzed was the surrounding environment between deposition S-DNTT-10 and post-annealing treatment since the post-annealing was executed under the air environment, including the air pressure and localization of annealed molecules into the air scattering with annealed S-DNTT-10 molecules. Therefore, the influence of environmental conditions could be taken into account.

Ignoring the contact characteristics at the interface between the electrode and S-DNTT-10, the electrical characteristics of S-DNTT-10-based OTFT are related to the topography of the S-DNTT-10 thin-film. More precisely, it is influenced by the degree of π-electron overlap formed due to the arrangement of S-DNTT-10 molecules. Here, a parameter $T_0 = T_0 (T_{post}, T_{sub})$ is envisioned to describe the state where the molecular arrangement within the S-DNTT-10 thin-film can be at a relatively high degree of π-electron overlap and relatively well charge transport characteristics. This parameter is related to the deposited substrate temperature and post-annealing temperature. In the fabrication process, the S-DNTTs molecules were thermally deposited under the approximate vacuum environment; however, the post-annealing treatment was implemented under the normal environment. This indicates that during the deposition process of the S-DNTT-10 thin-film, the morphology is influenced by the combined effect of the van der Waals force between S-DNTT-10 molecules and the influence of the deposition substrate temperature on the thermal movement of the molecules. During the post-annealing treatment process, as the temperature increases, the morphology of the thin-film is not only influenced by the van der Waals force and the intensified thermal movement of the molecules due to post-annealing, but also the atmospheric environments participated in further influencing the arrangement of S-DNTT-10 molecules, causing the molecular arrangement to approach or deviate from parameter T_0, thereby changing the performance of the device. In particular, overly high or inappropriate post-annealing could accelerate the S-DNTT-10 molecular movement, causing the degradation of the thin-film. Regarding the reduction of T_{post} with the substrate temperature, it might be easier to understand with the aid of parameter T_0. As mentioned previously, parameter T_0 is jointly influenced by T_{post} and T_{sub}. For T_{sub}, it affects the initial state of the molecular arrangement within the S-DNTT-10 thin-film. According to the current results,

the higher the T_{sub}, the closer the molecular arrangement within the thin-film is to the molecular arrangement and π-electron overlap state when it is at T_0. Therefore, when T_{sub} is higher, a relatively high post-annealing temperature is not required to make the molecular arrangement approach or reach the state at T_0. It also seems that the post-annealing treatment and the air environmental conditions could make a lesser contribution to improving the electrical performance of S-DNTT-10-based OTFT.

In this section, the variation of T_{post} with T_{sub} in S-DNTT-10-based OTFT was presented. It should be noted that the current presented results and analysis are considered to have limitations. On the one hand, only the post-annealing treatment processes of normal temperature, 110 °C and 140 °C -T_{sub} were presented. If the *IV* performance at 50 °C and 80 °C under different post-annealing temperatures could be presented, the research results would be more complete and systematic, and the analysis would be more persuasive. On the other hand, no advanced characterization methods were used. Because they can compare the morphological changes of the deposition of S-DNTT-10 thin-films and the S-DNTT-10 thin-film after post-annealing, and better explain the influence of T_{sub} on the morphology of the S-DNTT-10 thin-film. Limited by the research time, this discovery could only reach the current state for the time being. However, it is believed that this discovery and the completed preliminary research provide effective information for optimizing the preparation conditions of S-DNTT-10-based OTFT in the future.

5.4 Conclusion

In this chapter, we examined the influence of annealing treatment on the electrical performance of top-contact bottom-gate (TCBG) S-DNTT-10-based OTFTs. We found that both the post-annealing process and the specific annealing temperature significantly influence device performance. Notably, an optimal annealing temperature emerged that enhances device performance. The changes in electrical characteristics were attributed to the impact of varied temperatures on S-DNTT-10 thin films and the interfaces between Au electrodes and S-DNTT-10, as analyzed using AFM, Raman spectroscopy, and KPFM techniques.

For TCBG S-DNTT-10-based OTFTs, the electrical characteristics varied with post-annealing temperatures from 50 to 110 °C, in 30 °C increments. The devices exhibited improved output performance with increasing temperature up to 50 °C, followed by a decline at 80 °C and 110 °C. For the S-DNTT-10 thin films, higher annealing temperatures altered the film topography, with more significant damage and cracks observed at higher temperatures.

Raman spectroscopy revealed molecular changes, as evidenced by intensity variations and peak splitting in the Raman-shift bands, which affected charge transport in the channel. Intrinsic mobility measurements from KPFM showed that the initial $\mu_{intrinsic}$ of 1.28 $cm^2 \cdot V^{-1} \cdot s^{-1}$ increased to 1.44 $cm^2 \cdot V^{-1} \cdot s^{-1}$ at 50 °C, but decreased to 0.154 $cm^2 \cdot V^{-1} \cdot s^{-1}$ with further increases in post-annealing temperature. Additionally, contact-angle analysis with water and Dim revealed slight changes in the HMDS surface characteristics, likely contributing to the altered S-DNTT-10 film morphology. The combined effects of changes in both the S-DNTT-10 film and the HMDS layer may account for the observed topographical variations.

Furthermore, we found that higher annealing temperatures disrupted the contact characteristics between S-DNTT-10 and the electrodes, with the *RMS-Roughness* increasing from 1.910 nm to 19.15 nm at 110 °C. This suggests that higher post-annealing temperatures degrade charge injection and collection properties, as evidenced by increased contact resistance observed through KPFM.

Ultimately, we found that the specific post-annealing temperature (T_{post}), which results in enhanced device performance, varies with the substrate deposition temperature (T_{sub}) during the S-DNTT-10 fabrication process. It was roughly concluded that T_{post} decreases with higher T_{sub}.

6 A way to improve the charge injection in S-DNTT-10-based OTFTs

6.1 Introduction

OTFTs have been applied in commercial fields due to the unique properties of organic materials [206,224]. However, these materials degrade in air, significantly reducing device lifetime. While adjusting molecular orbitals (MOs), such as lowering the HOMO energy level, can improve the stability of p-type materials, it also increases the energy barrier at the interface of OSC and gold (commonly used as electrodes) and consequently leads to non-linear effect in output characteristics I_D-U_{DS}. This raises contact resistance (R_c) which affecting charge injection/extraction [91,121,128,129], and limits OTFT applications. Ideally, a low pure Ohmic contact is preferred, but a higher R_c owing to the presence of an obvious energy barrier at OSC/electrodes interfaces, causes non-ideal performance. It was evidenced by a nonlinear or 'S-shaped' output curve (I_D-U_{DS}) or a "kink" or "double slope" in the transfer characteristics (I_D-U_{GS}) [225]. High R_c reduces charge injection efficiency, increases the operating the voltages applied to the OTFTs, limit the operation frequency, shortens device lifetime, and causes nonlinear effects in *I-V* characteristics, hindering accurate extraction of electrical parameters [101,130,131], ultimately obstructing effective OSC design and OTFT optimization.

In this chapter, we propose a method for enhancing charge injection efficiency in top-contact bottom-gate (TCBG) S-DNTT-10-based OTFTs through the introduction of a pentacene thin film via the electrodes. Section 6.2 will primarily investigate the influence of the additional pentacene thin film on the electrical performance of TCBG S-DNTT-10-based OTFTs. In Section 6.2.1, we will briefly introduce the proposed use of pentacene from the perspective of DFT simulation and energy level analysis. Section 6.2.2 will present the optimization of pentacene thin-film thickness and the changes in electrical characteristics of TCBG S-DNTT-10/Pentacene-based OTFTs compared with TCBG S-DNTT-10-based OTFTs. In Section 6.2.3, we will explore electrical changes from the perspective of contact resistance, primarily using Kelvin Probe Force Microscopy (KPFM). Furthermore, we will modify the structure of the initial S-DNTT-10/Pentacene-based OTFTs to further enhance performance. Section 6.2.4 will highlight the changes in electrical stability induced by the additional pentacene thin film (on the whole S-DNTT-10 thin-film) after experiencing the bias-stress (*BS*) effect, compared to pure TCBG S-DNTT-10-based OTFTs. Finally, in Section 6.2.5, we will

examine the influence of post-annealing treatment on TCBG S-DNTT-10/Pentacene-based OTFTs.

6.2 Top-contacted bi-layers-based OTFTs

Despite the TCBG S-DNTT-based OTFT performed excellent electrical characteristics with high mobility, it inevitably suffered from the nonlinear electrical characteristics, and it correlated with the greater R_c. We speculate that the nonlinear effect originates from charge injection obstructing at the source, as Section 2.6.1 exhibited. To overcome it, we deposited pentacene on the S-DNTT-10 thin-film into the TCBG configuration. The changes in the properties of charge injection are characterized by R_C, which is extracted from Kelvin Probe Force Microscopy (KPFM) method expressing in Section 2.4.4.3. Compared with Transmission Line Mode (TLM) [170,202,226], it can separately measure R_s and R_d. and be used into OTFTs with linear and saturation-regime. However, the TLM method was only valided in the linear regime.

6.2.1 Design idea of S-DNTT-10-based OTFTs with extra OSC layers

The contact resistance R_c is located at source (R_s) and drain (R_d), and composed of two elements: the injection resistance (R_{inj}) and access resistance (R_{access}) as illustrated for R_s in **Figure 6.1 (a)** [128,227,228]. As Section 1.4.5.1.4 said, R_{inj} is caused by the Schottky energy barrier (Φ_B) for charge injection at the source/OSC interfacial layers [229] and R_{access} arises from the resistivity of OSC [91], where the injected charge from the source enters the edge of the conductive channel. [227] In addition, it existed the channel resistance, $R_{channel}$, located at the channel. It is only correlated with the charge transport characteristics of the OSC thin-film in the parallel direction.

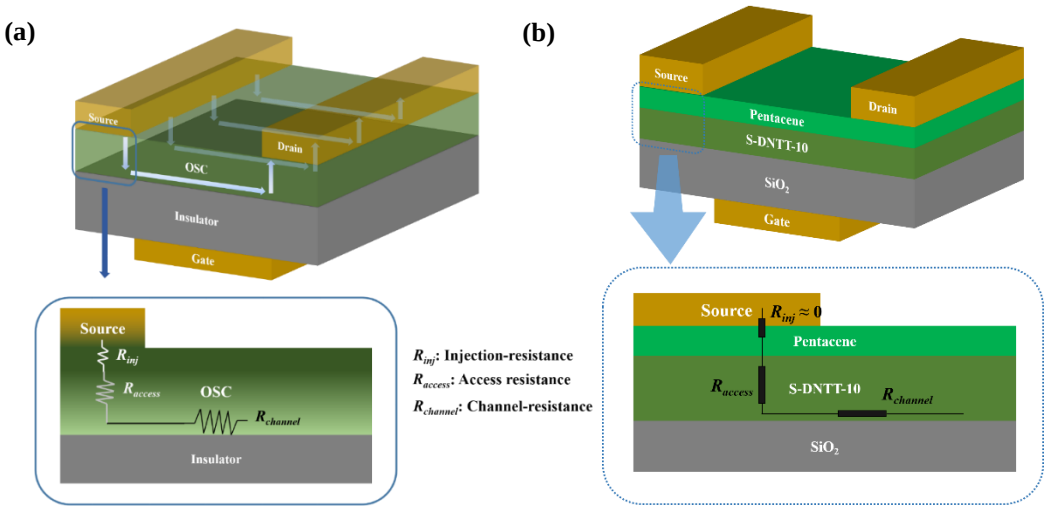


Figure 6.1 Schematic of (a) the contact resistance (R_c) consisting of injection resistance (R_{inj}) and access resistance (R_{access}). The channel resistance ($R_{channel}$) located at the interface of OSC thin-film and insulator layer, and (b) the designed structure of TCBG S-DNTT-10/Pentacene-based OTFT with R_{inj} almost equals to zero.

Currently, strategies to effectively reduce R_c include selecting appropriate contact materials [128,137,230,231], functionalizing electrodes with self-assembled monolayers (SAMs) [232–234], using carbon nanotubes (CNTs) as electrodes [235,236], incorporating metal oxides to adjust Φ_B [237,238], doping the OSC thin film [239–241], optimizing semiconductor thickness to reduce R_{access} [242–245], post-annealing treatment, using a thin gate dielectric, and optimizing the molecular arrangement at the source contact [98]. Based on the dependence of R_c on the Schottky barrier, reducing the barrier is an effective approach. In the past, organic small molecules were used as charge injection layers (CILs) to reduce contact resistance through doping, improving charge injection via an additional interface dipole. However, a persistent issue is the potential hybridization between dopants and substrate molecules [236,246,247]. Additionally, using multiple OSC layers, such as in organic heterojunction transistors (OHTs), can enhance electrical performance by forming a high-carrier-density channel due to quantum confinement and interface charge accumulation, outperforming OTFT with a single OSC layer [130,248–252]. However, there is limited research on the use of OHTs to reduce R_c and improve charge injection efficiency.

The charge injection is primarily determined by the energy barrier at the interface between the source and the OSC thin film, which depends on the difference between the work function of source and the energy level of the OSC MOs. The TCBG-OTFTs with a large energy barrier at the source, like the S-DNTT-10-based OTFTs in our study showing in Section 2.6.1, exhibit poor charge injection, as reflected by the lower effective mobility μ_{lin} extracted from the I_D-U_{GS}

transfer characteristics in linear regime. Herein, we propose a method to improve charge injection by depositing an additional OSC thin film (as **Figure 6.1 (b)** shown) with an energy level close to the work function of the source material onto the initial OSC active layer, ensuring no reaction with the substrate material. A small energy barrier height between electrodes and the additional OSC will facilitate hole injection into the S-DNTT-10 thin film. In this study we use pentacene as additional OSC thin film. This approach we think has several advantages:

(i) Additional pentacene below the electrodes increases the injection efficiency. The nonlinear effect in the output characteristics I_D-U_{DS} of S-DNTT-10-based OTFTs shown in Section 2.6.1, is not caused by the deposition process. This effect is attributed to significant R_c at the source, which mainly arises from the energy barrier between the Fermi level of gold and the HOMO energy level of S-DNTT-10 molecules, as indicated by DFT simulations in **Figure 6.2 (a)**. The simulated HOMO energy level of a single pentacene molecule is close to the Fermi level of gold, as shown in **Figure 6.2 (b)**. In **Figure 6.2**, they characterized the π-electron wave function distribution, depicted by red and green regions, which indicates the different phase of the function. And the molecular structures, π electron wave function distributions, and MO energy-levels (HOMO and LUMO) for pentacene and S-DNTT-10 are on the left and right, respectively. The pentacene has a lower HOMO energy level, closer to the work function of gold allowing theoretically efficient hole injection into the conductive channel at the S-DNTT-10/insulator interface [253]. The simulation exhibits that the HOMO and LUMO energy-levels of S-DNTT-10 differ from those of pentacene: HOMO (S-DNTT-10) ≈ -5.46 eV, HOMO (pentacene) ≈ -5.0 eV [38]; LUMO (S-DNTT-10) ≈ -1.69 eV, and LUMO (pentacene) ≈ -3.0 eV [253]. Since the results display that the π electron wave functions are distributed throughout the pentacene molecule, including C=C bonds and C-H bonds. Conversely, π electron wave functions of S-DNTT-10 molecule are mainly located at the S-shaped thiophene ring within the molecule. It implies that the different molecular structures results in the intrinsic different MOs energy-levels, under ignoring the arrangement impacting the MOs. Noted that the reference mainly displays the MOs of S-DNTT-1 [38], but the presented discrepancy between S-DNTT-1 (HOMO ≈ -5.318 eV) and S-DNTT-10 in our simulation can be attributed to one possible factor that the S-DNTT-1 and S-DNTT-10 have the different structure in the alkyl chains, and thus potentially affecting calculations of MOs. Nevertheless, given the limitation of research on S-DNTT-10, no published experimental MO energy-levels have been reported to date. Additionally, despite our DFT simulations providing HOMO and LUMO levels for single molecule, since the actual thin-film contains many molecules and according to band theory, the

exact MOs energy-levels are influenced by the overlapping MOs of adjacent molecules [188,254]. Hence, the exact value in HOMO of a thin-film diverges from that of a single molecule. For simplify, the subsequent discussion will refer to MO energy-levels of S-DNTT-10 molecule from DFT calculations.

The above results implied that the pentacene molecule has a lower HOMO energy level, closer to the work function of gold allowing efficient hole injection into the conductive channel at the S-DNTT-10/insulator interface [253]. These DFT simulations are also confirmed by *IV* characteristics of TCBG-pentacene-based OTFTs in which linear charge injection process is evidenced by a linear output curve at low drain voltages.[254,255]

(ii) The outstanding performance related to charge transport properties in S-DNTT-10 is maintained. Notably, thermally deposited TCBG S-DNTT-10-based OTFTs with gold (Au) electrodes in our lab have shown excellent electrical performance, with a saturation-mode effective field-effect mobility (μ_{sat}) exceeding 6.5 $cm^2 \cdot V^{-1} \cdot s^{-1}$ (seeing in Section 0, **Appendix**).

(iii) We confirmed that no hybridization occurs between S-DNTT-10 and pentacene, as the Raman spectrum of pentacene on S-DNTT-10 showed no significant changes (seeing in **Figure 6.3**). S-DNTT-10 molecules do not react with pentacene molecules. Since **Figure 6.3 (a)** displayed the Raman spectrum of pentacene thin-film and presented the Raman-shift peaks, and **Figure 6.3 (b)** exhibited the Raman spectrum of pentacene and S-DNTT-10 thin-films under the 532 nm excited source. We observed that the positions of Raman-shift peaks do not shift compared with them in the pentacene by several black lines marking peaks.

(iv) The additional pentacene layer can be directly deposited onto the S-DNTT-10 surface by PVD.

(v) Moreover, pentacene is inexpensive and well-studied.

Pentacene exhibits a notable susceptibility to environmental contaminants [210,256]. Nevertheless, it is pertinent to note that in this approach the layer of pentacene is situated beneath the electrodes. The electrodes will protect the pentacene and may be regarded as a form of encapsulation. Consequently, the instability associated with pentacene does not present a concern in this context. Therefore, pentacene is a good candidate for the additive layer and we decided to thermally deposit pentacene thin films around the electrodes to form S-DNTT-10/Pentacene-based OTFTs.

We will see in the following that these advantages collectively enhance charge injection efficiency and improve the performance of S-DNTT-10-based OTFTs.

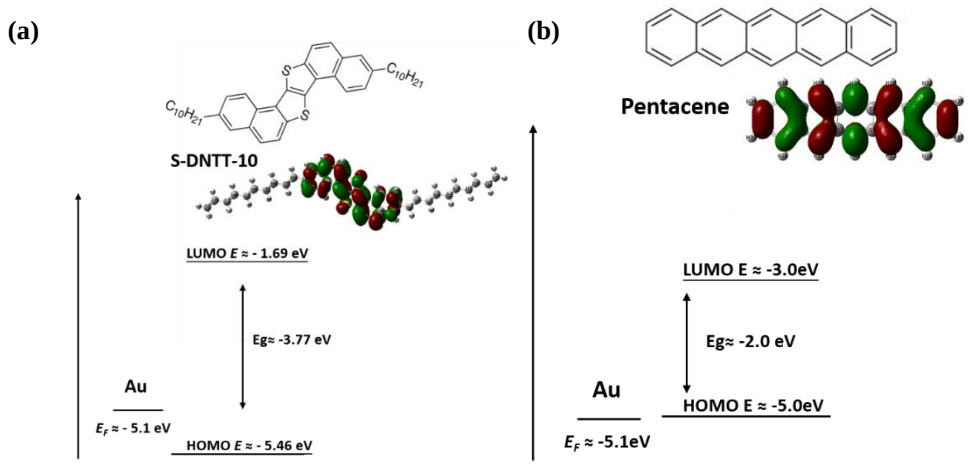


Figure 6.2 The Fermi level of gold (Au) respectively compared with (a) one S-DNTT-10 molecule and (b) the Pentacene molecule.

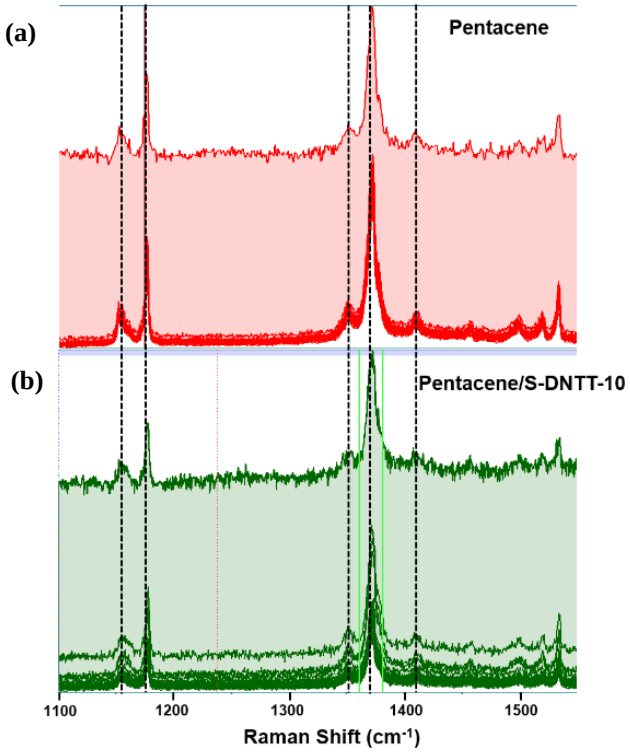


Figure 6.3 The Raman spectrum of (a) 25 nm pentacene thin-film and (b) the combination of 25 nm S-DNTT-10 and 20 nm pentacene thin-film, under 532 nm excitation light (power filter = 3.2%, acquisition time = 5s, accumulation time = 1, grating = 1800/mm) at air environment.

6.2.2 Changes in electrical performance

To investigate on the additional pentacene thin-films affecting the electrical performance of S-DNTT-10-based OTFTs, we measured the output characteristics (I_D-U_{DS}) and transfer characteristics (I_D-U_{GS}) under the same bias conditions within a glovebox. In this section, firstly we plan to optimize the thickness of the additional pentacene layer. Subsequently, we will show

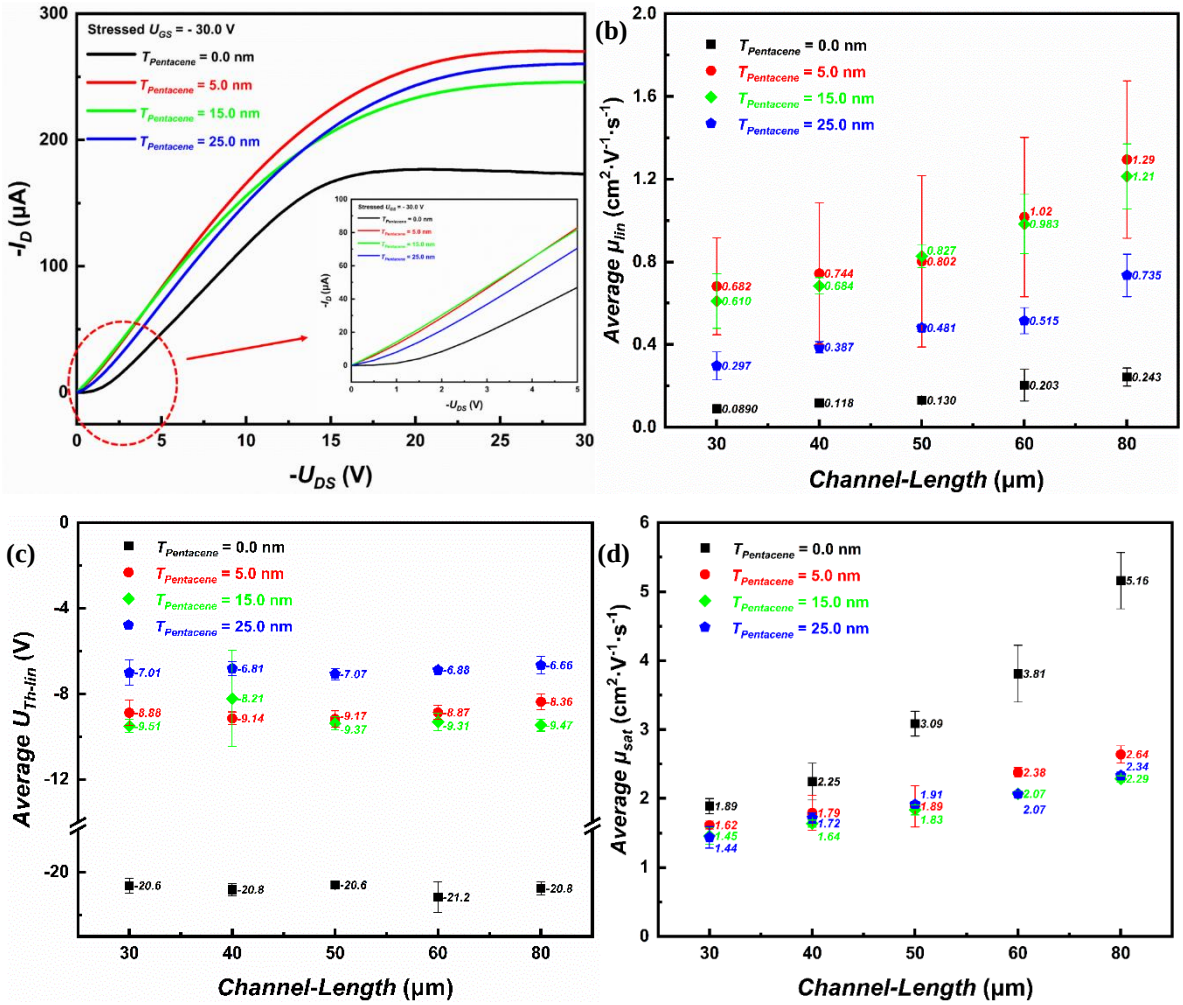
the *IV* improvements of our approach. Ultimately, we will confirm the *IV* improvements in term of contact resistances extract from KPFM.

6.2.2.1 Optimization of the additionnal pentacene layer

The electronic properties of OTFTs are affected by the thickness of the OSC thin film due to the presence of access resistance (R_{access}) (**Figure 6.1**). In this part, we investigated the influence of pentacene thin-film thickness on the performance of S-DNTT-10/Pentacene-based OTFTs and identified the optimal thickness. To explore the effect of pentacene on the electronic performance of TCBG S-DNTT-10-based OTFTs, we fabricated a series of devices under vacuum conditions. These included one S-DNTT-10-based OTFT and three S-DNTT-10/Pentacene-based OTFTs with pentacene thin films of 5 nm, 15 nm, and 25 nm. **Figure 6.4 (a)–(e)** summarizes the *IV* performance of these devices, including output characterisitcs, average effective field-effect mobility (μ_{lin} and μ_{sat}), and average threshold voltage (U_{Th}). The parameter "$T_{Pentacene}$ = 0.0 nm" in the figures refers to the TCBG S-DNTT-10-based OTFT without pentacene. **Figure 6.4 (a)** exhibited the drain current I_D of four different TCBG-OTFTs (channel length of 30 μm and channel width of 1000 μm) at biased U_{GS} = -30 V in output characteristics I_D-U_{DS}, and obviously showed that TCBG S-DNTT-10-based OTFT (black curve) with non-linear effect at small U_{DS} area nearly ranging from 0 V to -2.5 V. It is required to say that based on our *I-V* measurements on several tens of TCBG S-DNTT-10/Pentacene-based OTFTs, they didn't present the serious hysteresis effect in the output or transfer characteristics. Hence, we did not display the back-curve in the *I-V* characteristics. However, after depositing pentacene thin-film on the S-DNTT-10 thin-films, the improvement of this non-linear performance was appeared in the other three different kinds of devices. Herein, the inserted figure highlights the I_D measured at the initial U_{DS} bias range and the comparatively linear-effect in these devices with pentacene thin-film. Particularly, it seems that the device with a 25 nm pentacene thin-film (blue curve) exhibits a more pronounced non-linear shape compared to those with 5 nm (red curve) and 15 nm (green curve). The above results implied the changes in charge injection by extra pentacene thin-films.

Figure 6.4 (b) initially showed an improvement of charge injection efficiency in term μ_{lin} into TCBG S-DNTT-10/Pentacene-based OTFTs, including thickness of pentacene with 5 nm, 15 nm and 20 nm, compared with that in TCBG S-DNTT-10-based OTFTs. For instance, the average μ_{lin} of S-DNTT-10-based OTFT with channel length of 80 μm was 0.243 $cm^2 \cdot V^{-1} \cdot s^{-1}$ for, and after deposition of pentacene thin-films, it exhibited the enhancement of μ_{lin}. i.e., 1.29 $cm^2 \cdot V^{-1} \cdot s^{-1}$ (5 nm pentacene), 1.21 $cm^2 \cdot V^{-1} \cdot s^{-1}$ (15 nm pentacene) and 0.735 $cm^2 \cdot V^{-1} \cdot s^{-1}$ (25 nm

pentacene). On the other hand, **Figure 6.4 (b)** showed the μ_{lin} changed with the thickness of pentacene thin-films. It implied the highest improvement on μ_{lin} for pentacene thickness: 5 nm < $T_{Pentacene}$ < 15 nm. And for devices with 25 nm pentacene thin-film, it showed a decrease μ_{lin}. For example, in devices with L = 30 μm, the average μ_{lin} values are approximately 0.68 $cm^2 \cdot V^{-1} \cdot s^{-1}$ for 5 nm, 0.61 $cm^2 \cdot V^{-1} \cdot s^{-1}$ for 15 nm, and 0.30 $cm^2 \cdot V^{-1} \cdot s^{-1}$ for 25 nm. This suggests the trend μ_{lin} (5 nm) > μ_{lin} (15 nm) > μ_{lin} (25 nm) across different L values. The observed reduction in μ_{lin} suggests that charge injection from the source to the OSC layers was hindered, as demonstrated by the corresponding I_D-U_{DS} output characteristics at saturation, shown in **Figure 6.4 (a)**.



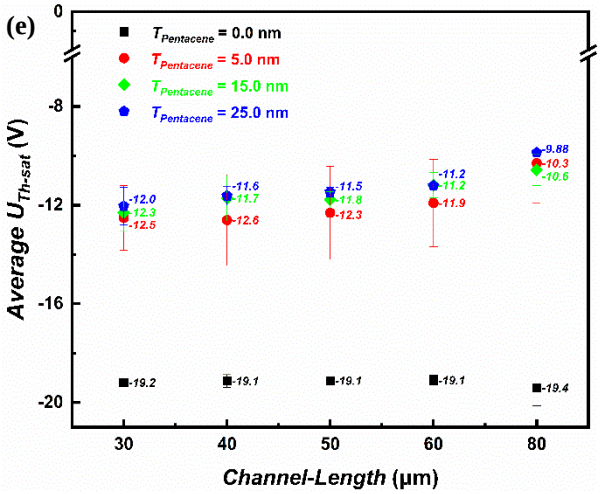


Figure 6.4 The electric characteristics of TCBG S-DNTT-10-based OTFTs stacked with different thickness of pentacene thin-films. (a) The output characteristics I_D-U_{DS} for S-DNTT-10/Pentacene-based OTFTs under U_{GS} of -30 V (b) The average linear-mode effective field-effect mobility μ_{lin} extracting at U_{DS} = -1 V. (c) The corresponding average threshold voltage U_{Th-lin}. (d) The average saturation-mode effective field-effect mobility μ_{sat} extracting at U_{DS} = -30 V. (e) The corresponding average threshold voltage U_{Th-sat}. The average value at each different channel length was extracted from 4 devices.

We speculate that the decrease in charge injection efficiency is related to the thicker pentacene thin films, as thickness was the variable parameter in this case. For average μ_{sat} in **Figure 6.4 (d),** it was observed the maximum value of average μ_{sat} was emerged at 5 nm pentacene thin-film expected for channel length of 50 μm. With regard to the comparison of average μ_{sat} (15 nm) and μ_{sat} (25 nm), it exhibited the similar value, even being identical at channel length of 60 μm. These results suggested that thicker pentacene layers degrade the charge transport properties in S-DNTT-10/Pentacene-based OTFTs. Thus, pentacene layers of 5 nm appear to offer better charge transport properties in TCBG S-DNTT-10/Pentacene-based OTFTs. The **Figure 6.4 (c)** shows that the absolute average threshold voltage in linear regime U_{Th-lin} for the 25 nm pentacene is smaller than that of the 5 nm and 15 nm. However, the shift is very small and does not compensate for the overall superior performance of the 5 nm and 15 nm layers in terms of charge transport. Additionally, U_{Th-sat} across all devices is similar, with no significant differences.

In TCBG S-DNTT-10-based OTFTs stacked with different thicknesses of pentacene thin films, varying electrical performance was observed, particularly lower μ_{lin} in devices with 25 nm-thick pentacene films. Since the molecular arrangement at the surface contacting the source can impact charge injection, and the surface properties of pentacene change with thickness [257], we hypothesize that the surface characteristics at the pentacene/source interface contribute to the varied μ_{lin}. Atomic Force Microscopy (AFM) was employed to characterize

surface molecular organization through roughness. AFM measurements were conducted on the channels (3 × 3 μm) of S-DNTT-10-based OTFTs with pentacene films of 5 nm, 15 nm, and 25 nm thickness. As shown in **Figure 6.5 (a)-(c)**, the pentacene grains on the surface exhibited dendritic structures, similar to those in reference [154]. However, clearer grain boundaries were observed in the 15 nm and 25 nm films compared to the 5 nm film. The values of ***RMS roughness*** were 2.982 nm, 4.019 nm, and 5.777 nm, respectively, suggesting that surface roughness possibly increases with film thickness and resulted in less-ordered π-conjugation of pentacene [258]. The references found that the surface roughness was one main factor to influence the charge transport characteristics [170,258]. Hence, we speculate that the different pentacene molecular arrangements in the three devices result in varied physical interface contact, which affects charge injection. These findings suggest that the molecular characteristics at the pentacene/electrode interface influence charge transport and electronic properties in the devices. Additionally, the reference [259] highlights the R_c is increased with the thickness of OSC thin-film. We assume that both the surface characteristics and thickness of pentacene films contribute to the observed changes in electrical performance.

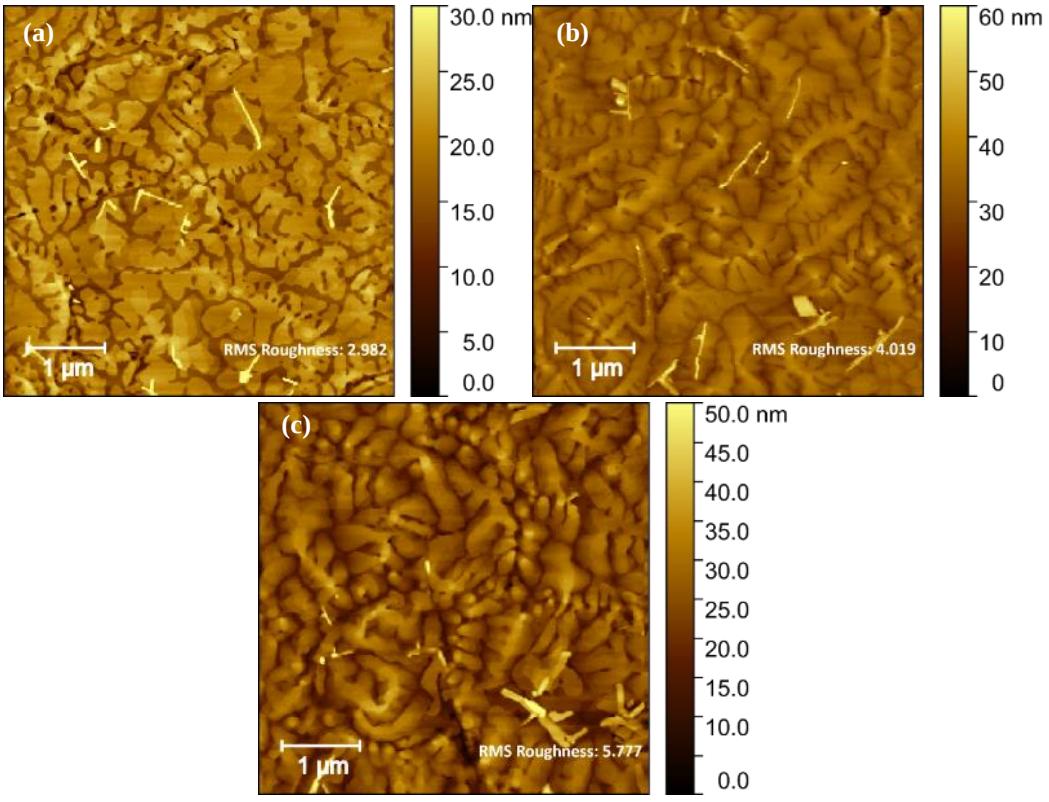


Figure 6.5 The related surface characterization of pentacene thin-films deposited on S-DNTT-10 thin-films. The AFM measurements with extracted *RMS roughness* on (a) 5 nm pentacene thin-film, (b) 15 nm pentacene thin-film, and (c) 25 nm pentacene thin-film.

This study shows that the OTFTs with 5 nm and 15 nm pentacene layers have better performance than the OTFTs with 25 nm indicating that both thicknesses are suitable for further enhancing S-DNTT-10/Pentacene-based OTFTs. However, the study is limited by the fact that only three pentacene thicknesses were tested. It is possible that a thickness between 5 nm and 15 nm may result in more effective improvements. Therefore, future experiments could investigate S-DNTT-10-based OTFTs stacked with pentacene layers between 5 nm and 15 nm.

Regarding the results show above, the optimize pentacene thickness is around 5 nm. In the following we continue the investigation of S-DNTT-10/Pentacene-based OTFTs with a 5 nm pentacene thin film.

6.2.2.2 5 nm S-DNTT-10/Pentacene-based OTFT electrical performance

In this section we discuss the electrical performance of 5 nm S-DNTT-10/Pentacene-based OTFT. First, we analyze in detail the output characteristics I_D-U_{DS} and then, the transfer *IV* characteristics.

Owing to the blurred effect in PVD by diffusion of atoms inevitably caused the decreased channel. It makes the fabricated devices actually have a narrower length, as illustrated in Section 0, Appendix. As similar to various channel length displaying in the following parts, the designed lengths of 30 µm, 40 µm, 50 µm, 60 µm and 80 µm, in practice, is respectively 24.75 µm, 34.65 µm, 44.55 µm, 54.45 µm and 74.25 µm.

6.2.2.2.1 Output characteristics

Figure 6.6 (a) displayed the comparison of I_D-U_{DS} characteristics for TCBG S-DNTT-10-based OTFT and TCBG S-DNTT-10/Pentacene-based OTFT, both having a channel width (W) and the length (L) of nearly 1000 µm and 54.45 µm, respectively. Dashed lines and solid lines correspond to TCBG S-DNTT-10-based OTFT, and TCBG S-DNTT-10/Pentacene-based OTFT, respectively. It showed the linear-region and saturation-region operation in the -U_{DS} range of 0 ~ 40 V at different U_{GS}. It can be summarized as the following points.

As mentioned previously and shown in **Figure 6.4 (f)**, the S-DNTT-10/Pentacene-based OTFTs showed an improvement in the nonlinear or S-shaped effect in the I_D-U_{DS} characteristics at low |U_{DS}| bias. Specifically, **Figure 6.6 (b)** compares the I_D-U_{DS} curves for -U_{DS} values ranging from 0 to 5 V, corresponding to **Figure 6.6 (a)**. The S-DNTT-10-based OTFTs exhibited poor linear-mode drain current ($I_{D\text{-}lin}$) at |U_{DS}| values up to 1 V, with $I_{D\text{-}lin}$ becoming significant only when -U_{DS} exceeded 1 V. This curved shape indicates poor linear-state performance and lower charge injection efficiency. In contrast, the S-DNTT-10/Pentacene-

based OTFTs displayed nearly linear I_D-U_{DS} characteristics and higher $I_{D\text{-}lin}$ under the same U_{GS}, suggesting enhanced charge injection and higher μ_{lin}. However, despite the improvement in the nonlinear effect, as we will see in the next section, the S-DNTT-10/Pentacene-based OTFTs showed lower saturation -state drain current ($I_{D\text{-}sat}$) when -U_{GS} exceeded 30 V, while they had higher $I_{D\text{-}sat}$ at -U_{GS} values below 30 V.

To go further on electrical characterization and comparison between S-DNTT-10-based OTFT and S-DNTT-10/Pentacene-based OTFT we extract OTFT parameters from transfer characteristics I_D-U_{GS} in the next section.

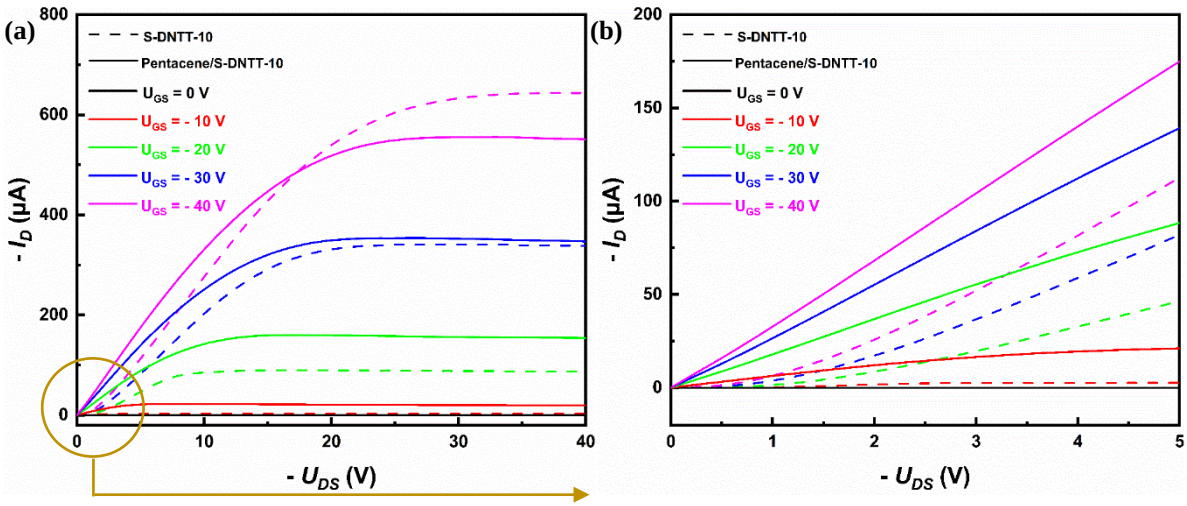
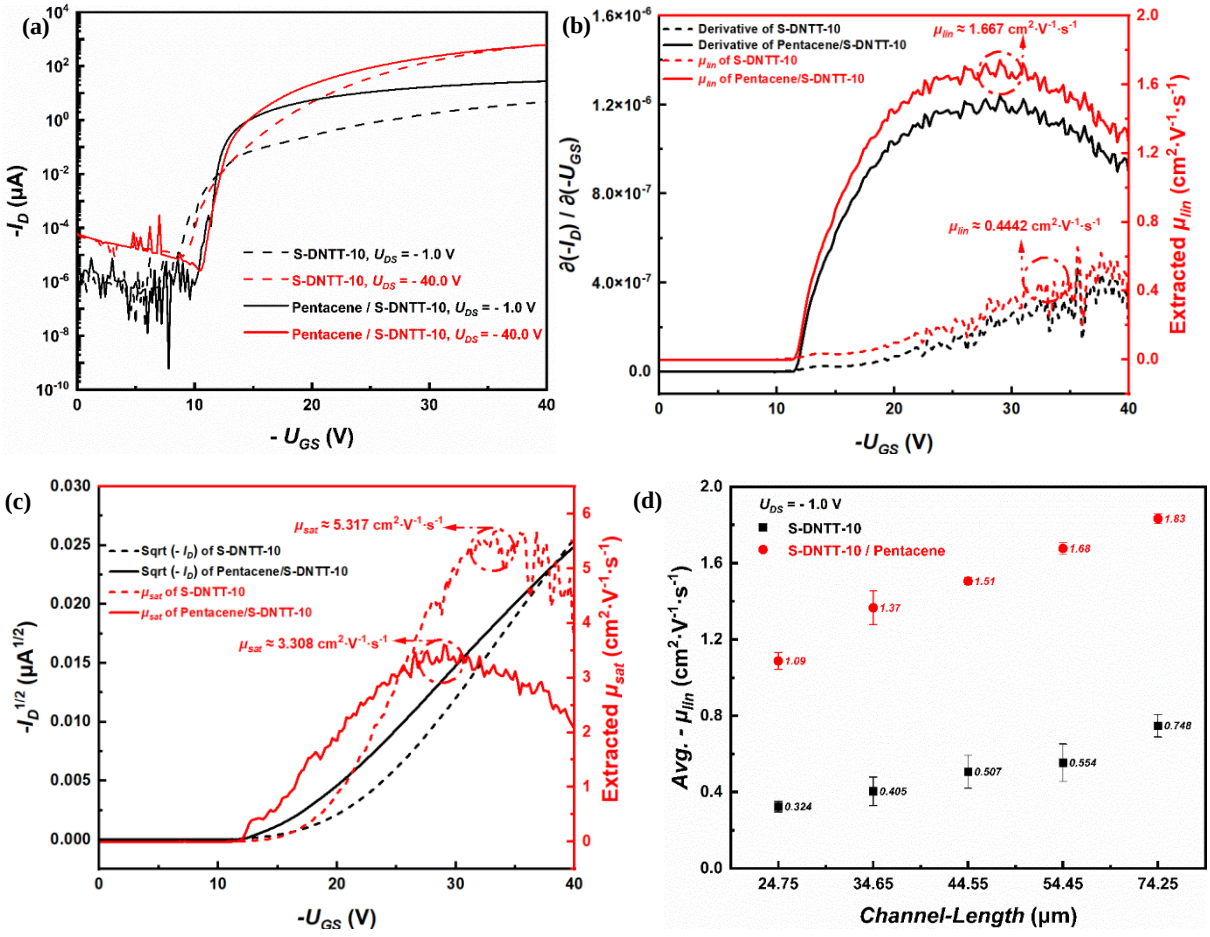


Figure 6.6 Typical I_D-U_{DS} characteristics in this study of (a) the TCBG S-DNTT-10-based OTFT and the TCBG S-DNTT-10/Pentacene-based OTFT (both channel length $L \approx 54.45$ µm and width $W \approx 1000$ µm). The biased U_{GS} and -U_{DS} respectively ranging from 0 V to -40 V with the step of -10 V, and from 0 to 40 V with the increment of 0.5 V. (b) The corresponding local presentations under the -U_{DS} ranging from 0 to 5 V corresponding to figure (a).

6.2.2.2.2 Transfer characteristics

We measured the transfer characteristics I_D-U_{GS} of both the TCBG S-DNTT-10-based OTFT and the TCBG S-DNTT-10/Pentacene-based OTFT by the identical bias conditions. Since it was not observed the great hysteresis effect, hence, we decided to ignore the errors caused by hysteresis effects on the experimental results and show only forward-curve. Based on the mentioned above output characteristics I_D-U_{DS}, the external bias conditions for linear- and saturation-mode respectively being at U_{DS} = -1 V and U_{DS} = -40 V. The comparative transfer characteristics I_D-U_{GS} results are illustrated in **Figure 6.7 (a)**. Ashort dashed line depicts the TCBG S-DNTT-10-based OTFTs measurements, and a solid line represents that for TCBG S-DNTT-10/Pentacene-based OTFTs.

According to the **Equation (1.13)** and **(1.14)** , we extracte the effective field-effect mobility and the threshold volatge for these devices. At the biased U_{DS} -1 V, the derivative of I_D on U_{GS} (labelled as black lines) and the related dependence of μ_{lin} on U_{GS} (labelled as red lines) of the TCBG S-DTT-10-based and TCBG S-DNTT-10/Pentacene-based OTFT as illustrated in **Figure 6.7 (b)**. Solid line and short dash line respectively represented the TCBG S-DNTT-10/Pentacene-based and TCBG S-DNTT-10-based OTFT. They display that the μ_{lin} for TCBG S-DNTT-10-based OTFT, which was extracted at the highest value, was of nearly 0.44 $cm^2 \cdot V^{-1} \cdot s^{-1}$, and the corresponding $U_{Th\text{-}lin}$ of -25 V. Conversely, the TCBG S-DNTT-10/Pentacene-based OTFT exhibited a μ_{lin} of approximately 1.67 $cm^2 \cdot V^{-1} \cdot s^{-1}$ and the related $U_{Th\text{-}lin}$ of -16 V. The μ_{lin} has improved almost four times. Subsequently, based on **Equation (1.14)**, at the U_{DS} bias of - 40 V, the square root of $I_{D\text{-}sat}$ changed with U_{GS} (labelled as black lines) and the correlated calculation of μ_{sat} (labelled as red lines) showing in **Figure 6.7 (c)**. They exhibited that the μ_{sat} for TCBG S-DNTT-10-based OTFT was to be almost 5.32 $cm^2 \cdot V^{-1} \cdot s^{-1}$, with a $U_{Th\text{-}sat}$ of -21.25 V. In comparison, the TCBG S-DNTT-10/Pentacene-based OTFT exhibited a μ_{sat} of nearly 3.31 $cm^2 \cdot V^{-1} \cdot s^{-1}$ and the correlated $U_{Th\text{-}sat}$ of -16 V.



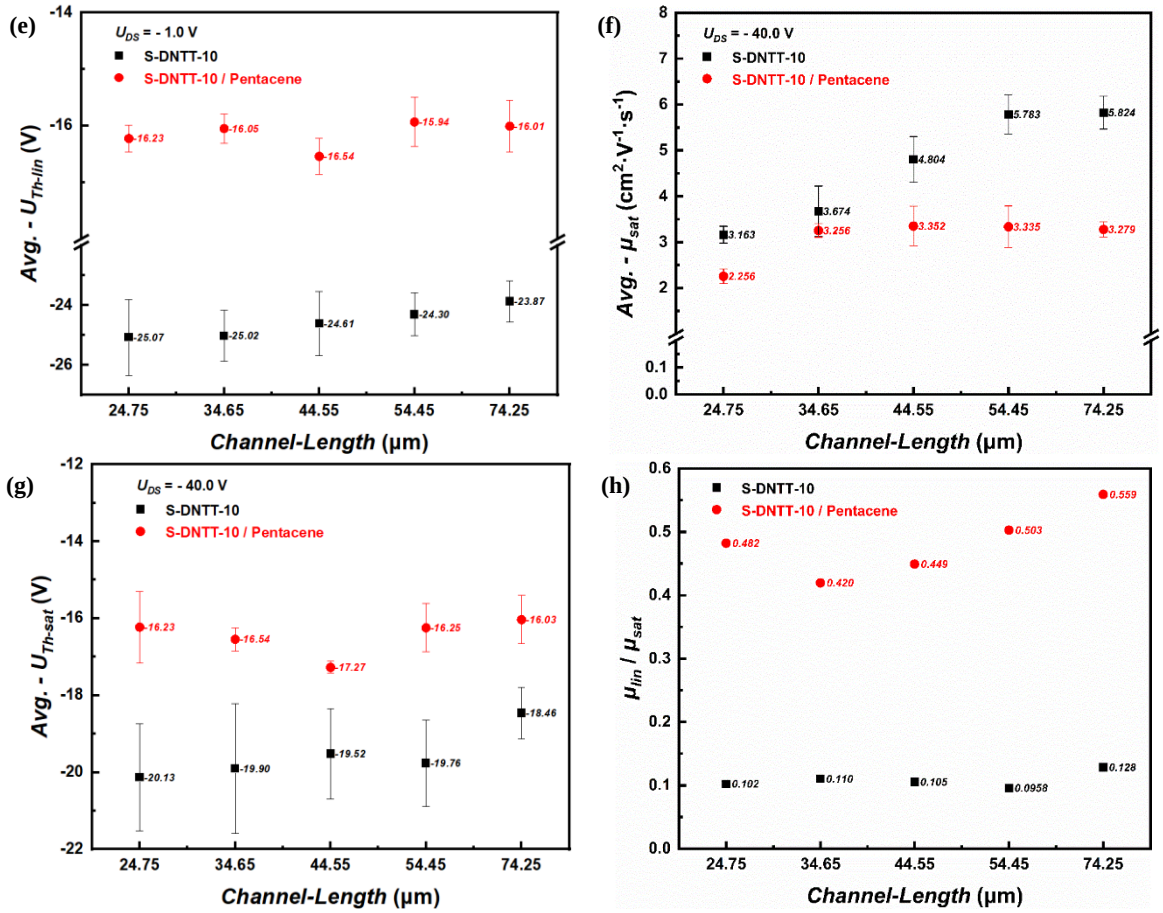


Figure 6.7 Typical I_D-U_{GS} in this study of (a) the comparison of TCBG S-DNTT-10-based OTFT and the TCBG S-DNTT-10/Pentacene-based OTFT (identical channel length $L \approx 54.45$ μm and width $W \approx 1000$ μm). The biased -U_{GS} ranging from 0 to -40 V with the increment of 0.2 V, and U_{DS} of -1 V and -40 V respective denoting for linear-mode and saturation -mode. (b) The extracted gate voltage dependence of linear-mode effective field-effect mobility μ_{lin} (the biased U_{DS} of -1 V), and (c) the extracted gate voltage dependence of saturation-mode effective field-effect mobility μ_{sat} (the biased U_{DS} of -40 V). (d) The compared μ_{lin}, (e) the corresponding extracted linear-mode threshold voltage U_{Th-lin}, (f) the saturation-mode effective field-effect mobility μ_{sat} (biased U_{DS} of - 40 V), (g) the related saturation -mode threshold voltage U_{Th-sat}, and (h) the μ_{lin}-to- μ_{sat}-ratio (μ_{lin}/μ_{sat}) was calculated by (d) and (f). The comparison of different extracted average electrical parameters from 4 TCBG devices under each different channel length.

The TCBG S-DNTT-10/Pentacene-based OTFTs showed an increased the average μ_{lin} and a positive shift in the average U_{Th} compared to the TCBG S-DNTT-10-based OTFTs. However, the unexpected reduced average μ_{sat} existing in all devices. **Figure 6.7 (d)** displayed the average μ_{lin} at the biased conditions of U_{DS} = -1 V, U_{GS} = 0 ~ -40 V for many devices. To simplify the expression of values, we utilized the '*average-value*' as a discussing value for following words. The average-μ_{lin} for TCBG S-DNTT-10-based OTFTs and TCBG S-DNTT-10/Pentacene-based OTFTs increased from approximately 0.32 to 0.75 $cm^2 \cdot V^{-1} \cdot s^{-1}$ and 1.09 to 1.83 $cm^2 \cdot V^{-}$

$^{1}\cdot s^{-1}$, respectively, as the L increased from 24.75 µm to 74.25 µm. The effective field-effect mobility varied with channel length in this way, seems to be one signature of emerged contact resistance. It is obvious that the μ_{lin} for TCBG S-DNTT-10/Pentacene-based OTFT is significantly higher than that of TCBG S-DNTT-10-based OTFT. Up to this point, only one published method indirectly demonstrated the enhancing performance of thermally deposited TCBG S-DNTT-10-based OTFTs by post-annealing treatment at various temperatures (T_a) in a nitrogen environment [38], however, not exhibited the changes in μ_{lin}. Compared with the nonlinear effects being observed in the I_D-U_{DS} characteristics, our method as shown in **Figure 6.6 (a)** and **(b)** significantly improved these effects, making them resemble linear *I-V* characteristics. In **Figure 6.7 (e)** it presents the average $U_{Th\text{-}lin}$ values, which is approximately -25 V for TCBG S-DNTT-10-based OTFTs and -16 V for TCBG S-DNTT-10/Pentacene-based OTFTs, respectively. **Figure 6.7 (f)** displays that the average-μ_{sat} for S-DNTT-10 and S-DNTT-10/Pentacene under U_{DS} = - 40.0 V and -U_{GS} = 0 ~ 40 V respectively increased from nearly 3.16 to 5.82 $cm^2\cdot V^{-1}\cdot s^{-1}$ and from 2.26 to 3.28 $cm^2\cdot V^{-1}\cdot s^{-1}$, as the L expanded from 24.75 µm to 74.25 µm. **Figure 6.7 (g)** shows the average-$U_{Th\text{-}sat}$ values are around -20 V for S-DNTT-10-based OTFTs and -16 V for S-DNTT-10/Pentacene-based OTFTs. In addition, the parameter, μ_{lin}-to-μ_{sat} ratio, (μ_{lin}/μ_{sat}), indicates that the increased μ_{lin}/μ_{sat} representing the decreased contact resistance in the device [98,260,261]. Thus, the μ_{lin}/μ_{sat} ratio in these samples was calculated from values in **Figure 6.7 (d)** and **(f)**, as depicted in **Figure 6.7 (h)**. For TCBG S-DNTT-10-based OTFTs, the value of μ_{lin}/μ_{sat} shows no clear correlation with L. The ratios in these device ratios are similar, average-μ_{lin}/μ_{sat} at 0.108. The μ_{lin}/μ_{sat} for TCBG S-DNTT-10/Pentacene-based OTFTs indepent with L as well, the related mean value is 0.483. Overall, TCBG S-DNTT-10-based OTFTs have a consistently lower μ_{lin}/μ_{sat} compared to that in TCBG S-DNTT-10/Pentacene-based OTFTs.

In summary, our method that depositing pentacene thin-film strengthen the electrical performance and linear-mode properties in OTFTs based on S-DNTT-10 thin-film. It is observed that the enhanced μ_{lin}, decreased $|U_{Th}|$, neverethless, reduced μ_{sat} for TCBG S-DNTT-10/Pentacene-based OTFTs. Moreover, the values of μ_{lin}/μ_{sat} imply that TCBG S-DNTT-10/Pentacene-based OTFTs might exhibit lower R_c than that in S-DNTT-10 counterparts. We focus on this point in the next section with the KPFM characterization technique.

6.2.3 Characterization of contact resistances

The I_D-U_{GS} measurements show that TCBG S-DNTT-10-based OTFTs exhibit changes in effective field-effect mobility (μ) and threshold voltage (U_{Th}) compared to TCBG S-DNTT-

10/Pentacene-based OTFTs. In this study, the S-DNTT-10 thin films in both TCBG S-DNTT-10-based and TCBG S-DNTT-10/Pentacene-based OTFTs were deposited on substrates with self-assembled monolayer (SAM) treatment, ensuring similar morphology in the channel regions. The observed difference lies in the OSC-electrode contact, specifically the Au/S-DNTT-10 and Au/Pentacene interfacial layers in the respective devices. We speculate that the distinct electrical characteristics result from the different source interfaces. We used Kelvin Probe Force Microscopy (KPFM) to characterize the contact interface by measuring the surface potential profiles along the channel, as Section 2.6.2 shown. The KPFM technique allows to extract separately the contact resistance at source and at drain and determine the type of charge injection process (linear or nonlinear injection). First, we focus on the source electrode and then, on the drain electrode.

6.2.3.1 Source-contact resistance evaluation

Source-contact resistance, R_s, is mainly consists of R_{inj} and R_{access} [262], where R_{inj} is associated with the electrode/OSC interface properties.[93] R_{access}, on the other hand, pertains to transport dynamics the charges of within the semiconductor layer from the electrode/semiconductor boundary to the accumulated charge channel. Factors determining R_{access} in the Top-contact OTFTs mainly contain the morphology of OSC active layer contacting the electrodes, intrinsic charge transport characteristics, and along with the injection distance of charge carriers to the accumulation layer [228,244]. We obtain the R_s and R_d from the voltage drop (U_{Drop}) located at source and drain in the KPFM surface potential profiles and from the corresponding drain current. Subsequently, according to the recorded U_{Drop} and the correlated the drain current in the measured range, fitting the linear part and then calculating the value of line-slope, which can be described as the conductive, to obtain the resistance. The more details are displayed in the reference [164] and in Section 2.4.4.2.

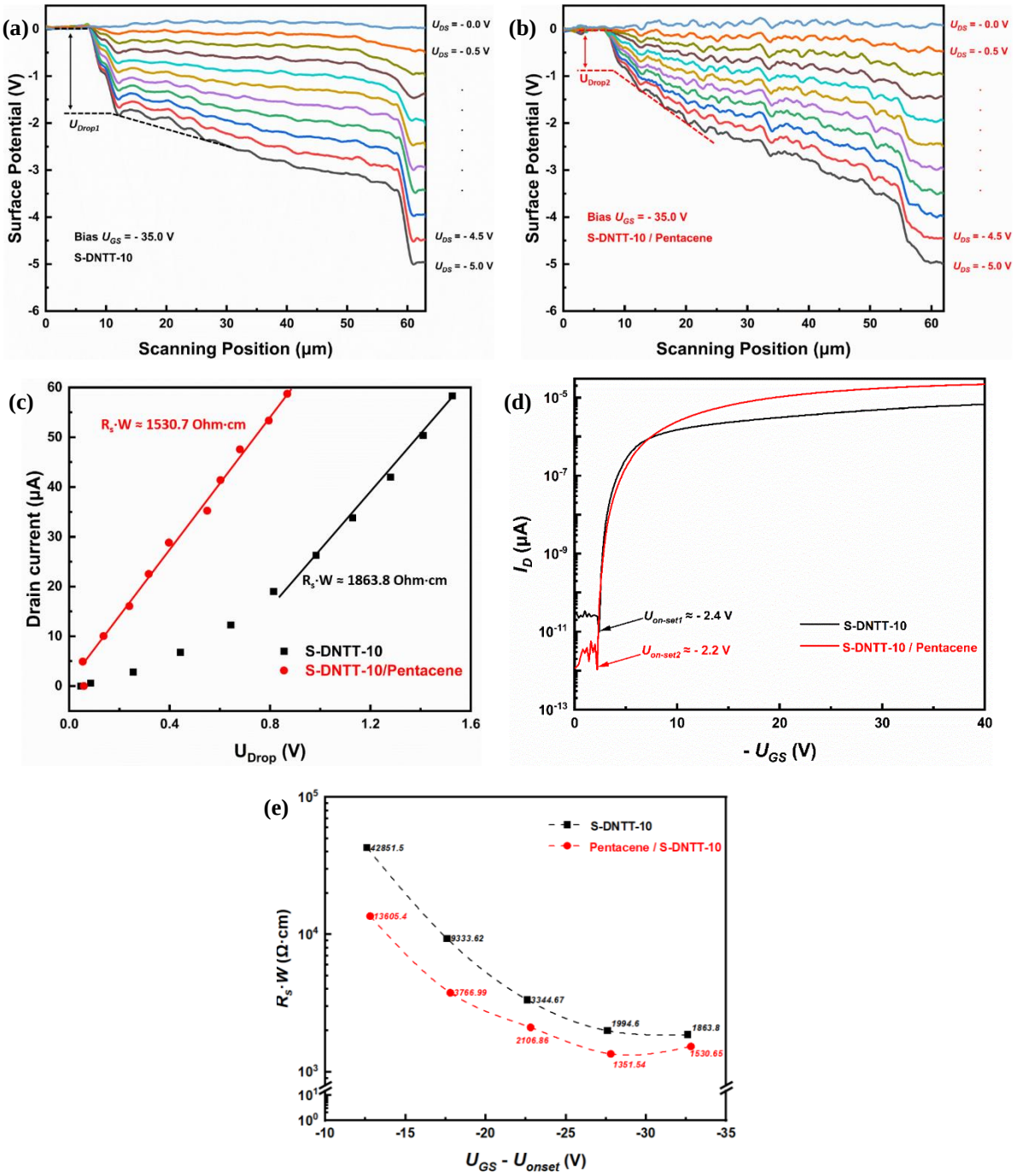


Figure 6.8 The surface potential profile after smooth treatments at bias U_{GS} = -35 V for (a) the TCBG S-DNTT-10-based OTFT and (b) TCBG S-DNTT-10/Pentacene-based OTFT. (c) The comparison of the drain current and voltage drop. (d) The I_D-U_{GS} characteristics for extracting the onset-voltage (U_{onset}). (e) Width-normalized Source-contact resistance (R_s·W) of the TCBG S-DNTT-10-based OTFT and TCBG S-DNTT/Pentacene-based OTFT in this study. (R_s W) as a function of (U_{GS}-U_{onset}) for this device.

The results of KPFM measurements and the correlated fitting and calculation of R_s as shown in **Figure 6.8**. The surface potential was implemented under U_{GS} ranging from -15 V to -35 V with the step of -5 V, while the U_{DS} was swept from 0 to -5 V in the increment of -0.5 V for each various U_{GS}. For instance, in **Figure 6.8 (a)** and **(b)**, it respectively exhibited the profile

under the bias U_{GS} of -35 V for the S-DNTT-10-based OTFT and S-DNTT-10/Pentacene-based OTFT both with channel width $W \approx 1000$ μm and channel length $L \approx 54.45$ μm. In these cases, the source and drain area is located at the left and right side, respectively. The voltage drop is extracted under each various U_{DS} and it is observed that the voltage drop is varied with applied U_{DS}. Particularly, in the comparison of the profile for these two devices, they display the different shapes of surface potential. The charge injection at source electrode in S-DNTT-10-based OTFT is nonlinear while it is linear (ohmic) in S-DNTT-10/Pentacene-based OTFT. The KPFM characterization shows experimentally the slight existence of an energy barrier height at source in the S-DNTT-10/Pentacene-based OTFT. We found that compared with the S-DNTT-10/Pentacene-based OTFT, it emerged the larger voltage drop at the source. Reversely, the drop distributing at the source seemingly is lower in the S-DNTT-10/Pentacene-based OTFT. Corresponding to **Figure 6.8 (c)**, which exhibiting the extracted relationship of drain current (I_D)-voltage drop (U_{Drop}), it demonstrated the effect that lower voltage drop in the S-DNTT-10/Pentacene-based OTFT. It suggested that in the resistance system of OTFT consisting by source contact resistance (R_s), channel resistance (R_{ch}) and drain contact resistance (R_d), the correlated weight of R_s in the total resistance of the S-DNTT-10/Pentacene-based OTFT became decreased, compared with that in the S-DNTT-10-based OTFT. It implied the emergence of lower R_s by using addition pentacene thin-film and thus illustrated the lower $R_s \cdot W$ of 1530.65 Ω·cm through fitting the linear area versus that of 1863.8 Ω·cm in S-DNTT-10-based OTFT.

Figure 6.8 (e) exhibited that the width-normalized $R_s \cdot W$ for TCBG S-DNTT-10-based OTFTs (represented by square black dots) and TCBG S-DNTT-10/Pentacene-based OTFTs (represented by circle red dots). It is worth noted that, resistance is correlated with the effective quantity of accumulated charges due to the existence of trap states, hence, it is required by (U_{GS} -U_{Th}). However, since the U_{Th} is influenced by external biased electric field and the duration of bias-stress effect [2,42], thus we considered that it possibly causes the inaccurate extraction of effective U_{Th} under changed U_{GS} and U_{DS} during KPFM measurements. Herein, we utilize the parameter, onset voltage (U_{onset}), and type into the (U_{GS}-U_{onset}) instead of (U_{GS}-U_{Th}). The onset voltage (U_{onset}) is identified at the U_{GS} value where the slope of the I_D-U_{GS} curve becomes obviously non-zero, indicating the initiation of I_D flow through the OTFT. The onset voltage is the gate-source voltage at which the drain current begins to increase beyond the off state. The U_{onset} is approximately -2.4 V and -2.2 V for S-DNTT-10-based and S-DNTT-10/Pentacene-based OTFT, respectively, as illustrated in **Figure 6.8 (d)**. **Figure 6.8 (e)** illustrates that the

$Rs{\cdot}W$ for S-DNTT-10-based OTFTs is approximately 42851.5 Ω·cm at a (U_{GS}-U_{onset}) of around -12.6 V, and decreases to 1863.8 Ω·cm as (U_{GS} -U_{onset}) stressed to -32.6 V. The contact resistance changed with bias condition, it aligns with the related research on TC DNTT-based OTFTs [98]. And for the S-DNTT-10/Pentacene-based OTFTs, at the (U_{GS}-U_{onset}) of approximately -12.8 V, the $R_s{\cdot}W$ is 13605.4 Ω·cm, and decreases to 1530.65 Ω·cm at (U_{GS} -U_{onset}) of -32.8 V. It illustrated that $R_s{\cdot}W$ (S-DNTT-10) is larger than that for $R_s{\cdot}W$ (S-DNTT-10/Pentacene). On the other hand, the $R_s{\cdot}W$ for each device is decreased with bias $|U_{GS}$-$U_{onset}|$ increasing.

It is observed that the contact resistance, $R_s{\cdot}W$ (S-DNTT-10/Pentacene) is lower than $R_s{\cdot}W$ (S-DNTT-10). Analysis suggests that, based on the follow: $R_s = R_{inj} + R_{access}$, the decrease in R_s comes mainly from changes in R_{inj}. Since considering the thickness change due to the introduction of the additional Pentacene thin-film of 5 nm, compared to the 25 nm S-DNTT-10 thick-film, one would expect a slight R_{access} increase due the pentacene film itself, but the observed $R_s{\cdot}W$ (S-DNTT-10/Pentacene) still remains lower than $R_s{\cdot}W$ (S-DNTT-10). Therefore, it suggests that the reduced component of $R_s{\cdot}W$ (S-DNTT-10/Pentacene) is the R_{inj} term, and correlated with the effect of pentacene thin-film on charge injection.

Upon contact between two different materials, charges redistribute at the interface, seeking thermal equilibrium and forming a unified Fermi level. In this case, the difference of energy-levels at the metal-OSC, *i.e.*, Schottky energy barrier particularly determine the charge injection process [136]. Our focus here is on how the Φ_B affecting the R_c, specifically R_{inj}. Based on the relationship between the R_c and the Φ_B, [225,259] given by the following **Equation (6.1)**.

$$\boldsymbol{R_C \sim exp\left(\frac{\phi_B}{k_B T}\right)} \qquad \textbf{(6.1)}$$

where k_B represents the Boltzmann constant ($1.380649{\cdot}10^{-23}$ m^2 kg s^{-2} K^{-1}), T stands for temperature in Kelvin, and Φ_B represents the energy difference of Schottky barrier. Herein, we suppose that R_{inj} discrepancies stem from the unique HOMO energy-levels between S-DNTT-10 and pentacene. To simplify the energy-level relationship of gold and OSC molecules, herein, we assume the gold with E_F of -5.1 eV with disregarding the push-back effects on the Fermi energy level of metallic electrode [92,264] and the dependence of MOs energy-level on molecular organizations. **Figure 6.1** (**a)** illustrates the energy alignment between gold ($E_F \approx$ -5.1 eV) and the S-DNTT-10 molecule (HOMO of ≈ -5.46 eV). Noted that the actual position of E_F of gold is changed by the fabricated parameters and push-back effect. The physical contact of the S-DNTT-10 molecules with source leads to charge rearrangement at the interface and

aligning to a uniform Fermi level and it caused a Schottky barrier, Φ_{B1} (≈ 0.36 eV). In contrast to the Au/S-DNTT-10 interface, the pentacene energy-level at HOMO of -5.0 eV, exhibits a lower energy barrier (approximately $\Phi_{B2} \approx 0.1$ eV), as illustrated in **Figure 6.1 (b)**. Therefore, considering the aforementioned **Equation (6.1)**, as Φ_{B2} is reduced the R_{inj} is reduced as well, and increases the charge injection efficiency into the OSC. It results in the increased quantity of induced charges, meanwhile, it can enhance the properties of charge transports inside the channel. Since the higher concentration of carriers could fill deep states and prevent carriers from falling into deep potential wells. Consequently, it leads to improvement of charge transport and mobility [81]. Therefore, it correlated with the observed result that the R_s of S-DNTT-10/Pentacene is less than that of S-DNTT-10 in our KPFM measurements, as **Figure 6.8 (e)** shown.

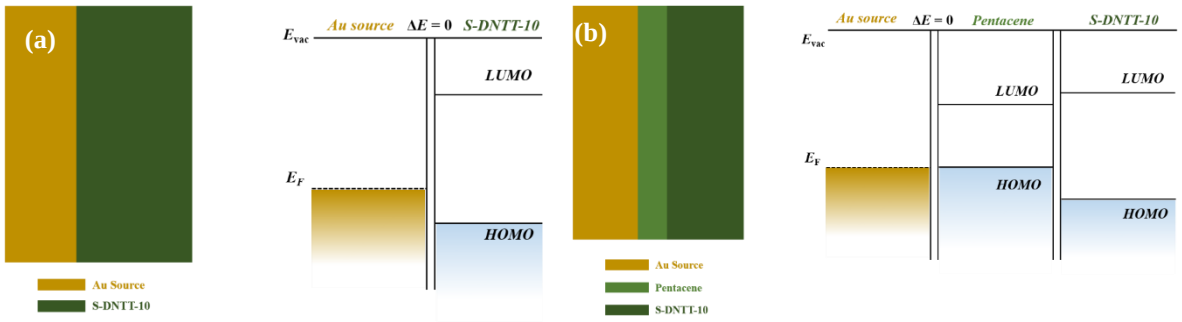


Figure 6.9 The energy-level diagrams of Au-organic semiconductor (OSC), (a). Au-S-DNTT-10, and (b) Au-Pentacene-S-DNTT-10.

The resistance is inversely proportional to the quantity of induced charges, $Q_{in} = C_i |U_{GS}-U_{Th}|$, which is controlled by the value of biased U_{GS} [121]. In addition, the influence of electric field on energy barrier also contribute to R_s with changed U_{GS}, $\Delta\Phi_B$, as given by the equation $\Delta\Phi_B \approx \sqrt{q \cdot E_M/4\pi\varepsilon_s}$ [225,265]. It exhibited that the stronger electric field E_M, results in the more reduction of energy barrier $\Delta\Phi_B$. It enables to lead the charges at the source facilitating to injection into OSC materials.

In summary, the Au-Pentacene interface in TCBG S-DNTT-10/Pentacene-based OTFTs presents a smaller energy barrier Φ_{B2}, resulting in a lower R_s and facilitating the injection of hole-charges into the OSC. Thereby enhancing charge injection efficiency and leading to variations in the effective μ_{lin} and U_{Th}, increasing the I_D at the initial U_{DS} area and improving nonlinear characteristics by pentacene thin-film.

6.2.3.2 Drain-contact resistance Evaluation

In the preceding KPFM measurements, it mainly demonstrates the enhanced performance that charge injection in TCBG S-DNTT-10-based OTFTs by pentacene thin-films, which correlates with the lower R_s at the source area. However, the obvious performance limitation was also emerged in the S-DNTT-10/Pentacene-based OTFTs, which is the lower saturation – mode effective field-effect mobility, μ_{sat}, as **Figure 6.4 (c)** and **Figure 6.7 (f)** shown.

In general, μ_{sat} is used to characterize charge transport within OTFTs. The reduced μ_{sat} in S-DNTT-10/Pentacene-based OTFTs compared to S-DNTT-10-based OTFTs suggests that charge transport is hindered. From a device configuration perspective, charge transport occurs in three regions: the source terminal, the accumulated channel, and the drain terminal. In S-DNTT-10/Pentacene-based OTFTs, the deposition of an additional pentacene thin film at the source effectively lowers the Schottky energy barrier, reducing R_{inj} and facilitating hole injection into the channel, thereby improving charge injection efficiency. Both types of OTFTs have S-DNTT-10 molecules in the channel, which were thermally deposited under identical conditions, resulting in similar film morphologies and intrinsic charge transport properties. The pentacene thin film likely has little effect on the channel morphology. Furthermore, the pentacene thin film reduces the Au/OSC contact resistance at the source, leading to a higher potential difference between the channel and gate (U_{GC}) under the same bias conditions in S-DNTT-10/Pentacene-based OTFTs, which theoretically increases hole concentration in the channel and enhances charge transport [81,266,267]. However, at the drain, the additional pentacene thin film may negatively affect device performance. Although the energy difference between the pentacene-HOMO and the Fermi level of gold is similar at both the source and drain, the barrier at the drain has a smaller impact on device performance, but R_{access} may influence R_d. The 5 nm Pentacene film, being of similar magnitude to the 25 nm S-DNTT-10 film, introduces additional bulk resistance at the drain. DFT simulations show that pentacene and S-DNTT-10 molecules have different π-electron distributions, potentially adding resistance at their interface, further obstructing charge transport at the drain. Thus, the pentacene thin film at the drain likely contributes to reduced charge transport in S-DNTT-10/Pentacene-based OTFTs, which could explain the lower μ_{sat}, potentially due to higher resistance R_d at the drain.

To assess the influence of the pentacene thin film on charge transport at the drain, we measured R_d using the KPFM method, similar to how R_s is measured. It's important to clarify that R_s depends on the source-gate potential drop (U_{GS}), while R_d relies on the drain-gate potential drop ($U_{GD} = U_{GS} - U_{DS}$). In this study, R_d was measured in the linear state. Initially,

we intended to measure R_d in the saturation state, as lower effective field-effect mobility was observed in the saturation regime. However, in saturation regime the pinch-off occurs at drain creating a big potential drop which hide the potential drop creates by R_d. Therefore, R_d cannot extract using KPFM in the saturation. As a result, the issue of lower μ_{sat} in S-DNTT-10/Pentacene-based OTFTs can only be investigated using linear-state R_d measurements for now.

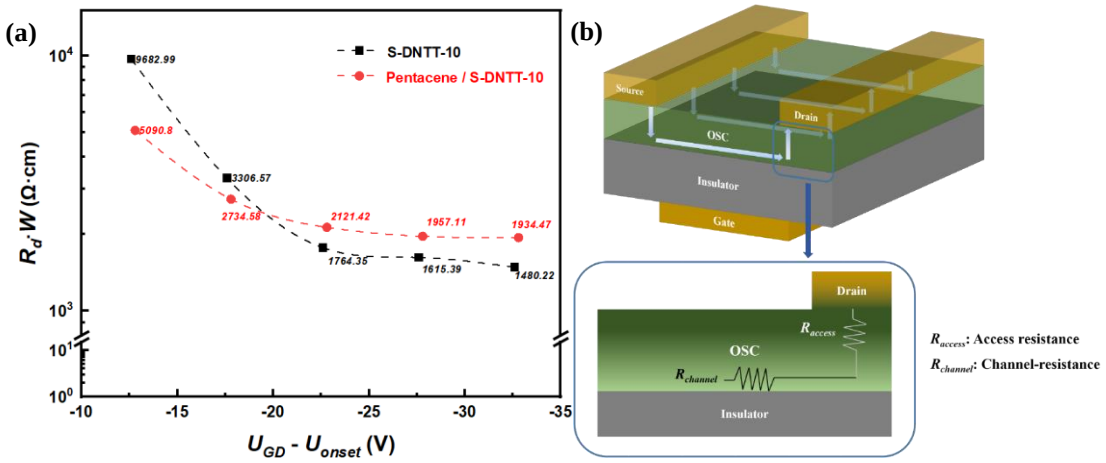


Figure 6.10 (a) Width-normalized drain-contact resistance (R_d) of the TCBG S-DNTT-10-based OTFT and TCBG S-DNTT/Pentacene-based OTFT in this study. The R_d as a function of (U_{GS}-U_{onset}) for this device. (b) The schematic of resistance system near the drain area.

Figure 6.10 (a) displays the results under the square black dots for the R_d of S-DNTT-10-based OTFTs and circle red dots for S-DNTT-10/Pentacene-based OTFTs. Furthermore, we use (U_{GD}-U_{onset}) as the variate to represent the R_d, for reasons analogous to those for R_s. In addition, as the same in the process of R_s measurements, as well the onset voltage (U_{onset1}) for the S-DNTT-10-based OTFTs was approximately -2.4 V and (U_{onset2}) for the S-DNTT-10/Pentacene-based OTFTs was nearly -2.2 V, derived from the linear-mode (bias U_{DS} = -1 V) transfer characteristics I_D-U_{GS}.

The data, as illustrated in **Figure 6.10 (a)**, revealed that the width-normalized drain contact resistance ($R_d \cdot W$), the $R_d \cdot W$ (S-DNTT-10), decreased from 9682.99 Ohm·cm to 1480.22 Ohm·cm with changes in (U_{GD}-U_{onset1}) from -12.6 V to -32.6 V. On the other hand, the $R_d \cdot W$ for Pentacene/S-DNTT-10-based OTFTs declining from 5090.8 Ohm·cm to 1934.47 Ohm·cm with (U_{GD}-U_{onset2}) shifting from -12.8 V to -32.8 V. It reveals the R_d-U_{GD} relationship with two main characteristics. One the one hand, $R_d \cdot W$ for S-DNTT-10/Pentacene-based OTFTs is larger than for that in S-DNTT-10-based OTFTs as the $|U_{GD}$-$U_{onset}|$ below 20 V, nevertheless, being lower under the $|U_{GD}$-$U_{onset}|$ above 20 V. On the other hand, R_d for each different type of device

both diminishes as biased $|U_{GD}\text{-}U_{onset}|$ increases. According to description of contact resistance [164,259], the R_d could be deduced as the **Equation (6.2)**,

$$R_d = \frac{T_{OSC}}{W \cdot \mu \cdot C_i |U_{GD} - U_{onset}|} \quad \textbf{(6.2)}$$

herein, herein, the T_{OSC} parameter represents the thickness of the OSC in the region where the current flows through the drain. W means the width of this region. μ as the mobility, characterizes the properties of charge transport around the drain area. C_i stands for the capacitance per area.

As for the result that comparison of $R_d \cdot W$ in the TCBG S-DNTT-10-based OTFT and S-DNTT-10/Pentacene-based OTFT showing in **Figure 6.10 (a)**, we think it can be seemingly regarded as one competition process of parameters with changed U_{GD} between the mibility, μ and the thickness of OSC, T_{osc}. Since, the trap states generally are existed in the OSC and the interface between the OSC and insulator layer, espeically, as the charge concentration is low, many induced charges are possibly localized at the trap states, which significantly reduces the mobility. However, as the charge concentration increases, more trap states are filled, allowing the remaining carriers to move more freely, leading to an increase in mobility. Hence, based on the situation that contributions of extra pentacene thin-film that lower injection energy barrier and enhancing charge injection, compared with TCBG S-DNTT-10/Pentacene-based OTFT, the presence of one greater charge injection energy barrier in TCBG S-DNTT-10-based OTFT possibly resulted in the reduced quantity of accumulated charges in the channel under the identical external biased conditions (particularly for the low applied voltage). It possibly couldn't fill the trap states in high degree and thus a lower horizontal mobility. It caused the mobility μ, which it can be regarded as the combination of horizontal mobility (the direction paralleling to the channel) and vertical mobility (the direction perpendicular to the channel), reduced when the charge transported from the channel to edge of drain. Consequently, based on the above **Equation (6.2)**, when $|U_{GD}\text{-}U_{onset}|$ is less than 20 V, the parameter μ more influence the resistance than parameter T_{OSC}, and thus $R_d \cdot W$ (S-DNTT-10) is greater than $R_d \cdot W$ (S-DNTT-10/Pentacene), although the T_{OSC} at the drain region is larger in TCBG S-DNTT-10/Pentacene-based OTFTs TCBG S-DNTT-10-based OTFTs than that in TCBG S-DNTT-10-based OTFTs and possible existence of resistance located at interface between S-DNTT-10 and pentacene thin-film.

However, we think that with the U_{GD} increasing the parameter T_{OSC} gradually mainly affects the drain contact resistance. Since despite the presence of the comparatively serious

energy barrier at the source electrode in S-DNTT-10-based OTFTs reduces the efficiency of charge injection, the quantity of induced charges increases due to the larger biased U_{GD}. Under one assumption that it can ignore the shift of U_{Th} during measurement operation that drain contact resistance since this is one short-term process compared with the long-term bias stress effects on U_{Th}, and as a result the density of trap states can be considered as approximately remained. Following the filling of trap states, the number of accumulated charges in the channel of TCBG S-DNTT-10-based OTFT becomes greater than that under $|U_{GD}$-$U_{onset}|$ lower 20V conditions. It resulted in one reduced dependence of charge transport properties on the concentration owing to fill the trap state in great degree. At this moment, the properties of charge transport at the channel into the both types of OTFTs perhaps became the similar. Hence, it was required to consider the influence of the parameter T_{OSC} on $R_d \cdot W$. According to the above formula, when $|U_{GD}$-$U_{onset}|$ exceeds 20 V, $R_d \cdot W$ (S-DNTT-10) consequently is less than $R_d \cdot W$ (S-DNTT-10/Pentacene) owing to extra pentacene thin-film at the drain in the TCBG S-DNTT-10/Pentacene-based OTFT. Additionally, with regard to the result that the $R_d \cdot W$ decreased with (U_{GD}-U_{onset}) for each OTFT, based on the **Equation (6.2)**, it speculated that the quantity of accumulated charges is increased with the bias U_{GD} near the drain area, resulting in the lower $R_d \cdot W$.

For this explanation, we consider that it perhaps exists the unreasonable point, for instance, the influence of interface of S-DNTT-10 and pentacene on charge transport characteristics. It is in the state of debate, and we will continue to further explore the mechanism of lower μ_{sat} in TCBG S-DNTT-10/Pentacene-based OTFTs.

Overall, the $R_d \cdot W$ of S-DNTT-10-based OTFTs is lower than that of the S-DNTT-10/Pentacene-based OTFTs. It suggested the presence of higher resistance at the drain is likely the contribution to the lower μ_{sat} observed. This data supports that the higher $R_d \cdot W$ introduced by the pentacene thin-film at the drain impacts the charge transport and thus the overall device performance adversely. At least, it seems that the extra pentacene layer is beneficial to the source electrode but not to the drain electrode. To evaluate this assumption, we plan to establish a new OTFT structure with the extra pentacene layer only depositing at the source. This is what we will show in the following section.

6.2.3.3 Local structure modification in the Bilayer-based OTFT

As the above results and discussion, we supposed that the lower μ_{sat} in the S-DNTT-10/Pentacene-based OTFT correlated with the higher value of $R_d \cdot W$. To address it, we planned to fabricate a new OTFT structure TCBG S-DNTT-10/Pentacene-based OTFTs with one-side-

deposited pentacene at source only. In this section, we show the process of fabrication of the new OTFT structure in Section 6.2.3.3.1, and making the comparison of electrical performance with both S-DNTT-10-based OTFTs and S-DNTT-10/Pentacene-based OTFTs in Section 6.2.3.3.2).

6.2.3.3.1 Fabrication process of the TCBG S-DNTT-10-based OTFTs with one-side-deposited pentacene

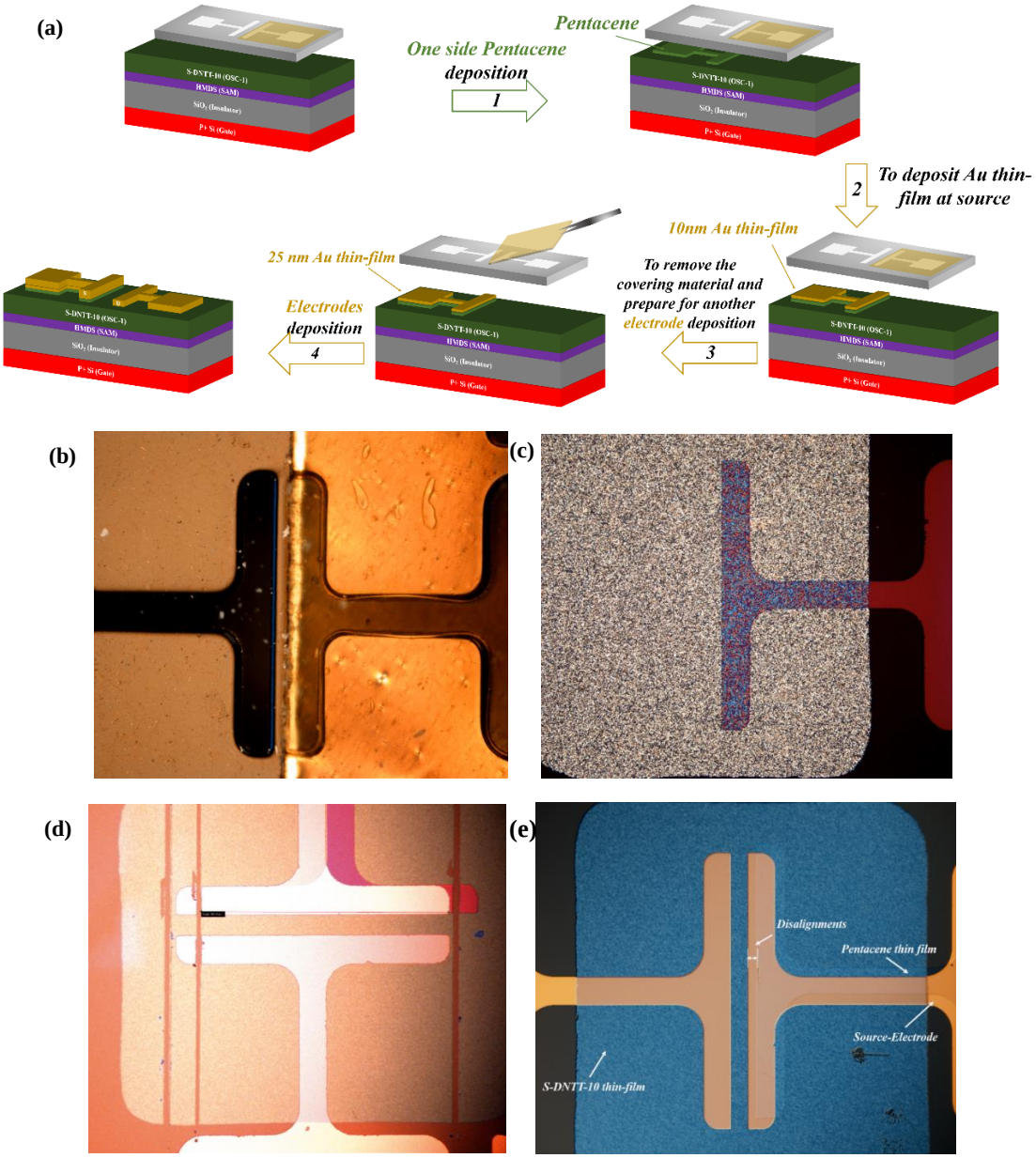


Figure 6.11 (a) The schematic of fabricating process of TCBG S-DNTT-10-based OTFT with one-side-deposited pentacene. (b) The covered electrode shadow mask with Kapton thin-film located at the right area. (c) The 5 nm pentacene thin-film stacked with 10 nm Au thin-film. (d) The accomplished devices with scratched-edges-treatment, and (e) top view of the fabrication of S-DNTT-10 based OTFT with one-side-deposited pentacene thin-films. The appearance of dis-alignment between source and pentacene thin-film.

During the fabrication of these devices, Kapton material was used to cover the single-electrode area on the electrode-shadow mask, as shown in **Figure 6.11 (b)**. Afterward, 5 nm of pentacene and 10 nm of gold were thermally deposited successively, as shown in steps 2 and 3. The deposited layers are illustrated as the dark purple area in **Figure 6.11 (c)**. Next, the Kapton material was peeled off using tweezers, followed by the thermal deposition of 25 nm of gold to form the final electrodes for the OTFTs after scratched-edges-treatment, as shown in **Figure 6.11 (d)**. This treatment is used to avoid fringe-effect influences on the electrical performance of devices [268]. It is important to note that misalignment of the unilateral electrode was observed, likely due to movement of the electrode-shadow mask caused by peeling off the Kapton material in step four. This issue also arose during initial fabrication attempts, as shown in **Figure 6.11 (e)**, where the misalignment was even more severe compared to **Figure 6.11 (d)**. This misalignment likely occurred because the source and drain terminals were deposited after removing the Kapton, and the removal direction was random. As a result, the pentacene thin film was not deposited on the edge of the source electrode, significantly reducing the intended impact of the one-sided pentacene deposition on the electrical performance of the TCBG S-DNTT-10-based OTFTs.

To address this issue, an additional step was introduced after the thermal deposition of the pentacene thin film, followed by the direct deposition of a 10 nm gold thin film. This approach ensured that, despite potential shifts in the electrode shadow mask during the peeling step, the pentacene remained positioned at the edge of the electrode. This placement is crucial for enhancing charge injection, thereby preserving the functional role of the pentacene in improving the device's electronic properties. However, this adjustment still resulted in a reduced channel width of approximately 902 μm, about 10% smaller than the designed width of 1000 μm. Despite this, compared to the first fabrication samples shown in **Figure 6.11 (e)**, the pentacene was now almost entirely positioned beneath the source electrode and along the channel edge.

6.2.3.3.2 Electrical characterizations

To analyze the linear- and saturation-mode field-effect motility (μ_{lin} and μ_{sat}) under respectively U_{DS} of -1 V and -40 V, both extracted from transfer characteristics (I_D-U_{GS}) within a U_{GS} range from 2 V to -40 V (in -0.2 V steps), various OTFT configurations were investigated. The devices, labeled OTFT-1, OTFT-2, and OTFT-3, represent TCBG S-DNTT-10-based OTFTs, TCBG S-DNTT-10/Pentacene-based OTFTs, and TCBG S-DNTT-10-based OTFTs with one-side-deposited pentacene, respectively. As shown in **Figure 6.12**, the S-DNTT-10-

based OTFTs (OTFT-1) exhibited a μ_{sat} of 3.2 $cm^2 \cdot V^{-1} \cdot s^{-1}$. In comparison, the S-DNTT-10/Pentacene-based OTFTs (OTFT-2) displayed a reduced μ_{sat} of 2.4 $cm^2 \cdot V^{-1} \cdot s^{-1}$, consistent with previous observations of lower μ_{sat} when pentacene is fully incorporated into the electrodes. Notably, OTFT-3, characterized by a high overlap between the pentacene and Au thin films, showed a μ_{sat} of 2.8 $cm^2 \cdot V^{-1} \cdot s^{-1}$, closely matching that of OTFT-1. The slight difference in μ_{sat} between OTFT-1 and OTFT-3 is likely due to slight variations in the S-DNTT-10 thin films, as they cannot be perfectly identical even when fabricated in the same batch, causing minor differences in charge transport properties under identical bias conditions. The μ_{lin} of OTFT-3 was measured at 0.8 $cm^2 \cdot V^{-1} \cdot s^{-1}$, similar to OTFT-2 at 0.8 $cm^2 \cdot V^{-1} \cdot s^{-1}$. These results suggest that devices using one-sided pentacene deposition can achieve efficient charge injection and transport, as indicated by the higher μ_{lin} and μ_{sat} values. More importantly, these findings confirm that the lower μ_{sat} observed in TCBG S-DNTT-10/Pentacene-based OTFTs is due to the additional pentacene thin film deposited at the drain as assumed in the previous Section 6.2.3.2.

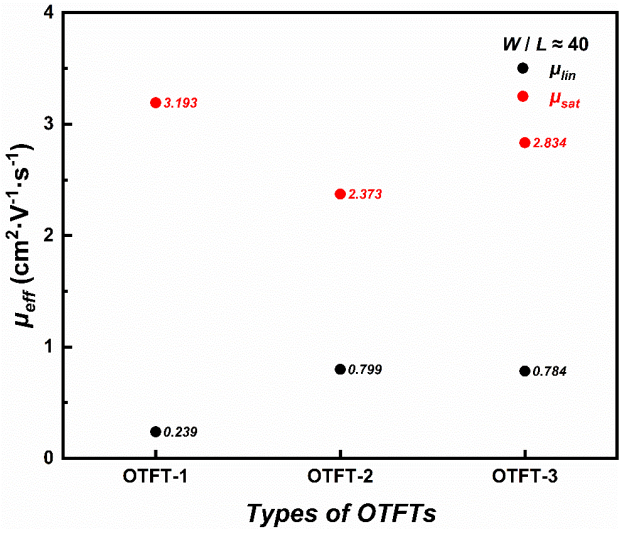


Figure 6.12 The comparison of effective mobility, μ_{lin} (U_{DS} = -1 V) and μ_{sat} (U_{DS} = -40 V).

To further elucidate the impact of additional pentacene thin-film at the drain on the lower μ_{sat} observed in TCBG S-DNTT-10/Pentacene-based OTFTs, we conducted an experimental alteration where the bias terminal was switched from the source to the drain for the deposited pentacene thin-film. Electrical performance results are presented in **Figure 6.13 (c)-(e)**, with OTFT-A and OTFT-B representing two different biased type at one-side pentacene thin-film on the same device where it is at the source and drain, respectively, and the electrodes only contacting with the S-DNTT-10 thin-films are at the drain and source, as shown in **Figure 6.13**

(a) and **(b)**. Because we did not find the obvious hysteresis effect, hence, we decided to neglect the errors caused by hysteresis effects on the experimental results and show only forward-curve.

Figure 6.13 (c) shows the output characteristics I_D-U_{DS} for different bias configurations of the one-side pentacene thin-film, with dashed and solid lines representing the performance under source bias (OTFT-A) and drain bias (OTFT-B), respectively. It was observed that the drain current significantly decreased as the injecting electrode at S-DNTT-10 thin-film stacking with pentacene in OTFT-A transferred into the injection electrode at S-DNTT-10 in OTFT-B. For instance, at U_{GS} = -40 V, the saturation drain current for OTFT-A was approximately $I_{sat\text{-}A}$ ≈ 1200 μA, while for OTFT-B, it dropped to around $I_{sat\text{-}B}$ ≈ 620 μA. This demonstrates the impact of the pentacene thin-film's location on the device's output characteristics and implied one possible difference in μ_{sat} between the two devices. Subsequent measurements of the transfer characteristics for μ_{lin} and μ_{sat} are shown in **Figure 6.13 (e)**. We found that μ_{sat} decreased from 2.8 $cm^2 \cdot V^{-1} \cdot s^{-1}$ in OTFT-A to 2.3 $cm^2 \cdot V^{-1} \cdot s^{-1}$ in OTFT-B. In OTFT-B, the structure resembles a standard S-DNTT-10-based OTFT, with S-DNTT-10 at the source electrode and pentacene at the drain. Compared to OTFT-1 (a TCBG S-DNTT-10-based OTFT), the μ_{lin} values for both devices were similar: 0.2 $cm^2 \cdot V^{-1} \cdot s^{-1}$ for OTFT-1 and 0.4 $cm^2 \cdot V^{-1} \cdot s^{-1}$ for OTFT-B. However, there was a notable difference in μ_{sat} of 3.2 $cm^2 \cdot V^{-1} \cdot s^{-1}$ for OTFT-1 versus 2.2 $cm^2 \cdot V^{-1} \cdot s^{-1}$ for OTFT-B. This confirms that the additional pentacene at the drain affects μ_{sat}. Additionally, shifting the one-side pentacene thin-film bias from source to drain reduced μ_{lin} from 0.8 $cm^2 \cdot V^{-1} \cdot s^{-1}$ in OTFT-A to 0.4 $cm^2 \cdot V^{-1} \cdot s^{-1}$ in OTFT-B, a decrease of about 100%. This suggests that charge injection at the S-DNTT-10/Au source electrode is less efficient than at the Pentacene/Au source electrode, as evidenced by the I_D-U_{DS} comparison curve in **Figure 6.13 (d)**. **Figure 6.13 (d)**, a close-up of **Figure 6.13 (c)**, shows a sharp decrease in the collected linear drain current when shifting from source to drain bias, with more pronounced non-linear effects. This is primarily attributed to the change in the source electrode interface from Au/Pentacene to Au/S-DNTT-10. Since pentacene has a lower HOMO level than S-DNTT-10, the transition from pentacene to S-DNTT-10 at the source increases the energy barrier, reducing charge injection efficiency.

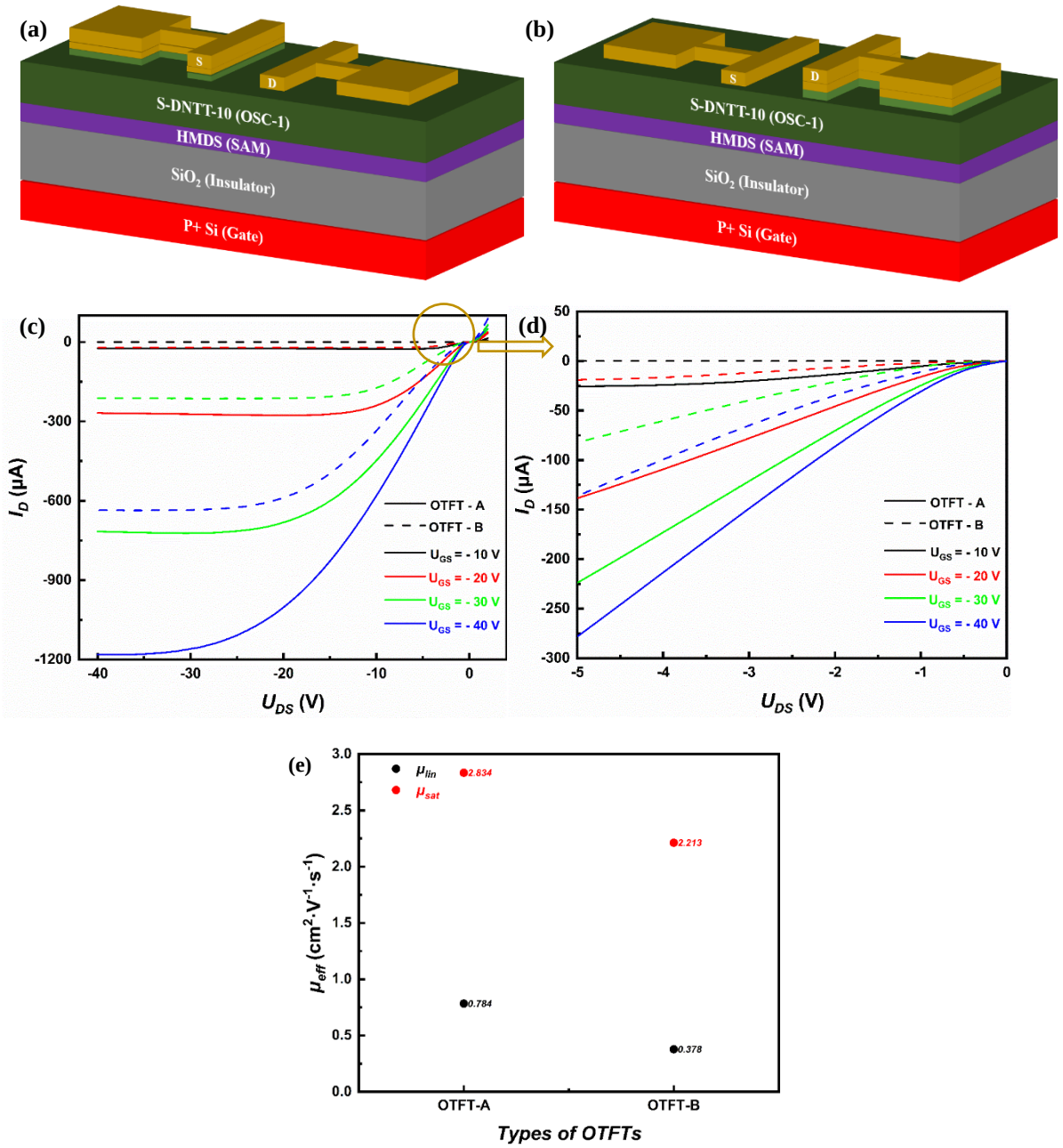


Figure 6.13 The schematic of pentacene respectively being biased as (a) source for OTFT-A and (b) drain for OTFT-B. (c) The comparison of output characteristics and (d) the correspond drain current at initial U_{DS} area. (e) The comparison of saturation-mode effective mobility.

According to the results and discussion, the observed correlation underscores the significance of utilized active OSC deposition in the design of OTFTs, suggesting that careful management of thin-film overlay can mitigate adverse effects like increased resistance at the drain. By optimizing the overlap and configuration of pentacene at the source electrode, it is possible to harness its benefits for enhanced device functionality while avoiding the drawbacks of excessive material deposition at non-critical areas.

Briefly summarizing, the above results in Section 6.2 suggested that the method of introducing extra pentacene thin-film could effectively enhance electrical performance of TCBG S-DNTT-10-based OTFTs. Actually, we also executed this guideline into Bottom-Contact-Bottom-gate (BCBG) configuration of S-DNTT-10-based OTFTs, in which deposited pentacene molecules around electrodes. It displayed that the deposition of pentacene into BCBG S-DNTT-10-bsaed enabled to improve the original poor electrical performance. The related results are listed at the Section 0, **Appendix**.

In the next section, we show results about the electrical stability of the characteristic that improved charge injection efficiency by pentacene under the long-term operation.

6.2.4 Electrical stability of Bilayer-based OTFTs under long-term operation

The bias-stressed (*BS*) effect as one common issue, it seriously degenerated the electric stability of OTFT when it is continuously operated for a prolonged time [206,269]. In this section, we plan to explore whether or not the *BS* effect could degenerate the effect of improving charge injection efficiency by pentacene. It exhibits the comparison of electrical performance between TCBG S-DNTT-10-based OTFT and TCBG S-DNTT-10/Pentacene-based OTFT (which the pentacene was deposited on the whole S-DNTT-10 thin-film).

To characterize the stability of the characteristic of improved μ_{lin} in the S-DNTT-10/Pentacene-based OTFTs, one device is continuously operated for 8 hours under the biased U_{GS} = -30 V and U_{DS} = -30 V, and quickly measured the transfer characteristics at the interval of 2 hours to obtain the changes in the μ_{eff} during this process. In addition, the measured range of U_{GS} is from 0 to -40 V

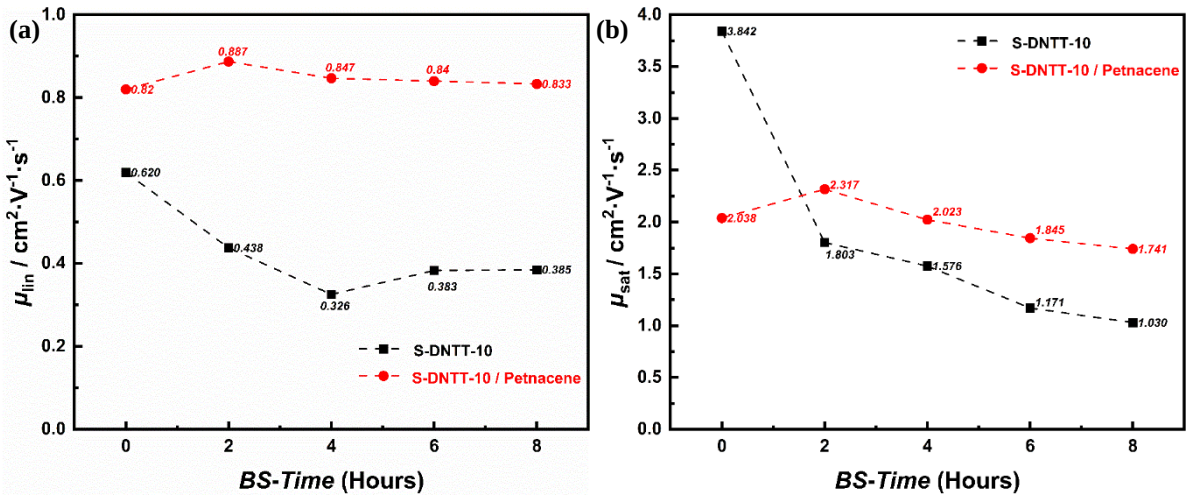


Figure 6.14 The comparison of electronic characteristics changed with the bias time, (a) the linear-mode effective field-effect mobility and (b) the saturation-mode field effect mobility.

Figure 6.14 (a) displays the μ_{lin} varied with the stressed time in 8 hours. The black square and red dot stand for the values in TCBG S-DNTT-10-based and TCBG S-DNTT-10/Pentacene-based OTFT, respectively. Note that the 0 in the *x*-axis means that the parameters are extracted before the bias-stressed experiments, and as identical as in **Figure 6.14 (b)** and **Figure 6.15**. For TCBG S-DNTT-10-based OTFT, it exhibited that the related μ_{lin} of 0.6 $cm^2 \cdot V^{-1} \cdot s^{-1}$ at 0 hour, and then it's decreased with the bias time until the μ_{lin} of 0.4 $cm^2 \cdot V^{-1} \cdot s^{-1}$ at the 8th hour. The reduced tendency was as similar as reported in the articles [255,269,270]. However, for S-DNTT-10/Pentacene-based OTFT, it exhibited that the μ_{lin} of 0.8 $cm^2 \cdot V^{-1} \cdot s^{-1}$ at 0h firstly increased as the 0.9 $cm^2 \cdot V^{-1} \cdot s^{-1}$ at the 2nd hour, and then it gradually decreased as the 0.8 $cm^2 \cdot V^{-1} \cdot s^{-1}$. Compared with that in the initial state, despite it appeared the slight enhancement and the reduction even can be regarded as the relatively identical. Based on the above results, the charge injection in the TCBG S-DNTT-10/Pentacene-based OTFT is stable, versus that in the TCBG S-DNTT-10-based OTFT. **Figure 6.14 (b)** presented the changes in the μ_{sat} during the continuously 8 hours operation. For S-DNTT-10-based OTFT, it displays that the initially corresponding μ_{sat} of 3.8 $cm^2 \cdot V^{-1} \cdot s^{-1}$ and is continuously reduced as 1 $cm^2 \cdot V^{-1} \cdot s^{-1}$ until at 8th hour. Nevertheless, despite it appeared the μ_{sat} decreasing from 2 to 1.7 $cm^2 \cdot V^{-1} \cdot s^{-1}$ at the 8th hour. Under the comparison, S-DNTT-10/Pentacene-based OTFT performed the comparatively stable properties of inner charge transport.

In the TCBG S-DNTT-10/Pentacene-based OTFT, μ_{lin} showed a slight increase after 2 hours of continuous operation but began to decline with prolonged operation beyond 8 hours. During this period, a peak value was observed at the 2nd hour for μ_{sat}. This result was not accidental and is likely due to the S-DNTT-10 thin film, as a similar experiment showed the highest μ_{lin} in a TCBG S-DNTT-10-based OTFT under the same stressed conditions, but with a operated duration of 5 hours. In the bias-stress measurement, μ_{lin} also exhibited a similar trend, with the peak appearing at the 4th hour, as shown in **Figure 6.15**. While the exact explanation is still debated, we believe the changes in the S-DNTT-10/Pentacene-based OTFT result from the molecular characteristics of the S-DNTT-10 thin film in combination with the response of pentacene to the electric field during the initial 2 hours. This phenomenon has been discussed in the study [210], it showed that μ_{sat} under U_{DS} of -40 V in the TCBG pentacene-based OTFT was improved from 0.1 to 0.18 $cm^2 \cdot V^{-1} \cdot s^{-1}$ after 20 hours continuous operation at $U_{DS} = U_{GS} =$ -40 V under high vacuum environment. With the main difference being that, in those cases, pentacene was deposited on the insulator surface and the S-DNTT-10 thin film, whereas in our

samples, it was deposited differently. This may have led to different molecular arrangements of pentacene and a varied response to the electric field.

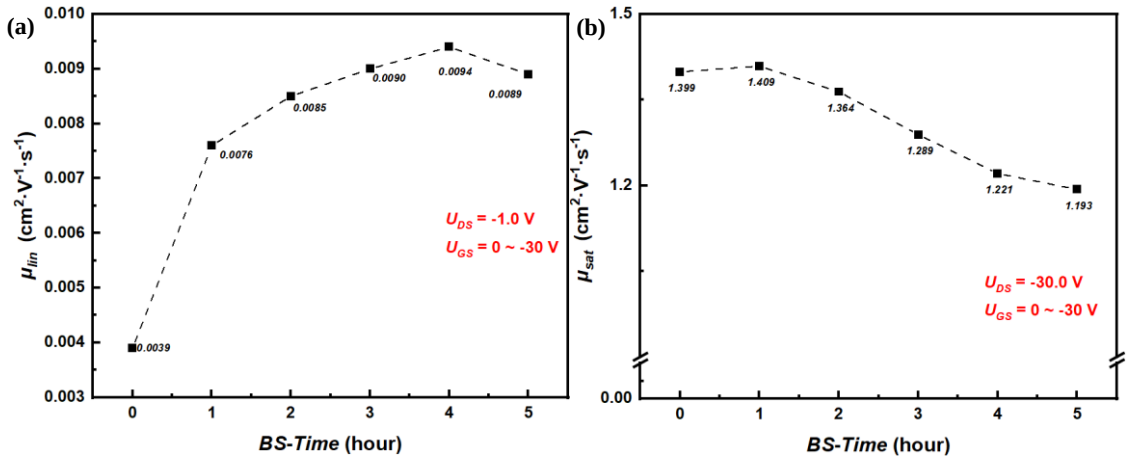


Figure 6.15 The electronic properties changed with the biased 5 hours, (a) the linear-mode field mobility μ_{lin}, and (b) the saturation-mode field mobility μ_{sat}.

6.2.5 Effect of post-annealing treatment on electrical performance

In Chapter 5, we studied on the influence of post-annealing treatment on the electrical performance of TCBG S-DNTT-10-based-OTFT, in particular, it was observed that it existed one post-annealing temperature which could enhance electrical performance. In the above results, it showed that the introduced pentacene thin-film can comparatively improve the charge injection efficiency. To demonstrate the post-annealing treatment impacting charge injection, it implemented the 30 mins post-annealing treatment on TCBG S-DNTT-10/Pentacene-based OTFTs, under different temperature ranging from 40 to 90 °C with the step of 10 °C. Meanwhile, it attempted to do the experiment on 3 nm-, 5 nm- and 10 nm-Pentacene related S-DNTT-10-based OTFTs. The linear and saturation effective field-effect mobility, μ_{lin} and μ_{sat}, are changed with post-annealing temperature, as **Figure 6.16 (a)** and **(b)** respectively shown. Note that these pre-measured devices have been stored for several weeks and we speculate the emergence of lower electrical performance compared with that in fresh samples.

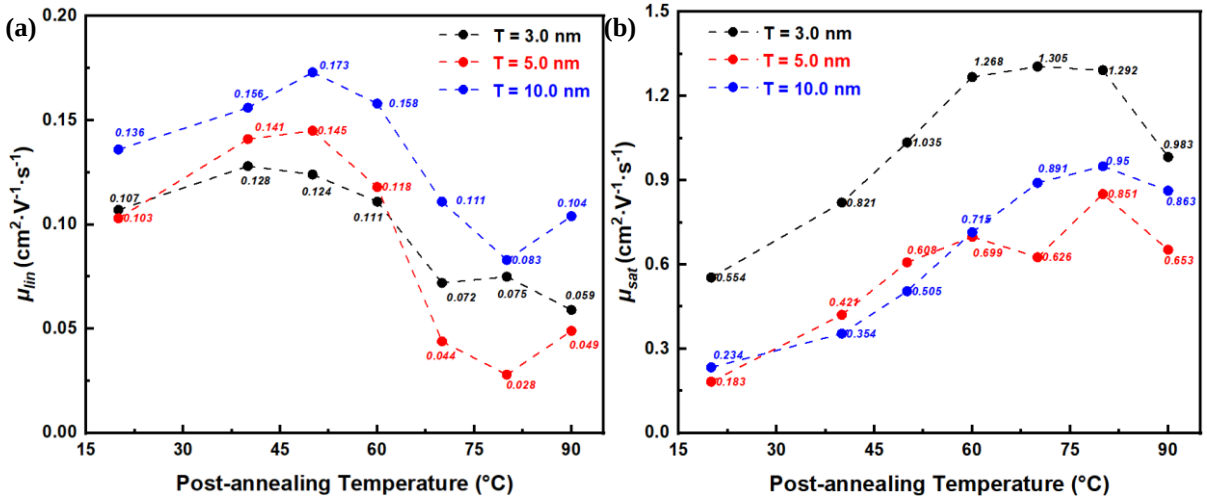


Figure 6.16 The influence of different post-annealing temperature on S-DNTT-10-based OTFT with different thickness of pentacene thin-film (L = 30 µm and W = 1000 µm): (a) Linear-mode effective field-effect mobility μ_{lin} under stressed U_{DS} = -1 V and (b) saturation-mode effective field-effect mobility μ_{sat} under stressed U_{DS} = -30 V.

Figure 6.16 (a) displayed that μ_{lin} is initially increased and then reduced with temperature compared with that before post-annealing treatment. For S-DNTT-10-based OTFT with 3 nm-Pentacene, μ_{lin} of 0.11 cm^2·V^{-1}·s^{-1} before the treatment, subsequently, it was improved as 0.13 cm^2·V^{-1}·s^{-1} by 30 °C temperature and descended as 0.06 cm^2·V^{-1}·s^{-1} with higher temperature. In this case, the μ_{lin} was almost identical, 0.13 cm^2·V^{-1}·s^{-1} and 0.12 cm^2·V^{-1}·s^{-1}, after 30 °C and 40 °C post-annealing treatment. For 5 nm-Pentacene-related OTFT, μ_{lin} of 0.10 cm^2·V^{-1}·s^{-1} before the treatment, subsequently, it was improved as 0.13 cm^2·V^{-1}·s^{-1} by 30 °C temperature and descended as 0.06 cm^2·V^{-1}·s^{-1} with higher temperature. In this case, the μ_{lin} was almost identical, 0.13 cm^2·V^{-1}·s^{-1} and 0.12 cm^2·V^{-1}·s^{-1}, after 30 °C and 40 °C post-annealing treatment. For 5 nm-Pentacene-related OTFT, μ_{lin} of 0.10 cm^2·V^{-1}·s^{-1} at beginning is increased until as 0.15 cm^2·V^{-1}·s^{-1} at 40 °C and then it was reduced as 0.05 cm^2·V^{-1}·s^{-1}. As well, the μ_{lin} was identically presented at after 30 °C and 40 °C post-annealing treatment. With regard to 10 nm-Pentacene related OTFT, μ_{lin} of 0.14 cm^2·V^{-1}·s^{-1} at beginning is increased until as 0.17 cm^2·V^{-1}·s^{-1}at 40 °C and then it was reduced as 0.10 cm^2·V^{-1}·s^{-1}.

Figure 6.16 (b) overall exhibited that the corresponding μ_{sat} is increased and subsequently reduced with temperature compared with that before post-annealing treatment. For TCBG S-DNTT-10-based OTFT with 3 nm pentacene, μ_{sat} of 0.55 cm^2·V^{-1}·s^{-1} at beginning is enhanced until as 1.30 cm^2·V^{-1}·s^{-1} after 70 °C and then decreased. With regard to 5 nm-Pentacene-related S-DNTT-10-based OTFT, μ_{sat} of 0.18 cm^2·V^{-1}·s^{-1} at beginning is enhanced until as 0.85 cm^2·V^{-1}·s^{-1} after 80 °C and then decreased. For 10 nm-Pentacene-related S-DNTT-10-based OTFT,

μ_{sat} of 0.23 $cm^2 \cdot V^{-1} \cdot s^{-1}$ at beginning is enhanced until as 0.95 $cm^2 \cdot V^{-1} \cdot s^{-1}$ after 80 °C and then decreased.

For changes in μ_{lin} with post-annealing temperature, it analyzed that the enhancement ranging from 30 °C to 50 °C is possibly caused by this treatment impacting on pentacene and S-DNTT-10 thin-films, but for the reduced μ_{lin}, it was supposed that the degradation in crystallinity pentacene was emerged under the higher post-annealing temperature since the pentacene is more sensitive to external factors including the temperature [271,272], and it implied that the higher temperature can destroy pentacene material. The damaged pentacene thin-film can be regarded to play a role of blocking charge injection. As for S-DNTT-10 thin-film, we think that it is impossibly attributed to the degeneration of μ_{lin} in less degree, and the related explanation was expressed in the following part about μ_{sat}.

With regard to the influence of post-annealing temperature on μ_{sat}, according to results that post-annealing impacting S-DNTT-10-based OTFT in Chapter 5, it implied that the enhancement on μ_{sat} is mainly correlated with changes in S-DNTT-10 thin-film. And pentacene thin-film possibly contribute to this enhancement as well, but it is limited before 50 °C. Since the temperature at the range of post-annealing between 60 °C and 80 °C that improving μ_{sat} could cause the degradation on pentacene material and **Figure 6.16 (a)** demonstrated the reduction of μ_{lin} at the range from 60 °C to 80 °C. Additionally, based on the variation of μ_{sat}, it is believed that if the charge transport capacity of the S-DNTT-10 thin-film decreases between 30-60 °C, then μ_{sat} should continuously decline rather than increase. Therefore, it is speculated that in this temperature region, the charge transport characteristics of the S-DNTT-10 thin-film do not deteriorate. This is also why it is speculated that the decrease in μ_{lin} is mainly caused by the temperature influence on the pentacene thin-film and the contact characteristics at the electrode interface, rather than related to the S-DNTT-10 thin-film.

In this part, the electrical performance of the device in response to different post-annealing temperatures was measured, especially regarding the influence of enhancing the charge injection characteristics of S-DNTT-10-based OTFT by introducing the pentacene thin-film. Pentacene has been found to be temperature sensitive. A lower post-annealing temperature improves the charge injection efficiency; but a higher temperature causes its attenuation.

6.3 Conclusion

Despite S-DNTT-10 material could display well charge transport characteristics and quite good stability, the S-DNTT-10-based OTFTs present a non-linear effect in output

characteristics related to electrodes contact issue which limits the performance. The non-linear effect is related to the presence of a Schottky energy barrier at the electrode/OSC interface.

In this chapter, we proposed one innovative approach that depositing additional OSC thin-film of pentacene between the source and drain electrodes and the S-DNTT-10 thin-film, to improve charge injection efficiency by weaken the effect of energy barrier. We successfully fabricated the TCBG S-DNTT-10/Pentacene-based OTFT with the higher linear-mode effective field-effect mobility (μ_{lin}), for instance that of 1.7 $cm^2 \cdot V^{-1} \cdot s^{-1}$ and lower $R_s \cdot W$ of $1.36 \cdot 10^4$ $\Omega \cdot cm$. Reversely, as for S-DNTT-10-based OTFT, it displayed the μ_{lin} of 0.4 $cm^2 \cdot V^{-1} \cdot s^{-1}$ and $R_s \cdot W$ of $4.28 \cdot 10^4$ $\Omega \cdot cm$. More importantly, encountered with additional pentacene thin-film which causing the TCBG S-DNTT-10/Pentacene-based OTFT with the lower saturation-mode effective field-effect mobility (μ_{sat}), to resolve it, we successfully fabricated TCBG S-DNTT-10-based OTFT solely stacked with pentacene thin-film located at source area only. The device performed the higher μ_{lin} like TCBG S-DNTT-10/Pentacene-based OTFT, simultaneously the similar μ_{sat} like TCBG S-DNTT-10-based OTFTs. This step further optimizes the method that employing additional layer into OTFTs. Moreover, it showed that the influence of various thickness of pentacene thin-film on the electrical performance of S-DNTT-10/Pentacene. The results suggest that a thickness between 5 and 15 nm pentacene thin-film help to improve the performance of OTFT.

We have also shown with a bias stress study that the additional pentacene layer, improving charge injection, is enabled to improve the stability of the device. In addition, it implemented the post-annealing treatment on TCBG S-DNTT-10/Pentacene-based OTFT, and results implied that despite this treatment could further improve charge injection efficiency, it needs to consider the annealed temperature since the sensitivity of pentacene material forwards temperature.

The aforementioned results suggest that the proposed approaches can efficaciously enhance the performance of S-DNTT-10-based OTFT, and it is believed that it offers a rational guidance for OTFTs. Nevertheless, there are still several points deserving further exploration. For example, how to maintain electrodes highly overlapping with the deposited one-side Pentacene thin-film in a more efficacious and simplistic manner, and employ other OSC materials with greater stability to substitute pentacene.

Not only being limited into Top-Contact-Bottom-Gate (TCBG) configuration, more significantly, potentially using in the Bottom-Contact-Bottom-Gate (BCBG) configuration. With regard to exhibited poor electrical performance in BCBG S-DNTT-10-based OTFTs, as

shown in Section 0, particularly, the charge injection was characterized by a considerably lower μ_{lin}. It is analyzed that it results from the poor morphology of S-DNTT-10 material at electrodes, and consequently it is not favorable for charge transport. We think that it is worthful to improve this phenomenon in the future.

As for further enhancing electrical performance of BCBG S-DNTT-10-based OTFTs, we have some perspectives on this issue. We propose to two different techniques: (i) to improve morphology of S-DNTT-10 thin-films at electrodes, and (ii) to increase charge injection area. To former one, it can be achieved by some treatments, such as SAM modification, towards electrode-surface with aim to change the surface energy and morphology of deposited S-DNTT-10 thin-films. To later one, we plan to embed Au electrodes into S-DNTT-10 thin-film with purpose of increasing charge injection area with a double charge injection process at the bottom surface of electrodes. We obtained some preliminary results. They showed that the drain current in transfer characteristics of Double-charge-injection S-DNTT-10-based OTFT is overall higher than that of BCBG S-DNTT-10-based OTFT (details seeing in Section 0, **Appendix**). Meanwhile, the extrated μ_{lin} for the Double-charge-injection S-DNTT-10-based OTFT is 0.15 $cm^2 \cdot V^{-1} \cdot s^{-1}$, and the related $U_{Th\text{-}lin}$ is -23 V, and the μ_{sat} and $U_{Th\text{-}sat}$ is 0.5 $cm^2 \cdot V^{-1} \cdot s^{-1}$ and -27 V. Nevertheless, the extracted parameters in BCBG S-DNTT-10-based OTFT was emerged the great degeneration. For μ_{lin} and $U_{Th\text{-}lin}$, it is respectively 0.0001 $cm^2 \cdot V^{-1} \cdot s^{-1}$ and -38 V, and for μ_{sat} and $U_{Th\text{-}sat}$, it is only 0.0652 $cm^2 \cdot V^{-1} \cdot s^{-1}$ and -41 V, respectively. Despite it already showed some improved results, it still exists some points to further explore them in the future.

7 Summary

Organic thin-film transistors (OTFTs) use organic semiconductor (OSC) materials as the active layer. Unlike inorganic semiconductors, OSCs offer advantages such as abundant material sources, low preparation temperature, simple processes, low cost, and ease of large-area fabrication. OTFTs are widely used in flexible displays, electronic paper, and sensors. They regulate output current by applying U_{DS} to generate charges in the OSC near the dielectric layer, forming a channel, and controlling the U_{DS}. The properties of OSCs, including molecular structure and thin-film morphology under various preparation conditions, are critical to OTFT performance. S-DNTT-10, a novel OSC material, has shown excellent charge transport characteristics in OTFTs. This study further investigates the molecular and electrical characteristics of S-DNTT-10-based OTFTs using advanced nano-characterization tools.

In this thesis, all S-DNTT-10 thin films were fabricated using Physical Vapor Deposition (PVD). The morphology of the 25 nm S-DNTT-10 thin film, deposited on SiO_2 modified with HMDS (a type of Self-Assembled Monolayer, SAM), was measured by Atomic Force Microscopy (AFM), revealing a layer-by-layer stacking morphology. It suggested that the film had a certain degree of continuity and interlayer overlapping, additionally indicating that charge transport is less affected by lattice boundaries and π-electron overlap is relatively high. These features are crucial for charge transport in S-DNTT-10 thin films. Moreover, contact-angle analysis using water showed that the thermally deposited S-DNTT-10 thin film exhibited hydrophobic properties, with an angle exceeding 90 degrees. The study also examined the effect of laser energy on the S-DNTT-10 thin film, showing that higher illumination energy could damage the molecular structure and cause burning on the surface. This emphasizes the need to adjust illumination parameters and protect the film when using Raman spectroscopy to study its molecular characteristics.

During exploring the molecular characteristics of S-DNTT-10, Raman scattered technique was used to obtain its molecular vibration modes and corresponding spectrum. Using Density Functional Theory (DFT) and the **Gaussian 16W** software, the theoretical Raman spectrum and specific vibrational modes of a single S-DNTT-10 molecule were recognized. These observed vibrations mainly centered on the S-shaped thiophene rings and the stretched rings coupled with alkyl chains, which are crucial for understanding experimental S-DNTT-10 Raman spectrum and the external factors influencing its molecular vibrations. Additionally, the simulation of the molecular orbital energy levels revealed that S-DNTT-10 has a relatively high HOMO of -5.46 eV, contributing to its stability in air. The π-electron wave function is primarily

concentrated in the central *S*-shaped thiophene rings. This information is valuable for studying how external factors affect the electrical properties of S-DNTT-10-based OTFTs through molecular vibrations and Raman signals. Meanwhile, it is the firstly revealing the Raman spectra and some molecular vibrational modes of S-DNTT-10 in details.

Regarding the experimental Raman spectrum of the S-DNTT-10 thin film, using three different wavelengths (532 nm, 633 nm, and 785 nm) in the setup, the results showed that the 532 nm light source, with a shorter wavelength and higher single-photon energy, was more comparatively effective to induce Raman spectrum under the same quantity of incident photon conditions. Additionally, as the S-DNTT-10 thin film thickness, both the intensity of the Raman scattering signal and the peak positions of certain Raman modes change. It suggests that increasing film thickness affects the molecular orientation and geometric structure of S-DNTT-10, which could impact the charge transport characteristics within the film. These findings highlight the requirements of optimizing the thickness of S-DNTT-10 thin films in OTFT applications.

To induce the Surface-Enhanced Raman Scattering (SERS) phenomenon and address the low signal-to-noise ratio of the Raman spectrum in 25 nm S-DNTT-10 thin-films with low molecular concentration, Au thin-films with nano-scale thickness were deposited on the S-DNTT-10 thin-film surface to form nano-structures. Initially, 1 nm-, 3 nm-, 5 nm-, and 6 nm-Au thin-films were deposited on SiO_2 at a rate of 1.0 Å/s under high vacuum. Scanning electron microscopy (SEM) confirmed that the geometric parameters of Au nano-structures increased with thickness, demonstrating the feasibility of this method that formation of Au nano-structures. Next, 3 nm-, 5 nm-, 10 nm-, and 20 nm -Au thin-films were deposited on 25 nm S-DNTT-10 thin-films. During adjusting excitation light wavelength, it was found that the 532 nm laser could not excite an effective Raman spectrum, but 633 nm and 785 nm lasers could collect SERS spectra, with the 633 nm laser producing the highest intensity. The 5 nm Au thin film also produced a relatively strong SERS signal. Furthermore, the SERS spectrum of S-DNTT-10 differed from its conventional Raman spectrum, possibly due to the influence of Au atoms on the molecular structure during Au deposition. This suggests that during the fabrication of Top-Contact-Bottom-Gate S-DNTT-10-based OTFTs via thermal deposition, the metal electrodes may increase molecular disorder in the local S-DNTT-10 layers they contact, reducing charge transport in this region.

In addition to study the molecular vibration characteristics of S-DNTT-10, further research was conducted on the electrical performance of S-DNTT-10-based OTFTs. A nonlinear effect

in the output characteristics was observed, caused by significant contact resistance R_C at the source, along with the *Early Saturation effect* in individual devices. Using the Gradual Channel Approximation (GCA) theory, a physical model was developed to explain this phenomenon. To avoid experimental errors, the Raman scattering technique was used to explore the electrical performance of the OTFTs and determine if the incident light affected device performance. The results showed that the incident light had no significant impact on the electrical performance, confirming the suitability of the Raman technique for studying S-DNTT-10-based OTFTs.

By innovatively integrating the multiple characterization tools which are conventional Raman spectrum, SERS spectrum and KPFM. Results comprehensively suggested that the reduction in OTFT performance after experiencing the bias-stress (BS) effect, primarily results from the continuous electric field affecting the molecular orientation of S-DNTT-10 in the channel and the increase in threshold voltage caused by water electrolysis. Additionally, KPFM characterization revealed that the continuous electric field enhances charge injection and extraction in TCBG S-DNTT-10-based OTFTs. These findings suggest that the *BS* effect mainly affects charge transport in the channel. This implies that effective encapsulation of the OTFT channel, preventing S-DNTT-10 molecules to contact with water molecules in the air and stabilizing the S-DNTT-10 molecular orientation, could mitigate the degradation in electrical performance caused by the *BS* effect.

Post-annealing treatment with varied temperature affect the performance of S-DNTT-10-based OTFTs. We innovatively proposed one comprehensive characterized system, which contains AFM, contact-angle analysis, Raman scattering, and KPFM measurements, with aim of further explore the inherent mechanism that the influence of post-annealing treatment on the electrical performance of OTFTs. Results revealed that post-annealing alters the properties of the S-DNTT-10 thin film, including its molecular characteristics and the surface energy of HMDS, as well as the contact properties between the S-DNTT-10 film and electrodes. These changes influnced the electrical performance of device. At higher post-annealing temperatures, the charge transport in the channel is damaged, molecular characteristics under the electrodes are affected, contact resistance increases, and charge injection and extraction efficiency decreases, weakening device performance. It indicates that post-annealing influences not only the channel region but also the interface contact between electrodes and S-DNTT-10. Additionally, there is an optimal post-annealing temperature (T_{post}) that maximizes device performance. T_{post} is also influenced by the deposition substrate temperature (T_{sub}) of S-DNTT-10 during PVD, with T_{post} decreasing as T_{sub} increases. This suggests an optimal molecular

arrangement for charge transport in the thermally deposited S-DNTT-10 film, achievable by adjusting T_{post} and T_{sub}. This provides valuable insights for optimizing the performance of S-DNTT-10-based OTFTs.

Previous DFT simulations of the orbital energy level of the S-DNTT-10 single molecule showed that S-DNTT-10 has a relatively high HOMO energy level (~ -5.46 eV), and the presence of an energy barrier with respect to the work function of gold. This explains the main cause of the non-linear effect in the output characteristics of TCBG S-DNTT-10-based OTFTs with gold electrodes. Depositing a pentacene thin film on the surface of S-DNTT-10 can alleviate the non-linear effect and reduce source contact resistance, as confirmed by KPFM measurements, improving charge injection efficiency. However, the additional OSC layer reduces the effective field-effect mobility (μ_{sat}) in the saturation-mode. Encountered with this issue, one innovative approach was proposed by depositing pentacene only on one side of a single electrode, which achieved the improvement of charge injection efficiency and μ_{sat} when stressed as the source. When used as the drain, the device showed a non-linear effect and reduced μ_{sat} compared to the TCBG S-DNTT-10-based OTFT. These findings explain the reduction in μ_{sat} and offer a new strategy for enhancing OTFT performance with additional OSC layers. For Bottom-Contact-Bottom-Gate (BCBG) S-DNTT-10-based OTFTs, the non-linear effect is severe, and the device performs poorly. By using the shadow mask blur effect to deposit pentacene only on the electrode surface, the performance improved significantly compared to pure BCBG S-DNTT-10-based OTFTs. This suggests that the low performance of BCBG S-DNTT-10-based OTFTs is related to the molecular characteristics of S-DNTT-10 at the electrode and the interface. Additionally, embedding the electrode closer to the SiO_2 dielectric layer and increasing the charge injection area further enhances device performance, offering another approach to improve BCBG S-DNTT-10-based OTFTs.

Building on previous research on S-DNTT-10, this thesis further explores S-DNTT-10 molecules through molecular vibration analysis, revealing the relationship between external factors affecting electrical performance and changes in molecular vibrations. Additionally, improvements were made to the interface characteristics between the S-DNTT-10 thin film and electrodes, enhancing the electrical performance of S-DNTT-10-based OTFTs. Expanding this understanding to other materials and processes will promote the development of organic thin-film transistors and enable unique electronic applications.

Finally, it is hoped that results and analyses in this thesis can provide guidance and meaningful reference information for the future development of S-DNTT-10-based - and OTFTs based on other OSC materials.

8 Bibliography

1. Berggren, M., Nilsson, D. & Robinson, N. D. Organic materials for printed electronics. *Nature materials* **6**, 3–5 (2007).
2. Sirringhaus, H. 25th Anniversary Article: Organic Field-Effect Transistors: The Path Beyond Amorphous Silicon. *Advanced Materials* **26**, 1319–1335 (2014).
3. Mei, J., Diao, Y., Appleton, A. L., Fang, L. & Bao, Z. Integrated Materials Design of Organic Semiconductors for Field-Effect Transistors. *J. Am. Chem. Soc.* **135**, 6724–6746 (2013).
4. Kang, B., Lee, W. H. & Cho, K. Recent Advances in Organic Transistor Printing Processes. *ACS Appl. Mater. Interfaces* **5**, 2302–2315 (2013).
5. Arias, A. C., MacKenzie, J. D., McCulloch, I., Rivnay, J. & Salleo, A. Materials and Applications for Large Area Electronics: Solution-Based Approaches. *Chem. Rev.* **110**, 3–24 (2010).
6. Schweicher, G. *et al.* Molecular Semiconductors for Logic Operations: Dead-End or Bright Future? *Advanced Materials* **32**, 1905909 (2020).
7. Allard, S., Forster, M., Souharce, B., Thiem, H. & Scherf, U. Organic Semiconductors for Solution-Processable Field-Effect Transistors (OFETs). *Angew Chem Int Ed* **47**, 4070–4098 (2008).
8. Anthony, J. E. The Larger Acenes: Versatile Organic Semiconductors. *Angew Chem Int Ed* **47**, 452–483 (2008).
9. Murphy, A. R. & Fréchet, J. M. J. Organic Semiconducting Oligomers for Use in Thin Film Transistors. *Chem. Rev.* **107**, 1066–1096 (2007).
10. Mullen, K. & Scherf, U. Organic light-emitting devices. *Ed. Wiley-vch, Germany* (2006).
11. Hains, A. W., Liang, Z., Woodhouse, M. A. & Gregg, B. A. Molecular Semiconductors in Organic Photovoltaic Cells. *Chem. Rev.* **110**, 6689–6735 (2010).
12. Sirringhaus, H. 25th Anniversary Article: Organic Field-Effect Transistors: The Path Beyond Amorphous Silicon. *Advanced Materials* **26**, 1319–1335 (2014).
13. Dimitrakopoulos, C. D. & Malenfant, P. R. L. Organic Thin Film Transistors for Large Area Electronics. *Adv. Mater.* **14**, 99–117 (2002).
14. Panzer, M. J. & Frisbie, C. D. Exploiting Ionic Coupling in Electronic Devices: Electrolyte-Gated Organic Field-Effect Transistors. *Advanced Materials* **20**, 3177–3180 (2008).
15. Guo, E., Dollinger, F., Amaya, B., Fischer, A. & Kleemann, H. Organic Permeable Base Transistors – Insights and Perspectives. *Advanced Optical Materials* **9**, 2002058 (2021).
16. Facchetti, A. Semiconductors for organic transistors. *materials today* **10**, 28–37 (2007).
17. Reese, C. & Bao, Z. Organic single-crystal field-effect transistors. *Materials Today* **10**, 20–27 (2007).
18. Podzorov, V. Organic single crystals: Addressing the fundamentals of organic electronics. *MRS bulletin* **38**, 15–24 (2013).
19. Jiang, L., Dong, H. & Hu, W. Organic single crystal field-effect transistors: advances and perspectives. *Journal of Materials Chemistry* **20**, 4994–5007 (2010).
20. Hasegawa, T. & Takeya, J. Organic field-effect transistors using single crystals. *Science and Technology of Advanced Materials* **10**, 024314 (2009).
21. Shi, L., Guo, Y., Hu, W. & Liu, Y. Design and effective synthesis methods for high-performance polymer semiconductors in organic field-effect transistors. *Materials Chemistry Frontiers* **1**, 2423–2456 (2017).
22. Ong, B. S., Wu, Y., Liu, P. & Gardner, S. High-Performance Semiconducting Polythiophenes for Organic Thin-Film Transistors. *J. Am. Chem. Soc.* **126**, 3378–3379 (2004).
23. Sirringhaus, H., Bird, M. & Zhao, N. Charge Transport Physics of Conjugated Polymer Field-Effect Transistors. *Advanced Materials* **22**, 3893–3898 (2010).
24. Tsumura, A., Koezuka, H. & Ando, T. Macromolecular electronic device: Field-effect transistor with a polythiophene thin film. *Applied Physics Letters* **49**, 1210–1212 (1986).
25. Horowitz, G., Fichou, D., Peng, X., Xu, Z. & Garnier, F. A field-effect transistor based on conjugated alpha-sexithienyl. *Solid State Communications* **72**, 381–384 (1989).
26. Akimichi, H., Waragai, K., Hotta, S., Kano, H. & Sakaki, H. Field-effect transistors using alkyl substituted oligothiophenes. *Applied physics letters* **58**, 1500–1502 (1991).
27. Horowitz, G., Peng, X.-Z., Fichou, D. & Garnier, F. Organic thin-film transistors using π-conjugated oligomers: Influence of the chain length. *Journal of molecular electronics* **7**, 85–89 (1991).
28. Haddon, R. C. *et al.* C60 thin film transistors. *Applied physics letters* **67**, 121–123 (1995).
29. Bao, Z., Dodabalapur, A. & Lovinger, A. J. Soluble and processable regioregular poly (3-hexylthiophene) for thin film field-effect transistor applications with high mobility. *Applied physics letters* **69**, 4108–4110 (1996).

30. Nelson, S. F., Lin, Y.-Y., Gundlach, D. J. & Jackson, T. N. Temperature-independent transport in high-mobility pentacene transistors. *Applied physics letters* **72**, 1854–1856 (1998).
31. Sirringhaus, H. *et al.* Two-dimensional charge transport in self-organized, high-mobility conjugated polymers. *Nature* **401**, 685–688 (1999).
32. Jurchescu, O. D., Baas, J. & Palstra, T. Effect of impurities on the mobility of single crystal pentacene. *Applied Physics Letters* **84**, 3061–3063 (2004).
33. Kline, R. J. *et al.* Dependence of Regioregular Poly(3-hexylthiophene) Film Morphology and Field-Effect Mobility on Molecular Weight. *Macromolecules* **38**, 3312–3319 (2005).
34. Ebata, H. *et al.* Highly Soluble [1]Benzothieno[3,2- *b*]benzothiophene (BTBT) Derivatives for High-Performance, Solution-Processed Organic Field-Effect Transistors. *J. Am. Chem. Soc.* **129**, 15732–15733 (2007).
35. Li, Y., Singh, S. P. & Sonar, P. A High Mobility P-Type DPP-Thieno[3,2- *b*]thiophene Copolymer for Organic Thin-Film Transistors. *Advanced Materials* **22**, 4862–4866 (2010).
36. Minemawari, H. *et al.* Inkjet printing of single-crystal films. *Nature* **475**, 364–367 (2011).
37. Giri, G. *et al.* Tuning charge transport in solution-sheared organic semiconductors using lattice strain. *Nature* **480**, 504–508 (2011).
38. Yamaguchi, Y. *et al.* Solution-Processable Organic Semiconductors Featuring S-Shaped Dinaphthothienothiophene (S-DNTT): Effects of Alkyl Chain Length on Self-Organization and Carrier Transport Properties. *Chem. Mater.* **32**, 5350–5360 (2020).
39. Paez-Sierra, B. A. Raman spectroscopy of metal/organic/inorganic heterostructures and pentacene-based OFETs. (2007).
40. Acharya, R. Ultrathin organic thin-film transistors: investigating hybrid gate dielectrics and stable semiconductor monolayers. (2021).
41. Kekulé, Aug. Ueber einige Condensationsproducte des Aldehyds. *Justus Liebigs Ann. Chem.* **162**, 77–124 (1872).
42. Scherr, C. W. Free-electron network model for conjugated systems. II. Numerical calculations. *The Journal of Chemical Physics* **21**, 1582–1596 (1953).
43. Troisi, A. & Orlandi, G. Band Structure of the Four Pentacene Polymorphs and Effect on the Hole Mobility at Low Temperature. *J. Phys. Chem. B* **109**, 1849–1856 (2005).
44. Cheng, Y. C. *et al.* Three-dimensional band structure and bandlike mobility in oligoacene single crystals: A theoretical investigation. *The Journal of chemical physics* **118**, 3764–3774 (2003).
45. Repp, J., Meyer, G., Stojković, S. M., Gourdon, A. & Joachim, C. Molecules on Insulating Films: Scanning-Tunneling Microscopy Imaging of Individual Molecular Orbitals. *Phys. Rev. Lett.* **94**, 026803 (2005).
46. Anthopoulos, T. D. *et al.* Air-Stable n-Channel Organic Transistors Based on a Soluble C_{84} Fullerene Derivative. *Advanced Materials* **18**, 1679–1684 (2006).
47. Jones, B. A., Facchetti, A., Wasielewski, M. R. & Marks, T. J. Tuning Orbital Energetics in Arylene Diimide Semiconductors. Materials Design for Ambient Stability of n-Type Charge Transport. *J. Am. Chem. Soc.* **129**, 15259–15278 (2007).
48. Jurchescu, O. D., Popinciuc, M., Van Wees, B. J. & Palstra, T. T. Interface-controlled, high-mobility organic transistors. *Advanced Materials* **19**, 688–692 (2007).
49. Luo, C. *et al.* General Strategy for Self-Assembly of Highly Oriented Nanocrystalline Semiconducting Polymers with High Mobility. *Nano Lett.* **14**, 2764–2771 (2014).
50. Yuan, Y. *et al.* Ultra-high mobility transparent organic thin film transistors grown by an off-centre spin-coating method. *Nature communications* **5**, 3005 (2014).
51. Garnier, F., Horowitz, G., Fichou, D. & Yassar, A. Molecular order in organic-based field-effect transistors. *Synthetic metals* **81**, 163–171 (1996).
52. Chen, X. *et al.* Charge transport in organic field-effect transistors. *Materials Today Electronics* 100077 (2023).
53. Nakayama, Y. *et al.* Single-Crystal Pentacene Valence-Band Dispersion and Its Temperature Dependence. *J. Phys. Chem. Lett.* **8**, 1259–1264 (2017).
54. Ishii, H., Honma, K., Kobayashi, N. & Hirose, K. Wave-packet approach to transport properties of carrier coupled with intermolecular and intramolecular vibrations of organic semiconductors. *Phys. Rev. B* **85**, 245206 (2012).
55. Yanagisawa, S., Morikawa, Y. & Schindlmayr, A. HOMO band dispersion of crystalline rubrene: Effects of self-energy corrections within the G W approximation. *Phys. Rev. B* **88**, 115438 (2013).
56. Temirov, R., Soubatch, S., Luican, A. & Tautz, F. S. Free-electron-like dispersion in an organic monolayer film on a metal substrate. *Nature* **444**, 350–353 (2006).
57. Karl, N. Charge carrier transport in organic semiconductors. *Synthetic Metals* **133**, 649–657 (2003).
58. Simonetti, O. & Giraudet, L. Transport models in disordered organic semiconductors and their application to the simulation of thin-film transistors. *Polym. Int.* **68**, 620–636 (2019).

59. Nenashev, A. V., Oelerich, J. O. & Baranovskii, S. D. Theoretical tools for the description of charge transport in disordered organic semiconductors. *J. Phys.: Condens. Matter* **27**, 093201 (2015).
60. Troisi, A. Charge transport in high mobility molecular semiconductors: classical models and new theories. *Chem. Soc. Rev.* **40**, 2347 (2011).
61. Horowitz, G., Hajlaoui, R. & Delannoy, P. Temperature dependence of the field-effect mobility of sexithiophene. Determination of the density of traps. *Journal de Physique III* **5**, 355–371 (1995).
62. Horowitz, G., Hajlaoui, M. E. & Hajlaoui, R. Temperature and gate voltage dependence of hole mobility in polycrystalline oligothiophene thin film transistors. *Journal of Applied Physics* **87**, 4456–4463 (2000).
63. Horowitz, G. Organic thin film transistors: From theory to real devices. *Journal of materials research* **19**, 1946–1962 (2004).
64. Street, R. A., Northrup, J. E. & Salleo, A. Transport in polycrystalline polymer thin-film transistors. *Phys. Rev. B* **71**, 165202 (2005).
65. Noriega, R. *et al.* A general relationship between disorder, aggregation and charge transport in conjugated polymers. *Nature materials* **12**, 1038–1044 (2013).
66. Rani, V., Sharma, A. & Ghosh, S. Charge carrier transport in polycrystalline organic thin film based field effect transistors. in *AIP Conference Proceedings* vol. 1731 (AIP Publishing, 2016).
67. Shur, M. & Hack, M. Physics of amorphous silicon based alloy field-effect transistors. *Journal of Applied Physics* **55**, 3831–3842 (1984).
68. Wang, X., Register, L. F. & Dodabalapur, A. Redefining the Mobility Edge in Thin-Film Transistors. *Phys. Rev. Applied* **11**, 064039 (2019).
69. Bässler, H. Charge transport in disordered organic photoconductors. A Monte Carlo simulation study. *Physica Status Solidi B (Basic Research);(Germany)* **175**, (1993).
70. Bässler, H. Localized states and electronic transport in single component organic solids with diagonal disorder. *Physica Status Solidi (b)* **107**, 9–54 (1981).
71. Zhang, X. *et al.* Molecular origin of high field-effect mobility in an indacenodithiophene–benzothiadiazole copolymer. *Nature communications* **4**, 2238 (2013).
72. Noriega, R. Efficient Charge Transport in Disordered Conjugated Polymer Microstructures. *Macromol. Rapid Commun.* **39**, 1800096 (2018).
73. Mollinger, S. A., Krajina, B. A., Noriega, R., Salleo, A. & Spakowitz, A. J. Percolation, Tie-Molecules, and the Microstructural Determinants of Charge Transport in Semicrystalline Conjugated Polymers. *ACS Macro Lett.* **4**, 708–712 (2015).
74. Northrup, J. E. Mobility enhancement in polymer organic semiconductors arising from increased interconnectivity at the level of polymer segments. *Applied Physics Letters* **106**, (2015).
75. Ji, L.-F., Fan, J.-X., Zhang, S.-F. & Ren, A.-M. Theoretical study on the charge transport in single crystals of TCNQ, F 2-TCNQ and F 4-TCNQ. *Physical Chemistry Chemical Physics* **20**, 3784–3794 (2018).
76. Baranovskii, S. D. Theoretical description of charge transport in disordered organic semiconductors. *Physica Status Solidi (b)* **251**, 487–525 (2014).
77. Tessler, N., Preezant, Y., Rappaport, N. & Roichman, Y. Charge Transport in Disordered Organic Materials and Its Relevance to Thin-Film Devices: A Tutorial Review. *Advanced Materials* **21**, 2741–2761 (2009).
78. van der Holst, J. J. M. Three-dimensional modeling of charge transport, injection and recombination in organic light-emitting diodes. (2010).
79. Groves, C. Simulating charge transport in organic semiconductors and devices: a review. *Rep. Prog. Phys.* **80**, 026502 (2017).
80. Miller, A. & Abrahams, E. Impurity Conduction at Low Concentrations. *Phys. Rev.* **120**, 745–755 (1960).
81. Simonetti, O. & Giraudet, L. Transport models in disordered organic semiconductors and their application to the simulation of thin-film transistors. *Polymer International* **68**, 620–636 (2019).
82. Marcus, R. A. Chemical and electrochemical electron-transfer theory. *Annual review of physical chemistry* **15**, 155–196 (1964).
83. Dong, J. & Wu, C. Crossover from hopping to band-like transport in crystalline organic semiconductors: The effect of shallow traps. *The Journal of Chemical Physics* **150**, (2019).
84. Morais, D., de Brito, P. E., Nazareno, H. N. & Dias, W. S. The superposed electric field effect on the charge transport and polaron formation in molecular crystals. *Journal of Physics: Condensed Matter* **34**, 455302 (2022).
85. Fratini, S., Ciuchi, S., Mayou, D., De Laissardière, G. T. & Troisi, A. A map of high-mobility molecular semiconductors. *Nature materials* **16**, 998–1002 (2017).
86. Shklovskii, B. I. & Efros, A. L. *Electronic Properties of Doped Semiconductors*. vol. 45 (Springer Science & Business Media, 2013).
87. Cottaar, J., Koster, L. J. A., Coehoorn, R. & Bobbert, P. A. Scaling Theory for Percolative Charge Transport in Disordered Molecular Semiconductors. *Phys. Rev. Lett.* **107**, 136601 (2011).
88. Fishchuk, I. I. *et al.* Electric field dependence of charge carrier hopping transport within the random energy

landscape in an organic field effect transistor. *Phys. Rev. B* **86**, 045207 (2012).
89. Oelerich, J. O., Huemmer, D. & Baranovskii, S. D. How to Find Out the Density of States in Disordered Organic Semiconductors. *Phys. Rev. Lett.* **108**, 226403 (2012).
90. Kim, J. S. *et al.* An Organic Vertical Field-Effect Transistor with Underside-Doped Graphene Electrodes. *Advanced Materials (Deerfield Beach, Fla.)* **28**, 4803–4810 (2016).
91. Borchert, J. W., Weitz, R. T., Ludwigs, S. & Klauk, H. A Critical Outlook for the Pursuit of Lower Contact Resistance in Organic Transistors. *Advanced Materials* **34**, 2104075 (2022).
92. Natali, D. & Caironi, M. Charge Injection in Solution-Processed Organic Field-Effect Transistors: Physics, Models and Characterization Methods. *Advanced Materials* **24**, 1357–1387 (2012).
93. Braun, S., Salaneck, W. R. & Fahlman, M. Energy-Level Alignment at Organic/Metal and Organic/Organic Interfaces. *Advanced Materials* **21**, 1450–1472 (2009).
94. Liu, Y. *et al.* Approaching the Schottky–Mott limit in van der Waals metal–semiconductor junctions. *Nature* **557**, 696–700 (2018).
95. Dodabalapur, A., Torsi, L. & Katz, H. E. Organic Transistors: Two-Dimensional Transport and Improved Electrical Characteristics. *Science* **268**, 270–271 (1995).
96. Dinelli, F. *et al.* Spatially Correlated Charge Transport in Organic Thin Film Transistors. *Phys. Rev. Lett.* **92**, 116802 (2004).
97. Brews, J. R. A charge-sheet model of the MOSFET. *Solid-State Electronics* **21**, 345–355 (1978).
98. Ye, X. *et al.* Blurred Electrode for Low Contact Resistance in Coplanar Organic Transistors. *ACS Nano* **15**, 1155–1166 (2021).
99. Weis, M. Gradual channel approximation models for organic field-effect transistors: The space-charge field effect. *Journal of Applied Physics* **111**, (2012).
100. Klauk, H. *Organic Electronics II: More Materials and Applications*. (John Wiley & Sons, 2012).
101. Paterson, A. F. *et al.* Recent Progress in High-Mobility Organic Transistors: A Reality Check. *Advanced Materials* **30**, 1801079 (2018).
102. Wong, H.-S., White, M. H., Krutsick, T. J. & Booth, R. V. Modeling of transconductance degradation and extraction of threshold voltage in thin oxide MOSFET's. *Solid-State Electronics* **30**, 953–968 (1987).
103. Boudinet, D. *et al.* Contact resistance and threshold voltage extraction in n-channel organic thin film transistors on plastic substrates. *Journal of Applied Physics* **105**, (2009).
104. Kumar Singh, V. & Mazhari, B. Measurement of threshold voltage in organic thin film transistors. *Applied Physics Letters* **102**, (2013).
105. Sze, S. M., Li, Y. & Ng, K. K. *Physics of Semiconductor Devices*. (John wiley & sons, 2021).
106. Borchert, J. W. On the minimization of contact resistance in organic thin-film transistors. (2020).
107. Baldacchini, C., Mariani, C. & Betti, M. G. Adsorption of pentacene on filled d-band metal surfaces: Long-range ordering and adsorption energy. *The Journal of chemical physics* **124**, (2006).
108. Lang, N. D. & Kohn, W. Theory of Metal Surfaces: Induced Surface Charge and Image Potential. *Phys. Rev. B* **7**, 3541–3550 (1973).
109. Osikowicz, W. *et al.* Energetics at Au top and bottom contacts on conjugated polymers. *Applied physics letters* **88**, (2006).
110. Fahlman, M. *et al.* Electronic structure of hybrid interfaces for polymer-based electronics. *Journal of Physics: Condensed Matter* **19**, 183202 (2007).
111. Miozzo, L., Yassar, A. & Horowitz, G. Surface engineering for high performance organic electronic devices: the chemical approach. *Journal of Materials Chemistry* **20**, 2513–2538 (2010).
112. Kymissis, I., Dimitrakopoulos, C. D. & Purushothaman, S. High-performance bottom electrode organic thin-film transistors. *IEEE Transactions on Electron Devices* **48**, 1060–1064 (2001).
113. Tulevski, G. S. *et al.* Chemical Complementarity in the Contacts for Nanoscale Organic Field-Effect Transistors. *J. Am. Chem. Soc.* **128**, 1788–1789 (2006).
114. Hamadani, B. H., Corley, D. A., Ciszek, J. W., Tour, J. M. & Natelson, D. Controlling Charge Injection in Organic Field-Effect Transistors Using Self-Assembled Monolayers. *Nano Lett.* **6**, 1303–1306 (2006).
115. Chu, C.-W., Li, S.-H., Chen, C.-W., Shrotriya, V. & Yang, Y. High-performance organic thin-film transistors with metal oxide/metal bilayer electrode. *Applied Physics Letters* **87**, (2005).
116. Gao, Y. *et al.* Efficient Charge Injection in Organic Field-Effect Transistors Enabled by Low-Temperature Atomic Layer Deposition of Ultrathin VO_x Interlayer. *Adv Funct Materials* **26**, 4456–4463 (2016).
117. Cho, S., Seo, J. H., Lee, K. & Heeger, A. J. Enhanced Performance of Fullerene n-Channel Field-Effect Transistors with Titanium Sub-Oxide Injection Layer. *Adv Funct Materials* **19**, 1459–1464 (2009).
118. Di, C. *et al.* High-Performance Low-Cost Organic Field-Effect Transistors with Chemically Modified Bottom Electrodes. *J. Am. Chem. Soc.* **128**, 16418–16419 (2006).
119. Yang, J.-P. *et al.* Fermi-level pinning appears upon weak electrode-organic contact without gap states: A universal phenomenon. *Organic Electronics* **48**, 172–178 (2017).

120. Bao, Q., Braun, S., Wang, C., Liu, X. & Fahlman, M. Interfaces of (Ultra)thin Polymer Films in Organic Electronics. *Adv Materials Inter* **6**, 1800897 (2019).
121. Waldrip, M., Jurchescu, O. D., Gundlach, D. J. & Bittle, E. G. Contact Resistance in Organic Field‐Effect Transistors: Conquering the Barrier. *Adv Funct Materials* **30**, 1904576 (2020).
122. Sarker, B. K. & Khondaker, S. I. Thermionic Emission and Tunneling at Carbon Nanotube–Organic Semiconductor Interface. *ACS Nano* **6**, 4993–4999 (2012).
123. Xu, Y. *et al.* Exploring the Charge Transport in Conjugated Polymers. *Advanced Materials* **29**, 1702729 (2017).
124. Li, J., Ou-Yang, W. & Weis, M. Electric-field enhanced thermionic emission model for carrier injection mechanism of organic field-effect transistors: understanding of contact resistance. *J. Phys. D: Appl. Phys.* **50**, 035101 (2017).
125. Li, H. & Brédas, J.-L. Quasi-One-Dimensional Charge Transport Can Lead to Nonlinear Current Characteristics in Organic Field-Effect Transistors. *J. Phys. Chem. Lett.* **9**, 6550–6555 (2018).
126. Wang, W., Lee, T. & Reed, M. A. Mechanism of electron conduction in self-assembled alkanethiol monolayer devices. *Phys. Rev. B* **68**, 035416 (2003).
127. Arkhipov, V. I., Emelianova, E. V., Tak, Y. H. & Bässler, H. Charge injection into light-emitting diodes: Theory and experiment. *Journal of Applied Physics* **84**, 848–856 (1998).
128. Zeng, J. *et al.* Ultralow contact resistance in organic transistors via orbital hybridization. *Nat Commun* **14**, 324 (2023).
129. Han, H. & Kim, C. Unexpected Benefits of Contact Resistance in 3D Organic Complementary Inverters. *Adv Elect Materials* **6**, 1900879 (2020).
130. Kim, C.-H. Contact resistance in organic transistors: Use it or remove it. *Applied Physics Reviews* **7**, 031306 (2020).
131. Tazuhara, S., Nagase, T., Kobayashi, T., Sadamitsu, Y. & Naito, H. Understanding the influence of contact resistances on short-channel high-mobility organic transistors in linear and saturation regimes. *Appl. Phys. Express* **14**, 041010 (2021).
132. Zschieschang, U. *et al.* Roadmap to Gigahertz Organic Transistors. *Adv Funct Materials* **30**, 1903812 (2020).
133. Luan, S. & Neudeck, G. W. An experimental study of the source/drain parasitic resistance effects in amorphous silicon thin film transistors. *Journal of Applied Physics* **72**, 766–772 (1992).
134. Liu, C., Xu, Y., Li, Y., Scheideler, W. & Minari, T. Critical Impact of Gate Dielectric Interfaces on the Contact Resistance of High-Performance Organic Field-Effect Transistors. *J. Phys. Chem. C* **117**, 12337–12345 (2013).
135. Berger, H. H. Contact resistance and contact resistivity. *Journal of the Electrochemical Society* **119**, 507 (1972).
136. Xu, Y. *et al.* Metal evaporation dependent charge injection in organic transistors. *Organic electronics* **15**, 1738–1744 (2014).
137. Liu, C., Xu, Y. & Noh, Y.-Y. Contact engineering in organic field-effect transistors. *Materials Today* **18**, 79–96 (2015).
138. Allain, A., Kang, J., Banerjee, K. & Kis, A. Electrical contacts to two-dimensional semiconductors. *Nature materials* **14**, 1195–1205 (2015).
139. Scott, J. C. Metal–organic interface and charge injection in organic electronic devices. *Journal of Vacuum Science & Technology A: Vacuum, Surfaces, and Films* **21**, 521–531 (2003).
140. Liu, C. *et al.* Universal diffusion-limited injection and the hook effect in organic thin-film transistors. *Sci Rep* **6**, 29811 (2016).
141. Rhoderick, E. H. & Williams, R. H. *Metal-Semiconductor Contacts*. vol. 129 (Clarendon press Oxford, 1988).
142. Virkar, A. A., Mannsfeld, S., Bao, Z. & Stingelin, N. Organic Semiconductor Growth and Morphology Considerations for Organic Thin‐Film Transistors. *Advanced Materials* **22**, 3857–3875 (2010).
143. Fratini, S., Nikolka, M., Salleo, A., Schweicher, G. & Sirringhaus, H. Charge transport in high-mobility conjugated polymers and molecular semiconductors. *Nature materials* **19**, 491–502 (2020).
144. Anthony, J. E. Functionalized Acenes and Heteroacenes for Organic Electronics. *Chem. Rev.* **106**, 5028–5048 (2006).
145. Liu, C. *et al.* A unified understanding of charge transport in organic semiconductors: the importance of attenuated delocalization for the carriers. *Materials horizons* **4**, 608–618 (2017).
146. Minari, T., Miyadera, T., Tsukagoshi, K., Aoyagi, Y. & Ito, H. Charge injection process in organic field-effect transistors. *Applied Physics Letters* **91**, (2007).
147. Sun, Y., Liu, Y. & Zhu, D. Advances in organic field-effect transistors. *Journal of materials Chemistry* **15**, 53–65 (2005).
148. Park, Y. D., Lim, J. A., Lee, H. S. & Cho, K. Interface engineering in organic transistors. *Materials today* **10**, 46–54 (2007).

149. Zen, A. *et al.* Improving the performance of organic field effect transistor by optimizing the gate insulator surface. *Japanese journal of applied physics* **44**, 3721 (2005).
150. Salleo, A., Chabinyc, M. L., Yang, M. S. & Street, R. A. Polymer thin-film transistors with chemically modified dielectric interfaces. *Applied Physics Letters* **81**, 4383–4385 (2002).
151. Di, C., Liu, Y., Yu, G. & Zhu, D. Interface Engineering: An Effective Approach toward High-Performance Organic Field-Effect Transistors. *Acc. Chem. Res.* **42**, 1573–1583 (2009).
152. Kahn, A., Koch, N. & Gao, W. Electronic structure and electrical properties of interfaces between metals and π-conjugated molecular films. *J Polym Sci B Polym Phys* **41**, 2529–2548 (2003).
153. Alves, H., Molinari, A. S., Xie, H. & Morpurgo, A. F. Metallic conduction at organic charge-transfer interfaces. *Nature materials* **7**, 574–580 (2008).
154. Rockson, T. K. *et al.* Macroscopic Interfacial Property as a Determining Parameter for Reliable Prediction of Charge Mobility in Organic Transistors. *J. Phys. Chem. C* **122**, 17695–17705 (2018).
155. Kobayashi, S. *et al.* Control of carrier density by self-assembled monolayers in organic field-effect transistors. *Nature materials* **3**, 317–322 (2004).
156. Takeya, J. *et al.* Effects of polarized organosilane self-assembled monolayers on organic single-crystal field-effect transistors. *Applied physics letters* **85**, 5078–5080 (2004).
157. Cho, J. H. *et al.* Printable ion-gel gate dielectrics for low-voltage polymer thin-film transistors on plastic. *Nature materials* **7**, 900–906 (2008).
158. Ito, Y. *et al.* Crystalline Ultrasmooth Self-Assembled Monolayers of Alkylsilanes for Organic Field-Effect Transistors. *J. Am. Chem. Soc.* **131**, 9396–9404 (2009).
159. Yang, H. *et al.* Conducting AFM and 2D GIXD Studies on Pentacene Thin Films. *J. Am. Chem. Soc.* **127**, 11542–11543 (2005).
160. Cinar, M. E. & Ozturk, T. Thienothiophenes, Dithienothiophenes, and Thienoacenes: Syntheses, Oligomers, Polymers, and Properties. *Chem. Rev.* **115**, 3036–3140 (2015).
161. Takimiya, K., Shinamura, S., Osaka, I. & Miyazaki, E. Thienoacene-Based Organic Semiconductors. *Advanced Materials* **23**, 4347–4370 (2011).
162. Takimiya, K., Osaka, I., Mori, T. & Nakano, M. Organic Semiconductors Based on [1]Benzothieno[3,2-*b*][1]benzothiophene Substructure. *Acc. Chem. Res.* **47**, 1493–1502 (2014).
163. Inokuchi, H. *et al.* A novel type of organic semiconductors. Molecular fastener. *Chemistry Letters* **15**, 1263–1266 (1986).
164. De Tournadre, G. *et al.* High voltage surface potential measurements in ambient conditions: Application to organic thin-film transistor injection and transport characterization. *Journal of Applied Physics* **119**, 125501 (2016).
165. Brouillard, M. *et al.* Experimental determination of the lateral resolution of surface electric potential measurements by Kelvin probe force microscopy using biased electrodes separated by a nanoscale gap and application to thin-film transistors. *Nanoscale Advances* **4**, 2018–2028 (2022).
166. Brouillard, M. Étude de l'injection des charges dans les transistors organiques à effet de champ par microscopie à sonde de Kelvin (KPFM). (2021).
167. Grégoire de TOURNADRE. Développement d'une méthode de mesure du potentiel de surface par AFM pour composants électroniques en fonctionnement, application aux transistors organiques. (2016).
168. Bürgi, L., Sirringhaus, H. & Friend, R. H. Noncontact potentiometry of polymer field-effect transistors. *Applied Physics Letters* **80**, 2913–2915 (2002).
169. Bürgi, L., Friend, R. H. & Sirringhaus, H. Formation of the accumulation layer in polymer field-effect transistors. *Applied Physics Letters* **82**, 1482–1484 (2003).
170. Chen, M., Peng, B., Sporea, R. A., Podzorov, V. & Chan, P. K. L. The Origin of Low Contact Resistance in Monolayer Organic Field-Effect Transistors with van der Waals Electrodes. *Small Science* **2**, 2100115 (2022).
171. Simonetti, O., Giraudet, L., Maurel, T., Nicolas, J.-L. & Belkhir, A. Organic transistor model with nonlinear injection: Effects of uneven source contact on apparent mobility and threshold voltage. *Organic Electronics* **11**, 1381–1393 (2010).
172. Kim, C.-H. Contact resistance in organic transistors: Use it or remove it. *Applied Physics Reviews* **7**, 031306 (2020).
173. Raman, C. V. & Krishnan, K. S. A new type of secondary radiation. *Nature* **121**, 501–502 (1928).
174. Ma, H. *et al.* Surface-Enhanced Raman Spectroscopy: Current Understanding, Challenges, and Opportunities. *ACS Nano* **18**, 14000–14019 (2024).
175. Schüller, C. Inelastic light scattering of semiconductor nanostructures: fundamentals and recent advances. (2006).
176. LeRu, E. C. & Etchegoin, P. Principles of Surface Enhanced Raman Spectroscopy Elsevier. (2009).
177. Long, D. A. The raman effect. *The Raman Effect: A Unified Treatment of the Theory of Raman Scattering by Molecules* (2002).

178. Fleischmann, M., Hendra, P. J. & McQuillan, A. J. Raman spectra of pyridine adsorbed at a silver electrode. *Chemical physics letters* **26**, 163–166 (1974).
179. Jeanmaire, D. L. & Van Duyne, R. P. Surface Raman spectroelectrochemistry: Part I. Heterocyclic, aromatic, and aliphatic amines adsorbed on the anodized silver electrode. *Journal of electroanalytical chemistry and interfacial electrochemistry* **84**, 1–20 (1977).
180. Albrecht, M. G. & Creighton, J. A. Anomalously intense Raman spectra of pyridine at a silver electrode. *J. Am. Chem. Soc.* **99**, 5215–5217 (1977).
181. Kneipp, K. *et al.* Single Molecule Detection Using Surface-Enhanced Raman Scattering (SERS). *Phys. Rev. Lett.* **78**, 1667–1670 (1997).
182. Nie, S. & Emory, S. R. Probing Single Molecules and Single Nanoparticles by Surface-Enhanced Raman Scattering. *Science* **275**, 1102–1106 (1997).
183. Gersten, J. I., Birke, R. L. & Lombardi, J. R. Theory of Enhance I Light Scattering from Molecules Adsorbed at the Metal-Solution Interface. *Phys. Rev. Lett.* **43**, 147–150 (1979).
184. Langer, J. *et al.* Present and Future of Surface-Enhanced Raman Scattering. *ACS Nano* **14**, 28–117 (2020).
185. Yamamoto, Y. S., Ozaki, Y. & Itoh, T. Recent progress and frontiers in the electromagnetic mechanism of surface-enhanced Raman scattering. *Journal of Photochemistry and Photobiology C: Photochemistry Reviews* **21**, 81–104 (2014).
186. Moskovits, M. Surface roughness and the enhanced intensity of Raman scattering by molecules adsorbed on metals. *The Journal of Chemical Physics* **69**, 4159–4161 (1978).
187. Hao-bing, W. *et al.* Absorption enhancement of silicon via localized surface plasmons resonance in blue band. *Chinese Optics* **13**, 1362–1384 (2020).
188. Enoch, S. & Bonod, N. *Plasmonics: From Basics to Advanced Topics*. vol. 167 (Springer, 2012).
189. Lombardi, J. R. & Birke, R. L. A Unified Approach to Surface-Enhanced Raman Spectroscopy. *J. Phys. Chem. C* **112**, 5605–5617 (2008).
190. Lee, C., Yang, W. & Parr, R. G. Development of the Colle-Salvetti correlation-energy formula into a functional of the electron density. *Phys. Rev. B* **37**, 785–789 (1988).
191. Coropceanu, V. *et al.* Charge Transport in Organic Semiconductors. *Chem. Rev.* **107**, 926–952 (2007).
192. Neamen, D. A. & Biswas, D. *Semiconductor Physics and Devices*. (McGraw-Hill higher education New York, 2011).
193. Le Ru, E. & Etchegoin, P. *Principles of Surface-Enhanced Raman Spectroscopy: And Related Plasmonic Effects*. (Elsevier, 2008).
194. Wang, Q. *et al.* Interfacial Flat-Lying Molecular Monolayers for Performance Enhancement in Organic Field-Effect Transistors. *ACS Appl. Mater. Interfaces* **10**, 22513–22519 (2018).
195. Adil, D. & Guha, S. Surface-Enhanced Raman Spectroscopic Studies of Metal–Semiconductor Interfaces in Organic Field-Effect Transistors. *J. Phys. Chem. C* **116**, 12779–12785 (2012).
196. Pilot *et al.* A Review on Surface-Enhanced Raman Scattering. *Biosensors* **9**, 57 (2019).
197. Sharma, B., Frontiera, R. R., Henry, A.-I., Ringe, E. & Van Duyne, R. P. SERS: Materials, applications, and the future. *Materials Today* **15**, 16–25 (2012).
198. Li, H. *et al.* Introducing a Surface-Enhanced-Raman-Scattering Enhancer for Experimental Estimation of the Debye Screening Length in Organic Field-Effect Transistors. *ACS Appl. Electron. Mater.* **3**, 1920–1930 (2021).
199. Adil, D. & Guha, S. Surface-enhanced Raman spectroscopic studies of the Au-pentacene interface: A combined experimental and theoretical investigation. *The Journal of Chemical Physics* **139**, 044715 (2013).
200. Yamaguchi, Y. *et al.* Solution-Processable Organic Semiconductors Featuring S-Shaped Dinaphthothienothiophene (S-DNTT): Effects of Alkyl Chain Length on Self-Organization and Carrier Transport Properties. *Chem. Mater.* **32**, 5350–5360 (2020).
201. Borchert, J. W. *et al.* Flexible low-voltage high-frequency organic thin-film transistors. *Sci. Adv.* **6**, eaaz5156 (2020).
202. Borchert, J. W. *et al.* Small contact resistance and high-frequency operation of flexible low-voltage inverted coplanar organic transistors. *Nat Commun* **10**, 1119 (2019).
203. Richards, T. & Sirringhaus, H. Bias-stress induced contact and channel degradation in staggered and coplanar organic field-effect transistors. *Applied Physics Letters* **92**, (2008).
204. Lee, B. *et al.* Origin of the bias stress instability in single-crystal organic field-effect transistors. *Phys. Rev. B* **82**, 085302 (2010).
205. Lee, W. H., Choi, H. H., Kim, D. H. & Cho, K. 25th Anniversary Article: Microstructure Dependent Bias Stability of Organic Transistors. *Advanced Materials* **26**, 1660–1680 (2014).
206. Park, S., Kim, S. H., Choi, H. H., Kang, B. & Cho, K. Recent Advances in the Bias Stress Stability of Organic Transistors. *Adv Funct Materials* **30**, 1904590 (2020).
207. Cheng, H.-L., Chou, W.-Y., Kuo, C. W., Tang, F.-C. & Wang, Y.-W. Electric field-induced structural changes in pentacene-based organic thin-film transistors studied by in situ micro-Raman spectroscopy. *Applied*

physics letters **88**, (2006).
208. Weber, W. H. & Merlin, R. *Raman Scattering in Materials Science*. vol. 42 (Springer Science & Business Media, 2013).
209. Kumar, C. S. *Raman Spectroscopy for Nanomaterials Characterization*. (Springer Science & Business Media, 2012).
210. Cheng, H. L. *et al.* Influence of Electric Field on Microstructures of Pentacene Thin-Films in Field-Effect Transistors. *Adv Funct Materials* **18**, 285–293 (2008).
211. Peng, B. *et al.* Crystallized Monolayer Semiconductor for Ohmic Contact Resistance, High Intrinsic Gain, and High Current Density. *Advanced Materials* **32**, 2002281 (2020).
212. Beechem, T. & Graham, S. Temperature Measurement of Microdevices using Thermoreflectance and Raman Thermometry. in *BioNanoFluidic MEMS* (ed. Hesketh, P. J.) 153–174 (Springer US, Boston, MA, 2008). doi:10.1007/978-0-387-46283-7_6.
213. Sharma, A., Mathijssen, S. G. J., Kemerink, M., De Leeuw, D. & Bobbert, P. A. Proton migration mechanism for the instability of organic field-effect transistors. *Applied Physics Letters* **95**, (2009).
214. Bobbert, P. A., Sharma, A., Mathijssen, S. G. J., Kemerink, M. & De Leeuw, D. M. Operational Stability of Organic Field-Effect Transistors. *Advanced Materials* **24**, 1146–1158 (2012).
215. Kline, R. J. *et al.* Critical Role of Side-Chain Attachment Density on the Order and Device Performance of Polythiophenes. *Macromolecules* **40**, 7960–7965 (2007).
216. DeLongchamp, D. M. *et al.* High carrier mobility polythiophene thin films: structure determination by experiment and theory. *Advanced Materials* **19**, 833–837 (2007).
217. Cho, S. *et al.* Thermal annealing-induced enhancement of the field-effect mobility of regioregular poly (3-hexylthiophene) films. *Journal of applied physics* **100**, (2006).
218. Iino, H., Usui, T. & Hanna, J. Liquid crystals for organic thin-film transistors. *Nature communications* **6**, 6828 (2015).
219. Sun, B., Hong, W., Yan, Z., Aziz, H. & Li, Y. Record High Electron Mobility of 6.3 $cm^2 V^{-1} s^{-1}$ Achieved for Polymer Semiconductors Using a New Building Block. *Advanced Materials* **26**, 2636–2642 (2014).
220. Rudawska, A. & Jacniacka, E. Analysis for determining surface free energy uncertainty by the Owen–Wendt method. *International journal of adhesion and adhesives* **29**, 451–457 (2009).
221. Janssen, D., De Palma, R., Verlaak, S., Heremans, P. & Dehaen, W. Static solvent contact angle measurements, surface free energy and wettability determination of various self-assembled monolayers on silicon dioxide. *Thin Solid Films* **515**, 1433–1438 (2006).
222. Okamoto, T. Next-generation organic semiconductors driven by bent-shaped π-electron cores. *Polym J* **51**, 825–833 (2019).
223. Mitsui, C. *et al.* High-performance solution-processable N-shaped organic semiconducting materials with stabilized crystal phase. *Advanced Materials (Deerfield Beach, Fla.)* **26**, 4546–4551 (2014).
224. Huang, H., Yang, L., Facchetti, A. & Marks, T. J. Organic and Polymeric Semiconductors Enhanced by Noncovalent Conformational Locks. *Chem. Rev.* **117**, 10291–10318 (2017).
225. Liu, C. *et al.* Universal diffusion-limited injection and the hook effect in organic thin-film transistors. *Sci Rep* **6**, 29811 (2016).
226. Pei, K., Lau, A. H. Y. & Chan, P. K. L. Understanding molecular surface doping of large bandgap organic semiconductors and overcoming the contact/access resistance in organic field-effect transistors. *Physical Chemistry Chemical Physics* **22**, 7100–7109 (2020).
227. Han, L. *et al.* Reducing contact resistance in bottom contact organic field effect transistors for integrated electronics. *J. Phys. D: Appl. Phys.* **53**, 014002 (2019).
228. Wang, Q. *et al.* Role of Schottky Barrier and Access Resistance in Organic Field-Effect Transistors. *J. Phys. Chem. Lett.* **11**, 1466–1472 (2020).
229. Gruber, M., Schürrer, F. & Zojer, K. Relation between injection barrier and contact resistance in top-contact organic thin-film transistors. *Organic Electronics* **13**, 1887–1899 (2012).
230. Kim, C.-H. *et al.* Decoupling the effects of self-assembled monolayers on gold, silver, and copper organic transistor contacts. *Advanced Materials Interfaces* **2**, 1400384 (2015).
231. Bürgi, L., Richards, T. J., Friend, R. H. & Sirringhaus, H. Close look at charge carrier injection in polymer field-effect transistors. *Journal of Applied physics* **94**, 6129–6137 (2003).
232. Liu, D. & Miao, Q. Recent progress in interface engineering of organic thin film transistors with self-assembled monolayers. *Materials Chemistry Frontiers* **2**, 11–21 (2018).
233. Casalini, S., Bortolotti, C. A., Leonardi, F. & Biscarini, F. Self-assembled monolayers in organic electronics. *Chemical Society Reviews* **46**, 40–71 (2017).
234. Petritz, A. *et al.* Embedded Dipole Self-Assembled Monolayers for Contact Resistance Tuning in p-Type and n-Type Organic Thin Film Transistors and Flexible Electronic Circuits. *Adv Funct Materials* **28**, 1804462 (2018).
235. Lee, E. K. *et al.* Organic Transistors: Chemically Robust Ambipolar Organic Transistor Array Directly

Patterned by Photolithography (Adv. Mater. 11/2017). *Advanced Materials* **29**, adma.201770077 (2017).
236. Chen, H., Zhang, W., Li, M., He, G. & Guo, X. Interface Engineering in Organic Field-Effect Transistors: Principles, Applications, and Perspectives. *Chem. Rev.* **120**, 2879–2949 (2020).
237. Kotadiya, N. B. *et al.* Universal strategy for Ohmic hole injection into organic semiconductors with high ionization energies. *Nature materials* **17**, 329–334 (2018).
238. Yang, Z. *et al.* Enhanced Organic Thin-Film Transistor Stability by Preventing MoO_3 Diffusion with Metal/MoO_3/Organic Multilayered Interface Source-Drain Contact. *ACS Appl. Mater. Interfaces* **15**, 1704–1717 (2023).
239. Yamamura, A. *et al.* High‐Speed Organic Single‐Crystal Transistor Responding to Very High Frequency Band. *Adv Funct Materials* **30**, 1909501 (2020).
240. Sawada, T. *et al.* Correlation between the static and dynamic responses of organic single-crystal field-effect transistors. *Nature Communications* **11**, 4839 (2020).
241. Hu, Y. *et al.* Doping Polymer Semiconductors by Organic Salts: Toward High-Performance Solution-Processed Organic Field-Effect Transistors. *ACS Nano* **12**, 3938–3946 (2018).
242. Matsumoto, T., Ou-Yang, W., Miyake, K., Uemura, T. & Takeya, J. Study of contact resistance of high-mobility organic transistors through comparisons. *Organic Electronics* **14**, 2590–2595 (2013).
243. Natali, D. *et al.* Injection Length in Staggered Organic Thin Film Transistors: Assessment and Implications for Device Downscaling. *Adv Elect Materials* **2**, 1600097 (2016).
244. Xu, Y., Sun, H. & Noh, Y.-Y. Schottky Barrier in Organic Transistors. *IEEE Trans. Electron Devices* **64**, 1932–1943 (2017).
245. Hwang, T. *et al.* Buried‐Contact Organic Field‐Effect Transistor: The Way of Alleviating Drawbacks from Interfacial Charge Transfer. *Adv Funct Materials* **34**, 2312232 (2024).
246. Günther, A. A., Sawatzki, M., Formánek, P., Kasemann, D. & Leo, K. Contact Doping for Vertical Organic Field‐Effect Transistors. *Adv Funct Materials* **26**, 768–775 (2016).
247. Tietze, M. L., Pahner, P., Schmidt, K., Leo, K. & Lüssem, B. Doped Organic Semiconductors: Trap‐Filling, Impurity Saturation, and Reserve Regimes. *Adv Funct Materials* **25**, 2701–2707 (2015).
248. Kim, C.-H. Organic Heterojunction Transistors. *ACS Appl. Electron. Mater.* **4**, 2581–2588 (2022).
249. Zhang, P., Wang, H. & Yan, D. Organic High Electron Mobility Transistors Realized by 2D Electron Gas. *Advanced Materials* **29**, 1702427 (2017).
250. Kösemen, Z. A. *et al.* Performance improvement in photosensitive organic field effect transistor by using multi-layer structure. *Thin Solid Films* **672**, 90–99 (2019).
251. Kim, C. H., Bonnassieux, Y. & Horowitz, G. Fundamental benefits of the staggered geometry for organic field-effect transistors. *IEEE Electron Device Letters* **32**, 1302–1304 (2011).
252. Lee, S., Han, H. & Kim, C.-H. Nanodielectrics approaches to low-voltage organic transistors and circuits. *The European Physical Journal Applied Physics* **91**, 20201 (2020).
253. Hanic, M., Vincze, T., Rezo, V. & Weis, M. Nature of Ohmic and Schottky contacts on pentacene-based organic field-effect transistor. *Synthetic Metals* **305**, 117590 (2024).
254. Rani, V. *et al.* Carrier induced hopping to band conduction in pentacene. *Scientific Reports* **9**, 20193 (2019).
255. Zschieschang, U., Weitz, R. T., Kern, K. & Klauk, H. Bias stress effect in low-voltage organic thin-film transistors. *Appl. Phys. A* **95**, 139–145 (2009).
256. Wang, Y.-W. *et al.* Influence of measuring environment on the electrical characteristics of pentacene-based thin film transistors. *Thin Solid Films* **467**, 215–219 (2004).
257. Cheng, H. ‐L., Mai, Y. ‐S., Chou, W. ‐Y., Chang, L. ‐R. & Liang, X. ‐W. Thickness‐Dependent Structural Evolutions and Growth Models in Relation to Carrier Transport Properties in Polycrystalline Pentacene Thin Films. *Adv Funct Materials* **17**, 3639–3649 (2007).
258. Kim, A. *et al.* Surface-induced orientation of pentacene molecules and transport anisotropy on nanogroove SiO2 dielectric layer by simple scratched method: The study of surface roughness and molecular alignment on the mobility of organic thin film transistors. *Organic Electronics* **42**, 316–321 (2017).
259. Marinkovic, M., Belaineh, D., Wagner, V. & Knipp, D. On the Origin of Contact Resistances of Organic Thin Film Transistors. *Adv. Mater.* **24**, 4005–4009 (2012).
260. Lamport, Z. A. *et al.* A simple and robust approach to reducing contact resistance in organic transistors. *Nat Commun* **9**, 5130 (2018).
261. He, K. *et al.* Five-ring-fused asymmetric thienoacenes for high mobility organic thin-film transistors: the influence of the position of the S atom in the terminal thiophene ring. *Journal of Materials Chemistry C* **7**, 3656–3664 (2019).
262. Un, H., Wang, J. & Pei, J. Recent Efforts in Understanding and Improving the Nonideal Behaviors of Organic Field‐Effect Transistors. *Advanced Science* **6**, 1900375 (2019).
263. Park, S., Choi, W., Kim, S. H., Lee, H. & Cho, K. Protonated Organic Semiconductors: Origin of Water‐Induced Charge‐Trap Generation. *Advanced Materials* **35**, 2303707 (2023).

264. Stadtmüller, B., Kröger, I., Reinert, F. & Kumpf, C. Submonolayer growth of CuPc on noble metal surfaces. *Phys. Rev. B* **83**, 085416 (2011).
265. Brondijk, J. J., Torricelli, F., Smits, E. C. P., Blom, P. W. M. & De Leeuw, D. M. Gate-bias assisted charge injection in organic field-effect transistors. *Organic Electronics* **13**, 1526–1531 (2012).
266. Pasveer, W. F. *et al.* Unified Description of Charge-Carrier Mobilities in Disordered Semiconducting Polymers. *Phys. Rev. Lett.* **94**, 206601 (2005).
267. Massé, A. *et al.* Ab initio charge-carrier mobility model for amorphous molecular semiconductors. *Phys. Rev. B* **93**, 195209 (2016).
268. Oshima, K., Kuribara, K. & Sato, T. Layout Design for DNTT-based Organic TFTs Considering Fringe Leakage Current. *IEEE Journal on Flexible Electronics* (2024).
269. Za'aba, N. K. & Taylor, D. M. Bias and related stress effects in organic thin film transistors based on dinaphtho [2, 3-b: 2′, 3′-f] thieno [3, 2-b] thiophene (DNTT). *Organic Electronics* **62**, 382–393 (2018).
270. Adil, D. & Guha, S. Surface-Enhanced Raman Spectroscopic Studies of Metal–Semiconductor Interfaces in Organic Field-Effect Transistors. *J. Phys. Chem. C* **116**, 12779–12785 (2012).
271. Guo, D., Ikeda, S., Saiki, K., Miyazoe, H. & Terashima, K. Effect of annealing on the mobility and morphology of thermally activated pentacene thin film transistors. *Journal of applied physics* **99**, (2006).
272. Ahn, T., Jung, H., Suk, H. J. & Yi, M. H. Effect of postfabrication thermal annealing on the electrical performance of pentacene organic thin-film transistors. *Synthetic Metals* **159**, 1277–1280 (2009).
273. Bürgi, L., Sirringhaus, H. & Friend, R. H. Noncontact potentiometry of polymer field-effect transistors. *Appl. Phys. Lett.* **80**, 2913–2915 (2002).
274. Acharya, R. Ultrathin organic thin-film transistors: Investigating Hybrid Gate Dielectrics and Stable Semiconductor Monolayers. 242.

9 Appendix

9.1 Eerly saturation effect

In the Section 2.6.3, we roughly displayed the results that simulating *Early Saturation effect* in initial S-DNTT-10-based OTFTs according to the Gradual Channel Approximation (*GCA*) as the fundamental theory. Herein, we plan to show details about mathematical simulating *Early Saturation effect.* Firstly, we retrospected this effect in the S-DNTT-10-based OTFTs.

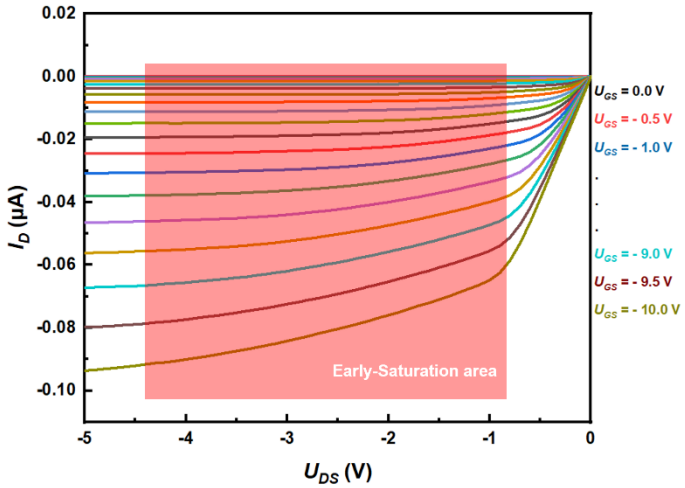


Figure 9.1 S-DNTT-10-based OTFT, Width (*W*) = 1000 μm, Channel Length (*L*) = 30 μm, $T_{S\text{-}DNTT10}$ = 25 nm, T_{ox} = 300 nm, C_i = 0.00011505 F/m^2. Output characteristics, U_{DS} = 2 ~ -5 V, Step- U_{DS} = 0.1 V, U_{GS} = 2 ~ -5 V, Step-U_{GS} = 0.5 V. (The apparent red area is noted as the area of emerging early saturation effect, and the collected drain current suddenly appeared into saturation-regime tendence)

To explore the effect, it was calculated the conductivity (G_{diff}), at a given gate-source voltage drop U_{GS},

$$G_{diff} = \frac{\partial I_D}{\partial U_{DS}} \tag{9.1}$$

based on **Figure 9.1** showed the experimental data in the I_D - U_{DS}, then calculated the value of differential initially occurred larger reduction at small drain voltage, as **Figure 9.2** shown. According to the acquired I_D-U_{DS} curve, no obvious S-shape or nonlinear effect was observed in the output characteristics curve at the initial small drain voltage, even under a significantly lower gate voltage. Therefore, it can be inferred that the injection barrier between the work function of the gold source electrode and the HOMO energy level did not dominate in this device.

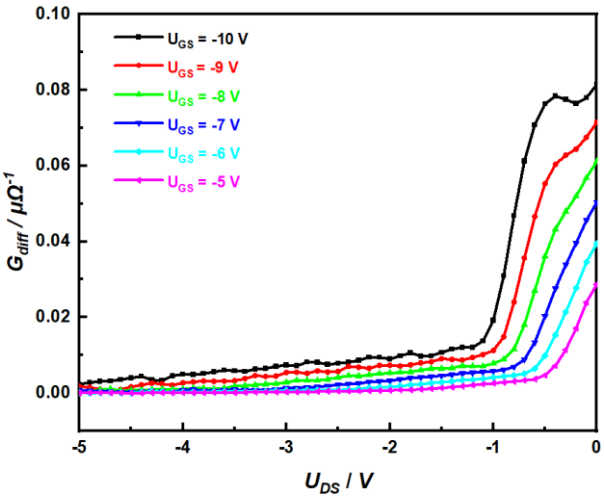


Figure 9.2 The differential of drain current I_D corresponding to drain voltage U_{DS} under variable gate voltage U_{GS} and source penitential referenced to V_S=0.

As *GCA* theory [273] for expressing the *I-V* relationship in the linear mode,

$$I_D = \frac{W}{L}\mu_{eff}C_i\left[(U_{GS} - U_{Th})U_{DS} - \frac{1}{2}U_{DS}^2\right] \quad \textbf{(9.2)}$$

W, *L*, μ_{eff}, C_i, and U_T respectively indicated as the width of the channel, channel length, and effective mobility regarded as constant, the threshold voltage. And G_{diff} enabled to be expressed [140],

$$G_{diff} = \frac{\partial I_D}{\partial U_{DS}} = \frac{W}{L}\mu_{eff}C_i[U_{GS} - U_{Th} - U_{DS}] \quad \textbf{(9.3)}$$

To compare with the I_D-U_{DS} characteristics it was also calculated on I_D-U_{DS} based on *CGA* theory, the corresponding parameter in the following **Table 9.1** and **Figure 9.3** were respectively relationships of I_D - U_{DS} and G_{diff} - U_{DS}.

Table 9.1 Setting parameters in the Equation.(9.2) and (9.3).

Parameter	W/μm	L/μm	T_{SiO2}/nm	C_i /F·m^{-2}	μ_{eff}/cm^2·V^{-1}·s^{-1}	U_{GS}/V	U_{Th}/V
Value	1000	30	300	1.1505·10^{-4}	0.0285	-10	-2.8

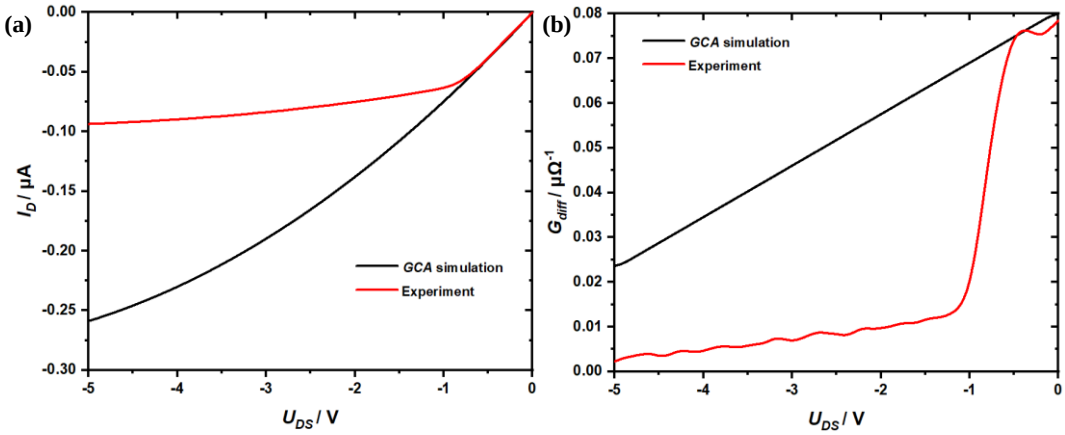


Figure 9.3 (a) Experimental and simulation I_D-U_{DS} curve of the S-DNTT10-OTFT at U_{GS} = -10 V showed in Figure 2.15, (b) the corresponding to the differential calculation through the differential function.

Combined with one of the available conditions from *GCA* theory, where the supposed effective field-effect mobility μ_{eff} is considered a constant parameter, **Equation.(9.3)** does not seem to accurately simulate the early saturation effect. Therefore, based on the above simulation, it can be hypothesized that the effective mobility μ_{eff} may vary with the drain voltage U_{DS} at a given gate voltage U_{GS}. Using the physical model of charge transport [58,171,172], a new model was established in which the effective field-effect mobility μ (U_{GS}, U_{CS}) is correlated with the parameter σ and various U_{CS} values at a given gate voltage U_{GS},

$$\mu(U_{GS}, U_{CS}) \propto (k \cdot U_{GS}) \cdot U_{CS}^{\sigma} \tag{9.4}$$

in which U_{CS} was the drop voltage between channel-potential V_C and source-potential V_S, *i.e.*, $U_{CS} = V_C - V_S$, and the drain-gate potential drop at the drain was U_{DS}. The coefficient k was a positive factor that accounted for the influence of the threshold voltage U_{Th} on the drain current, and the term, ($k \cdot U_{GS}$), represented the effect of various gate-source voltages U_{GS} on the mobility. The parameter σ was a negative coefficient, indicating that the field-effect mobility μ in the channel varied with increasing drain voltage U_{DS} at a given gate voltage U_{GS}.

The mode of the mobility in the channel was expressed as,

$$\mu(U_{GS}, U_{CS}) = \beta |U_{GS} - U_{Th} - U_{cs}|^{\alpha} \tag{9.5}$$

in which the β was a mobility-fitting parameter and the α was a voltage-fitting parameter. And based on the *GCA* theory, the *I-V* relationship was deduced as,

$$I_D = -W \cdot \mu(U_{GS}, U_{CS}) \cdot C_i (U_{GS} - U_{Th} - U_{CS}) \frac{dU_{CS}}{dx} \tag{9.6}$$

then the I_D-U_{DS} formula was expressed as,

$$I_D = -\frac{WC_i\beta}{L(\alpha+2)}\left[(U_{GS}-U_{Th})^{\alpha+2}-(U_{GS}-U_{Th}-U_{DS})^{\alpha+2}\right] \quad (9.7)$$

And the parameters were set in the **Table 9.2** and plotted the corresponding compared **Figure 9.4**.

Table 9.2 Defined parameters in the Equation. Erreur ! Source du renvoi introuvable.Erreur ! Source du renvoi introuvable.**).**

Parameter	W/μm	L/μm	C_i /F·m^{-2}	β	α	U_{GS} /V	U_{Th}/V
Value	1000	30	$1.1505\cdot10^{-4}$	$5\cdot10^{-8}$	1.8	-10	-2.8

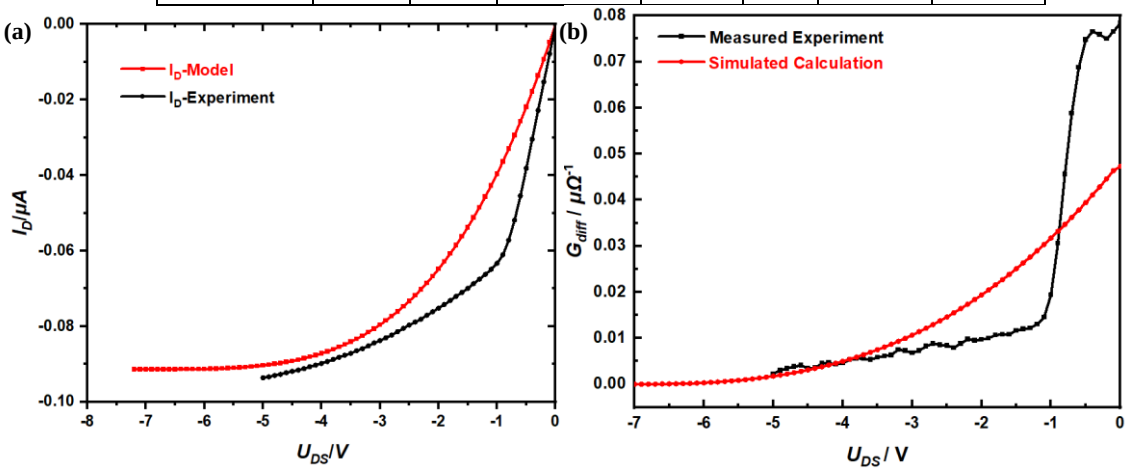


Figure 9.4 (a) The calculation on I_D -U_{DS} compared with experimental results, and (b) the corresponding compared G_{diff}-U_{DS}.

As shown in **Figure 9.4 (a)**, the calculated results, indicated by the red solid line, were somewhat similar. However, the corresponding G_{diff} differed significantly from the experimental data. It was thus concluded that the channel resistance was not dominant in the total resistance system, and other types of resistance should be considered. The fundamental equation used was Ohm's Law: $I_D = U_{DS} / R_{tot}$. It was assumed that the injection contact resistance R_{inj} was not dominant in the total resistance system R_{tot}. The total resistance in the linear operation of OTFTs can be regarded as consisting of bulk resistance (R_{bulk}), channel resistance (R_{ch}), and a parasitic resistance (R_0) caused by the lower quality or disordered molecular arrangement of the organic material, which hindered charge transport [172]. Hence, $R_{tot} = R_0 + R_{bulk} + R_{ch}$, as illustrated in **Figure 9.5**. In this case, we assumed that R_0 consists of R_{01} and R_{02}, and R_{bulk} is made up of R_{bulk1} and R_{bulk2}.

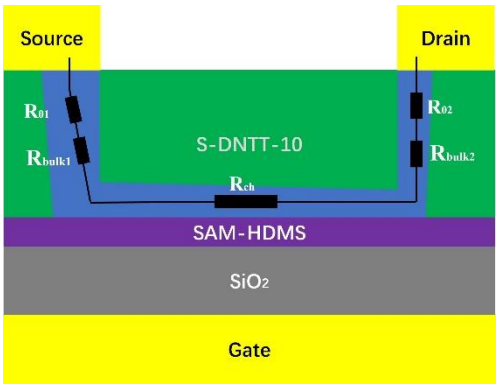


Figure 9.5 The diagram of the resistance system in OTFTs.

Based on the expression of channel resistance from the reference [140], the R_{bulk} can be expressed as,

$$R_{bulk} = \frac{d}{W \cdot \beta} \cdot \frac{1}{C_i |U_{GS} - U_{Th} - U_{DS}|^{\alpha+1}} \tag{9.8}$$

β was a mobility-fitting parameter depended on organic material. And based on the semiconductor knowledge related to the resistance [274], which was presented as,

$$dR = \frac{dx}{W \cdot \mu \cdot Q} \tag{9.9}$$

the W meaning of the width of the resistance, Q was expressed as the concentration of the charge in the area, the μ was the mobility of charge in the regime, and dx was the length over the resistance. Then the d was regarded as the thickness of organic material in the measured sample, in which the thickness of S-DNTT-10 material was 25 nm and the channel length was 30 μm. In the linear operation mode, according to **Equation.(9.5)** the channel resistance, R_{ch} [140], can be expressed as,

$$R_{ch} = \frac{L}{W \cdot \beta} \cdot \frac{1}{C_i |U_{GS} - U_{Th} - U_{DS}|^{\alpha+1}} \tag{9.10}$$

Then the differential of drain current I_D corresponding to drain voltage U_{DS} under a fixed gate voltage U_{GS} can be expressed as,

$$G_{diff} = \frac{\partial I_D}{\partial U_{DS}} = \frac{1}{R_{tot}} - \frac{U_{DS}\left\{\frac{\partial R_{ch}}{\partial U_{DS}} + \frac{\partial R_{bulk}}{\partial U_{DS}}\right\}}{R_{tot}^2} \tag{9.11}$$

the voltage-fitting parameters of α, parasite resistance R_0 and mobility-fitting parameter β, they were presented in **Table 9.3** and plotted the corresponding **Figure 9.6**.

Table 9.3 Setting parameters in the Equation.(9.11).

Parameter	W/μm	L/μm	C_i /F·m^{-2}	β	α	R_0/Ω	U_{GS} /V	U_{Th} /V

Value	1000	30	$1.1505 \cdot 10^{-4}$	$2.5 \cdot 10^{-7}$	1.35	$3 \cdot 10^{6}$	-10	-2.8

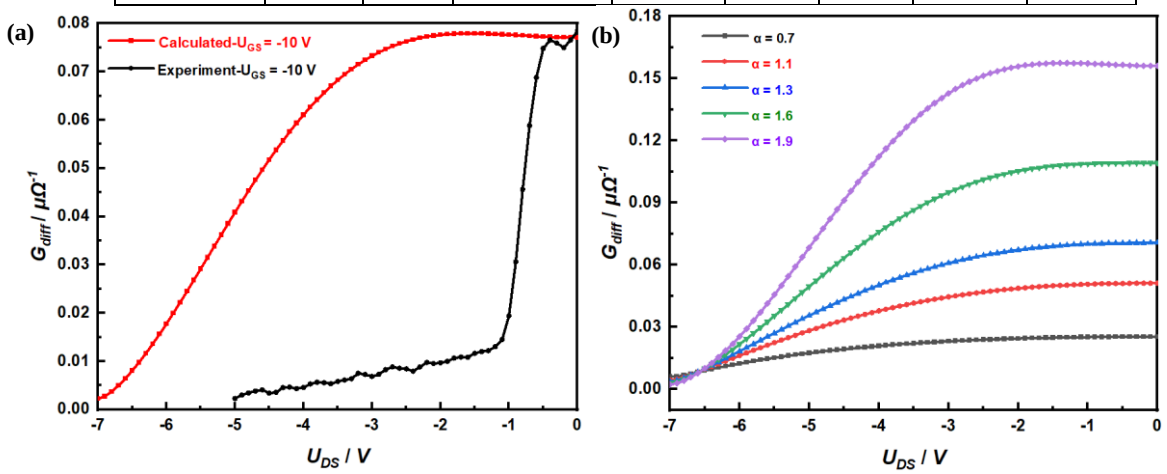


Figure 9.6 (a) The calculation on G_{diff} -U_{DS} compared with experimental results. (b) The modulated α under other parameters fixed.

Figure 9.6 (a) shows that the value of G_{diff} in the simulated calculation, represented by the red solid line, remained nearly constant at approximately 0.08 within the initial range of the drain voltage (U_{DS}) until U_{DS} approached -2.5 V. After this point, G_{diff} began to decrease as U_{DS} increased, and when U_{DS} reached -7 V, G_{diff} dropped to zero. In comparison to the experimental data, represented by the black solid line, the calculated curve shares some similarities but also shows two notable differences: (1) The range over which G_{diff} remained constant was broader. In contrast, the experimental G_{diff} remained stable only over a very narrow range, from roughly 0 V to -0.6 V. (2) The calculated G_{diff} decreased more slowly than the experimental data. This suggests that while it is difficult to perfectly replicate the experimental results using variable fitting parameters—namely α, β, and R_0, as shown in **Figure 9.3**—there are still noticeable similarities. Moreover, adjusting parameter α, as shown in **Figure 9.6 (b)**, affects both the value and shape of the curve. Since α is closely related to the variation of field-effect mobility (μ) with U_{DS}, as described in **Equation.**Erreur ! Source du renvoi introuvable.**)**, it is hypothesized that the *early saturation effect* may be caused by the exponential decrease in mobility. It is further speculated that this exponential term is related to an impediment in charge transport. Therefore, the effect of different linear slopes may be linked to a new charge transport phenomenon, where effective mobility decreases with increasing U_{DS}.

Following the above analysis, combined with **Figure 9.3 (b)** presented the rapidly decreased the value of G_{diff}, it was considered an exponential form. Then it was established of calculated mobility-model μ (U_{GS}, U_{CS}),

$$\mu(U_{GS}, U_{CS}) = (\beta \cdot |U_{GS}|^{\gamma}) exp(k \cdot U_{CS}) \quad \textbf{(9.12)}$$

the fitting parameters of β, γ, and k. Since the experimental sample was p-type OTFT, the γ and k were both positive constants. It was assumed that the channel resistance R_{ch} possessed a dominant role in the measured sample and the injection contact resistance was slight and negligible. Then it was deduced the I_D-U_{DS} equation based on the *GCA theory*,

$$I_D = -W \cdot \mu(U_{CS}) \cdot C_i \cdot (U_{GS} - U_{Th} - U_{CS}) \frac{dU_{CS}}{dx} \quad \textbf{(9.13)}$$

i.e.,

$$I_D = -\frac{W \cdot C_i}{L} \cdot (\beta \cdot |U_{GS}|^{\beta}) \cdot k^{-1} \cdot \{[(U_{GS} - U_{Th} - U_{DS}) \cdot exp(k \cdot U_{DS}) - (U_{GS} - U_{Th})] + k^{-1}[exp(kU_{DS}) - 1]\} \quad \textbf{(9. 14)}$$

The simulated parameters were present in **Table 9.4** and then plotted the compared **Figure 9.7** of the simulation and measured results, including I_D-U_{DS} curve and G_{diff}-U_{DS} curve.

Table 9.4 Setting parameters in the Equation. Erreur ! Source du renvoi introuvable.**).**

Parameter	W/μm	L/μm	C_i /F·m^{-2}	β	k	γ	U_{GS} /V	U_{Th} /V
Value	1000	30	$1.1505 \cdot 10^{-4}$	$8 \cdot 10^{-7}$	1.25	0.8	-10	-2.8

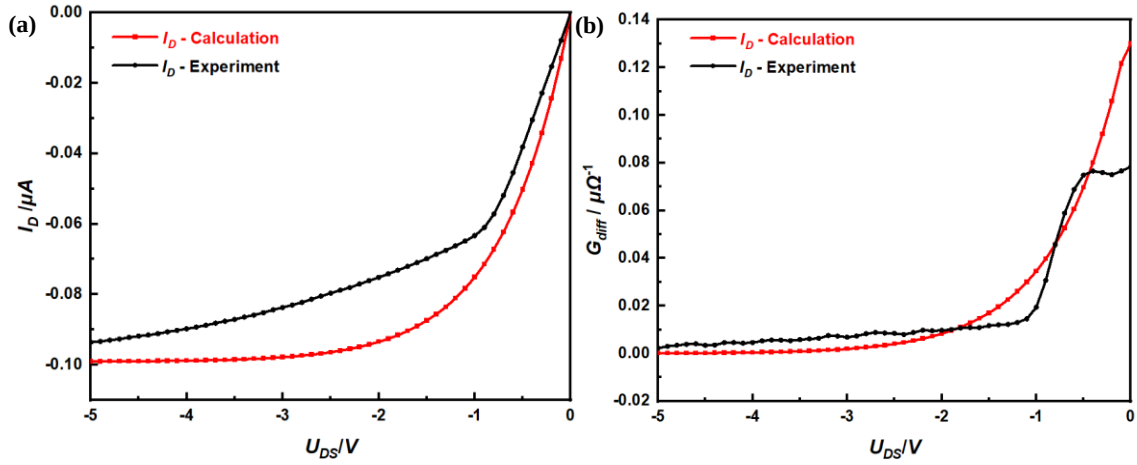


Figure 9.7 The calculation compared with measured data on (a) I_D-U_{DS}, and (b) the related G_{diff}-U_{DS}.

And if it were taken into account that the total resistance within the sample comprised bulk resistance (R_{bulk}), channel resistance (R_{ch}), and one parasitic resistance (R_0), precisely as depicted in **Figure 9.5**. It was also examined from the perspective presented in **Equation.(9.8**) and **(9.10)**, and owing to the variation of the mobility μ with the drain voltage U_{DS}. Subsequently, in accordance with **Equation.(9. *14*)**, the expressions of the channel resistance [140] and the bulk resistance [140] were modified as follows:

$$R_{ch} = \left(\frac{\partial I_D}{\partial U_{DS}}\right)^{-1} = \left\{\left[\frac{W \cdot C_i}{L} \cdot (\beta |U_{GS}|^{\gamma}) \cdot k^{-1}\right] \cdot [k \cdot (U_{GS} - U_{Th} - U_{DS}) \cdot exp(k \cdot U_{DS})]\right\}^{-1} \quad \textbf{(9.15)}$$

$$R_{bulk} = \left\{\left[\frac{W \cdot C_i}{\Delta L} \cdot (\beta |U_{GS}|^{\gamma}) \cdot k^{-1}\right] \cdot [k \cdot (U_{GS} - U_{Th} - U_{DS}) \cdot exp(k \cdot U_{DS})]\right\}^{-1} \quad \textbf{(9.16)}$$

to better learn about the effect of different parameters on the G_{diff} and obtain the optimized fitting parameters, then it was set the initial ones as the **Table 9.5** showed and modulated one parameter with fixed others as the **Figure 9.8** shown. It is noteworthy that the parameter of the parasitic resistance R_0 remained constant as it was associated with the fabrication process and could not be influenced by other external factors, such as U_{DS} and U_{GS}.

Table 9.5 Setting initial fitting parameters in Equation.(9.15) and (9.16).

Parameter	W/μm	L/μm	ΔL/nm	C_i /F·m^{-2}	β
Value	1000	30	25	$1.1505\cdot10^{-4}$	$2.2\cdot10^{-6}$
Parameter	k	γ	R_0/Ω	U_T/V	U_{GS}/V
Value	2.5	1.0	$8\cdot10^{6}$	-2.8	-10

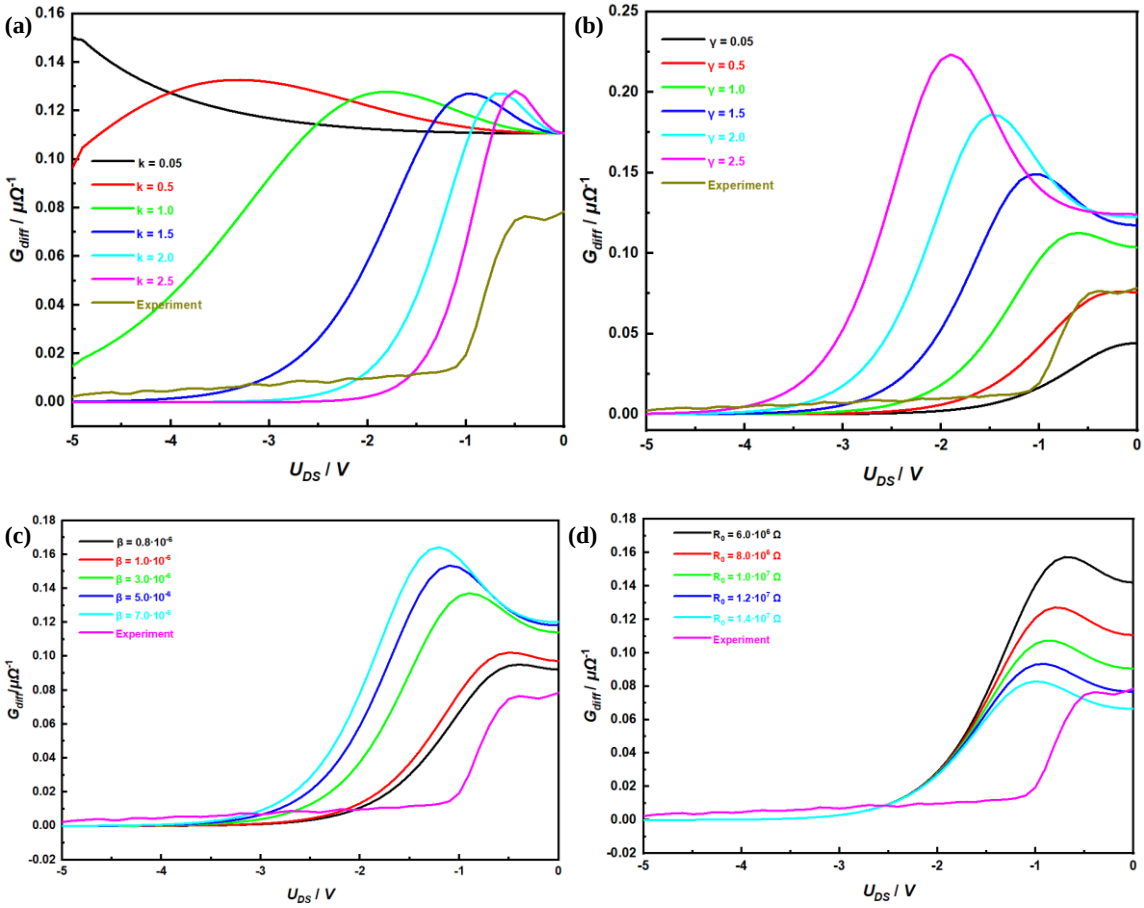


Figure 9.8 The graphic of the influence of different fitting parameters on G_{diff}, (a) modulation of k, (b) γ , (c) mobility-fitting parameter β and (d) parasite resistance R_0.

In **Figure 9.8 (a)**, the value of G_{diff} is shown to vary with parameter k, while the parameters γ, β, and R_0 remain constant. Four key observations are made. First, G_{diff} increases with the initial drain voltage, but the range of this increase narrows as k grows. Afterward, G_{diff} decreases nonlinearly, approaching 0 V, with the corresponding points ranging from -0.6 V to -3.6 V for smaller values of k, except for k = 0.05. Second, the rate of nonlinear decrease varies with k; specifically, the decrease accelerates as k increases. Third, the rate at which G_{diff} rises with U_{DS}

also increases with k, particularly for smaller values of k. For instance, at $k = 0.05$, G_{diff} increases steadily with the drain voltage, indicating a continuous rise in the rate of change of the drain current relative to the drain voltage. Finally, except for the case of $k = 0.05$, the calculated range of G_{diff} remains nearly constant.

In **Figure 9.8 (b)**, the correlation of G_{diff} with parameter γ is shown, while the parameters k, β, and R_0 remain constant. With variable γ, three main characteristics are observed. First, γ directly influences the shape of the G_{diff}-U_{DS} curve, and the 'hook effect' becomes more pronounced as γ increases. Specifically, G_{diff} initially rises, with the range of this increase narrowing as γ grows, and then decreases nonlinearly until it reaches zero. Additionally, the rate of increase is enhanced with increasing γ. This suggests that a larger γ initially amplifies the effect of the U_{GS} on mobility or charge transport, but as the U_{DS} increases, resistance increases, subsequently impacting charge transport. Second, for the descending part of the G_{diff} curve, the rate of decrease increases with γ. Third, the peak value of G_{diff} rises with γ, increasing from approximately 0.04 to 0.225 $\mu\Omega^{-1}$, along with the corresponding absolute value of the U_{DS}, which shifts from about -0.1 to -2 V.

In **Figure 9.8 (c)**, the relationship between G_{diff} and the mobility-fitting parameter β is shown, highlighting three main features. First, G_{diff} increases with β, suggesting that the fitting parameter significantly influences charge transport; generally, a larger β enhances transport. However, the range of increase narrows as β grows. Second, G_{diff} initially rises with the U_{DS} and then decreases nonlinearly. The peak value of G_{diff} follows a similar trend to **Figure 9.8 (b)**, ranging from approximately 0.09 to 0.17 $\mu\Omega^{-1}$, with the corresponding drain voltage ranging from -0.6 to -1.3 V. Third, in the descending phase, the rate of decrease becomes larger as β increases.

In **Figure 9.8 (d)**, the relationship between G_{diff} and the parasitic resistance R_0, which arises from the fabrication process, is described. Two main features are observed. First, G_{diff} increases as R_0 decreases, indicating that improved fabrication processes can lead to higher-quality organic materials, reducing resistance and enhancing charge transport. Additionally, while the range of increase grows with R_0, the overall value of G_{diff} decreases. Second, G_{diff} initially rises and then decreases nonlinearly with the drain voltage. The peak value of G_{diff} and the corresponding U_{DS} are influenced by the parasitic resistance R_0. Specifically, as R_0 decreases, the peak value ranges from approximately 0.08 to 0.159 $\mu\Omega^{-1}$, and the corresponding drain voltage shifts from -1.1 to -0.7 V.

Table 9.6 Setting optimized parameters in Equation.(9.15) and (9.16).

Parameter	W/μm	L/μm	ΔL/nm	C_i /F·m^{-2}	β
Value	1000	30	25	$1.1505\cdot10^{-4}$	$1.75\cdot10^{-6}$
Parameter	k	γ	R_0/Ω	U_T/V	U_{GS}/V
Value	3.55	0.78	$1.0\cdot10^{7}$	-2.8	-10

After optimization of the fitting parameters, it was obtained the suitable parameters as **Table 9.6** showed. They were setting parameters and plotted **Figure 9.9** which was a comparison between simulated calculation and measured results.

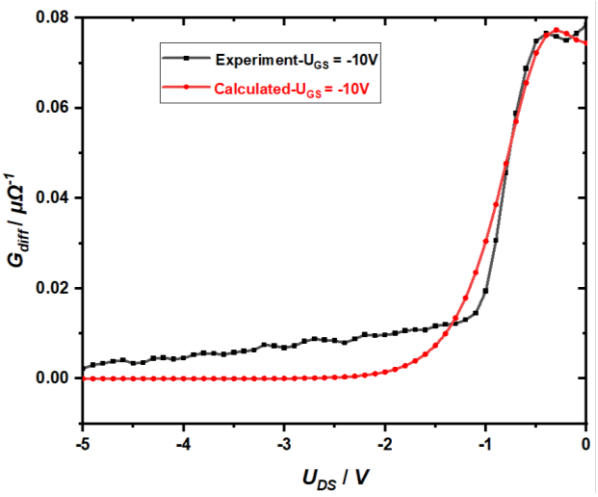


Figure 9.9 The graphic of calculated G_{diff}-U_{DS} compared with measured data.

Figure 9.7 and **Figure 9.9** show that the calculated results had a better match with the experiments, especially the curve considering other factors of bulk resistance and parasite resistance in the G_{diff}-U_{DS} relation, which was more obvious. Then it is indicated that the mobility model as expressed in **Equation (9.15)** can better describe the *early saturation effect*.

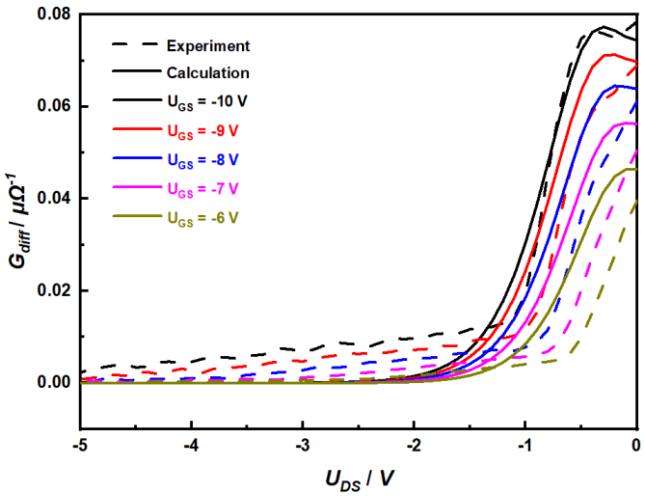


Figure 9.10 The diagram of calculation of G_{diff} under different U_{GS}.

Equation.(9.12)-.(9.16) were incorporated into diverse gate voltages U_{GS}, and the corresponding results are presented in **Figure 9.10**. The solid and dashed lines represent the calculated and experimental data, respectively, while different colors indicate varying gate voltages U_{GS}. Overall, the figure shows an excellent match between the calculated results and the experimental data. This confirms that the mobility model represented by **Equation.(9.12)**, along with the consideration of bulk resistance (R_{bulk}) and parasitic resistance (R_0), is relatively accurate.

It was concluded that certain factors contributed to the higher parasitic resistance R_0, which dominated the total resistance at small initial U_{DS}. As the U_{DS} increased, the R_{ch} and R_{bulk} became significant compared to R_0. Additionally, the variation in effective mobility with U_{DS} was also influenced by another factor, which is mathematically expressed in **Equation.(9.12)**.

The *early saturation effect* is a common characteristic of short-channel monolayer OFETs. For instance, premature saturation occurs in C_{10}-DNTT monolayer OFETs. Studies have shown that this premature saturation in OTFTs is linked to source contact depletion under high U_{DS} in monolayer transistors. It is suggested that monolayer C_{10}-DNTT OFETs meet the basic conditions for the formation of a source-gate transistor (SGT), which includes the Schottky barrier at the source-semiconductor interface, the gate extension beneath the source on the opposite side of the semiconductor, and the ultrathin semiconductor layer. At low U_{DS}, a large number of charges provide high conductivity for the channel in the linear operation state. However, as U_{DS} increases, the reverse bias at the source-semiconductor interface causes carrier depletion in the source region. This depletion occupies the majority of the applied U_{DS} [38], limiting the voltage drop across the channel, which leads to I_D limitation and early saturation.

Unlike the short-channel C_{10}-DNTT monolayer OFET, the *early saturation effect* is observed in the S-DNTT-10-based OTFT discussed in this section. The S-DNTT-10 thin film in this device is multilayer rather than monolayer and does not meet the conditions required for the formation of an SGT. Furthermore, the designed channel length is 30 μm. It is suspected that during the fabrication process, the thermally deposited metal electrode may have excessively penetrated the S-DNTT-10 thin film for some reason, resulting in a device where the surface distance between the electrode and the SiO_2—i.e., the thickness of the S-DNTT-10 thin film—is less than 25 nm, approaching that of a monolayer. Additionally, due to the mismatch between the HOMO energy level of S-DNTT-10 and the work function (Fermi level) of the gold electrode, which will be discussed later, a natural barrier forms at the metal-semiconductor interface. This interface between the metal and S-DNTT-10 forms a structure

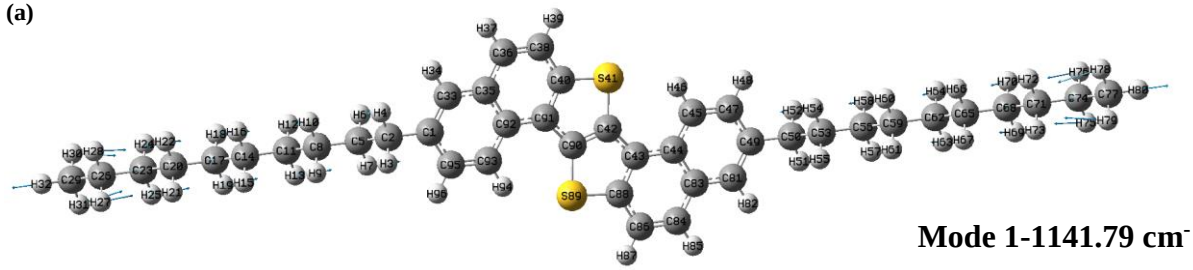
similar to a Schottky diode. As U_{DS} increases, the reverse bias causes carrier depletion beneath the source region, with most of the applied U_{DS} being concentrated in this depletion region. This creates a region similar to the pinch-off region, which should typically form near the drain when $|U_{DS}| > |U_{GS} - U_{T}h|$. This not only affects carrier transport, causing μ_{eff} to be influenced by U_{GS} and to vary exponentially with increasing U_{DS}, but also possibly creates a depletion region similar to the R_0 term in the formula beneath the source. These factors may contribute to the *early saturation effect*.

In this section, to address the premature saturation effect exhibited by the S-DNTT-10-based OTFT and based on the *GCA* theory, an additional resistor R_0 was introduced. It was hypothesized that μ_{eff} was no longer constant but was jointly regulated by U_{GS} and U_{DS} in order to simulate and model this phenomenon. Compared with the *GCA* theory, these additional modifications were thought to be linked to the reduction in the thickness of the S-DNTT-10 thin film beneath the electrode and the formation of additional depletion regions caused by the increase in U_{DS}. Notably, when the thickness of the SiO_2 layer was adjusted to 89 nm, this phenomenon no longer occurred. Therefore, it is suggested that this effect might be related to the electric field strength and the quantity of induced charges.

9.2 The description S-DNTT-10 molecular vibration

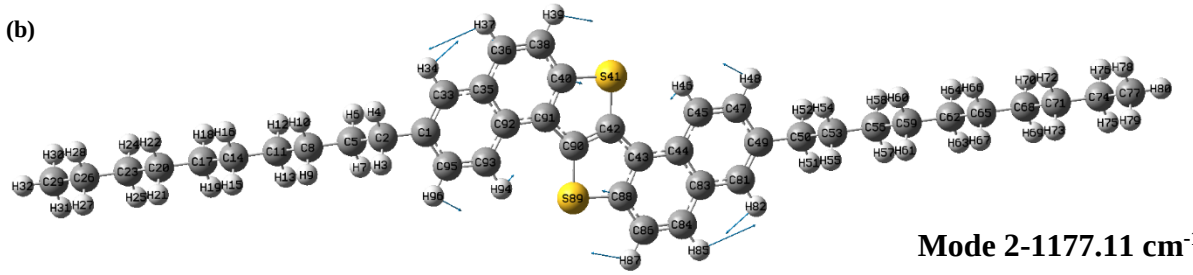
The following images as shown in **Figure 9.11** are describing details of molecular vibration in S-DNTT-10 Raman spectrum with corresponding to **Figure 3.4** and **Table 3.1**.

(a)



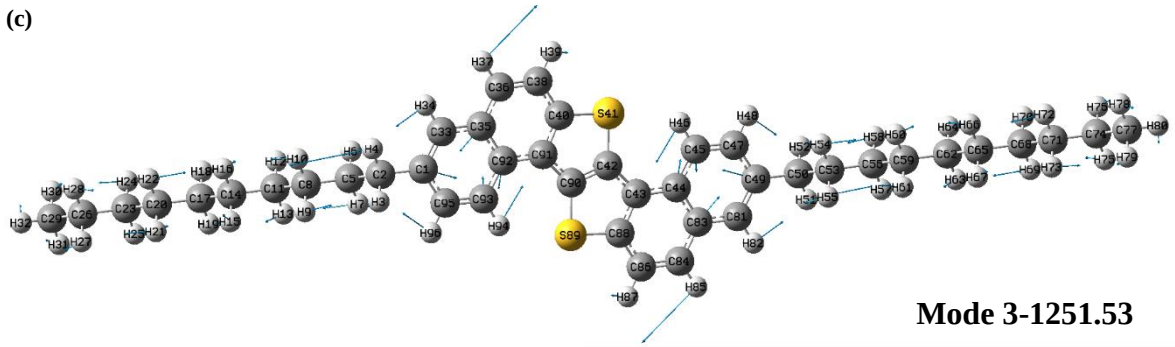
Mode 1-1141.79 cm^{-}

(b)



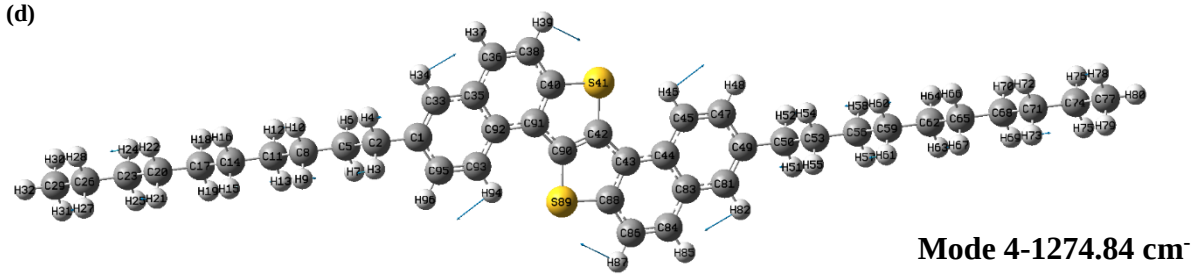
Mode 2-1177.11 cm^{-1}

(c)



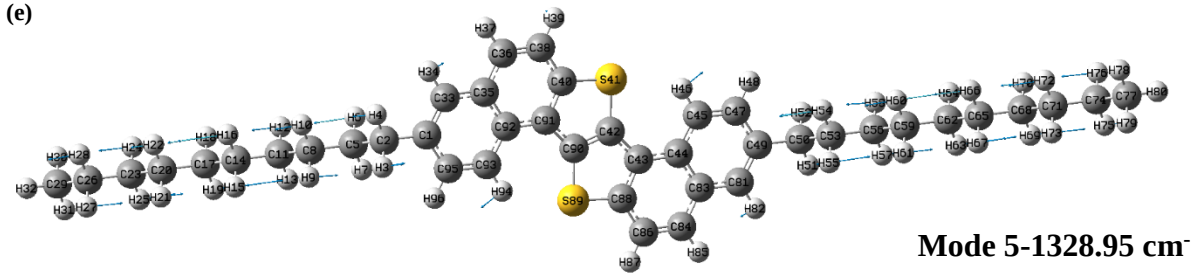
Mode 3-1251.53

(d)



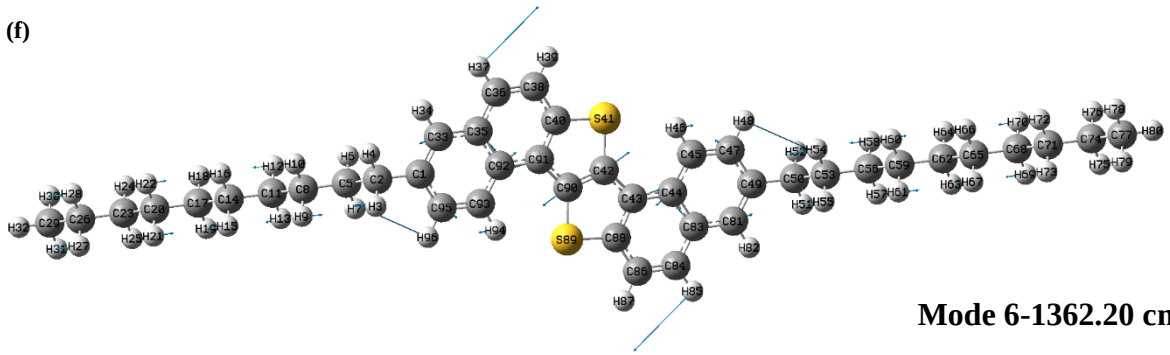
Mode 4-1274.84 cm^{-}

(e)



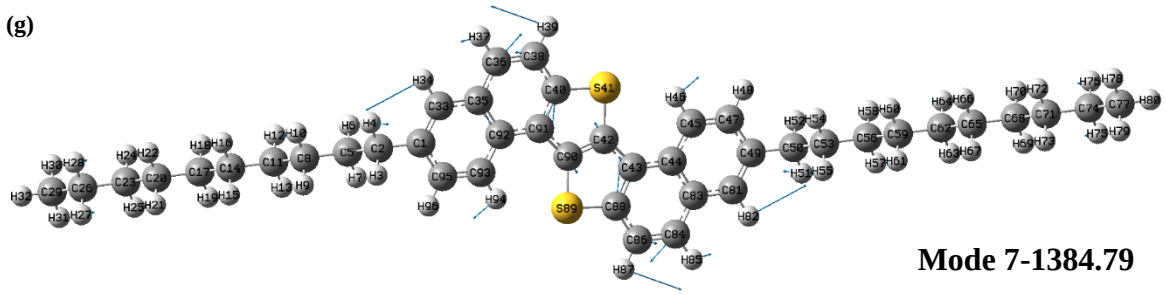
Mode 5-1328.95 cm^{-}

(f)



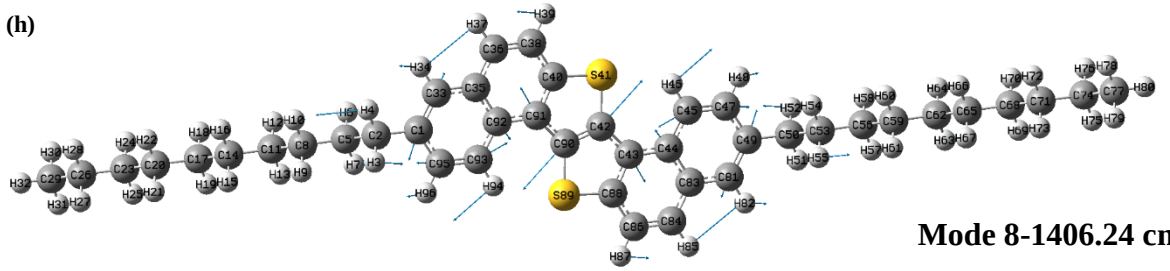
Mode 6-1362.20 cm^{-}

(g)



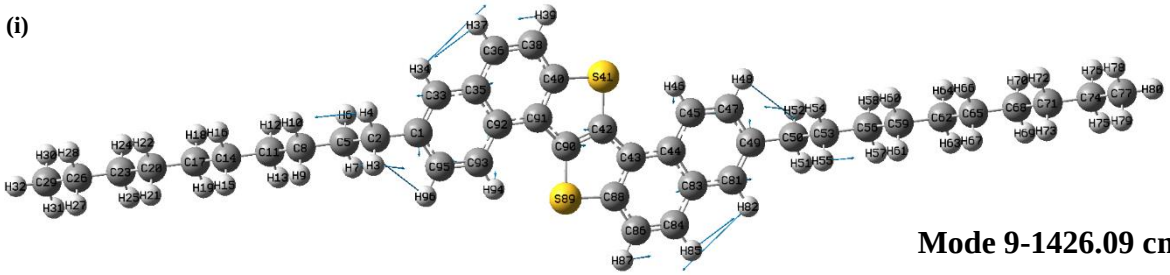
Mode 7-1384.79

(h)



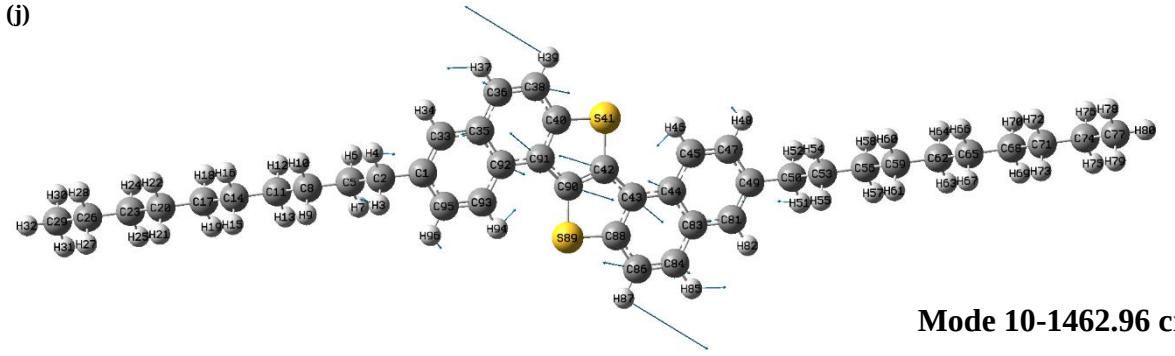
Mode 8-1406.24 cm^{-1}

(i)



Mode 9-1426.09 cm^{-}

(j)



Mode 10-1462.96 cm^{-1}

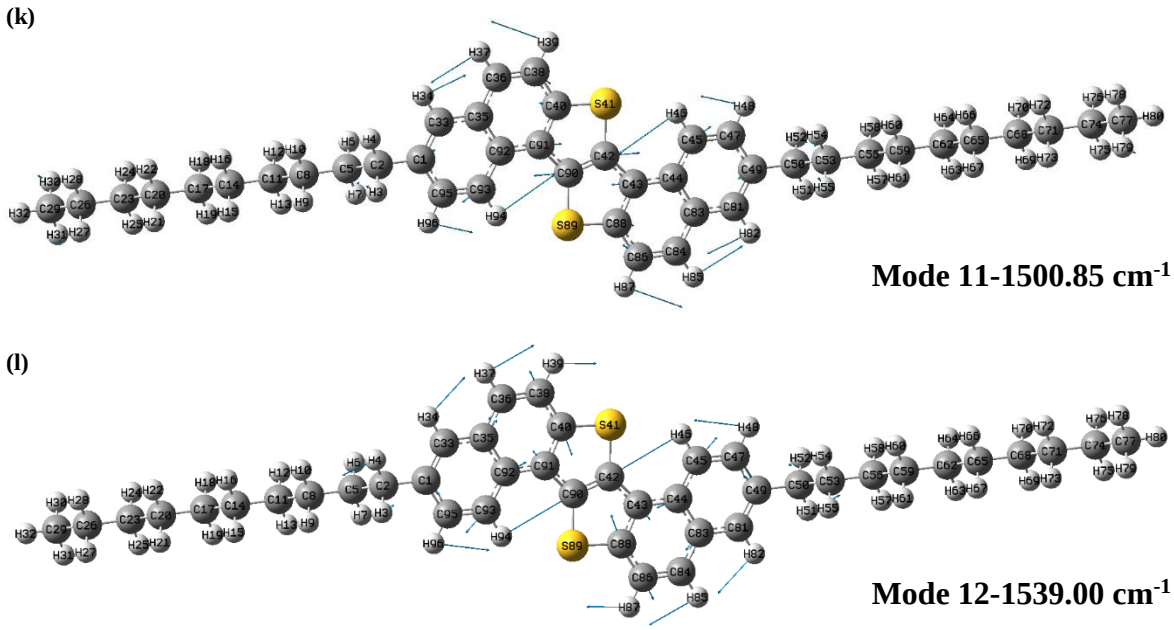


Figure 9.11 The representation of details in S-DNTT-10 molecular vibration ranging 1100 to 1550 cm^{-1} corresponding to Table 3.1. (a) 1141.79 cm^{-1}, (b) 1177.11 cm^{-1}, (c) 1251.53 cm^{-1}, (d) 1274.84 cm^{-1}, (e) 1328.95 cm^{-1}, (f) 1362.20 cm^{-1}, (g) 1384.79 cm^{-1}, (h) 1406.24 cm^{-1}, (i) 1426.09 cm^{-1}, (j) 1462.96 cm^{-1}, (k) 1500.85 cm^{-1}, and (l) 1539.00 cm^{-1}.

9.3 KPFM for intrinsic mobility

In Section 5.2.2.1.2, we mentioned the measured surface potential under different post-annealing temperature by KPFM method with the aim of intrinsic mobility. Herein, we plan to display the related results in **Figure 9.12**.

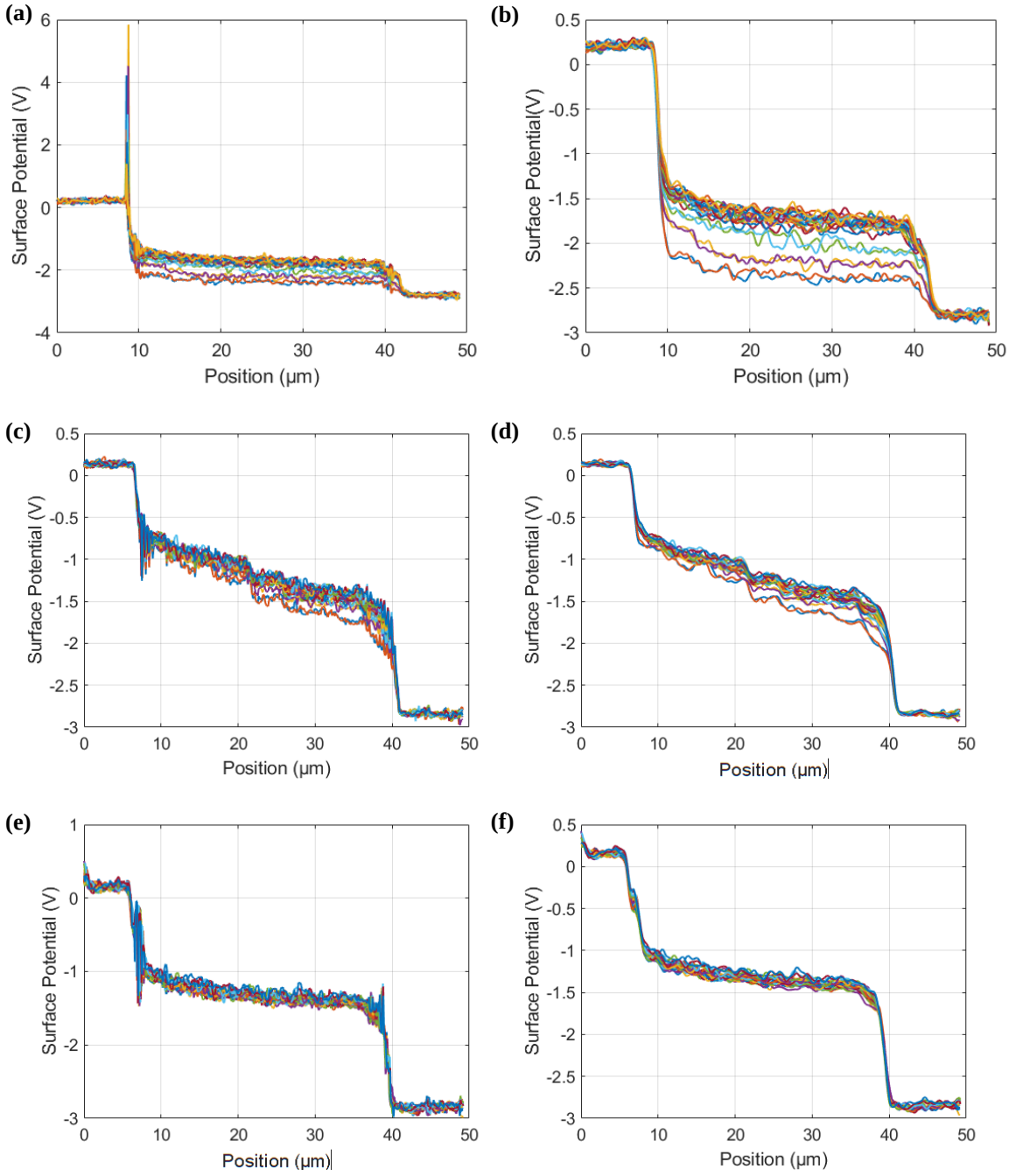


Figure 9.12 The profile of surface potential by KPFM under varied post-annealing temperature. (a) before post-annealing raw data and (b) the treated data. (c) 80 °C raw data and (d) the treated data. (e) 110 °C raw data and (f) the treated data.

9.4 Nano-characterization at Au drain electrode

In Section 5.2.2.3, it mentioned the influence of post-annealing treatment on source characteristics. Considered that results at drain is similar to that at source, we didn't put the results in the main text. Herein, it exhibited the related results at drain.

At the drain, it was found through AFM measurement that the morphology of the electrodes had similar changes to that of the source with the post-annealing temperature, *i.e.*, the Au thin-films were affected as nanoparticles after 110 °C post-annealing temperature, as illustrated in **Figure 9.13 (a)-(d)**. Moreover, they showed that the ***RMS-roughness*** of 2.08 nm before post-annealing was reduced to 1.314 nm after 50 °C post-annealing. Subsequently, with a higher post-annealing temperature, the roughness started to become higher, with the ***RMS-roughness*** of 4.805 nm and 19.2 nm at 80 °C and 110 °C post-annealing, respectively.

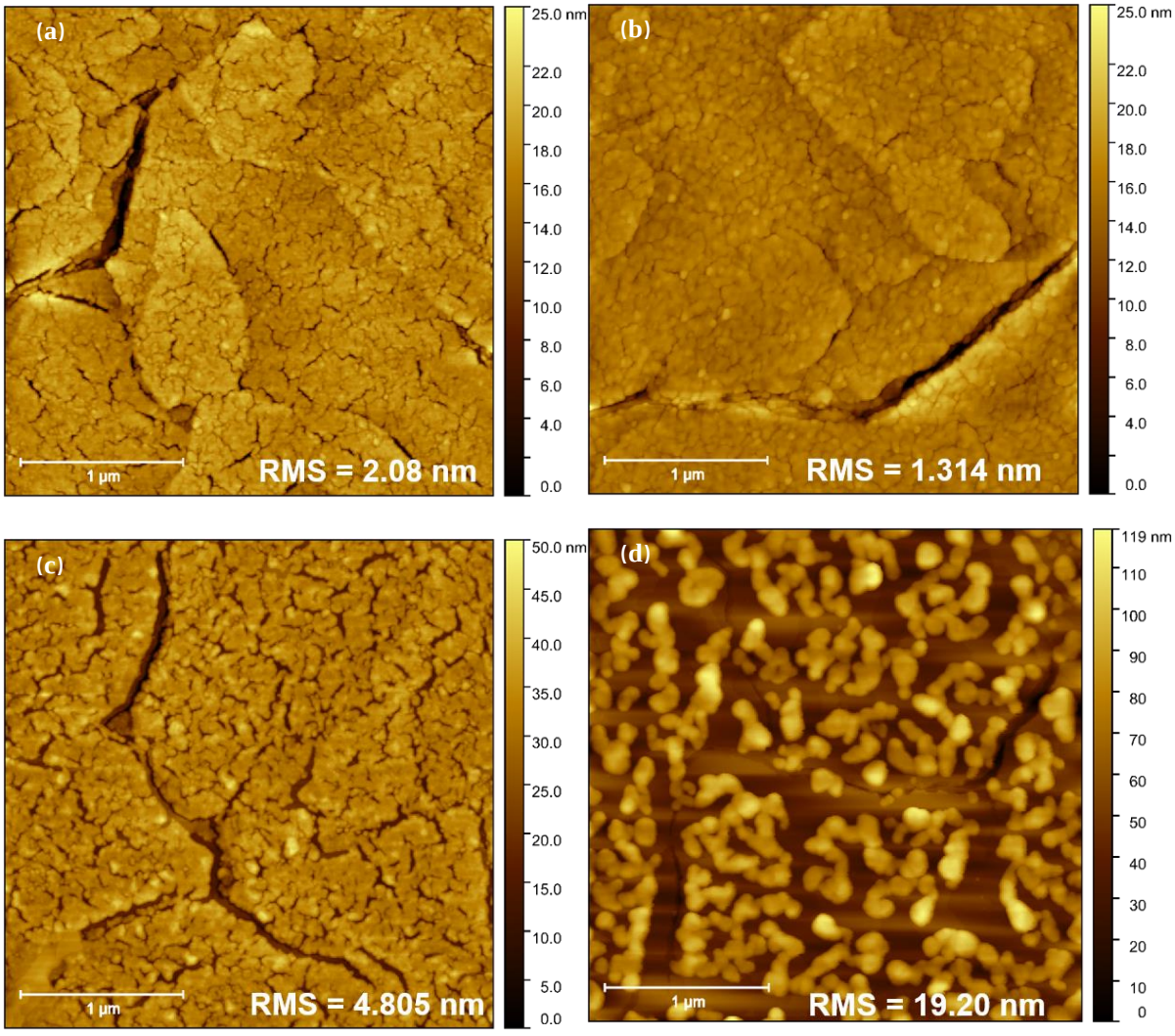


Figure 9.13 The AFM-topography with calculated *RMS-roughness* located at source under different post-annealing temperature: (a) before post-annealing, (b) after 50 °C post-annealing, (c) after 80 °C post-annealing and (d) after 50 °C post-annealing. (Noted that the value of roughness is extracted from the well surface area)

And it was as well measured in Raman spectrums as we did in the source showing in **Figure 9.14 (a**). It was observed that there were similar results as in the source. We think it was caused by identical reasons since it had the same S-DNTT-10 thin-films and the identical thickness of Au thin-films, and they were simultaneously annealed. Briefly speaking that the molecular characteristics of S-DNTT-10 molecules which are below the drain were changed by the different post-annealing temperature, and it possibly blocked transport with resulting in the greater contact resistance by the higher post-annealing temperature. Hence, it implemented the KPFM measurements to study the influence of post-annealing temperature on drain-contact resistance, as **Figure 9.14 (b)**. It displayed that the similar changes in $R_d{\cdot}W$ with higher post-annealing temperature as showing in the source, *i.e.*, $R_d{\cdot}W$ initially decreased after 50°C post-annealing, however, the subsequently emerging increased $R_d{\cdot}W$ with higher temperature, except for that under U_{GD} of -20 V. In particular, after 110 °C post-annealing treatment, it appeared drastically great $R_d{\cdot}W$. It suggested that the properties of charge collecting at the drain were degenerated by higher post-annealing temperature.

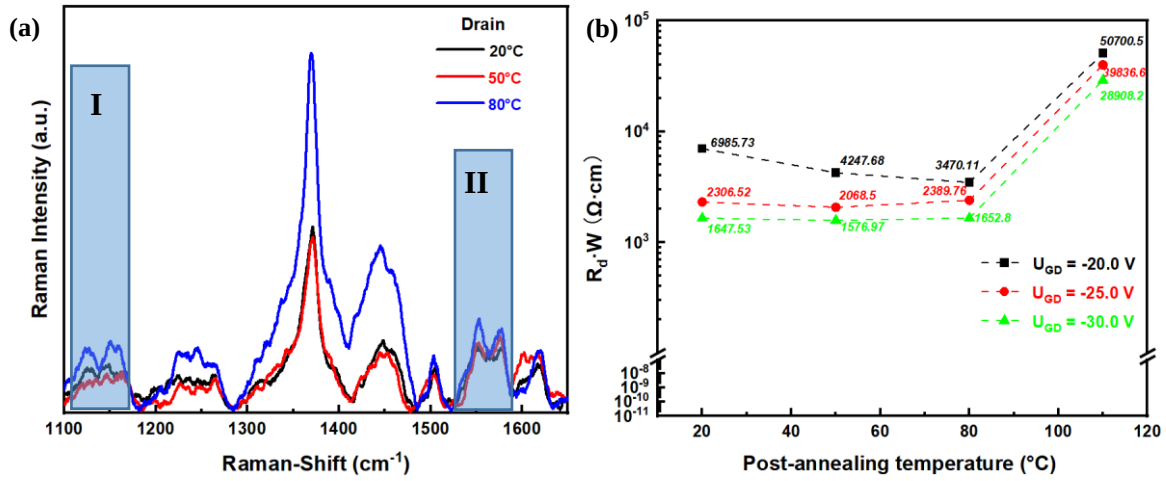


Figure 9.14 (a) The related SERS spectrum (Illumination time of 20 s, accumulation time of 2, grating number of 1800/mm, laser of 633 nm) at drain under different post-annealing treatment temperature. (b) The width-contact resistance at drain, $R_d{\cdot}W$, changed with temperature by using device with 25 nm Au-electrodes.

9.5 Electrical performance of TCBG S-DNTT-10-based OTFT with 6.5 $cm^2 \cdot V^{-1} \cdot s^{-1}$

In particular, the S-DNTT-10 molecules shows that the correlated thermally deposited Top-contact-Bottom-gate (TCBG) S-DNTT-10-based OTFTs with gold (Au) electrodes displaying well electrical performance in our lab, even it performed the saturation-mode effective field-effect mobility (μ_{sat}) exceeding 6.5 $cm^2 \cdot V^{-1} \cdot s^{-1}$, as shown in **Figure 9.15**.

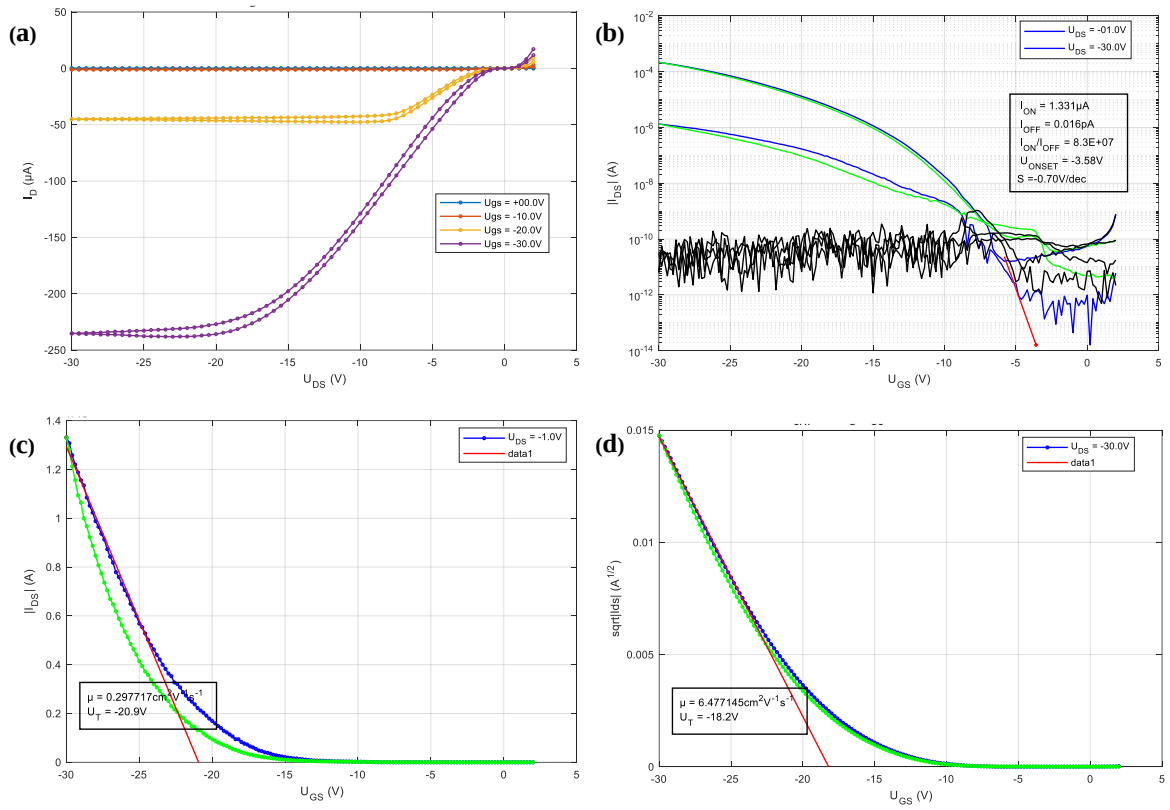


Figure 9.15 The electrical characteristics of TCBG S-DNTT-10-based OTFT performing effective mobility of approximate 6.5 $cm^2 \cdot V^{-1} \cdot s^{-1}$: (a)Output characteristics I_D-U_{DS}, (b)transfer characteristics I_D-U_{GS},(c) the linear-state effective field-effect mobility μ_{lin} extracting from I_D-U_{GS} under stressed U_{DS} of -1 V, and (d) the saturation-state effective field-effect mobility μ_{sat} extracting from I_D-U_{GS} under stressed U_{DS} of -30 V.

9.6 Blurred effect caused shrinking channel length

In Section 6.2.2.2, we mentioned the actual channel length in the fabricated TCBG S-DNTT-10-based and TCBG S-DNTT-10/Pentacene-based OTFTs. We think that it was caused by the diffusion of evaporation atoms along the edges of the shadow mask in the Physical Vapor Deposition (PVD) approach.

Figure 9.16 illustrated the narrow-channel-length effect during the process of depositing Au-electrodes via shadow mask. It showed that as thermally vapored Au materials at the source, the motion of Au atoms was affected by the edges, and the deposited slight Au thin-films were emerged at the two sides of electrodes, as marked as blurred areas in the figure. It caused that the designed channel length, L_1, was shrunken as physical length, L_2.

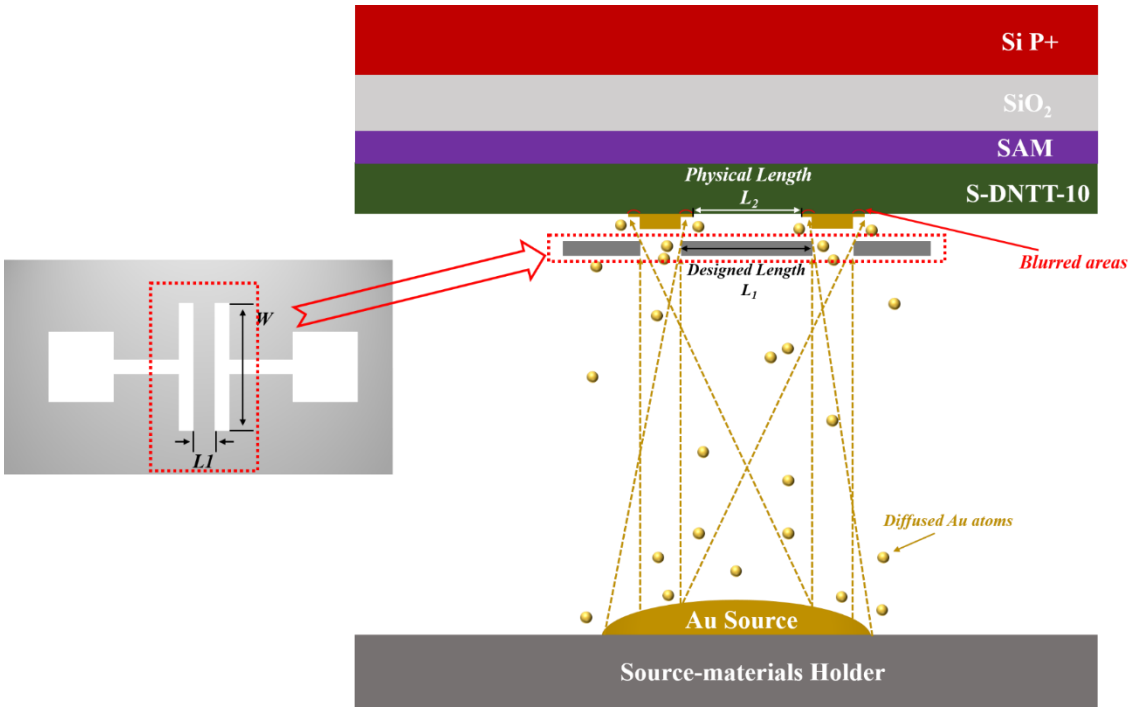
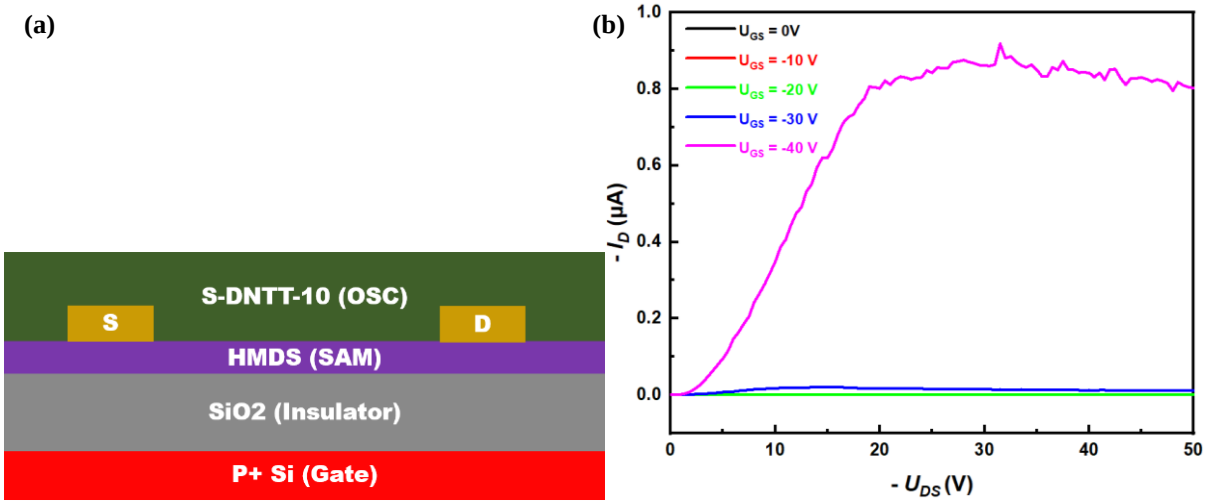


Figure 9.16 The schematic of the channel shrinking effect during fabrication of OTFTs.

9.7 Bottom-contacted bi-layers-based OTFTs

Another common OTFT structure is the Bottom-Contact-Bottom-Gate (BCBG) OTFT showing in **Figure 9.17 (a)**. In BCBG-OTFTs, the final fabrication step involves vapor-depositing the OSC material onto the surface of the electrodes, reducing the risk of thermal damage compared to the PVD process in TCBG-OTFTs. Although this approach seems beneficial for protecting OSCs, the morphology of OSC thin-film to the surface energy into substrate material degenerated performance.

In the fabricating process of BCBG S-DNTT-10-based OTFTs, we directly deposited the S-DNTT-10 thin film on the bare gold electrodes (source and drain), as **Figure 9.17 (a)** shown. The *I-V* characteristics of one BCBG S-DNTT-10-based-OTFT (L = 30 μm, W = 1000 μm) are shown in **Figure 9.17 (b)** and **(c)**. The *I-V* characteristics show very bad performance. **Figure 9.17 (b)** presents the output characteristics I_D-U_{DS} (U_{DS} = 2 ~ -50 V) and illustrates the following points: (i) The rough or not smooth curve of output, in which it means the unstable output drain current. (ii) The lower drain current I_D under the identical biasing conditions. (iii) A much higher onset voltage. Subsequently **Figure 9.17 (c)** displays the transfer characteristics I_D-U_{GS} in the linear- (U_{DS} = -1 V) and saturation-regime (U_{DS} = -40 V). And then according to the results, the near extraction of μ_{lin} and μ_{sat} is respectively 0.0001 $cm^2 \cdot V^{-1} \cdot s^{-1}$ and 0.0652 $cm^2 \cdot V^{-1} \cdot s^{-1}$, and the corresponding threshold voltage $U_{Th\text{-}lin}$ of -38.4 V and $U_{Th\text{-}sat}$ of -41.1 V.



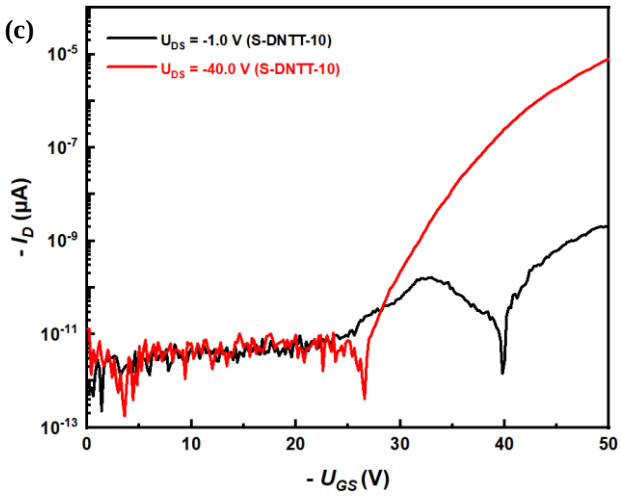


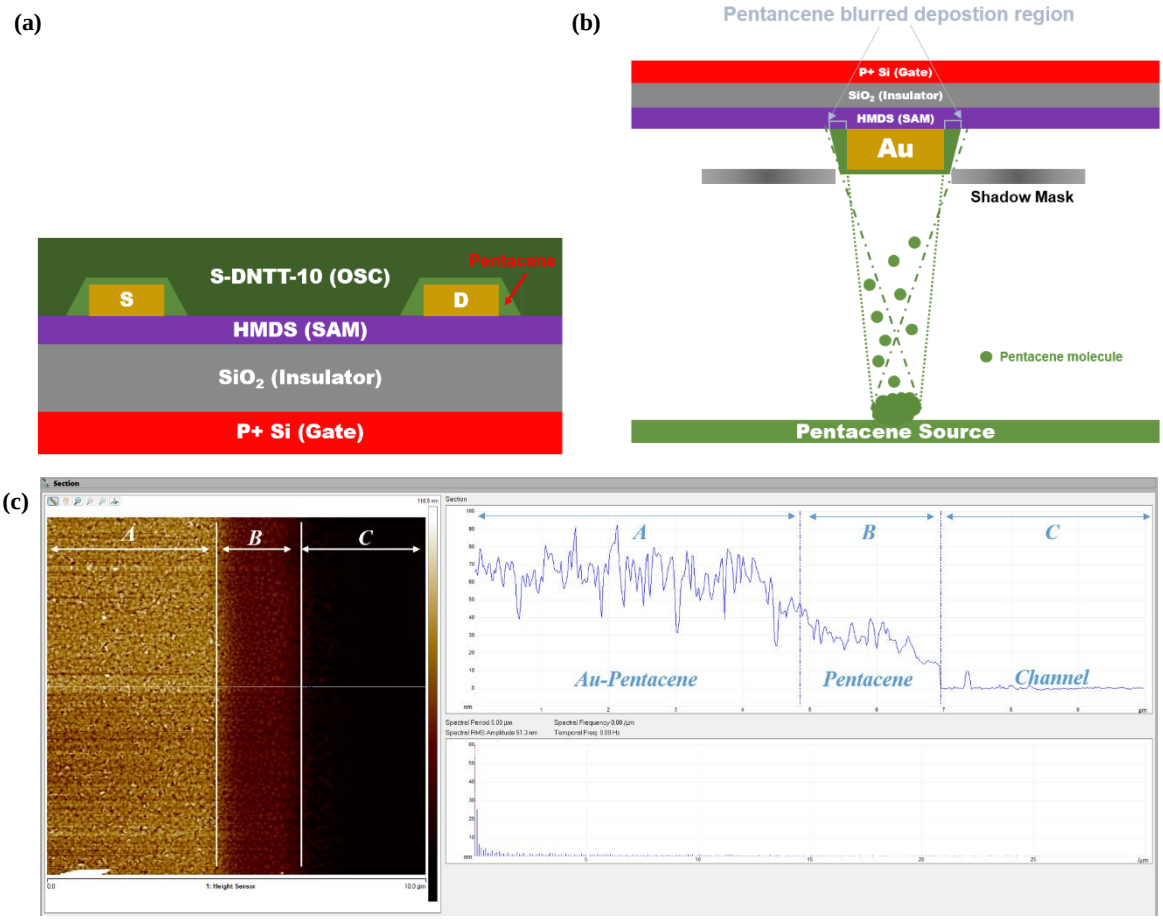
Figure 9.17 (a) Schematic representation of Bottom-Contact-Bottom-Gate S-DNTT-10-based OTFT. (b) The corresponding output characteristics I_D-U_{DS}, and (c) transfer characteristics I_D-U_{GS}.

To address this issue, we decided to deposit pentacene thin film only on the electrodes, excluding the channel, as shown in **Figure 9.18 (a)**. **Figure 9.18 (b)** illustrates how pentacene atoms blur at the electrode edges due to diffraction from the metal shadow mask, creating blurred regions. To verify that pentacene was deposited only on the electrodes, we performed an AFM surface topography test after pentacene deposition, as shown in **Figure 9.18 (c)**. The 25 nm Au electrodes were designed and pentacene was deposited with thicknesses of 30 nm. The height measurements in regions A, B, and C were approximately 60 nm, 30 nm, and 0 nm, respectively, confirming that pentacene was deposited in the electrode region. **Figure 9.18 (d)** displays the I_D-U_{DS} characteristics (U_{DS} = 2 ~ -50 V) and shows the following improvements compared to the previous performance of BCBG-OTFT based on S-DNTT-10: (i) The I_D was significantly higher under the same U_{GS}, such as when the device was biased at U_{GS} = -40 V, the saturation current reached nearly 45 μA, compared to only 0.8 μA in the S-DNTT-10-based OTFT. (ii) The output characteristics became smoother, showing clear linear and saturation regimes, despite the appearance of a non-linear region at low U_{DS} due to larger charge injection barrier and R_c. (iii) The device exhibited a higher onset voltage or higher threshold voltage, with effective drain current starting at U_{GS} = -30 V.

And then the **Figure 9.18 (d)** severally illustrated the compared transfer characteristics I_D-U_{GS} in the linear (U_{DS} = -1 V) and saturation regime (U_{DS} = -40 V). According to the results, for BCBG S-DNTT-10/Pentacene-based OTFT, the approximate extraction of μ_{lin} and μ_{sat} is respectively 0.0196 $cm^2 \cdot V^{-1} \cdot s^{-1}$ and 0.8852 $cm^2 \cdot V^{-1} \cdot s^{-1}$, and the corresponding threshold voltage $U_{Th\text{-}lin}$ of -37.8 V and $U_{Th\text{-}sat}$ of -30.8 V. In contrast to performance of BCBG OTFT based on S-DNTT-10, the field effect mobility μ_{lin} located in the linear region (U_{DS} = -1 V)

increases from 0.0001 to 0.0196 $cm^2 \cdot V^{-1} \cdot s^{-1}$, and the mobility in the saturation region (U_{DS} = -40 V) μ_{sat} grows from 0.0652 to 0.8852 $cm^2 \cdot V^{-1} \cdot s^{-1}$, in which the μ_{lin} increases almost 200 times and the improvement of μ_{sat} of 15 times. The corresponding threshold voltage changes from -38.4 V and -41.1 V to -37.8 V and -30.8 V, respectively.

The illustrated increasing effect-field mobility indicates the improvement of charge transporting from the source to drain. And the corresponding changes in threshold voltage indicate a reduction of the contact barrier at the interface between the source-drain electrode and the OSC. We suppose that improvements of the *I-V* characteristics result from the source depositing by pentacene which possibly leads to the different surface energy and then it optimizes the deposited S-DNTT-10 molecular orientation. As the consequence, the BCBG - OTFT based on the S-DNTT-10 and pentacene carried out the better performance.



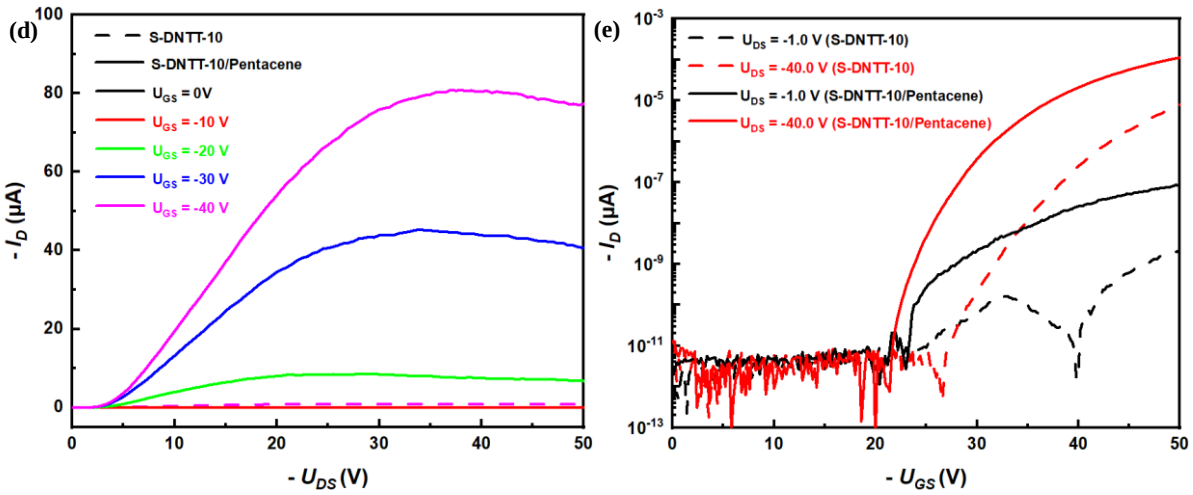


Figure 9.18 Schematic representation of (a) the BCBG S-DNTT-10/Pentacene-based OTFT, (b) the fabrication of Pentacene at electrodes. (c) The topography around Au electrodes with 30 nm pentacene thin-film via AFM tool. The comparison of electrical performance in BCBG S-DNTT-10/Pentacene-based OTFT and BCBG S-DNTT-10 -based OTFT: (d) Output characteristics I_D-U_{DS} and (e) transfer characteristics I_D-U_{GS}.

9.8 S-DNTT-10-based OTFTs with double injection-area

In practice, the charge injection area indirectly affects the performance of OTFTs, particularly, the region is varied with the geometric structure of OTFTs. As **Figure 9.19 (a)** and **(b)** shown, it respectively displays the Top-Contact-Bottom-Gate-(TCBG) and Bottom-Contact-Bottom-Gate-(BCBG) configuration of S-DNTT-based OTFT. As for the former one, the charge injection area is mainly located at the region with $L_{inj} \times W_{inj}$, but for the latter one, the related area with $T_{inj} \times W_{inj}$. Generally, regardless of the geometric structure of TCBG-OTFT or BCBG-OTFT, without considering the charge injection efficiency, their charge injection regions are single. If the charge injection region is increased in the same device, it is speculated that the drain current of the device can be enhanced under the same bias condition.

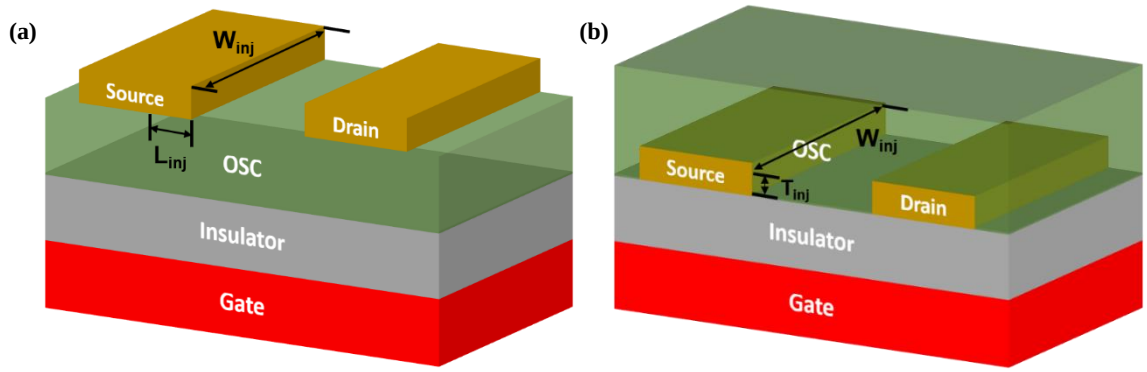


Figure 9.19 Schematic diagram of configuration in OTFT: (a) Top-Contact-Bottom-Gate and (b) Top-Contact-Bottom-Gate.

Compared with TCBG-OTFT, the different fabrication steps of BCBG-type OTFT make it easier to achieve large-area and high-density fabrication. However, not only does it have only a single charge injection region, but also since the size of T_{inj} is usually at the nanoscale, this results in a smaller charge injection area, limiting the charge injection. To improve the performance and charge injection of BCBG-type OTFT, it is planned to take BCTG-S-DNTT-10-based OTFT as the research object and increase the additional charge injection area to achieve a double charge injection area, as shown in **Figure 9.20 (a)**. Among them, it is planned to achieve charge injection at the side and lower surface of the source, as shown in **Figure 9.20 (b)**. The basic method is as shown in **Figure 9.20 (c)**. Firstly, a S-DNTT-10 thin-film with a thickness of T_1 is thermally deposited on the surface of the dielectric layer SiO_2 with modification of HMDS through PVD. In order to enable effective charge injection on both sides under the induction of the electric field and reduce R_{bulk}, considering that the thickness of the general conductive channel is several nanometers, therefore, the thickness of T_1 is expected to be 10 nm. Subsequently, 25 nm Au electrodes are thermally deposited on the surface of the S-

DNTT-10 thin-film using the electrode-shadow mask. Finally, based on the previous two steps, the S-DNTT-10 thin-film is thermally deposited again.

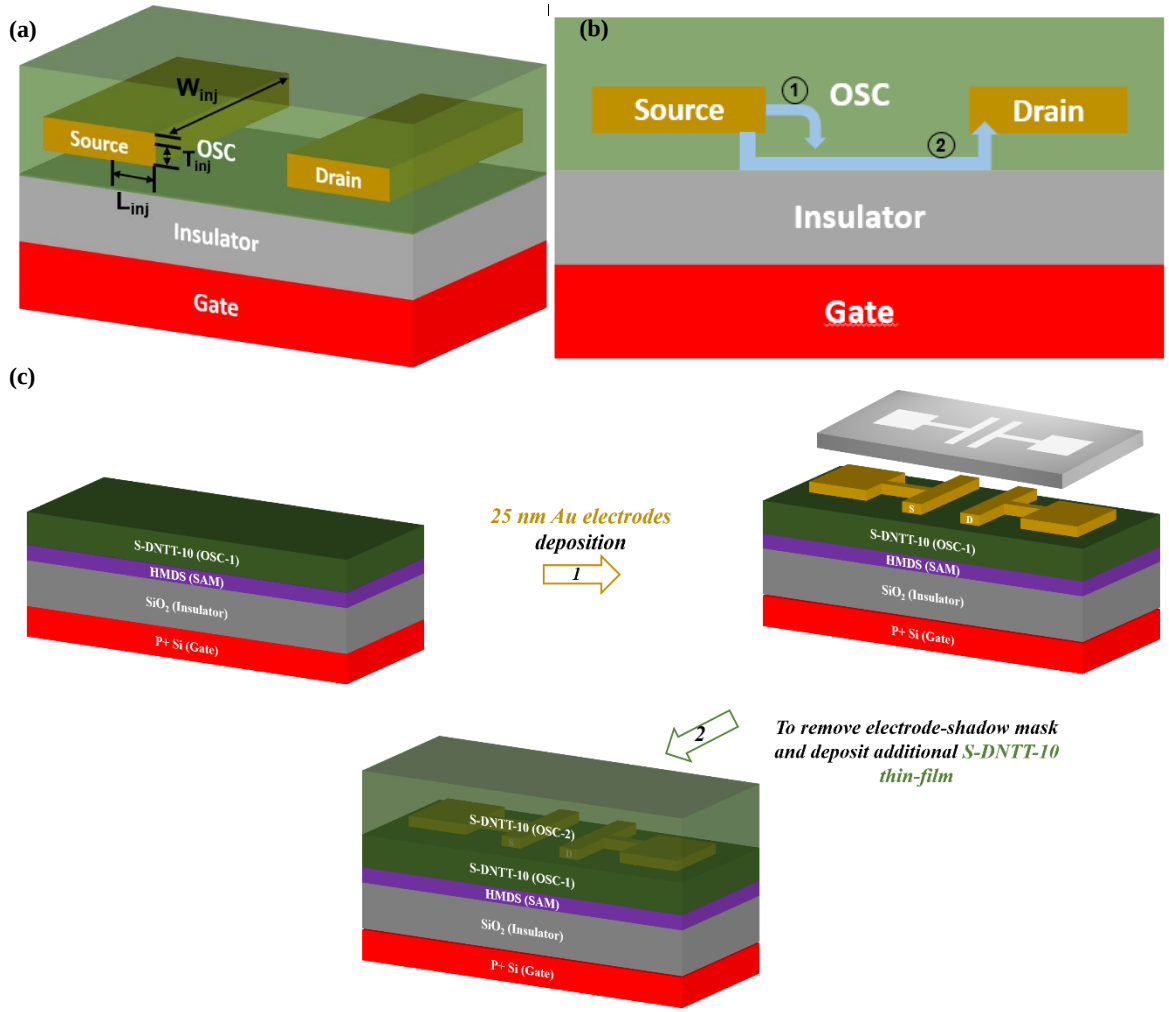


Figure 9.20 Schematic representation of (a) the expected structure with double charge injection area, (b) drain current inside the device, and (c) the related fabricated process by PVD method.

To test changes in electrical characteristics of double-charge injection area compared with pure BCBG-S-DNTT-10, it implemented the output characteristics (I_D-U_{DS}) and transfer charateristics (I_D-U_{GS}), respectively, as shown in **Figure 9.21 (a)** and **(b)**.

The I_D-U_{DS} characteristics in **Figure 9.21 (a)** exhibited that the related electrical properties for BCBG S-DNTT-10-based OTFT (representing into dash lines) and Double-charge-injection S-DNTT-10-based OTFT (representing into solide line), under different $|U_{GS}|$ ranging from 0 to 40 V with step of 10 V (representing into varied color) and $|U_{DS}|$ ranging from 0 to 40 with step of 0.5V. It illustrated that : (i) the I_D-U_{DS} in Double-charge-injection S-DNTT-10-based OTFT as well performed the non-linear effect at initial small $|U_{DS}|$ area; (ii) in comparison of collected drain current in BCBG S-DNTT-10-based OTFT, it displayed the great enhancement

on the current and even it seemingly overwhelmed that in BCBG S-DNTT-10-based OTFT; (iii) as for Double-charge-injection S-DNTT-10-based OTFT, it exhibited that the drain current is increased and then degenerated with stressed U_{DS} and this change is more obvious with U_{GS}.

Figure 9.21 (b) showed the comparison of transfer characteristics (I_D-U_{GS}) for the BCBG S-DNTT-10-based OTFT and Double-charge-injection S-DNTT-10-based OTFT under stressed |U_{GS}| ranging from 0 to 50 V and 0 to 40 V, respectively, stressed U_{DS} of -1V for linear-mode and -40 V for saturation-mode. It exhibited that the drain current in transfer characteristics of Double-charge-injection S-DNTT-10-based OTFT is overall higher than that of BCBG S-DNTT-10-based OTFT. Meanwhile, the extrated linear-state effective field-effect mobility (μ_{lin}) for former one OTFT is 0.15 $cm^2 \cdot V^{-1} \cdot s^{-1}$, and the related threshold voltage ($U_{Th\text{-}lin}$) is -22.98V, and the saturated-state effective field-efffect mobility (μ_{sat}) and threshold voltage ($U_{Th\text{-}sat}$) is 0.4627 $cm^2 \cdot V^{-1} \cdot s^{-1}$ and -27 V. Nevertheless, the extracted parameters in BCBG S-DNTT-10-based OTFT was emerged the great degeneration. For μ_{lin} and $U_{Th\text{-}lin}$, it is respectively 0.0001 $cm^2 \cdot V^{-1} \cdot s^{-1}$ and -38.4V, and for μ_{sat} and $U_{Th\text{-}sat}$, it is only 0.0652 $cm^2 \cdot V^{-1} \cdot s^{-1}$ and -41.1V, respectively.

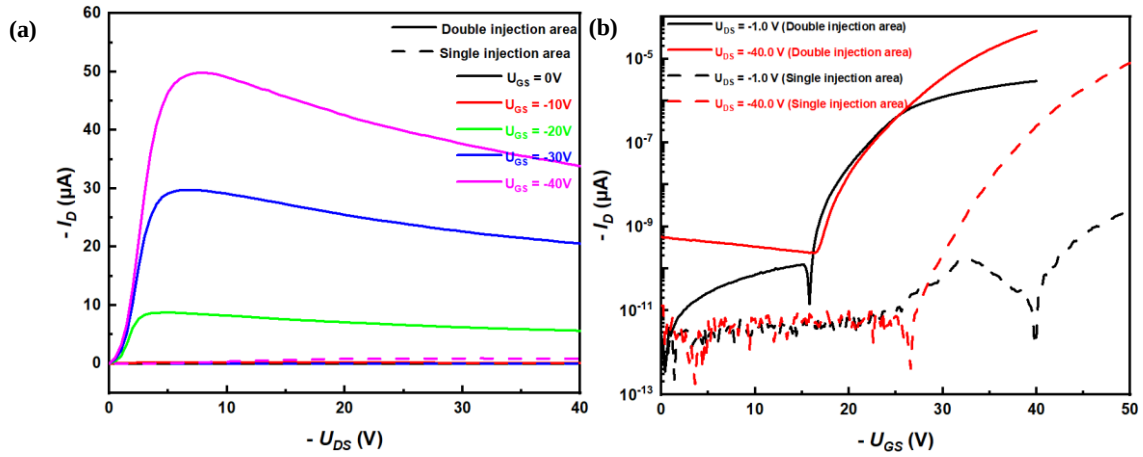


Figure 9.21 The comparison of electrical perofrmance for Double-charge-injection S-DNTT-10-based OTFT and BCBG S-DNTT-10-based OTFT. (a) Output characteristics and (b) transfer characteristics. Both devices with channel of 30 μm and width of 1000 μm and for Double-charge-injection S-DNTT-10-based OTFT the thickness T1 of first deposited S-DNTT-10 thin-film is 10 nm.

Based on the above electrical comparison, it illustrated the enhancement for Double-charge-injection S-DNTT-10-based OTFT versus BCBG S-DNTT-10-based OTFT in terms of I_D-U_{DS} and I_D-U_{GS} charateristics. Through I_D-U_{GS} charateristics, it was found that Double-charge-injection S-DNTT-10-based OTFT possessed higher field-effect mobility and lower |U_{Th}|, and it could be regarded to result in the higher drain current in I_D-U_{DS} charateristics. We speculated that it was casued by the additional charge injection area beneath Au electrodes and

increased the amount of charge injection in Double-charge-injection S-DNTT-10-based OTFT, compared with BCBG S-DNTT-10-based OTFT. Despite it preliminarily illustrated that the role of addition charge injection layer into the Double-injection OTFT, we found that it is still mainly limited by two factors that the non-linear effect and the reduction of saturation-state current with U_{DS} in I_D-U_{DS} characteristics. As for the former one, we think that it resulted from the injection contact resistance by parasitic energy diffferent between Fermi level of Au electrode, and unappropriate S-DNTT-10 molecular orientation closing to source electrode blocked the charge transport around electrodes area. With regard to the later one, it can be understood one hysterisis effect in running device, which is related to trap state. Encountered with this unstable effect, supposed that it was possibly originated from interface characteristics between first deposited S-DNTT-10 thin-film and the subsequent S-DNTT-10 thin-film. Since the S-DNTT-10 molecules are linked by the weaken interaction force named Van der Waals Force, hence, during the deposition of second S-DNTT-10 thin-film, it caused the disordered arrangement around the source showing in **Figure 9.22**. It possibly introduced the additional trap state and blocked the charge transport. Therefore, it resulted in the formation of hysteresis effect in output characteristics.

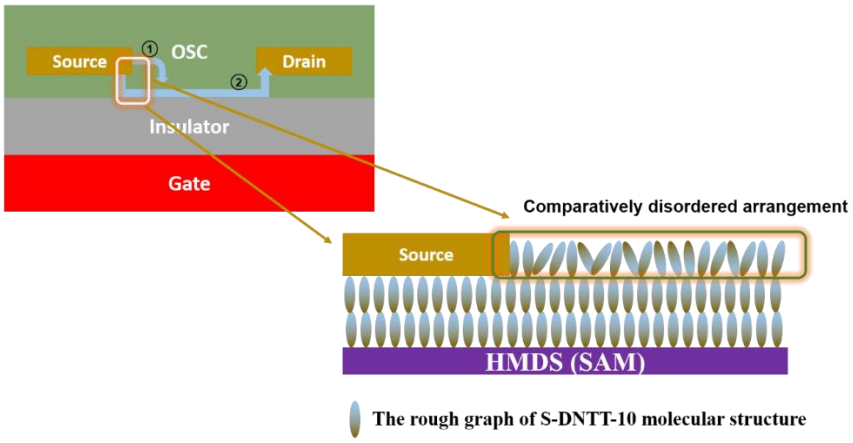


Figure 9.22 Schematic diagram of estimated disorder characteristics at interface between first and second thermal deposited S-DNTT-10 thin-films in the Double-charge-injection S-DNTT-10-based OTFT.

In this part, it was preliminarily achieved double-charge injection area by seemingly inserting electrodes into S-DNTT-10 thin-films. Compared with BCBG S-DNTT-10-based OTFT, it displayed the enhancement of performance. But it as well has some pre-improved space and potential research on it. For instance, how to optimize the molecular arrangement in the second deposited S-DNTT-10 thin-film, especially, located at the vicinity of electrodes. Meanwhile, the utilized thickness of first deposited S-DNTT-10 thin-film as well could impact electrical performance of device

10 French Summary

10.1 Présentation générale

Avec l'avènement et l'usage généralisé des ordinateurs, la technologie de l'information nous fait passer de l'ère industrielle à l'ère de l'information, permettant une transmission et un échange rapides et efficaces des données. L'optoélectronique et la microélectronique ont transformé nos vies de manière révolutionnaire. Un support physique clé pour l'avancée de la technologie de l'information est le transistor et le circuit intégré. Parmi eux, le transistor a eu un impact profond sur l'évolution future de la technologie électronique et peut être considéré comme le précurseur de la révolution microélectronique. Le transistor à effet de champ (FET), largement utilisé dans les produits électroniques, est l'élément central et fondamental des circuits intégrés modernes. Il constitue la base du développement des technologies de l'information et joue un rôle crucial dans ce domaine.

Depuis la création du premier OTFT en 1986, le domaine a évolué pendant 38 ans. En raison des contraintes d'espace, il est difficile de détailler chaque avancée et résultat de recherche. Malgré des progrès significatifs et des améliorations notables des performances des OTFT par rapport aux premiers dispositifs, des défis persistent en raison des propriétés des OSC, limitant le développement et l'application à grande échelle. Ces défis incluent la forte dépendance de la performance des dispositifs à la qualité du film organique, la résistance de contact due au décalage des niveaux d'énergie à l'interface électrode-semi-conducteur, la dégradation des performances avec le temps, et la sensibilité aux facteurs externes. Par conséquent, comprendre les mécanismes physiques sous-jacents est crucial pour le développement futur des OTFT.

Cette étude porte sur les OTFT basés sur le 3,10-Didécylnafto[2,1-b]nafto[1',2':4,5]thiéno[2,3-d]thiophène 21DNTT-10 (S-DNTT-10). Des rapports antérieurs montrent que le S-DNTT-10 peut être utilisé pour fabriquer des films OTFT par dépôt thermique et trempage. La solubilité de ce matériau est liée à ses longues chaînes alkyles, et il présente une stabilité à l'air ainsi que d'excellentes propriétés de transport de charge. Cette stabilité est due à son niveau d'énergie HOMO plus élevé, tandis que les propriétés de transport de charge sont liées à sa structure moléculaire et à la distribution des électrons pi. Bien que le S-DNTT-10 présente un potentiel pour les applications OTFT, la recherche sur ce matériau est limitée, notamment en ce qui concerne les vibrations moléculaires et certaines propriétés électriques. Par exemple, l'effet non linéaire dans les caractéristiques de sortie (I_D-U_{DS}) et les variations de mobilité des porteurs avec la température de recuit ne sont pas entièrement compris. De plus, les OTFT basés sur le S-DNTT-10 sont sujets aux effets de contrainte de polarisation, ce qui impacte leurs performances après une utilisation prolongée. Pour mieux comprendre et optimiser le S-DNTT-10 pour les applications OTFT, des OTFT ont été

fabriqués par dépôt thermique avec des électrodes en or. Des techniques de caractérisation avancées telles que la microscopie à force atomique (AFM), la microscopie à force de sonde Kelvin (KPFM) et la spectroscopie Raman ont été utilisées pour étudier les performances électriques des dispositifs et l'influence de facteurs tels que la température et le champ électrique. Des stratégies visant à améliorer les performances des dispositifs, comme l'ajout de couches supplémentaires de semi-conducteurs organiques et la conception de nouvelles architectures, sont proposées. Les sections suivantes résument brièvement les recherches menées dans cette étude.

Le chapitre 1 donne un aperçu des fondements théoriques des OTFT. Tout d'abord, les propriétés des matériaux des semi-conducteurs organiques (OSC) et la théorie du transport de charge seront présentées. Ensuite, un résumé de la théorie de base des OTFT sera proposé. Enfin, l'accent sera mis sur l'impact des caractéristiques de l'interface sur les performances des dispositifs.

Le chapitre 2 détaillera le processus de fabrication des OTFT basés sur le S-DNTT-10 ainsi que les techniques de caractérisation utilisées, accompagnées de leurs principes sous-jacents. Les propriétés du film S-DNTT-10 seront mesurées à l'aide de techniques de caractérisation nano-technologiques. Enfin, les propriétés électriques des OTFT basés sur le S-DNTT-10 seront discutées.

Le chapitre 3 se concentrera sur les caractéristiques de vibration moléculaire du S-DNTT-10. En utilisant des simulations basées sur la théorie de la fonctionnelle de la densité (DFT), les modes de vibration moléculaire et la distribution du nuage d'électrons π dans les molécules de S-DNTT-10 seront étudiés, comblant le manque de recherches sur les vibrations moléculaires du S-DNTT-10. Par la suite, nous étudierons l'influence du laser incident à différentes longueurs d'onde sur les performances électriques des OTFT à contact supérieur et grille inférieure (TCBG) basés sur le S-DNTT-10, ainsi que le signal de diffusion Raman du S-DNTT-10. Nous explorerons également l'effet de l'épaisseur du film mince de S-DNTT-10 sur le spectre Raman du S-DNTT-10. De plus, nous développerons une approche pour améliorer les signaux Raman du S-DNTT-10. Cela fournira une base expérimentale solide pour l'exploration approfondie de l'impact du stress de polarisation sur l'efficacité de l'injection et de la collecte de charge dans les OTFT TCBG basés sur le S-DNTT-10.

Le chapitre 4 discutera principalement de l'influence de l'effet de stress de polarisation sur les OTFT TCBG basés sur le S-DNTT-10. Il analysera l'impact d'une utilisation à long terme sur les performances électriques. L'impact de l'effet de stress de polarisation sur l'efficacité d'injection et d'extraction de charge du dispositif sera exploré à l'aide de la microscopie à force de sonde Kelvin (KPFM), en combinaison avec des mesures in situ utilisant la technologie de diffusion Raman, incluant la diffusion SERS aux électrodes et le spectre Raman conventionnel au niveau du canal, afin d'étudier ce phénomène de dégradation.

Le chapitre 5 explorera principalement l'analyse approfondie de l'impact des traitements de recuit sur les performances des OTFT TCBG basés sur le S-DNTT-10. Ces traitements incluent le recuit post-fabrication des dispositifs ainsi que l'ajustement de la température du substrat pendant le dépôt du film mince de S-DNTT-10. Pour le premier, l'influence des différentes températures de recuit post-fabrication sur les caractéristiques électriques des OTFT TCBG basés sur le S-DNTT-10 sera étudiée. Pendant ce processus, l'AFM, la spectroscopie Raman et la KPFM seront respectivement utilisées pour examiner la morphologie des électrodes et du film de S-DNTT-10, les spectres Raman des molécules de S-DNTT-10 et la résistance de contact. Pour le second, nous étudierons les variations de T_{post} (qui correspond à la mobilité effective maximale du dispositif) en fonction de la température de dépôt du substrat, T_{sub}. En ajustant la relation entre ces deux paramètres, l'impact de la température de dépôt sur les performances du dispositif sera initialement révélé.

Dans le chapitre 6, en tenant compte du phénomène d'efficacité relativement faible d'injection de charge observé dans les dispositifs OTFT TCBG basés sur le S-DNTT-10 (chapitre 2), nous développerons une méthode améliorée en introduisant un matériau OSC supplémentaire, des films minces de pentacène. Nous utiliserons les mesures I-V accompagnées de la caractérisation KPFM dans le but d'évaluer l'influence du pentacène sur les OTFT TCBG basés sur le S-DNTT-10. De plus, nous introduirons une méthode optimisée pour déposer la couche supplémentaire afin d'améliorer encore les performances des dispositifs TCBG S-DNTT-10/Pentacène. Ensuite, nous discuterons de l'effet de la température de recuit post-fabrication sur les performances électriques des OTFT TCBG basés sur le S-DNTT-10 empilés avec des films minces de pentacène. Enfin, nous explorerons l'impact de l'effet de stress de polarisation sur les performances électriques des OTFT TCBG S-DNTT-10/Pentacène, comparé aux OTFT TCBG basés uniquement sur le S-DNTT-10.

10.2 Transistors organiques à couches minces

10.2.1 Introduction

Ce chapitre traite principalement de la théorie fondamentale des transistors à film mince organique (OTFT). La Section 1.2 introduit brièvement la formation des orbitales hybrides dans les matériaux organiques, en prenant comme exemple des matériaux organiques basés sur des atomes de carbone et d'hydrogène et des orbitales hybrides sp^2 pour les décrire. Dans la section 1.3, nous présentons le mécanisme de transport de charge dans les matériaux organiques, en nous concentrant principalement sur le transport de type bande, le mécanisme de libération multiple des pièges (MRT) et le transport par saut. La Section 1.4 introduit la théorie des OTFT. Elle comprend la structure courante des OTFT, le mécanisme fondamental de fonctionnement des OTFT, les caractéristiques I-V, les paramètres de caractérisation électrique et les caractéristiques des interfaces dans les OTFT.

10.2.2 Conclusions

Dans ce chapitre, nous avons brièvement introduit les concepts fondamentaux liés à l'injection et au transport de charge dans les matériaux semi-conducteurs organiques (OSC), les performances électriques et les caractéristiques des interfaces des OTFT, ainsi que le dépôt des OSC par dépôt physique en phase vapeur (PVD). Ces notions fournissent une base solide pour la section suivante et les chapitres à venir.

10.3 Techniques de fabrication et de caractérisation des OTFT basées sur S-DNTT-10

10.3.1 Introduction

L'une des principales questions examinées dans cette étude concernera la caractérisation des OTFT basés sur le S-DNTT-10 à l'aide de techniques avancées de nano-caractérisation. La Section 2.2 introduira brièvement la structure moléculaire et le processus de synthèse des molécules de S-DNTT-10. Actuellement, cet article est le seul document académique disponible sur le S-DNTT-10. Ensuite, le processus de fabrication des OTFT basés sur le S-DNTT-10 sera décrit dans la Section 2.3. La Section 2.4 présentera les principes fondamentaux des techniques de caractérisation utilisées dans cette étude, couvrant à la fois les matériaux à film mince et les propriétés électriques des dispositifs. Plus précisément, un système de co-mesure I-V et de spectroscopie Raman adapté aux OTFT a été développé dans notre laboratoire, permettant des mesures de spectroscopie Raman sur des OTFT en fonctionnement. Puis, dans la Section 2.5, la AFM sera utilisée pour montrer les conditions de surface des films de S-DNTT-10 déposés thermiquement par PVD, et la mouillabilité du film mince de S-DNTT-10 sera mesurée par la technique de l'angle de contact. Enfin, dans la Section 2.6, les caractéristiques électriques des OTFT basés sur le S-DNTT-10 déposés thermiquement seront présentées et analysées. Nous analyserons les courbes caractéristiques de sortie conventionnelles (I_D-U_{DS}), de transfert (I_D-U_{GS}) et la distribution du potentiel de surface des OTFT basés sur le S-DNTT-10 par microscopie à force de potentiel Kelvin (KPFM). De plus, nous discuterons brièvement de l'« effet de saturation précoce » dans nos OTFT basés sur le S-DNTT-10.

10.3.2 Conclusions

Dans cette section, nous avons présenté les informations concernant les OTFT basés sur le S-DNTT-10 que nous avons explorées dans cette étude. Tout d'abord, la structure moléculaire et le processus chimique de base des molécules de S-DNTT-10 ont été brièvement exposés. Ensuite, nous avons décrit le processus de fabrication fondamental des OTFT basés sur le S-DNTT-10 utilisés dans cette étude. Les équipements de fabrication ont été présentés, ainsi que la plateforme de test électrique et les équipements de caractérisation des matériaux utilisés, incluant la plateforme de test combinée du spectromètre IV-in-situ Raman maison, l'AFM, la KPFM et la technique de l'angle de contact.

Grâce aux tests AFM et de l'angle de contact, la morphologie du film mince de S-DNTT-10 et son angle de contact de 101,8° ont été observés. Les résultats de l'AFM ont révélé que les

couches de S-DNTT-10 se superposent les unes aux autres, tandis que la mesure de l'angle de contact a indiqué que le film mince de S-DNTT-10 possède des propriétés hydrophobes. Ensuite, les caractéristiques électriques des OTFT basés sur le S-DNTT-10 ont été présentées, comme les caractéristiques de sortie I_D-U_{DS}, les caractéristiques de transfert I_D-U_{GS}, la mobilité à effet de champ et la tension de seuil, incluant des caractéristiques électriques non linéaires. Dans ce cas, la mobilité à effet de champ efficace en mode linéaire (μ_{lin}) était d'environ 0,062 $cm^2 \cdot V^{-1} \cdot s^{-1}$ et la tension de seuil associée ($U_{Th\text{-}lin}$) de -21,2 V. La mobilité à effet de champ efficace en mode saturation (μ_{sat}) était de presque 3,395 $cm^2 \cdot V^{-1} \cdot s^{-1}$ et la tension de seuil associée ($U_{Th\text{-}sat}$) de -24,9 V. La distribution du potentiel de l'OTFT basé sur le S-DNTT-10 a été obtenue par une caractérisation KPFM, révélant que la majorité de la chute de potentiel se produit à la source, ce qui suggère la présence d'une résistance de contact considérable à la source, indiquant que l'injection de charge est entravée. Enfin, nous avons discuté des résultats de l'effet de saturation précoce dans les OTFT basés sur le S-DNTT-10. Bien que nous n'ayons pas encore trouvé d'explication physique concluante, cet effet a été simulé avec succès à l'aide d'un modèle mathématique. Les résultats suggèrent que cet effet pourrait être lié aux variations de U_{DS}, et nous prévoyons d'approfondir cette question dans les études futures.

10.4 Diffusion Raman sur matériau S-DNTT-10

10.4.1 Introduction

Dans ce chapitre, les caractéristiques moléculaires du S-DNTT-10 sont principalement étudiées à l'aide des techniques de diffusion Raman, incluant l'utilisation de la spectroscopie Raman conventionnelle et de la spectroscopie Raman amplifiée de surface (SERS). Pour commencer, les principes fondamentaux de la diffusion Raman et de la SERS sont succinctement présentés dans la Section 3.2. Ensuite, le spectre de diffusion Raman du S-DNTT-10 est simulé et calculé à l'aide de la théorie de la fonctionnelle de densité (DFT), et les modes de vibration moléculaire sont obtenus dans la Section 3.3. Étant donné que des tests in situ de diffusion Raman des OTFT sont nécessaires dans les expériences ultérieures, il est essentiel de déterminer si la longueur d'onde de la lumière d'excitation a une influence sur les OTFT, c'est pourquoi des mesures des caractéristiques électriques sont effectuées dans la Section 3.4. Enfin, des mesures de diffusion Raman sont réalisées sur le film mince de S-DNTT-10 dans la Section 3.5.

10.4.2 Conclusions

Ce chapitre explore principalement les vibrations moléculaires du S-DNTT-10, comblant les lacunes dans la compréhension de ses propriétés matérielles. En utilisant la théorie de la fonctionnelle de densité (DFT), nous avons simulé les spectres Raman du S-DNTT-10, fournissant à la fois les spectres de diffusion Raman, comme le montre la **Figure 10.1 (a)**, et des informations détaillées sur les vibrations moléculaires associées aux différents modes Raman. Les résultats montrent que les vibrations moléculaires du S-DNTT-10 sont principalement centrées sur les vibrations du cycle central de thiophène et sur les vibrations combinées du cycle thiophène et des chaînes alkyles. De plus, les simulations DFT ont fourni

les niveaux d'énergie de l'HOMO et du LUMO et révélé la distribution de la fonction d'onde des électrons π, ce qui est crucial pour comprendre les caractéristiques de transport de charge du S-DNTT-10. Les spectres Raman expérimentaux du S-DNTT-10 ont été mesurés à différentes longueurs d'onde d'excitation, comme le montre la **Figure 10.1 (b)**, révélant que le signal de diffusion Raman est influencé par l'épaisseur du film mince de S-DNTT-10. Pour améliorer le signal Raman via la SERS, un film mince nano-structuré en or a été déposé sur la surface du film de S-DNTT-10, comme le montre la **Figure 10.1 (c)**. Cette étude fournit des informations de référence précieuses pour la détection future des signaux de diffusion Raman provenant des films minces de S-DNTT-10.

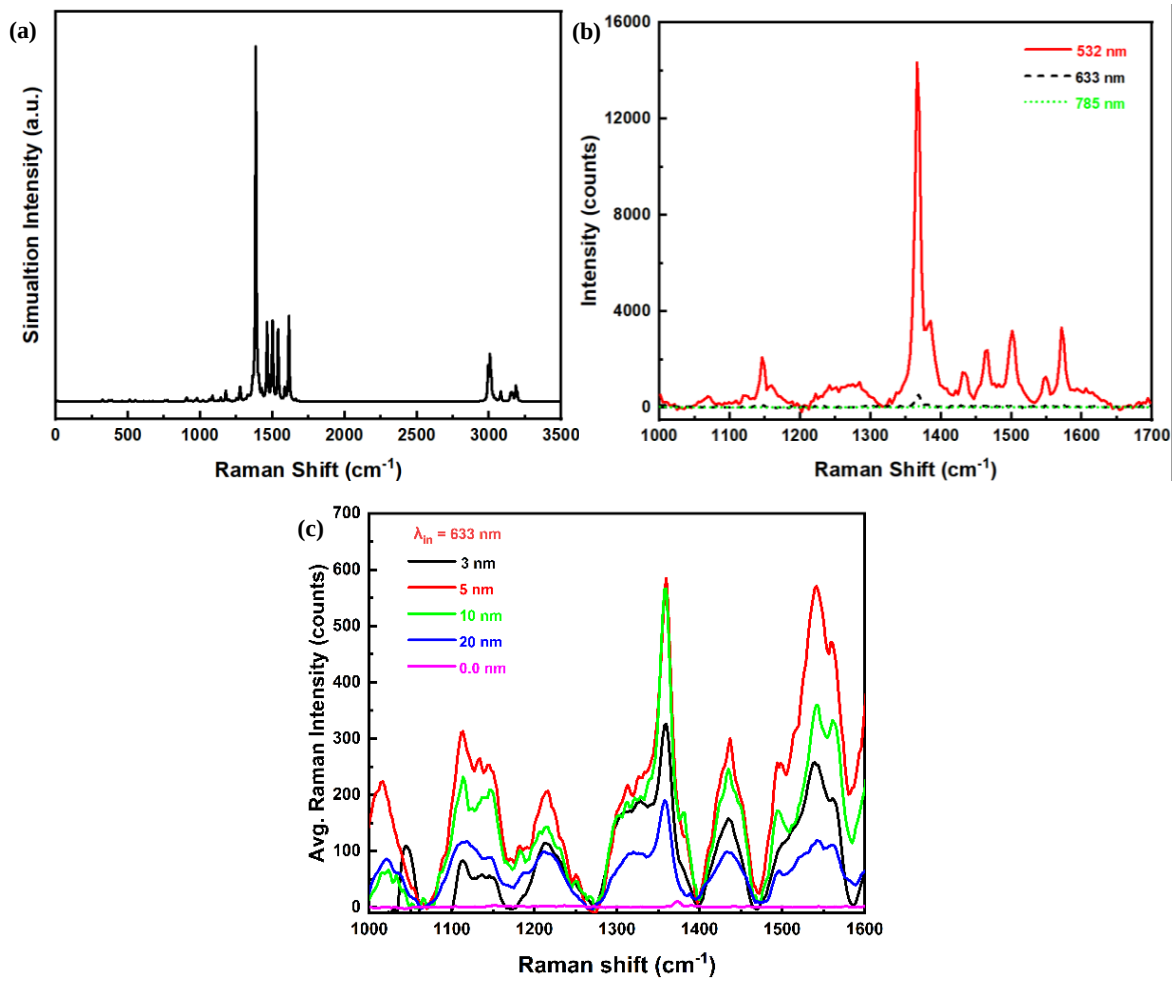


Figure 10.1 (a) La simulation schématique du spectre Raman non résonant du S-DNTT-10 à l'aide de la méthode DFT. (b) Le spectre Raman expérimental non résonant du S-DNTT-10 sous 532 nm, 633 nm et 785 nm. And (c) Les spectres SERS des molécules de S-DNTT-10 déposées avec différentes épaisseurs de films minces d'or sous un laser de 633 nm.

10.5 Étude de l'influence de l'effet de stress de polarisation sur les OTFT basés sur le S-DNTT-10 via la technique de diffusion Raman

10.5.1 Introduction

Après des décennies de développement, les OTFT sont progressivement devenus de forts candidats pour les applications électroniques commerciales. Cependant, la stabilité électrique des OTFT lors d'un fonctionnement prolongé est cruciale. En pratique, lorsqu'un OTFT

fonctionne en continu dans un environnement aéré, il est inévitablement soumis à l'influence de plusieurs facteurs parasites, tels que le champ électrique appliqué, l'échauffement par effet Joule et la dégradation du matériau semi-conducteur organique (OSC).

Dans ce chapitre, nous explorerons l'influence de l'effet de stress de polarisation (BS) sur les caractéristiques électriques des OTFT à contact supérieur et grille inférieure (TCBG) basés sur le S-DNTT-10 en environnement aéré. Au cours de ce processus, nous présenterons principalement une proposition innovante en exécutant plusieurs méthodes de caractérisation sur l'effet BS pour les OTFT TCBG basés sur le S-DNTT-10, incluant les caractéristiques IV (voir Section 4.2), la microscopie à force de sonde Kelvin (KPFM) (voir Section 4.2), la simulation DFT (voir Section 4.3) et les techniques de diffusion Raman, tant conventionnelles que SERS (voir Section 4.4). Nous pensons que cela permettra non seulement de mettre en évidence les changements de performances électriques en corrélation avec les caractéristiques moléculaires affectées, mais également de montrer l'impact à long terme du champ électrique sur l'efficacité d'injection et d'extraction de charge via la méthode KPFM. Cela peut également révéler le facteur potentiel qui cause principalement la dégradation des performances électriques des OTFT TCBG basés sur le S-DNTT-10.

10.5.2 Conclusions

Dans ce chapitre, nous nous sommes principalement concentrés sur l'exploration de l'influence de l'effet de stress de polarisation (BS) sur les caractéristiques électriques des OTFT TCBG basés sur le S-DNTT-10 après 8 heures sous U_{GS} et U_{DS} de -40,0 V en environnement aéré. En particulier, durant ce processus, nous avons habilement utilisé plusieurs méthodes de caractérisation ensemble. Après 8 heures de stress, il a été observé que la mobilité à effet de champ efficace μ_{lin} et μ_{sat} avait respectivement diminué de 0,62 à 0,385 $cm^2 \cdot V^{-1} \cdot s^{-1}$, et de 3,842 à 1,03 $cm^2 \cdot V^{-1} \cdot s^{-1}$. La tension de seuil correspondante $U_{Th\text{-}lin}$ et $U_{Th\text{-}sat}$ a respectivement évolué de -20,3 à -23,5 V, et de -29,2 à -28,8 V, comme le montrent la **Figure 10.2 (a)**, **(b)** et le **Table 10.1**. Parallèlement, les mesures de diffusion Raman ont montré des changements dans le spectre Raman des molécules de S-DNTT-10 au niveau des électrodes et de la zone du canal en raison de l'interférence du champ électrique à long terme, comme l'illustrent les **Figure 10.2 (c)-(e)**. Cependant, les résultats du KPFM pour extraire la résistance de contact aux électrodes avant et après l'effet BS ont montré que la résistance de contact à la source $R_s \cdot W$ avait diminué de 36808 à 29634 Ω·cm, et la résistance de contact au drain $R_d \cdot W$ avait diminué de 8918 à 8668 Ω·cm. Cela indique que le champ électrique à long terme n'a pas dégradé l'efficacité de l'injection et de l'extraction de charge dans ce dispositif, du moins il n'a pas causé de destruction.

Par conséquent, nous avons suggéré que la dégradation observée de la mobilité effective et le décalage de la tension de seuil étaient principalement liés à l'effet du champ électrique à long terme sur les molécules de S-DNTT-10 dans la région du canal. Cela implique que la réduction des performances des OTFT TCBG basés sur le S-DNTT-10 sous champ électrique provient des modifications des caractéristiques moléculaires au niveau du canal. De plus, il convient de noter que l'analyse et les conclusions ci-dessus sont probablement spécifiques aux

OTFT TCBG basés sur le S-DNTT-10 mesurés et ne peuvent pas être directement appliquées à d'autres dispositifs électroniques à base de matériaux semi-conducteurs organiques (OSC), car les caractéristiques de transport de charge, régies par le recouvrement ou la délocalisation des électrons π, dépendent de la structure moléculaire de chaque matériau.

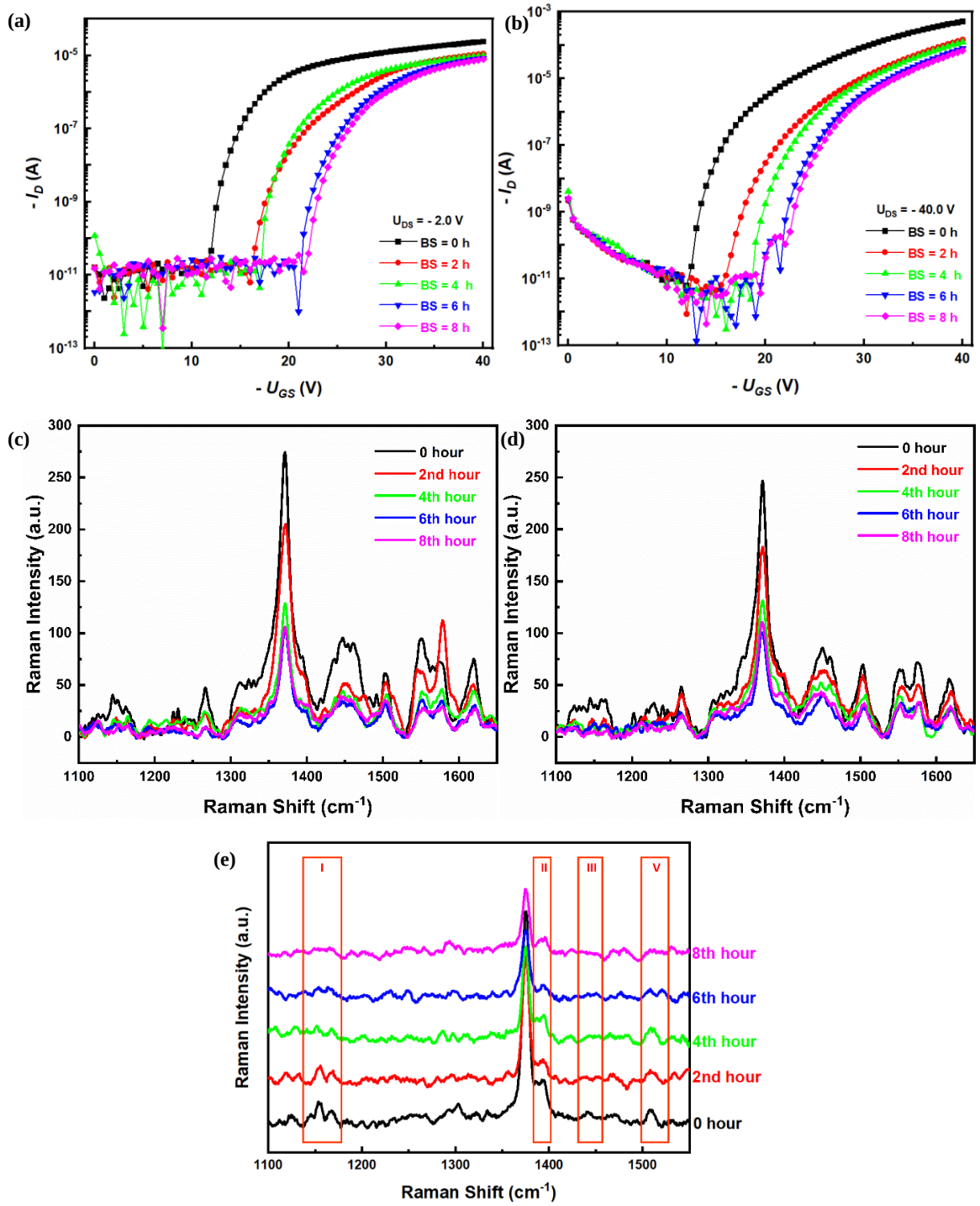


Figure 10.2 Les caractéristiques de transfert de l'OTFT S-DNTT-10 mesuré avant et après 8 heures de stress de polarisation (*BS*). (a) Mode linéaire (U_{DS} stressé = -2,0 V) et (b) mode saturation (U_{DS} stressé = -40,0 V). Le spectre SERS lié au stress de polarisation de 8 heures, utilisant un laser de 633 nm au niveau de (c) la source et (d) du drain. (e) Le spectre Raman non résonant du S-DNTT-10 dans le canal utilisant un laser de 532 nm en fonction du temps de stress de polarisation.

Table 10.1 La comparaison de l'OTFT avant et après 8 heures d'effet de stress de polarisation (*BS*).

Parameters	Before 8hours *BS*	After 8hours *BS*
μ_{lin} (U_{DS} = -2 V)	0.62 $cm^2 \cdot V^{-1} \cdot s^{-1}$	0.385 $cm^2 \cdot V^{-1} \cdot s^{-1}$
$U_{Th\text{-}lin}$ (U_{DS} = -2 V)	- 20.3 V	- 29.2 V
μ_{sat} (U_{DS} = -40 V)	3.842 $cm^2 \cdot V^{-1} \cdot s^{-1}$	1.03 $cm^2 \cdot V^{-1} \cdot s^{-1}$
$U_{Th\text{-}sat}$ (U_{DS} = -40 V)	-23.5 V	-28.8 V

10.6 Traitement de recuit sur les OTFT basés sur le S-DNTT

10.6.1 Introduction

Les recherches ont montré que la morphologie des films minces OSC fabriqués est corrélée aux caractéristiques de transport de charge, influençant ainsi les performances électriques des OTFT. Il a été observé que le traitement de recuit post-fabrication influence efficacement l'agencement ou la cristallinité des molécules organiques dans les films minces, ce qui impacte les propriétés des OTFT. Dans ce chapitre, nous nous concentrerons sur l'influence du traitement de recuit sur les performances électriques des OTFT à contact supérieur et grille inférieure (TCBG) basés sur le S-DNTT-10. Nous visons à explorer cette influence à l'aide d'outils de caractérisation avancés à l'échelle nanométrique, tels que l'AFM, la KPFM et les techniques de diffusion Raman. Ces outils seront utilisés pour examiner les changements dans les caractéristiques moléculaires du S-DNTT-10, le film mince de S-DNTT-10 et les électrodes en or, ainsi que les interfaces entre le film mince de S-DNTT-10/électrodes et le film mince de S-DNTT-10/couches HMDS (comme discuté en Section 5.2). De plus, nous étudierons la température de recuit post-fabrication spécifique (T_{post}) qui permet d'obtenir les performances optimales du dispositif, car elle varie avec la température du substrat de dépôt du S-DNTT-10 (comme discuté en Section 5.3).

10.6.2 Conclusions

Dans ce chapitre, nous avons examiné l'influence du traitement de recuit sur les performances électriques des OTFT à contact supérieur et grille inférieure (TCBG) basés sur le S-DNTT-10. Nous avons constaté que le processus de recuit post-fabrication ainsi que la température de recuit spécifique influencent de manière significative les performances des dispositifs. Notamment, une température de recuit optimale a été identifiée, améliorant les performances du dispositif. Les changements dans les caractéristiques électriques ont été attribués à l'impact des différentes températures sur les films minces de S-DNTT-10 et les interfaces entre les électrodes en or et le S-DNTT-10, comme analysé à l'aide des techniques AFM, de spectroscopie Raman et KPFM.

Pour les OTFT TCBG basés sur le S-DNTT-10, les caractéristiques électriques ont varié en fonction des températures de recuit post-fabrication, allant de 50 à 110 °C, avec des paliers de 30 °C. Les dispositifs ont montré une amélioration des performances de sortie avec une augmentation de la température jusqu'à 50 °C, suivie d'une diminution à 80 °C et 110 °C, comme illustré dans la **Figure 10.3 (a)**. Pour les films minces de S-DNTT-10, des températures

de recuit plus élevées ont modifié la topographie du film, avec des dommages et des fissures plus importants observés à des températures plus élevées. La spectroscopie Raman a révélé des changements moléculaires, mis en évidence par des variations d'intensité et une séparation des pics dans les bandes de décalage Raman, affectant le transport de charge dans le canal. Les mesures de mobilité intrinsèque à partir de la KPFM ont montré que la $\mu_{intrinsèque}$ initiale de 1,28 $cm^2 \cdot V^{-1} \cdot s^{-1}$ a augmenté à 1,44 $cm^2 \cdot V^{-1} \cdot s^{-1}$ à 50 °C, mais a chuté à 0,154 $cm^2 \cdot V^{-1} \cdot s^{-1}$ avec des augmentations supplémentaires de la température de recuit post-fabrication, comme illustré dans la **Figure 10.3 (b)**. De plus, l'analyse de l'angle de contact avec de l'eau et du Dim a révélé de légers changements dans les caractéristiques de surface de la couche de HMDS, contribuant probablement aux modifications de la morphologie du film S-DNTT-10. Les effets combinés des changements dans le film de S-DNTT-10 et la couche de HMDS pourraient expliquer les variations topographiques observées.

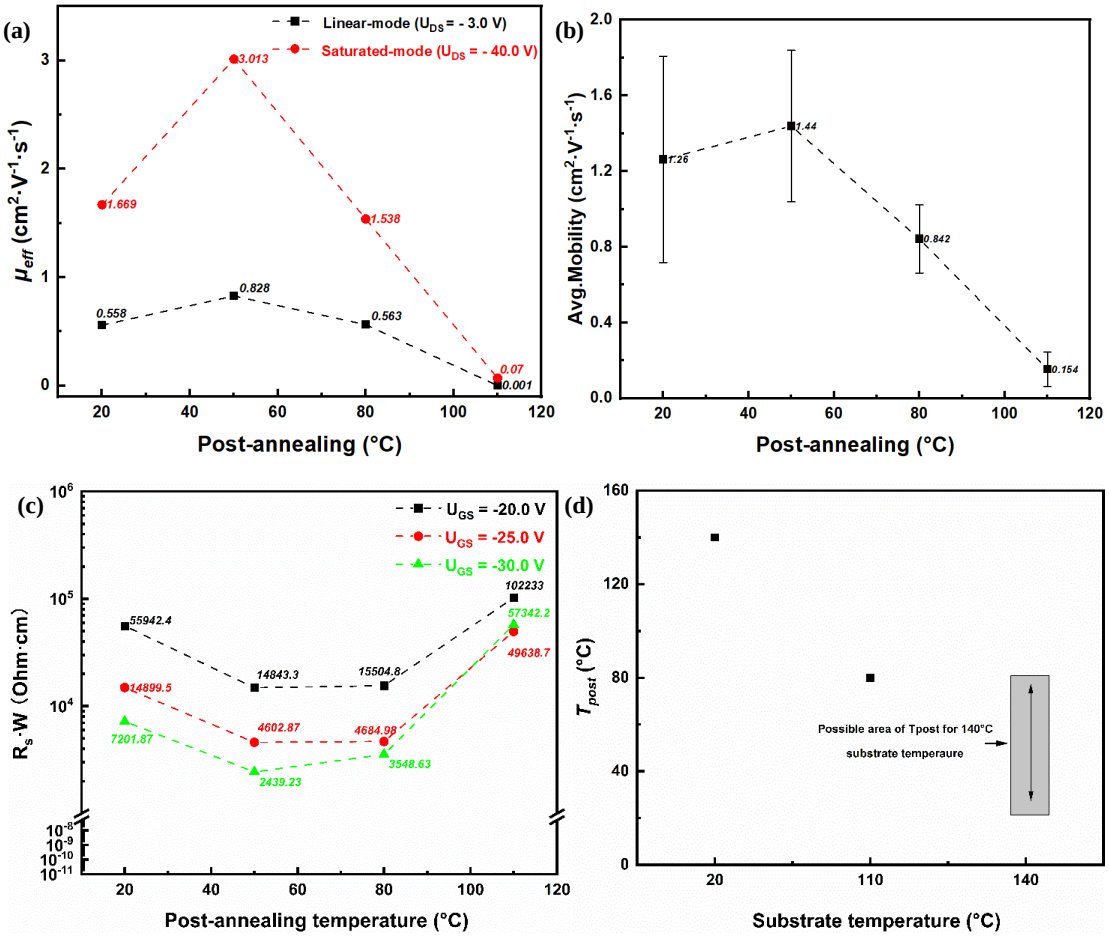


Figure 10.3 (a) L'extraction de la mobilité effective à effet de champ en fonction de la température de recuit post-fabrication. (La longueur de canal est de 50 µm, la largeur de canal de 1000 µm, la capacité par surface C_i de 0,00038781 F/m², l'épaisseur des électrodes en or de 10 nm, et les résultats pour T = 20 °C correspondent à la mobilité extraite avant chauffage). (b) L'extraction de la mobilité intrinsèque moyenne en fonction des différentes températures de recuit post-fabrication. (c) La résistance de contact à la source, $R_s \cdot W$, en fonction de la température avec un dispositif ayant des électrodes en or de 25 nm. (d) La relation approximative entre T_{post} et T_{sub}.

De plus, nous avons constaté que des températures de recuit plus élevées perturbaient les caractéristiques de contact entre le S-DNTT-10 et les électrodes, avec une augmentation de la rugosité RMS de 1,910 nm à 19,15 nm à 110 °C. Cela suggère que des températures de recuit

post-fabrication plus élevées dégradent les propriétés d'injection et de collecte de charge, comme en témoigne l'augmentation de la résistance de contact observée à travers la KPFM, illustrée dans la **Figure 10.3 (c)**. Finalement, nous avons constaté que la température de recuit post-fabrication spécifique (T_{post}), qui améliore les performances du dispositif, varie avec la température de dépôt du substrat (T_{sub}) pendant le processus de fabrication du S-DNTT-10. Il a été conclu de manière approximative que T_{post} diminue avec l'augmentation de T_{sub}, comme montré dans la **Figure 10.3 (d)**.

10.7 Amélioration de l'injection de charge dans les OTFT basés sur le S-DNTT-10

10.7.1 Introduction

Les OTFT ont été appliqués dans des domaines commerciaux en raison des propriétés uniques des matériaux organiques. Cependant, ces matériaux se dégradent à l'air libre, réduisant considérablement la durée de vie des dispositifs. Bien que l'ajustement des orbitales moléculaires (OM), comme la réduction du niveau d'énergie HOMO, puisse améliorer la stabilité des matériaux de type p, cela augmente également la barrière énergétique à l'interface entre les OSC et l'or (souvent utilisé comme électrodes), ce qui conduit à un effet non linéaire dans les caractéristiques de sortie I_D-U_{DS}. Cela augmente la résistance de contact (R_c), affectant l'injection/extraction de charge, et limite les applications des OTFT. Idéalement, un contact ohmique pur faible est préféré, mais une R_c plus élevée, due à la présence d'une barrière énergétique évidente aux interfaces OSC/électrodes, provoque des performances non idéales. Cela se manifeste par une courbe de sortie non linéaire ou en forme de "S" (I_D-U_{DS}) ou un "coude" ou une "double pente" dans les caractéristiques de transfert (I_D-U_{GS}). Une R_c élevée réduit l'efficacité d'injection de charge, augmente les tensions de fonctionnement appliquées aux OTFT, limite la fréquence d'opération, raccourcit la durée de vie des dispositifs et provoque des effets non linéaires dans les caractéristiques I-V, ce qui entrave l'extraction précise des paramètres électriques, et finalement, freine la conception efficace des OSC et l'optimisation des OTFT.

Dans ce chapitre, nous proposons une méthode pour améliorer l'efficacité de l'injection de charge dans les OTFT à contact supérieur et grille inférieure (TCBG) basés sur le S-DNTT-10, par l'introduction d'un film mince de pentacène via les électrodes. La Section 6.2 étudiera principalement l'influence du film mince de pentacène supplémentaire sur les performances électriques des OTFT TCBG basés sur le S-DNTT-10. Dans la Section 6.2.1, nous introduirons brièvement l'utilisation proposée du pentacène du point de vue de la simulation DFT et de l'analyse des niveaux d'énergie. La Section 6.2.2 présentera l'optimisation de l'épaisseur du film mince de pentacène et les changements dans les caractéristiques électriques des OTFT TCBG basés sur le S-DNTT-10/Pentacène, comparés aux OTFT TCBG basés sur le S-DNTT-10. Dans la Section 6.2.3, nous explorerons les changements électriques du point de vue de la résistance de contact, en utilisant principalement la microscopie à force de sonde Kelvin (KPFM). De plus, nous modifierons la structure initiale des OTFT basés sur le S-DNTT-10/Pentacène pour

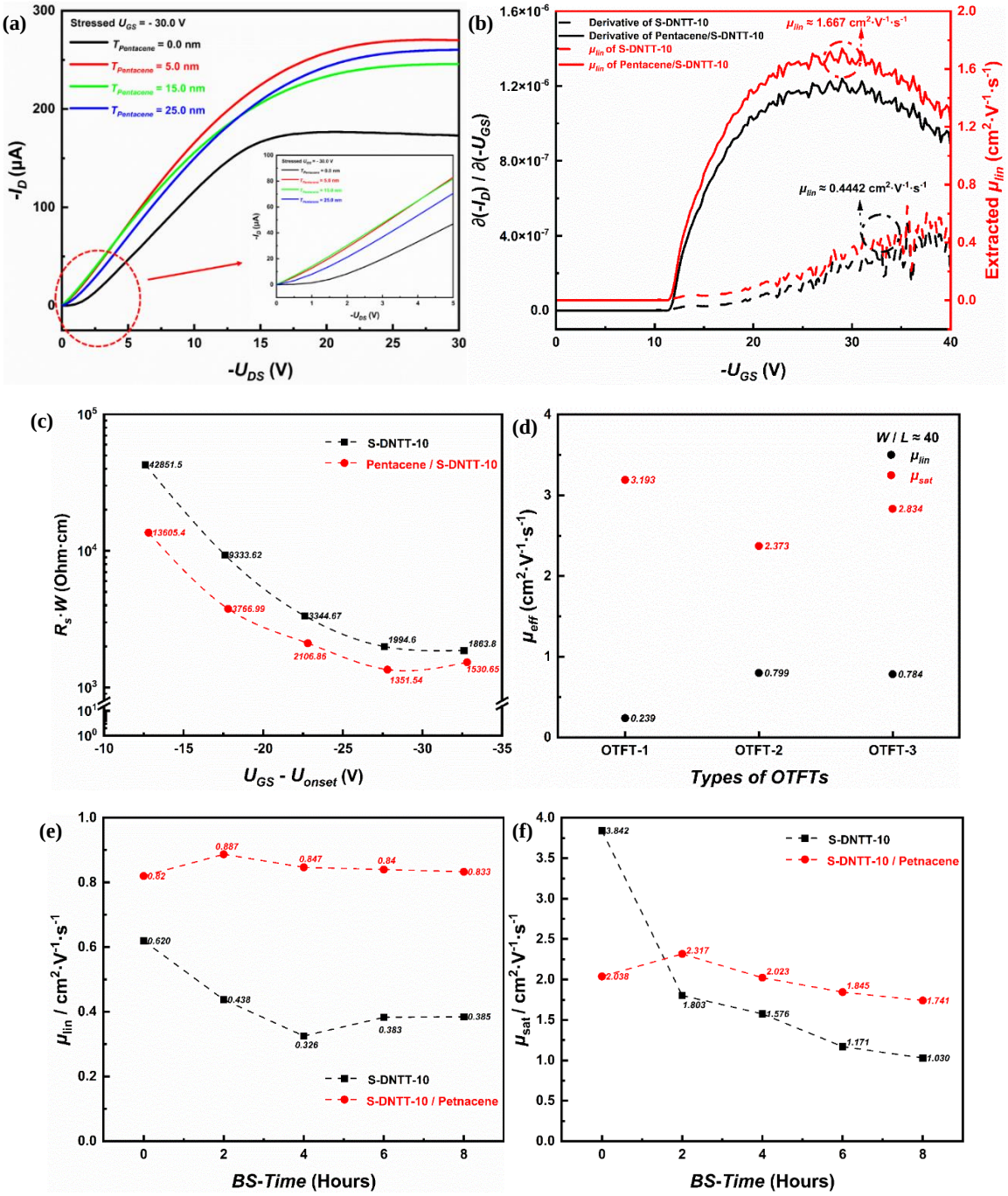
améliorer davantage leurs performances. La Section 6.2.4 mettra en lumière les changements dans la stabilité électrique induits par le film mince de pentacène supplémentaire après avoir subi l'effet de stress de polarisation (BS), en comparaison avec les OTFT TCBG basés uniquement sur le S-DNTT-10. Enfin, dans la Section 6.2.5, nous examinerons l'influence du traitement de recuit post-fabrication sur les OTFT TCBG basés sur le S-DNTT-10/Pentacène.

10.7.2 Conclusions

Bien que le matériau S-DNTT-10 présente de bonnes caractéristiques de transport de charge et une bonne stabilité, les OTFT basés sur le S-DNTT-10 affichent un effet non linéaire dans les caractéristiques de sortie en raison de problèmes liés aux contacts des électrodes, ce qui limite leurs performances. Cet effet non linéaire est lié à la présence d'une barrière énergétique de Schottky à l'interface électrode/OSC.

Dans ce chapitre, nous avons proposé une approche innovante consistant à déposer un film mince de semi-conducteur organique supplémentaire, le pentacène, entre les électrodes de source et de drain et le film mince de S-DNTT-10, afin d'améliorer l'efficacité de l'injection de charge en atténuant l'effet de la barrière énergétique. Nous avons étudié l'effet de différentes épaisseurs de films minces de pentacène sur les performances électriques des OTFT basés sur le S-DNTT-10/Pentacène, comme illustré à la **Figure 10.4 (a)**. Les résultats suggèrent qu'une épaisseur de film mince de pentacène comprise entre 5 et 15 nm est optimale pour améliorer les performances des OTFT. Nous avons fabriqué avec succès des OTFT TCBG basés sur le S-DNTT-10 et un film mince de 5 nm de pentacène, avec une mobilité à effet de champ en mode linéaire (μ_{lin}) plus élevée, telle que 1,7 $cm^2 \cdot V^{-1} \cdot s^{-1}$, et une $R_s \cdot W$ plus faible de 1,36 × 10^4 Ω·cm. En revanche, l'OTFT basé sur le S-DNTT-10 a montré une μ_{lin} de 0,4 $cm^2 \cdot V^{-1} \cdot s^{-1}$ et une $R_s \cdot W$ de 4,28 × 10^4 Ω·cm, comme le montrent les **Figure 10.4 (b)** et **(c)**. Cependant, le film mince de pentacène supplémentaire a entraîné une mobilité à effet de champ en mode saturation (μ_{sat}) plus faible dans l'OTFT TCBG basé sur le S-DNTT-10/Pentacène. Pour remédier à cela, nous avons fabriqué avec succès un OTFT TCBG basé sur le S-DNTT-10 avec un film mince de pentacène uniquement dans la zone de la source. Ce dispositif a montré une μ_{lin} plus élevée, similaire à celle de l'OTFT TCBG basé sur le S-DNTT-10/Pentacène, tout en maintenant une μ_{sat} comparable à celle de l'OTFT TCBG basé sur le S-DNTT-10, comme illustré à la **Figure 10.4 (d)**. Cette étape optimise davantage la méthode d'utilisation d'une couche supplémentaire dans les OTFT.

Nous avons également démontré, à travers une étude de stress de polarisation, que la couche supplémentaire de pentacène, qui améliore l'injection de charge, renforce également la stabilité du dispositif, comme le montrent les **Figure 10.4 (e)** et **(f)**. De plus, un traitement de recuit post-fabrication a été appliqué aux OTFT TCBG basés sur le S-DNTT-10/Pentacène, et les résultats présentés dans la **Figure 10.4 (g)** et **(h)** suggèrent que, bien que ce traitement puisse améliorer encore l'efficacité de l'injection de charge, la température de recuit doit être soigneusement prise en compte en raison de la sensibilité du pentacène à la température.


(a)
Stressed U_{GS} = - 30.0 V
$T_{Pentacene}$ = 0.0 nm
$T_{Pentacene}$ = 5.0 nm
$T_{Pentacene}$ = 15.0 nm
$T_{Pentacene}$ = 25.0 nm
$-I_D$ (μA)
$-U_{DS}$ (V)
(b)
Derivative of S-DNTT-10
Derivative of Pentacene/S-DNTT-10
μ_{lin} of S-DNTT-10
μ_{lin} of Pentacene/S-DNTT-10
μ_{lin} ≈ 1.667 cm²·V⁻¹·s⁻¹
μ_{lin} ≈ 0.4442 cm²·V⁻¹·s⁻¹
$\partial(-I_D) / \partial(-U_{GS})$
Extracted μ_{lin} (cm²·V⁻¹·s⁻¹)
$-U_{GS}$ (V)
(c)
S-DNTT-10
Pentacene / S-DNTT-10
42851.5
13605.4
9333.62
3766.99
3344.67
2106.86
1994.6
1351.54
1863.8
1530.65
$R_s \cdot W$ (Ohm·cm)
U_{GS} - U_{onset} (V)
(d)
W / L ≈ 40
μ_{lin}
μ_{sat}
3.193
0.239
2.373
0.799
2.834
0.784
μ_{eff} (cm²·V⁻¹·s⁻¹)
OTFT-1
OTFT-2
OTFT-3
Types of OTFTs
(e)
0.82
0.887
0.847
0.84
0.833
0.620
0.438
0.326
0.383
0.385
S-DNTT-10
S-DNTT-10 / Petnacene
μ_{lin} / cm²·V⁻¹·s⁻¹
BS-Time (Hours)
(f)
3.842
1.803
1.576
1.171
1.030
2.038
2.317
2.023
1.845
1.741
S-DNTT-10
S-DNTT-10 / Petnacene
μ_{sat} / cm²·V⁻¹·s⁻¹
BS-Time (Hours)

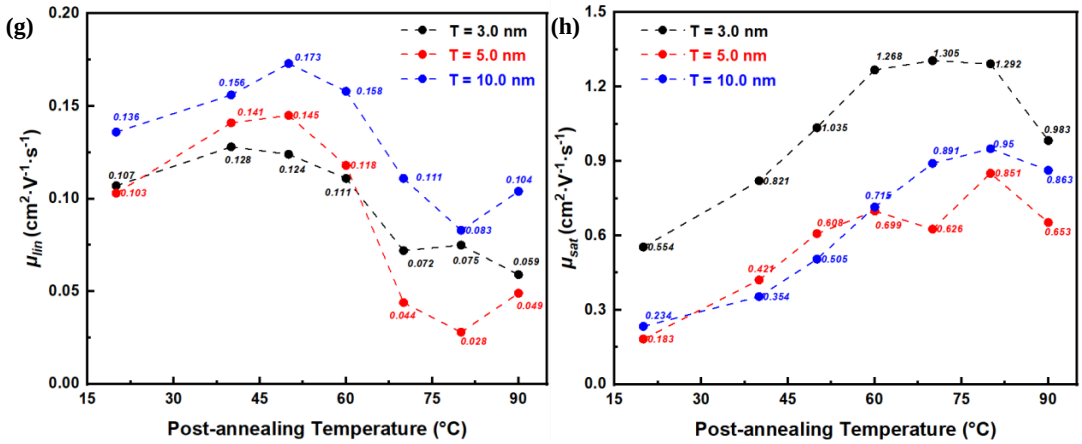


Figure 10.4 (a) Les caractéristiques électriques des courbes de sortie I_D-U_{DS} pour les OTFT basés sur S-DNTT-10/Pentacène (sous U_{GS} de -30,0 V) dans les OTFT TCBG basés sur S-DNTT-10 empilés avec différentes épaisseurs de films minces de pentacène. (b) La dépendance en tension de grille de la mobilité efficace en mode linéaire μ_{lin} (avec un U_{DS} biaisé à -1,0 V). (c) Résistance de contact source normalisée en largeur (R_S·W) des OTFT TCBG basés sur S-DNTT-10 et des OTFT TCBG basés sur S-DNTT-10/Pentacène dans cette étude. (R_S·W) en fonction de (U_{GS}-U_{onset}) pour ce dispositif. (d) La comparaison de la mobilité efficace à effet de champ, μ_{lin} (U_{DS} = -1,0 V) et µsat (U_{DS} = -40,0 V). Les dispositifs, étiquetés OTFT-1, OTFT-2 et OTFT-3, représentent respectivement les OTFT TCBG basés sur S-DNTT-10, les OTFT TCBG basés sur S-DNTT-10/Pentacène et les OTFT TCBG basés sur S-DNTT-10 avec pentacène déposé d'un côté. La comparaison des caractéristiques électroniques en fonction du temps de polarisation, (e) la mobilité à effet de champ en mode linéaire et (f) la mobilité à effet de champ en mode saturation. L'influence de différentes températures de recuit post-fabrication sur les OTFT basés sur S-DNTT-10 avec différentes épaisseurs de films minces de pentacène (L = 30 µm et W = 1000 µm) : (g) Mobilité à effet de champ linéaire μ_{lin} sous U_{DS} stressé = -1,0 V et (h) Mobilité à effet de champ en mode saturation μ_{sat} sous U_{DS} stressé = -30,0 V.

Les résultats mentionnés ci-dessus suggèrent que les approches proposées peuvent améliorer efficacement les performances des OTFT basés sur le S-DNTT-10, et il est à croire qu'elles offrent une orientation rationnelle pour le développement futur des OTFT. Néanmoins, plusieurs points méritent encore d'être explorés davantage. Par exemple, comment maintenir les électrodes parfaitement alignées avec le film mince de pentacène déposé d'un côté de manière plus efficace et simplifiée, ainsi que la possibilité d'employer d'autres matériaux semi-conducteurs organiques (OSC) avec une plus grande stabilité pour remplacer le pentacène.

De plus, il a été noté que les OTFT basés sur le S-DNTT-10 en configuration BCBG présentaient de mauvaises performances électriques, caractérisées notamment par une μ_{lin} significativement plus faible en raison d'une injection de charge inefficace. Ce problème a été attribué à la mauvaise morphologie et cristallinité du matériau S-DNTT-10 au niveau des électrodes, ce qui est défavorable au transport de charge. Nous pensons qu'améliorer ce phénomène vaut la peine d'être exploré dans les recherches futures. Pour améliorer davantage les performances électriques des OTFT basés sur le S-DNTT-10 en configuration BCBG, nous proposons deux approches différentes : (i) améliorer la morphologie des films minces de S-DNTT-10 au niveau des électrodes, et (ii) augmenter la zone d'injection de charge. Pour la première approche, des traitements tels que la modification par une monocouche auto-assemblée (SAM) sur la surface des électrodes pourraient être appliqués pour modifier l'énergie de surface et améliorer la morphologie des films minces de S-DNTT-10 déposés. Pour la deuxième approche, nous envisageons d'intégrer des électrodes en or dans le film mince de S-

DNTT-10 afin d'augmenter la zone d'injection de charge à la surface inférieure des électrodes. Nous avons obtenu des résultats préliminaires qui montrent que le courant de drain dans les caractéristiques de transfert des OTFT basés sur le S-DNTT-10 à double injection de charge est généralement plus élevé que celui des OTFT basés sur le S-DNTT-10 en configuration BCBG. Parallèlement, la μ_{lin} extraite pour ces OTFT est de 0,15 $cm^2 \cdot V^{-1} \cdot s^{-1}$, et le $U_{Th\text{-}lin}$ associé est de -22,98 V, tandis que la μ_{sat} et le $U_{Th\text{-}sat}$ sont respectivement de 0,463 $cm^2 \cdot V^{-1} \cdot s^{-1}$ et -27,0 V. Néanmoins, les paramètres extraits pour les OTFT basés sur le S-DNTT-10 en configuration BCBG montrent une grande dégradation. Pour μ_{lin} et $U_{Th\text{-}lin}$, ils sont respectivement de 0,0001 $cm^2 \cdot V^{-1} \cdot s^{-1}$ et -38,4 V, et pour μ_{sat} et $U_{Th\text{-}sat}$, ils sont respectivement de 0,0652 $cm^2 \cdot V^{-1} \cdot s^{-1}$ et -41,1 V. Bien que ces résultats montrent déjà quelques améliorations, il reste encore des points à explorer davantage dans l'avenir.

10.8 Résumé

Les transistors à film mince organique (OTFT) utilisent des matériaux semi-conducteurs organiques (OSC) comme couche active. Contrairement aux semi-conducteurs inorganiques, les OSC offrent des avantages tels que des sources de matériaux abondantes, une faible température de préparation, des processus simples, un coût réduit et une fabrication facile sur de grandes surfaces. Les OTFT sont largement utilisés dans les écrans flexibles, le papier électronique et les capteurs. Ils régulent le courant de sortie en appliquant une tension entre les électrodes de grille et de source, générant des charges dans l'OSC près de la couche diélectrique, formant ainsi un canal, et contrôlant la tension entre la source et le drain. Les propriétés des OSC, telles que leur structure moléculaire et la morphologie des films minces sous diverses conditions de préparation, sont essentielles aux performances des OTFT. Le S-DNTT-10, un nouveau matériau OSC, a montré d'excellentes caractéristiques de transport de charge dans les OTFT. Cette étude explore plus en profondeur les caractéristiques moléculaires et électriques des OTFT basés sur le S-DNTT-10 à l'aide d'outils avancés de nano-caractérisation.

Dans cette étude, tous les films minces de S-DNTT-10 ont été fabriqués par dépôt physique en phase vapeur (PVD). La morphologie du film mince de 25 nm de S-DNTT-10, déposé sur du SiO2 modifié avec de l'HMDS (une monocouche auto-assemblée, SAM), a été mesurée par microscopie à force atomique (AFM). Elle a révélé une structure en empilement couche par couche, suggérant une certaine continuité et un chevauchement entre les couches, ce qui indique que le transport de charge est peu influencé par les limites du réseau et que le chevauchement des électrons π est relativement important. Ces caractéristiques sont cruciales pour le transport de charge dans les films minces de S-DNTT-10. De plus, l'analyse de l'angle de contact avec de l'eau a montré que le film mince de S-DNTT-10 déposé thermiquement présente des propriétés hydrophobes, avec un angle supérieur à 90 degrés. L'étude a également examiné l'effet de l'énergie laser sur le film mince de S-DNTT-10, révélant qu'une énergie d'illumination plus élevée peut endommager la structure moléculaire et provoquer des brûlures en surface. Cela souligne la nécessité d'ajuster les paramètres d'illumination et de protéger le film lors de l'utilisation de la spectroscopie Raman pour étudier ses caractéristiques moléculaires.

Dans l'exploration des caractéristiques moléculaires du S-DNTT-10, la diffusion Raman a été utilisée pour obtenir ses modes de vibration moléculaire et les spectres correspondants. En utilisant la théorie de la fonctionnelle de la densité (DFT) et le logiciel **Gaussian 16W**, le spectre Raman théorique et les modes vibratoires spécifiques d'une molécule unique de S-DNTT-10 ont été identifiés. Ces vibrations sont principalement centrées sur les cycles thiophène en forme de S et les cycles étirés couplés aux chaînes alkyles, ce qui est essentiel pour comprendre le spectre Raman expérimental du S-DNTT-10 et les facteurs externes influençant ses vibrations moléculaires. De plus, la simulation des niveaux d'énergie des orbitales moléculaires a révélé que le S-DNTT-10 possède un HOMO relativement élevé de -5,46 eV, contribuant à sa stabilité dans l'air. La fonction d'onde des électrons π est principalement concentrée dans les cycles thiophène en forme de S. Ces informations sont précieuses pour étudier l'impact des facteurs externes sur les propriétés électriques des OTFT basés sur le S-DNTT-10 à travers les vibrations moléculaires et les signaux Raman.

Concernant le spectre Raman expérimental du film mince de S-DNTT-10, en utilisant trois longueurs d'onde différentes (532 nm, 633 nm et 785 nm), les résultats ont montré que la source lumineuse de 532 nm, avec une longueur d'onde plus courte et une énergie photonique plus élevée, était plus efficace pour générer un spectre Raman dans les mêmes conditions de photons incidents. De plus, à mesure que l'épaisseur du film mince de S-DNTT-10 augmente, l'intensité du signal de diffusion Raman et les positions des pics de certains modes Raman changent. Cela suggère que l'épaississement du film influence l'orientation moléculaire et la structure géométrique du S-DNTT-10, ce qui pourrait affecter les caractéristiques de transport de charge au sein du film. Ces résultats soulignent l'importance d'optimiser l'épaisseur des films minces de S-DNTT-10 pour les applications OTFT.

Pour induire le phénomène de diffusion Raman amplifiée de surface (SERS) et résoudre le faible rapport signal/bruit du spectre Raman dans les films minces de S-DNTT-10 à faible concentration moléculaire, des films minces d'or (Au) de quelques nanomètres ont été déposés sur la surface du S-DNTT-10 pour former des nano-structures. Initialement, des films d'or de 1 nm, 3 nm, 5 nm et 6 nm ont été déposés sur du SiO2 à un taux de 1,0 Å/s sous vide. La microscopie électronique à balayage (SEM) a confirmé que la taille des nano-structures augmentait avec l'épaisseur, prouvant la faisabilité de cette méthode. Ensuite, des films d'or de 3 nm, 5 nm, 10 nm et 20 nm ont été déposés sur des films de S-DNTT-10 de 25 nm. Lors de l'ajustement de la longueur d'onde de la lumière d'excitation, il a été constaté que le laser de 532 nm ne pouvait pas exciter un spectre Raman efficace, tandis que les lasers de 633 nm et 785 nm pouvaient collecter des spectres SERS, celui de 633 nm produisant l'intensité la plus élevée. Le film d'or de 5 nm a également généré un signal SERS relativement fort. En outre, le spectre SERS du S-DNTT-10 différait de son spectre Raman conventionnel, probablement en raison de l'influence des atomes d'or sur la structure moléculaire lors du dépôt. Cela suggère que, lors de la fabrication d'OTFT basés sur le S-DNTT-10 en configuration Top-Contact-Bottom-Gate par dépôt thermique, les électrodes métalliques peuvent augmenter le désordre

moléculaire dans les couches de S-DNTT-10 en contact, réduisant ainsi le transport de charge dans cette région.

En plus de l'étude des caractéristiques de vibration moléculaire du S-DNTT-10, des recherches supplémentaires ont été menées sur les performances électriques des OTFT basés sur ce matériau. Un effet non linéaire a été observé dans les caractéristiques de sortie, dû à une résistance de contact importante à la source, ainsi qu'un effet de saturation précoce dans certains dispositifs. En utilisant la théorie de l'Approximation du Canal Progressif (GCA), un modèle physique a été développé pour expliquer ce phénomène. Afin d'éviter les erreurs expérimentales, la technique de diffusion Raman a été utilisée pour explorer les performances électriques des OTFT et vérifier si la lumière incidente affectait le dispositif. Les résultats ont montré que la lumière incidente n'avait aucun impact significatif sur les performances électriques, confirmant l'aptitude de la technique Raman à l'étude des caractéristiques moléculaires du S-DNTT-10 dans les OTFT.

En intégrant les résultats des analyses du spectre Raman et SERS, il a été déterminé que la réduction des performances des OTFT sous l'effet du stress de polarisation est principalement due à l'influence du champ électrique continu sur l'orientation moléculaire du S-DNTT-10 dans le canal, ainsi qu'à l'augmentation de la tension de seuil causée par l'électrolyse de l'eau. De plus, la caractérisation par KPFM a révélé que le champ électrique continu améliore l'injection et l'extraction de charge dans les OTFT TCBG basés sur le S-DNTT-10. Ces résultats suggèrent que l'effet de stress de polarisation affecte principalement le transfert de charge dans le canal. Cela implique qu'une encapsulation efficace du canal des OTFT, empêchant le contact avec les molécules d'eau dans l'air et stabilisant l'orientation moléculaire, pourrait atténuer la dégradation des performances électriques causée par cet effet.

Le champ électrique continu et le traitement de recuit post-fabrication influencent tous deux les performances des OTFT basés sur le S-DNTT-10. Les mesures par AFM, analyse de l'angle de contact, diffusion Raman et KPFM ont révélé que le recuit post-fabrication modifie les propriétés du film mince de S-DNTT-10, notamment ses caractéristiques moléculaires, l'énergie de surface de l'HMDS et les propriétés de contact entre le film S-DNTT-10 et les électrodes. Ces modifications affectent les performances électriques du dispositif. À des températures de recuit plus élevées, le transport de charge dans le canal est altéré, les caractéristiques moléculaires sous les électrodes sont modifiées, la résistance de contact augmente et l'efficacité d'injection et d'extraction de charge diminue, affaiblissant ainsi les performances globales du dispositif. Cela montre que le recuit affecte non seulement la région du canal, mais aussi l'interface entre les électrodes et le S-DNTT-10. De plus, il existe une température de recuit optimale (T_{post}) qui maximise les performances du dispositif. T_{post} est également influencée par la température de dépôt du substrat (T_{sub}) du S-DNTT-10 pendant la PVD, T_{post} diminuant avec l'augmentation de T_{sub}. Cela suggère qu'il existe un arrangement moléculaire optimal pour le transport de charge dans le film mince de S-DNTT-10 déposé

thermiquement, ajustable en modifiant T_{post} et T_{sub}. Ces informations sont précieuses pour optimiser les performances des OTFT basés sur le S-DNTT-10.

Les simulations DFT précédentes du niveau d'énergie orbitale de la molécule unique de S-DNTT-10 ont montré que ce matériau possède un niveau HOMO relativement élevé et une barrière énergétique avec le niveau de Fermi de l'or. Cela explique l'effet non linéaire observé dans les caractéristiques de sortie des OTFT TCBG basés sur le S-DNTT-10 avec des électrodes en or. Le dépôt d'un film mince de pentacène sur la surface du S-DNTT-10 permet de réduire cet effet non linéaire et de diminuer la résistance de contact à la source, comme confirmé par des mesures KPFM, améliorant ainsi l'efficacité de l'injection de charge. Cependant, l'ajout de cette couche OSC réduit la mobilité effective (μ_{sat}) en régime de saturation. Une approche créative a été adoptée en ne déposant du pentacène que sur un côté d'une électrode, améliorant ainsi l'efficacité de l'injection de charge et le μ_{sat} lorsque l'électrode est utilisée comme source. En revanche, lorsque l'électrode est utilisée comme drain, le dispositif présente un effet non linéaire et un μ_{sat} réduit par rapport aux OTFT TCBG basés sur le S-DNTT-10. Ces résultats expliquent la réduction du μ_{sat} et proposent une nouvelle stratégie pour améliorer les performances des OTFT en utilisant des couches supplémentaires d'OSC. Pour les OTFT BCBG basés sur le S-DNTT-10, l'effet non linéaire est plus sévère et les performances sont faibles. En utilisant l'effet flou du masque d'ombre pour ne déposer le pentacène que sur la surface des électrodes, les performances se sont considérablement améliorées par rapport aux OTFT BCBG sans modification. Cela suggère que les faibles performances des OTFT BCBG sont liées aux caractéristiques moléculaires du S-DNTT-10 au niveau des électrodes et de l'interface. En outre, rapprocher les électrodes de la couche diélectrique de SiO_2 et augmenter la zone d'injection de charge améliorent encore les performances, offrant une autre approche pour optimiser les OTFT BCBG basés sur le S-DNTT-10.

En s'appuyant sur les recherches précédentes sur le S-DNTT-10, cette thèse approfondit l'analyse des vibrations moléculaires du S-DNTT-10, révélant la relation entre les facteurs externes influençant les performances électriques et les changements dans les vibrations moléculaires. De plus, des améliorations ont été apportées aux caractéristiques d'interface entre le film mince de S-DNTT-10 et les électrodes, améliorant ainsi les performances électriques des OTFT basés sur ce matériau. L'élargissement de cette compréhension à d'autres matériaux et procédés favorisera le développement des transistors à film mince organique et permettra des applications électroniques uniques

Enfin, nous espérons que les résultats et analyses de cette thèse pourront servir de guide et fournir des informations utiles pour le développement futur des OTFT basés sur le S-DNTT-10 et d'autres matériaux semi-conducteurs organiques (OSC).

List of contribution in Ph. D study

Two pre-submissions in international journals

- **H.B. Wang**, O. Simonetti, N. Bercu, F. Etienne, S. Potiron, O. Et Thakafy, R. Mittapalli, P.M. Adam, L. Giraudet; 36 pages; "The improvement of electrical characteristics in S-DNTT-10-based OTFTs via extra OSC thin-film" – (to be submitted soon)
- **H.B. Wang**, O. Simonetti, N. Bercu, F. Etienne, S. Potiron, O. Et Thakafy, R. Mittapalli, A. Rumyantseva, P.M. Adam, L. Giraudet; 34 pages; "The studies of Raman scattered technology on S-shaped dinaphtho[2,1-b:2′,1′-f] thieno[3,2-b] thiophene-10 (S-DNTT-10) and the biased OTFTs"

Presentation of papers with abstracts at international conferences

- **H.B Wang**, Olivier Simonetti, Oumaima Et-Thakafy, Nicolas Bercu, Rakesh Mittapalli, Pierre-Michel Adam, Louis Giraudet, "Investigations of instabilities in organic transistors using in-situ Raman Spectroscopy" TERS-8 conference, Sorbonne University Paris, November 2022 – Poster
- **H.B. Wang**, O. Simonetti, N. Bercu, F. Etienne, S. Potiron, O. Et Thakafy, R. Mittapalli, A. Rumyantseva, P.M. Adam, L. Giraudet, "Analysis of bias-stress effect on S-DNTT-10-based OTFTs via SERS", International Workshop on Metallic Nano-Objects, MNO2023, UT Troyes September 2023. – Poster
- **H.B. Wang**, O. Simonetti, N. Bercu, F. Etienne, S. Potiron, O. Et Thakafy, R. Mittapalli, P.M. Adam, L. Giraudet, "The improvement of electrical characteristics in S-DNTT-10-based OTFTs via extra OSC thin-film" EMRS Spring Meeting, 2024 - **Oral presentation**

Publications at national conferences with abstracted papers

- **H.B. Wang**, O. Simonetti, O. Et Thakafy, R. Mittapalli, P.M. Adam, L. Giraudet, "The exploration of uneven early saturated effect in S-DNTT-10–OTFT based", Science et Technologie des Systèmes π-Conjugués (SPIC), Saint Malo, December 2022 – Poster
- Et-thakafy, **H.B. Wang**, O. Simonetti, N. Bercu, R. Mittapalli, F. Etienne, S. Potiron, P.M. Adam, L. Giraudet, "Caractérisations couplées I-V/Raman/KPFM des transistors organiques à film mince à base S-DNTT-10", Science et Technologie des Systèmes π-Conjugués (SPIC), Saint Malo, December 2022 – Oral presentation
- Nicolas BERCU, Oumaima ET THAKAFY, **Haobing WANG**, Olivier SIMONETTI, Pierre-Michel ADAM, Louis GIRAUDET, « Développement d'un système pour des mesures couplées spectroscopie Raman / caractérisation électrique IV sur des composants semi-conducteurs », Science et Technologie des Systèmes π-Conjugués (SPIC), Saint Malo, December 2022 – Poster

Oral presentations at national or international conferences without proceedings

- **H.B. Wang,** O. Simonetti, O. Et-thakafy Obaidi, N. Bercu, R. Mittapalli, F. Etienne, S. Potiron, P.M. Adam, L. Giraudet. 2023 NANO-PHOT Research Day at Université de Reims. Oral presentation “Investigations of instabilities in organic transistors using in-situ Raman Spectroscopy” - Oral presentation
- **H.B. Wang**, O. Simonetti, N. Bercu, F. Etienne, S. Potiron1, O. Et Thakafy, R. Mittapalli, P.M. Adam, L. Giraudet. 2024 NANO-PHOT Research Day at Université de Reims. Oral presentation “The improvement of electrical characteristics in S-DNTT-10-based OTFTs via extra OSC thin-film” - Oral presentation

Haobing WANG

Doctorat : Matériaux, Mécanique, Optique et Nanotechnologie

Année 2024

Étude approfondie des capacités et optimisation des transistors organiques à couche mince à base de S-DNTT-10

Avec les avancées technologiques, les dispositifs électroniques à semi-conducteurs sont devenus essentiels dans la vie quotidienne et l'industrie. Initialement fabriqués avec des semi-conducteurs inorganiques, les TFT ont évolué vers les transistors organiques à film mince (OTFT), utilisant des semi-conducteurs organiques (OSC) comme couche active. Leurs performances se sont améliorées, faisant des OTFT une alternative prometteuse aux TFT inorganiques. Cette thèse se concentre sur le matériau OSC et examine ses propriétés moléculaires, les performances électriques des OTFT basés sur le S-DNTT-10, ainsi que des stratégies d'optimisation. Nous avons combiné des simulations théoriques avec des techniques expérimentales comme l'AFM, la KPFM, la spectroscopie Raman, et des simulations DFT. La spectroscopie Raman, incluant la SERS, a révélé et détaillé les propriétés vibratoires du S-DNTT-10. Nous avons également étudié les effets d'une exposition prolongée à un champ électrique et d'un recuit sur les performances des OTFT. Cette étude intègre pour la première fois l'AFM, la KPFM, la spectroscopie Raman et les mesures IV pour analyser ces effets. Nous avons proposé d'ajouter une couche d'OSC sur le S-DNTT-10 pour améliorer la stabilité et les performances. Les résultats montrent que l'optimisation du processus de fabrication réduit la résistance de contact, améliore l'injection de charge et renforce les performances, soulignant le potentiel du S-DNTT-10 pour l'électronique flexible.

Mots clés : électronique organique – transistors en couches minces – spectroscopie Raman – microscopie en champ proche.

Comprehensive Performance Study and Optimization of S-DNTT-10-based Organic Thin-film Transistors

With technological advancements, semiconductor-based electronic devices have become indispensable. Among these, thin-film transistors (TFTs) play a crucial role in electronic systems. Initially, TFTs were made from inorganic semiconductors, and with the development have shifted to organic thin-film transistors (OTFTs), which employed the organic semiconductor (OSC) material as the active layer. This thesis focuses on the S-DNTT-10, and explores its molecular properties, the electrical characteristics of S-DNTT-10-based OTFTs, and strategies for optimizing performance. In this study, we combined theoretical simulations with experimental techniques such as atomic force microscopy (AFM), Kelvin probe force microscopy (KPFM), and Raman spectroscopy, along with density functional theory (DFT) simulations. Raman spectroscopy was employed to investigate the molecular vibrations of S-DNTT-10, revealing and replenishing its detailed vibrational properties for the first time. Additionally, we conducted a comprehensive study on the effects of prolonged stressed electric field exposure and annealing treatment on the electrical performance of S-DNTT-10-based OTFTs. This study marks the first integration of AFM, KPFM, Raman spectroscopy, and IV characteristics to examine these effects, providing insights into how external factors influence device performance. Moreover, we proposed the addition of an extra OSC layer on the S-DNTT-10 surface to enhance device performance and stability. These findings underscore the potential of S-DNTT-10 as a promising material for future flexible electronics.

Keywords: organic electronics – thin film transistors – Raman spectroscopy – near-field microscopy.

Thèse réalisée en partenariat entre :